INFLUENCE OF SOLUTION TEMPERATURE ON CHEMICAL DEPOSITED MAGNESIUM AND CORROSION BEHAVIOR OF BARE AND COATED MAGNESIUM IN SIMULATED BODY FLUID

By

JIAYING WANG

A dissertation submitted in partial fulfillment of
the requirements for the degree of

DOCTOR OF PHILOSOPHY

WASHINGTON STATE UNIVERSITY
School of Mechanical and Materials Engineering

DECEMBER 2023

To the Faculty of Washington State University:

The members of the Committee appointed to examine the dissertation of JIAYING WANG find it satisfactory and recommend that it be accepted.

Qizhen Li, Ph.D., Chair

Yuehe Lin, Ph.D.

Min-Kyu Song, Ph.D.

David P. Field, Ph.D.

ACKNOWLEDGMENTS

I received invaluable help during my graduate study. Firstly, special acknowledgment is given to Washington State University (WSU) for providing me with an academic, creative, and encouraging environment to study. Furthermore, I would like to thank the School of Mechanical and Material Engineering (MME) Department for its excellent facilities and services. The teaching assistant experience in the School of Mechanical and Material Engineering (MME) Department not only financially supported me but also gave me good working experience.

I shall extend my deepest gratitude to Dr. Qizhen (Katherine) Li for her patient guidance, special instructions, and continuous support during my Ph.D. study and research life. Without her professional advice, unconditional support, and insightful feedback throughout, my dissertation could not have been completed. She also encouraged and inspired me to have strong faith and a clear academic career plan for the future as a valuable friend. I am indebted to her for her encouragement, wisdom, and friendship over the last few years.

Then, I would like to mainly express my deepest and special thanks to Dr. Yuehe Lin, Dr. Min-Kyu Song, and Dr. David Field for their time and patience as my academic committee members and for presenting my defense. They taught me a lot in their courses and inspired my research ideas. Their constructive and scientific comments and advice contributed to the accomplishment of my thesis.

Next, I want to express my heartfelt gratitude and special thanks to all the professors and staff who gave me considerable knowledge and help during my graduate life.

My sincere thanks also go to all my group members: Dr. Ning Zou, Dr. Yuzhi Zhu, Wenli Zhao, and Junyan Liang. I had the great pleasure of working with them during these years. I also appreciate their kind help and advice on my project.

Most importantly, my heartfelt thanks also go to my beloved parents for their selfless love and mental and financial support. Their unshakable love and care are the source of my strength and the great fortune of my life. Finally, I want to thank all my close friends Xiaoqing Ma, Panpan Dong, Xiahui Zhang, Xiaoyu Li, Fanhe Meng, Hua Deng, Xuesi Zhu, Hangyu Tian, Xuewei Fu, Shaofang Fu, and Chenxu Wang. It was their help and invariable encouragement that made my study and life in Pullman enjoyable.

INFLUENCE OF SOLUTION TEMPERATURE ON CHEMICAL DEPOSITED MAGNESIUM AND CORROSION BEHAVIOR OF BARE AND COATED MAGNESIUM IN SIMULATED BODY FLUID

Abstract

by Jiaying Wang, Ph.D.
Washington State University
December 2023

Chair: Qizhen Li

Magnesium (Mg) is a promising biomedical material due to its suitable mechanical properties and biocompatibility. The rapid dissolution in the physiological environment limits its application. There has been growing attention to pure Mg with different microstructures and coated Mg by chemical bath deposition method for bone tissue clinical use. However, the influences of microstructure on mechanical property and corrosion resistance of Mg and the relationships among the substrate, bath temperature, and coating quality are undetermined. This research achieved the pure Mg sheet by rolling and post-heat treatment. The in-situ coating was produced in a chemical solution containing Ca^{2+} and HPO_4^{2-} under different temperatures of 37 °C-100 °C. The polarization and 30-day immersion tests were carried out to study the anti-corrosion performance of bare and coated Mg. The Mg mechanical property and the coating formation mechanism were discussed. According to the test results, it was concluded that the grain boundaries played a dual role in the mechanical property and corrosion behavior. Because they worked as physical barriers to improve strength and corrosion resistance, they also acted as

crystallographic defects resulting in the adverse function when the crystalline size was super fine. The corrosion products were primarily $Mg(OH)_2$. Calcium/magnesium phosphates and carbonates were deposited as thin outer precipitates. For the coated Mg, although improving the applied temperature offered more energy for the nucleation and growth of the precipitations, the substrate dissolution was accelerated. The coated Mg obtained at 70 ℃ on the substrate rolled at 200 ℃ had the best anti-corrosion behavior. The coating was in a double-layer structure. The inner layer was $Mg(OH)_2$, and the outer one contained good-crystallized $CaHPO_4{\cdot}2H_2O$ and a small amount of $Ca_{10}(PO_4)_6(OH)_2$ and MgO. Due to plenty of Ca and P from the coating dissolution, the newly formed corrosion products had the same element content as the outer layer of the coating. They could retard the further erosion of the inner substrate. Because of this self-healing effect, the substrate was protected during the whole immersion process. This dissertation provides a combined strategy of substrate preparation and coating deposition to develop Mg-based materials for practical applications.

TABLE OF CONTENTS

Page

LIST OF TABLES

Page

LIST OF FIGURES

Page

Dedication

To my beloved parents

CHAPTER ONE: INTRODUCTION

1.1 Motivations

In recent years, more and more magnesium (Mg) and Mg alloys have been applied in vast fields such as industry, aerospace [1-2], and biomedical applications [3-5]. It is because of their outstanding mechanical and physical properties. They have low densities, good electrical and thermal conductivities, nontoxicity, and biocompatibility [6-9]. It is also very economical and sustainable to apply the Mg- series materials widely [10]. Because the amount of element Mg is abundant [11], especially in the ocean [12].

The most potential application of Mg in recent years is biomaterial implants [13-15]. Since solvable Mg-based materials do not need to be taken off after the first implantation [16-17], this will avoid the follow-up surgical operation, extra healing time, additional medicine, or costs [16, 18]. As an implanted biomaterial, it should be long-period stable for bone tissue growth and healing [19-20]. However, Mg is active [21-22]. Mg implants would be highly corroded in the human body [23-24]. It is because of the low standard potential [25]. In addition, the porous oxide film formed on the Mg surface during the eroding procedure cannot effectively protect the inner Mg substrate [26]. When chloride ions are present in the corrosion environment or the pH value is lower than 11.4, the corrosion is greatly accelerated [27-28]. In the human body fluid, there are many kinds of ions, including chloride ions, and the pH value is about 7.4 [29-30]. From this, Mg will be highly corroded, and its mechanical properties will also be declined in the human body [31-32]. Thus, the rapid corrosion rate limits Mg applications [33-34]. Moreover, reducing the corrosion rate of pure Mg is significant and necessary [29, 35].

For the problem mentioned above, there are two effective mainstream ways. The first method is changing the microstructure [36-38]. Many studies have found that Mg with different grain sizes has different corrosion resistance [39-41]. However, the current findings are contradictory [42-48]. Some studies have pointed out that grain boundaries can be regarded as crystallographic defects. So the refined microstructure would be harmful to the anti-corrosion behavior [49-50]. On the contrary, some results have shown that the grain boundaries could be protective barriers to slow corrosion [51-52]. Therefore, in this work, it is crucial to find the relationship between the microstructure and the corrosion behavior of pure Mg.

The second direct way is making an in-situ coating on the Mg substrate [31, 53]. A thin coating layer deposited on the Mg surface can be a barrier to separate the substrate from the corrosive environment. Therefore, the substrate will be protected [24, 54]. At present, the non-toxic and biocompatible calcium phosphate coatings obtained by the easy chemical bath deposition method are attractive [55-57]. Because many different types of calcium phosphate materials can convert each other through simple pH value changes [58-59], the coating composites and quality largely depend on preparation conditions [60-64]. Thus, in this research, finding a suitable condition to obtain a uniform and effective coating is imperative. Besides, studying the influence of the substrate and bath temperature on coating quality is valuable and instructional.

1.2 Objectives of the Research

It has excellent potential to improve the corrosion behavior of pure Mg by changing the substrate microstructure and preparing coatings in situ. The overall goal of this study is to enhance the mechanical properties and corrosion resistance of pure Mg in simulated body fluid (SBF) by

designing the plastic deformation routines and coating process temperatures. The related mechanism also needs to be analyzed and studied. The specific objectives of this research are as follows.

Objective 1: To explore the effect of processing conditions on microstructure and correlated mechanical properties of pure Mg. Mg samples with different grain sizes are obtained by different rolling and thermal treating processes. The change in the microstructure is characterized by Optical Microscopy (OM).

Objective 2: To reveal the effect of microstructure on the corrosion resistance of pure Mg. The electrochemical and long-term anti-corrosion behavior is tested by polarization and 30-day immersion tests in static SBF. According to the test results of Scanning Electron Microscopy (SEM), Energy Dispersive Spectrometer (EDS), X-ray Diffraction (XRD), and water contact angle, the degradation process and mechanism of pure Mg in SBF are discussed.

Objective 3: To design and synthesize a protective coating directly on the pure Mg substrate by the traditional chemical bath deposition method at different temperatures. After a series of characterizations and electrochemical examinations, the coating formation mechanism is explained. Also, the effect of coating temperature on coating quality is presented.

Objective 4: To demonstrate the anti-corrosion mechanism of the coated Mg. The 30-day soaking performances in SBF are recorded and studied to understand the dissolution process.

1.3 Significance of the Research

This study provides comprehensive insights into improving the pure Mg corrosion behavior in the SBF. Pure Mg is first rolled and heated under different conditions and then coated by chemical bath deposition under different temperatures. The relationships between the rolling process conditions, microstructures, mechanical properties, and corrosion performances of bare Mg are systematically investigated. Furthermore, the coating characterization and the mechanism of coating formation are comprehensively studied. Meanwhile, the influence of bath temperature on the quality of coating on the pure Mg is also explained and discussed. Besides the electrochemical test, the exploration of the pH value of SBF containing the bare Mg and coated Mg indicates their corrosion performance. It helps a fundamental understanding of corrosion and anti-corrosion mechanisms.

This research is significant because exploring the relationship between the grain size and corrosion resistance of pure Mg helps predict the corrosion properties of Mg and Mg alloys. It is also essential to explore the appropriate solutions to solve the problems caused by the poor corrosion resistance of Mg. In addition, this research is guiding significant for the further study of improving the anti-corrosion behavior of Mg-based materials.

1.4 Organization of the Dissertation

This dissertation is composed of seven chapters. The specific contents of each chapter are shown in **Figure 1.1** and described below.

Chapter 1 presents a comprehensive introduction, including the motivations, objectives, objectives, significance, and organization of this dissertation.

Chapter 2 provides a reference review of pure Mg as a biomaterial and its remaining challenges. The existing solutions and their development in enhancing the performance of Mg in the SBF are also shown.

Chapter 3 demonstrates the raw materials, bare and coated Mg sample preparation processes, characterizations, and corrosion tests in details.

Chapter 4 presents the pure Mg different microstructures after different preparation conditions and discusses the relationship between the microstructure and mechanical properties.

Chapter 5 highlights the effect of grain refinement on the corrosion behavior of pure Mg in the electrochemical and 30-day SBF immersion tests. And the corrosion mechanism is discussed.

Chapter 6 presents the mechanism of coating growth on the Mg substrate by the traditional chemical deposition method under different bath temperatures. Also, the effect of operating temperature on the coating quality is analyzed by an electrochemical test and immersion experiment in static simulated body fluid. The long-term anti-corrosion resistance mechanism of the best-coated Mg is discussed in detail.

Finally, **Chapter 7** demonstrates the result conclusions and further work directions of this dissertation. Besides, the following progress ideas and precautions for future work are indicated.

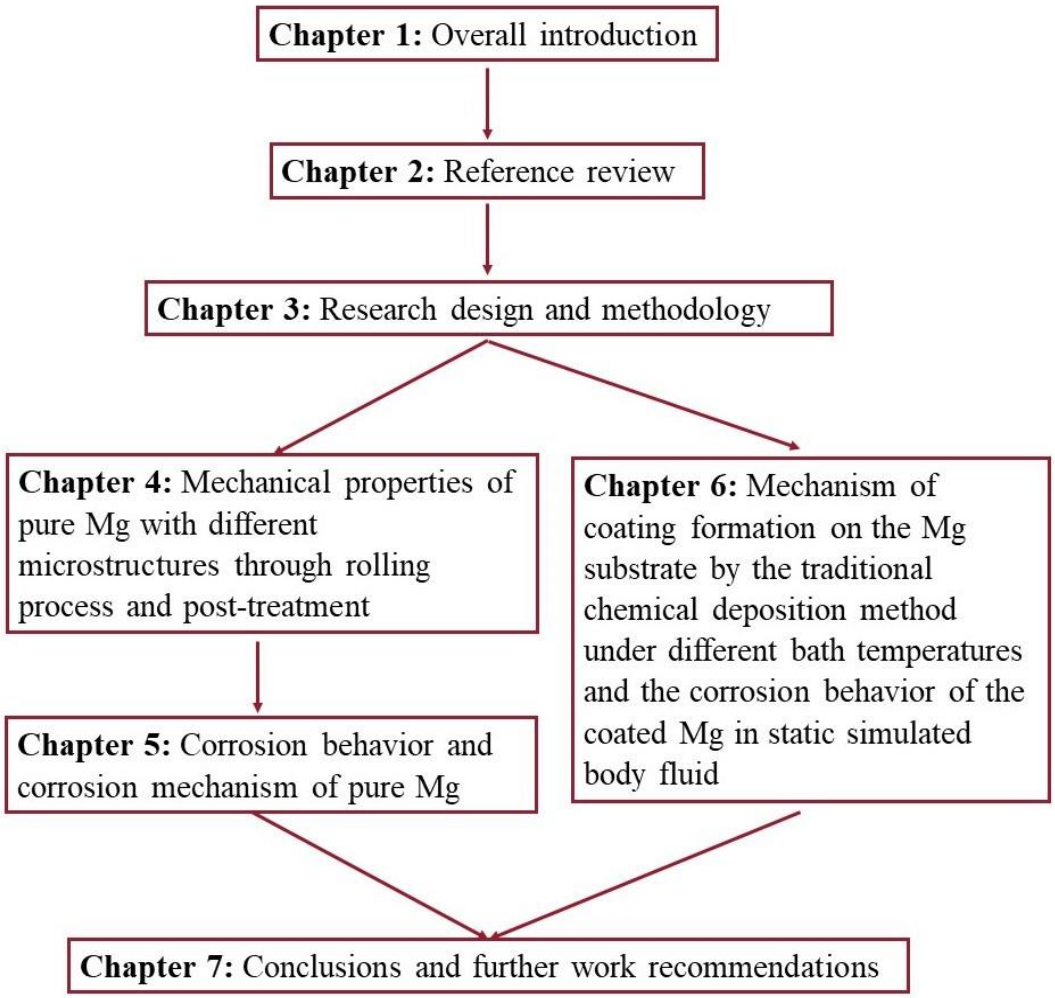

Figure 1.1: Schematic diagram of the dissertation outline.

REFERENCES

1. Friedrich, H.; Schumann, S., Research for a “new age of magnesium” in the automotive industry. Journal of Materials Processing Technology **2001,** 117 (3), 276-281.

2. Blawert, C.; Hort, N.; Kainer, K., Automotive applications of magnesium and its alloys. Trans. Indian Inst. Met **2004,** 57 (4), 397-408.

3. Kulekci, M. K., Magnesium and its alloys applications in automotive industry. The International Journal of Advanced Manufacturing Technology **2008,** 39 (9-10), 851-865.

4. Li, N.; Zheng, Y., Novel magnesium alloys developed for biomedical application: a review. Journal of Materials Science & Technology **2013,** 29 (6), 489-502.

5. Witte, F.; Kaese, V.; Haferkamp, H.; Switzer, E.; Meyer-Lindenberg, A.; Wirth, C.; Windhagen, H., In vivo corrosion of four magnesium alloys and the associated bone response. Biomaterials **2005,** 26 (17), 3557-3563.

6. Mordike, B.; Ebert, T., Magnesium: Properties—applications—potential. Materials Science and Engineering: A **2001,** 302 (1), 37-45.

7. Wang, Y.; Wei, M.; Gao, J., Improve corrosion resistance of magnesium in simulated body fluid by dicalcium phosphate dihydrate coating. Materials Science and Engineering: C **2009,** 29 (4), 1311-1316.

8. Ezhilselvi, V.; Nithin, J.; Balaraju, J.; Subramanian, S., The influence of current density on the morphology and corrosion properties of MAO coatings on AZ31B magnesium alloy. Surface and Coatings Technology **2016,** 288, 221-229.

9. Easton, M.; Gibson, M.; Beer, A.; Barnett, M.; Davies, C.; Durandet, Y.; Blacket, S.; Chen, X.; Birbilis, N.; Abbott, T., The application of magnesium alloys to the lightweighting of automotive structures. In Sustainable Automotive Technologies 2012, Springer: 2012; pp 17-23.

10. Aghion, E.; Bronfin, B. In Magnesium alloys development towards the 21st century, Materials Science Forum, Trans Tech Publ: 2000; pp 19-30.

11. Handler, M. R.; Baker, J. A.; Schiller, M.; Bennett, V. C.; Yaxley, G. M., Magnesium stable isotope composition of Earth's upper mantle. Earth and Planetary Science Letters **2009,** 282 (1-4), 306-313.

12. Culkin, F.; Cox, R. In Sodium, potassium, magnesium, calcium and strontium in sea water, Deep Sea Research and Oceanographic Abstracts, Elsevier: 1966; pp 789-804.

13. Kirkland, N. T.; Birbilis, N.; Staiger, M., Assessing the corrosion of biodegradable magnesium implants: a critical review of current methodologies and their limitations. Acta biomaterialia **2012,** 8 (3), 925-936.

14. Sanchez, A. H. M.; Luthringer, B. J.; Feyerabend, F.; Willumeit, R., Mg and Mg alloys: how comparable are in vitro and in vivo corrosion rates? A review. Acta biomaterialia **2015,** 13, 16-31.

15. Jafari, S.; Raman, R. S.; Davies, C. H., Corrosion fatigue of a magnesium alloy in modified simulated body fluid. Engineering Fracture Mechanics **2015,** 137, 2-11.

16. Shuai, C.; Li, S.; Peng, S.; Feng, P.; Lai, Y.; Gao, C., Biodegradable metallic bone implants. Materials Chemistry Frontiers **2019,** 3 (4), 544-562.

17. Prakasam, M.; Locs, J.; Salma-Ancane, K.; Loca, D.; Largeteau, A.; Berzina-Cimdina, L., Biodegradable materials and metallic implants—a review. Journal of functional biomaterials **2017,** 8 (4), 44.

18. Chandra, G.; Pandey, A., Biodegradable bone implants in orthopedic applications: a review. Biocybernetics and Biomedical Engineering **2020,** 40 (2), 596-610.

19. Wang, H.; Guan, S.; Wang, X.; Ren, C.; Wang, L., In vitro degradation and mechanical integrity of Mg–Zn–Ca alloy coated with Ca-deficient hydroxyapatite by the pulse electrodeposition process. Acta Biomaterialia **2010,** 6 (5), 1743-1748.

20. Kraus, T.; Fischerauer, S. F.; Hänzi, A. C.; Uggowitzer, P. J.; Löffler, J. F.; Weinberg, A. M., Magnesium alloys for temporary implants in osteosynthesis: in vivo studies of their degradation and interaction with bone. Acta biomaterialia **2012,** 8 (3), 1230-1238.

21. Baril, G.; Pebere, N., The corrosion of pure magnesium in aerated and deaerated sodium sulphate solutions. Corrosion Science **2001,** 43 (3), 471-484.

22. Zeng, R.-c.; Zhang, J.; Huang, W.-j.; Dietzel, W.; Kainer, K.; Blawert, C.; Wei, K., Review of studies on corrosion of magnesium alloys. Transactions of Nonferrous Metals Society of China **2006,** 16, s763-s771.

23. Zeng, R.; Dietzel, W.; Witte, F.; Hort, N.; Blawert, C., Progress and challenge for magnesium alloys as biomaterials. Advanced engineering materials **2008,** 10 (8), B3-B14.

24. Gray, J.; Luan, B., Protective coatings on magnesium and its alloys—a critical review. Journal of alloys and compounds **2002,** 336 (1-2), 88-113.

25. Genders, J. D.; Pletcher, D., Studies using microelectrodes of the Mg (II)/Mg couple in tetrahydrofuran and propylene carbonate. Journal of electroanalytical chemistry and interfacial electrochemistry **1986,** 199 (1), 93-100.

26. Peng, X.; Barteau, M., Characterization of oxide layers on Mg (0001) and comparison of H2O adsorption on surface and bulk oxides. Surface Science **1990,** 233 (3), 283-292.

27. Song, Y.; Shan, D.; Han, E., Electrodeposition of hydroxyapatite coating on AZ91D magnesium alloy for biomaterial application. Materials letters **2008,** 62 (17-18), 3276-3279.

28. Zhao, M.-C.; Liu, M.; Song, G.-L.; Atrens, A., Influence of pH and chloride ion concentration on the corrosion of Mg alloy ZE41. Corrosion Science **2008,** 50 (11), 3168-3178.

29. He, S.-Y.; Yue, S.; Chen, M.-F.; Liu, D.-B.; Ye, X.-Y., Microstructure and properties of biodegradable β-TCP reinforced Mg-Zn-Zr composites. Transactions of Nonferrous Metals Society of China **2011,** 21 (4), 814-819.

30. Feng, A.; Han, Y., The microstructure, mechanical and corrosion properties of calcium polyphosphate reinforced ZK60A magnesium alloy composites. Journal of Alloys and Compounds **2010,** 504 (2), 585-593.

31. Bakhsheshi-Rad, H.; Hamzah, E.; Kasiri-Asgarani, M.; Jabbarzare, S.; Iqbal, N.; Kadir, M. A., Deposition of nanostructured fluorine-doped hydroxyapatite–polycaprolactone duplex coating to enhance the mechanical properties and corrosion resistance of Mg alloy for biomedical applications. Materials Science and Engineering: C **2016,** 60, 526-537.

32. Liu, G.-y.; Tang, S.-w.; Chuan, W.; Jin, H.; Li, D.-c., Formation characteristic of Ca–P coatings on magnesium alloy surface. Transactions of Nonferrous Metals Society of China **2013,** 23 (8), 2294-2299.

33. Ferrando, W., Review of corrosion and corrosion control of magnesium alloys and composites. Journal of Materials Engineering **1989,** 11 (4), 299-313.

34. Zhao, L.; Cui, C.; Wang, Q.; Bu, S., Growth characteristics and corrosion resistance of micro-arc oxidation coating on pure magnesium for biomedical applications. Corrosion Science **2010,** 52 (7), 2228-2234.

35. Xu, L.; Pan, F.; Yu, G.; Yang, L.; Zhang, E.; Yang, K., In vitro and in vivo evaluation of the surface bioactivity of a calcium phosphate coated magnesium alloy. Biomaterials **2009,** 30 (8), 1512-1523.

36. Jiang, B.; Xiang, Q.; Atrens, A.; Song, J.; Pan, F., Influence of crystallographic texture and grain size on the corrosion behaviour of as-extruded Mg alloy AZ31 sheets. Corrosion Science **2017,** 126, 374-380.

37. Chen, J.; Chen, G.; Yan, H.; Su, B.; Gong, X.; Zhou, B., Correlation Between Microstructure and Corrosion Resistance of Magnesium Alloys Prepared by High Strain Rate Rolling. Journal of Materials Engineering and Performance **2017,** 26 (10), 4748-4759.

38. Anne, G.; Ramesh, M.; Nayaka, H. S.; Arya, S. B.; Sahu, S., Microstructure Evolution and Mechanical and Corrosion Behavior of Accumulative Roll Bonded Mg-2% Zn/Al-7075 Multilayered Composite. Journal of Materials Engineering and Performance **2017,** 26 (4), 1726-1734.

39. Aung, N. N.; Zhou, W., Effect of grain size and twins on corrosion behaviour of AZ31B magnesium alloy. Corrosion Science **2010,** 52 (2), 589-594.

40. Seong, J.; Kim, W., Development of biodegradable Mg–Ca alloy sheets with enhanced strength and corrosion properties through the refinement and uniform dispersion of the Mg2Ca phase by high-ratio differential speed rolling. Acta biomaterialia **2015,** 11, 531-542.

41. Ralston, K.; Birbilis, N., Effect of grain size on corrosion: a review. Corrosion **2010,** 66 (7), 075005-075005-13.

42. Harris, I.; Varley, P., Factors influencing brittleness in aluminium-magnesium-silicon alloys. J. Inst. Metals **1954,** 82.

43. Chandrasekaran, M.; John, Y. M. S., Effect of materials and temperature on the forward extrusion of magnesium alloys. Materials Science and Engineering: A **2004,** 381 (1-2), 308-319.

44. Hassan, S.; Gupta, M., Development of high performance magnesium nano-composites using nano-Al2O3 as reinforcement. Materials Science and Engineering: A **2005,** 392 (1-2), 163-168.

45. Ambat, R.; Aung, N. N.; Zhou, W., Evaluation of microstructural effects on corrosion behaviour of AZ91D magnesium alloy. Corrosion science **2000,** 42 (8), 1433-1455.

46. Liao, J.; Hotta, M.; Motoda, S.-i.; Shinohara, T., Atmospheric corrosion of two field-exposed AZ31B magnesium alloys with different grain size. Corrosion Science **2013,** 71, 53-61.

47. Birbilis, N.; Ralston, K.; Virtanen, S.; Fraser, H.; Davies, C., Grain character influences on corrosion of ECAPed pure magnesium. Corrosion Engineering, Science and Technology **2010,** 45 (3), 224-230.

48. Ralston, K.; Williams, G.; Birbilis, N., Effect of pH on the grain size dependence of magnesium corrosion. Corrosion **2012,** 68 (6), 507-517.

49. Song, G.-L.; Xu, Z., The surface, microstructure and corrosion of magnesium alloy AZ31 sheet. Electrochimica Acta **2010,** 55 (13), 4148-4161.

50. Zhang, T.; Shao, Y.; Meng, G.; Cui, Z.; Wang, F., Corrosion of hot extrusion AZ91 magnesium alloy: I-relation between the microstructure and corrosion behavior. Corrosion Science **2011,** 53 (5), 1960-1968.

51. Argade, G.; Panigrahi, S.; Mishra, R., Effects of grain size on the corrosion resistance of wrought magnesium alloys containing neodymium. Corrosion Science **2012,** 58, 145-151.

52. Alvarez-Lopez, M.; Pereda, M. D.; Del Valle, J.; Fernandez-Lorenzo, M.; Garcia-Alonso, M.; Ruano, O. A.; Escudero, M., Corrosion behaviour of AZ31 magnesium alloy with different grain sizes in simulated biological fluids. Acta Biomaterialia **2010,** 6 (5), 1763-1771.

53. Feng, A.; Han, Y., Mechanical and in vitro degradation behavior of ultrafine calcium polyphosphate reinforced magnesium-alloy composites. Materials & Design **2011,** 32 (5), 2813-2820.

54. Hornberger, H.; Virtanen, S.; Boccaccini, A., Biomedical coatings on magnesium alloys–a review. Acta biomaterialia **2012,** 8 (7), 2442-2455.

55. Cai, Y.; Tang, R., Calcium phosphate nanoparticles in biomineralization and biomaterials. Journal of Materials Chemistry **2008,** 18 (32), 3775-3787.

56. Vallet-Regi, M.; González-Calbet, J. M., Calcium phosphates as substitution of bone tissues. Progress in solid state chemistry **2004,** 32 (1-2), 1-31.

57. Biltz, R. M.; Pellegrino, E. D., The nature of bone carbonate. Clinical orthopaedics and related research **1977,** (129), 279-292.

58. Oryan, A.; Alidadi, S., Application of Bioceramics in Orthope-dics and Bone Tissue Engineering. **2017**.

59. Hou, C.-h.; Chen, C.-w.; Hou, S.-m.; Li, Y.-t.; Lin, F.-h., The fabrication and characterization of dicalcium phosphate dihydrate-modified magnetic nanoparticles and their performance in hyperthermia processes in vitro. Biomaterials **2009,** 30 (27), 4700-4707.

60. Gonzalez-Nunez, M.; Nunez-Lopez, C.; Skeldon, P.; Thompson, G.; Karimzadeh, H.; Lyon, P.; Wilks, T., A non-chromate conversion coating for magnesium alloys and magnesium-based metal matrix composites. Corrosion Science **1995,** 37 (11), 1763-1772.

61. Chen, X.-B.; Birbilis, N.; Abbott, T., A simple route towards a hydroxyapatite–Mg (OH) 2 conversion coating for magnesium. Corrosion Science **2011,** 53 (6), 2263-2268.

62. Song, Y.; Shan, D.; Chen, R.; Zhang, F.; Han, E.-H., Formation mechanism of phosphate conversion film on Mg–8.8 Li alloy. Corrosion Science **2009,** 51 (1), 62-69.

63. Su, Y.; Li, G.; Lian, J., A chemical conversion hydroxyapatite coating on AZ60 magnesium alloy and its electrochemical corrosion behaviour. Int. J. Electrochem. Sci **2012,** 7 (11), 11497-11511.

64. Jung, H.-G.; Jeong, Y. S.; Park, J.-B.; Sun, Y.-K.; Scrosati, B.; Lee, Y. J., Ruthenium-based electrocatalysts supported on reduced graphene oxide for lithium-air batteries. ACS Nano **2013,** 7 (4), 3532-3539.

CHAPTER TWO: LITERATURE REVIEW

2.1 Mg in Biomaterial Field

It is acknowledged that tissue implants should have some distinguishing features, like good mechanical properties, high stability, and good biocompatibility. However, after healing, the traditional implant materials must be taken out through the following surgery, which makes the patients suffer the secondary operation and extra costs. The need for temporary soluble implants encourages scientists to explore the possibility of using magnesium-series materials which are supposed to be good fits and are desirable for degradable bio-implants. In recent years, more and more magnesium (Mg) and Mg alloys, as fixation implants in bone fracture surgery, have been applied in medical science. As biomaterials, Mg is safe and reliable and has attracted considerable attention because of the following outstanding advantages [1-2].

First, the density of Mg (about 1.7g/cm^3) is the approach to the density of natural human bones (about 1.75 g/cm^3) [3-4], which is much lower than the density of currently used titanium (Ti) and Ti alloys (about 4.5 g/cm^3) [5-6]. Moreover, Young's modulus of Mg is about 45 GPa [7-8]. Compared with Ti alloys (about 100 GPa), Young's modulus of Mg is closer to that of human bone (about 20 GPa) [5, 9]. Thus, the stress-shielding issue existing in traditional metallic implants can be minimized by using Mg-based materials as the ideal therapy biomaterials. Besides, the high specific stiffness and strength of Mg can meet the requirements of implants [10-11]. Due to these natural and excellent mechanical properties, Mg becomes desirable for repairing or reconstructing damaged hard tissues. The second aspect, Mg implants are biodegradable and bio-friendly, which can bring an appropriate and positive host response. An adult body contains

approximately 25 grams of Mg, which is the eleventh element in the human body [12-14]. Mg ions are essential and necessary in all living body cells, and about half of these ions are in the bones. Mg ions also take part in almost all metabolic processes in the human body, including the formation of bone cells [5, 15-16]. So, dissolved Mg has the ability to assist and accelerate bone healing [5, 17-18]. Besides, extra Mg ions can be excreted in the urine without implant residues [19-21]. All in all, Mg and Mg alloys are promising biomaterial implants [22-24]. It is due to their mechanical properties, nontoxicity, and biocompatibility [25-26].

Mg and Mg alloys have a long period of being implant materials. The history of biodegradable Mg implants started as early as the 1878s. After this, the door of Mg biomaterial was opened. In the beginning stage, these pioneers focused on pure Mg and Mg alloys. The coated Mg and Mg alloys are also produced and investigated with the development of plastic deformation technology and coating technology. They had much better corrosion behavior in the immersion tests. Especially after the 20th century, various processed Mg and Mg alloys were prepared, studied, and even applied to modern medical materials. **Table 2.1**. summarizes an overview of the authors who report the results of the biomedical application of Mg.

Table 2.1: A review of Mg and its alloys as biomedical materials in historical order.

Year	Material	Author
1878	Pure Mg	Huse [27]
1892-1905	High-purity Mg	Payr [28-34]

1903	Pure Mg	Höpfner [35]
1900-1905	High-purity Mg	Chlumský[36-37]
1906-1932	Pure Mg (99.7%)	Lambotte [38-39]
1910	Metallic Mg	Lespinasse [40]
1924	Pure Mg (99.99%)	Seelig [41]
1925	Pure Mg (99.8-99.9%)	Glass [42]
1928	Pure Mg	Heinzhoff [43]
1933-1937	Mg-Al6-Zn3-Mn0.2%-wt., Mg-Al8%-wt.	Verbrugge [44-46]
1938	Mg-Mn3%-wt., Mg-Al4-Mn0.3%-wt.	McBride [47-48]
1940	Pure Mg	Maier [49]
1951	Mg-Al2%-wt., Pure Mg	Stone [50]
1980	Mg-Al2%-wt.	Wexler [51]
1981	Pure Mg (99.8%)	Hussl [52]
1981	Pure Mg (99.8%)	Wilflingseder [53]
1997	Pure Mg	G. SONG [54]
1998	AZ10 and AZ80 Mg alloys	G. SONG [55]
1999	AZ91D Mg alloy	Rajan Ambat [56]
2001	Surface modified Mg by $NaHCO_3$	Yousef Al-Abdullat, Sadami Tsutsumi [57]
2002	Pure Mg, AZ31, AZ91E Mg alloys	H. Inoue [58]

2003	Electrodeposited on AZ91 Mg alloys	Y.F. Jiang [59]
2005	Ti-coated pure Mg	Erlin Zhang [60]
2006	Pure Mg, AZ31, Mg-12Li and Mg-Ca Mg alloys	C. D. YFANTIS [61]
2007	Pure Mg	Ming Liu [62]
2007	Mg-Y-RE alloy	Ngoc-Chang Quach [63]
2008	Mg-Zn alloy	Shaoxiang Zhang [64]
2008	Pure Mg (99.9 %)	C. Hoog, N. Birbilis [65]
2009	Alkaline heat-treated Mg-Ca alloy	X.N. Gu [66]
2009	AZ31B Mg alloy	Naing Naing Aung [67]
2010	Fluorine-doped hydroxyapatite coated Mg-Zn-Ca alloy	E.C. Meng [68]
2010	Calcium phosphate coated Mg-Al and Mg-Ca alloys	Zhang Chun-Yan [69]
2011	Pure Mg, AZ31, and AZ91D Mg alloys	Dingchuan Xue [70]
2011	Pure Mg, AZ31, Mg-0.8Ca, Mg-1Zn, Mg-1Mn and Mg-1.34Ca-3Zn Mg alloys	Jemimah Walker [71]
2012	Mg-Y-RE alloy	G.R. Argade [72]
2013	Nano-hydroxyapatite reinforced AZ31 Mg alloy	B. Ratna Sunil [73]

2014	Ultrahigh-purity Mg	Joëlle Hofstetter [74]
2014	MAO-coated AZ31 Mg alloy	B. Salami [75]
2015	Micro-arc oxidized Mg	Lichen Zhao [76]
2015	Pure Mg, Mg-0.25Zr, and Mg-1.0Zr Mg alloys	Partha Saha [77]
2015	Binary Mg alloys and pure Mg	Anastasia Myrissa [78]
2016	Fluoride coated AZ31B Mg alloy	Wei Sun [79]
2017	AZ91 Mg alloy coated with a thin nanostructured hydroxyapatite	T.M. Mukhametkaliyev [80]
2017	Hydroxyapatite/magnesium phosphate/zinc phosphate composite coating deposited on AZ31 Mg alloy	Wei Huang [81]
2017	Silicon-substituted nano hydroxyapatite coating on Mg-5Zn- 0.3Ca (%wt.) alloy	Changiz Dehghanian [82]
2018	Super-hydrophobic stearic acid layer formed on anodized high purified Mg	Sohrab Khalifeh [83]
2019	Hydroxyapatite coating on AZ31 Mg alloy	Jin'e Sun [84]
2019	Micro-arc oxidation coating on porous Mg foam	J. M.Rúa [85]
2019	Glucose-induced hydrothermal calcium phosphate coating on pure Mg	Ling-Yu Li [86]

2020	Coating of bioactive glass on Mg alloys	V.S. Yadav [87]
2020	Nanopatterned silk-coated AZ31 Mg alloy	Babak Mehrjou [88]
2020	Poly(L-lactic acid) (PLLA)/$MgSO_4 \cdot 7H_2O$ Composite Coating on Mg	Yuwei Zhu [89]
2021	PMMA-co-PMAA coated on Mg	Tayara C. Gonsalves [90]

However, the development of Mg metal and its alloys are limited because of the active chemical properties. It is known that Mg has a low standard potential [91], and the degradation rate of Mg is faster than most metals and alloys in an aqueous environment [92-93]. Moreover, the porous corrosion products on its surface cannot effectively protect Mg [94-95]. If chloride ions exist in the corrosive environment and the pH value is lower than 11.4, the corrosion will be significantly accelerated [96-97]. In the human body fluid, there are many kinds of ions, including chloride ions, and the pH value is about 7.4 [5, 98]. Therefore, Mg has rapid corrosion in the human body.

Rapid dissolution of Mg-series implants will bring some harmful effects on the human body. First, the fast degradation can result in local alkalization and even alkaline poisoning when the local pH is over 7.8. It has a bad influence on the biological response of bone tissues. In addition, during the fast corrosion, the rapid hydrogen evolution and appearance of subcutaneous gas cavities will cause incomplete healing by obstructing the blood flow. The previous investigations show an overall hydrogen absorption rate of about 0.954 ml every hour [70]. The hydrogen absorption from gas pockets decides by the hydrogen diffusion coefficient in the tissue [92-93].

Moreover, the accumulation of large amounts of gas will probably result in significantly over the tolerance level of the human tissue. This phenomenon will induce a mismatch with the bone growth rate, as well as an interval between the implant and the surrounding tissue. Another critical issue is the mechanical stability of the implant. As corrosion proceeds, the corrosion also leads to a severe loss, and the mechanical properties will also decline [99-100]. The most common corrosion type of Mg is pitting corrosion [101-103]. The corrosion pits can be the micro-crack initiating places. The hydrogen released during the rapid degradation can also lead to hydrogen embrittlement and micro-porous. Since implants with sufficient strength are crucial, the reduction in mechanical properties under physiological conditions is severe. The negative body response will come out. In addition, as a functional implant biomaterial, it needs to be stable for at least 12 weeks after implantation so that bone tissue has sufficient time for growth and healing [104-105]. It means that Mg needs much better anti-corrosion behavior as biomaterials.

In a word, the fast degradation undermines the recovery in the healing process and limits Mg application in bio-implants [106-107]. Thus, the corrosion resistance must be improved to achieve the feasible use of Mg as biomaterials [98, 108].

2.2 Methods of Improving the Corrosion Resistance of Mg

Here are three most common and effective ways to solve the problem mentioned before. They are doping Mg with alloy elements [109-110], changing the Mg and Mg alloy microstructures [2, 111-112], and making a resistant coating on the Mg and Mg alloy substrates [99, 113].

2.2.1 Mg alloy elements

The previous research results show that the specific alloying elements addition can indeed change corrosion behavior to a certain extent [114-116]. Moreover, the corrosion behavior and mechanical behaviors are also greatly affected by the addition of the alloying elements [117-119]. Some elements can enhance the corrosion resistance, but others can accelerate the implant dissolution rate in biomedical Mg alloy design [114, 120]. In binary Mg alloys, the addition of 1wt.% Zn, Al, Mn, In, or Zr show good anti-corrosion performance in SBF and Hank's solutions [109]. On the contrary, the most common impurities in Mg are Fe, Ni, and Cu, which are harmful to anti-corrosion. Thanks to their solution limit in Mg being very low, they provide an active cathode position [120].

As a biomaterial, safety is the most important besides good corrosion resistance. Some elements are harmful to the human body [121-122]. Pb, Cd, and Th are well-known toxic to the human body. Pb is noxious to the kidney, the hematopoietic system, and the nervous system [123]. Cd affects many body parts, including the lung, heart, liver, and kidney [123]. The hazard radioactivity of the Th element is no dispute [124]. For some human nutrient elements (Ca, Cr, Mn, Zn, Sn, Si), the human body needs minimal daily [123, 125-126]. Therefore, once the implant material dissolves, it is worth studying how to metabolize the excess elements out of the body quickly and whether it will adversely affect the human body. Besides, some elements are innocuous, but the side effects on the human body are not very clear [121, 127]. The representatives are rare earth elements. They are unessential for humans because they are not found in the human body [128]. Therefore, the biological safety of these elements is worthy of long-term observation and study. As for rare earth elements, they are also controversies regarding their biological effects. Some research had

cytotoxicity tests, and the results did not show apparent cell viability reduction, no significant toxicity, or no destructive impact on blood vessel-related cells [5, 17-18]. Nevertheless, it does not mean the material is absolutely safe and reliable for application [109].

In addition, when two or more alloy elements are added, the alloy elements can also interact with each other, possibly forming additional compounds and phases [56, 129]. It makes the situation more complicated [130]. Based on the above discussions, pure Mg is the safest and most reliable implant material [1-2]. It is instructive to enhance the anti-corrosion behavior of pure Mg.

2.2.2 Changes in Microstructures

A familiar method of increasing corrosion resistance is changing microstructure. Currently, most Mg and Mg alloys on the market are processed with casting methods. The grain size is not fine enough, and there is segregation of composition, which cannot fundamentally solve the problems of brittleness and corrosion [56, 131-136]. Therefore, casting Mg is challenging to have excellent performance and broader application. Severe plastic deformation-based processes have shown great potential in producing ultrafine-grained materials [137-139]. Some researchers found that large plastic deformation is efficient in grain refinement [139-141], and refined grain would be helpful to the anti-corrosion performance of Mg and Mg alloys [111, 142]. However, previous research showed that plastic deformation processing would also obviously change the mechanical properties of Mg and Mg alloys [7, 143-146]. Some mechanical properties were improved, and others were not [147-148]. Plastic deformation processing should be carried out appropriately to refine the grain cell size. Most severe deformation is carried out under heating conditions to ensure the proper mechanical properties of implants. However, dynamic recrystallization of Mg alloys is very easy

to occur during hot deformation [149-151], which is mainly due to the following three factors: First, Mg is a metal with low stacking fault energy [152-154]. Dislocations are easy to expand [155-156], and dynamic recovery is not easy to occur, which consumes deformation energy [157]. Therefore, dynamic recrystallization has a great driving force. Second, there are few slip systems in Mg [158-159], and dislocations tend to accumulate during deformation. It leads to an increase in energy storage. Third, Mg has fast grain boundary diffusion, and dislocation is easily absorbed by the grain boundary [149, 160-162]. Therefore, attention should be paid to the heating temperature during plastic deformation. For Mg and Mg alloys, here are several common serious plastic deformation processing, such as hot-rolling (HR) [111, 142, 163], friction stir processing (FSP) [164-165], high strain rate rolling (HSRR) [166-167], and equal channel angular pressing (ECAP) [168-169]. **Table 2.2**. exhibits the change of grain size and corrosion resistance of different Mg-based materials after plastic deformation. It is concluded from the table that the ultimate corrosion resistance of different materials with different treatment methods is also different. Under the different processing parameters, even if the same material and the same processing method, the results are not the same. Among these studies, the most controversial point is the relationship between grain size, dislocation density, and corrosion resistance. Thus, this point needs further exploration.

Table 2.2: A literature review of the effect of plastic deformation on the corrosion properties of Mg and Mg alloys.

Material	**Method**	**Original grain size (μm)**	**Final grain size (μm)**	**Higher corrosion resistance**

Pure Mg [65]	ECAP	875	16.9	Yes
Mg-4Y-3Nd alloy [72]	FSP	20±12	3.75±0.87	Yes
Mg-5Gd alloy [142]	HR	130	13	No
Mg-6Al alloy [142]	HR	70	16	No
Mg-5Sn alloy [142]	HR	150	49	No
Mg-0.7La alloy [142]	HR	132	13	No
Mg-0.3Ca alloy [142]	HR	100	18	No
Mg-1Mn alloy [142]	HR	400	9	No
Mg-0.1Sr alloy [142]	HR	230	17	No
Mg-0.6Nd alloy [142]	HR	850	12	No
Mg-0.9Ce alloy [142]	HR	450	23	No
Mg-0.1Zr alloy [142]	HR	470	18	Yes
Mg-0.3Si alloy [142]	HR	83	15	Yes
AZ31 Mg alloy [170]	FSP	16.4±6.8	3.2±1.2	No
Mg-3wt%Zn alloy [171]	HR	157	27	No
AZ80 Mg alloy [172]	ECAP	18±0.5	6±0.5	Yes
AZ31 Mg alloy [173]	ECAP	25.7	4.5	Yes
AZ31 Mg alloy [174]	HR	450	20	Yes
AZ31 Mg alloy [174]	ECAP	20	2.5	No
Pure Mg [175]	ECAP	800-1500	50-100	No
Mg-4Zn alloy [176]	HSRR	80	4.0	Yes
Mg-4Zn-0.1Sr alloy [176]	HSRR	45	3.6	Yes
Mg-4Zn-0.2 Sr alloy [176]	HSRR	57	3.3	Yes

Mg-4Zn alloy [177]	HSRR	69	4.5	Yes
AZ91 Mg alloy [178]	FSP	246	1.3-1.6	Yes
AZ31B Mg alloy [179]	FSP	29±9	10.2±2.4	Yes
AZ91 Mg alloy [180]	FSP	30	16	Yes
WE43 Mg alloy [181]	FSP	12.4	1.43	Yes
AZ91 Mg alloy [182]	FSP	166.5-8.7	8.77-1.3	No
WE43 Mg alloy [183]	FSP	53	2.7	Yes

According to the above literature summary, it is found the two most common routes are rolling and ECAP. From the operational point of view, rolling has more advantages. First, ECAP requires precise processing of the initial size of the sample. Lubricants are also needed. Therefore, rolling is a more convenient process. The process is easy, and the expense is low. Rolling is traditional and has been widely used for a long history. From an operational perspective, rolling is more commonly used to get the desired shape of Mg. When Mg is a medical material, taking the bone plate as an example, its main forming process is rolling [184-185]. It also provides the possibility of large-scale production of Mg as the medical plate. Besides, rolling can crush coarse grains effectively, reduce and even eliminate casting defects, alter as-cast structures into deformed structures, and improve the processing ability of metal and alloy [186-189].

Mg is a densely arranged hexagonal crystal structure with a low slip coefficient. Therefore, at low temperatures, the macroscopic behavior of Mg has poor plasticity. Because of the poor plastic deformation ability of Mg and Mg alloys, the rolling temperature is generally the key to

practical operation. The metal fracture will occur if the rolling temperature is too low [190]. If the temperature is too high, the grain size is not well controlled, and the phenomenon of rapid grain growth is prone to occur, which increases the tendency of hot brittleness, thus affecting performance [191-192]. A suitable rolling temperature assumes an essential key in the experiment. Therefore, the ideal condition is that the metal can be rolled smoothly at the lowest possible temperature without cracking.

2.2.3 Formation of Coatings

The most direct way to solve their low corrosion resistance issue is to prepare a coating on its surface [95, 193]. A layer of thin film added between the implant and the environment can be a barrier to separate the implant from the corrosive environment for a corrosion rate reduction. The coating would contact the corrosive environment first, so the implant is protected. Surface coating can not only improve the biodegradation behaviors of Mg alloys in the physiological environment but also enhances the biocompatibility, bioactivity, and mechanical stability of implants for load-bearing applications. In a word, making coated Mg-based alloys can obtain a lot of attention because this way provides the possibility to meet all the above applied-limitation requirements.

There are many different methods of making a protective coating on biomaterial implants, such as micro-arc oxidation (MAO) [194-196], electrochemical deposition [197-199], physical vapor deposition (PVD), and chemical bath deposition (CBD) [200-201].

2.2.3.1 Micro-Arc Oxidation (MAO)

MAO is the most common way to make ceramic coatings on the substrates directly in situ [202-203]. It is a widely used anodizing process for Mg alloy based on traditional anodizing. Its advantages are that it is insensitive to the kind of alloy, and the coating has good adhesion and wear resistance [204]. The MAO operation includes electrochemical and electrothermal oxidation of a group of active metals [205]. Except for many applications in the engineering field, MAO coatings have the potential for the progress of biomedical films on Mg-based substrates. In the specific field of MAO coatings on Mg-based materials, the research reports began in around year 2004. Then, the number of relative articles has increased significantly since 2009. Until now, some MAO coatings have already been extensively applied [193, 206-208].

Here are some examples of MAO-coated Mg-based substrate in **Table 2.3**. The immersion and electrochemical test results illustrate the MAO coating protective effect. In the MAO process, many parameters influence the coating properties. Such as electrolyte solution [209-210], current density, voltage, and deposition time [211-212]. Under different conditions, the composition, microstructure, thickness, and corrosion resistance of the final product are different. Moreover, these parameters are easy to be controlled [213]. So, according to the working environments and working conditions, the coatings with different properties can be produced through the MAO process easily [214-215]. However, MAO also has some disadvantages that could be improved. Among them, high cost is the biggest problem [216-217]. MAO is one of the most expensive coating techniques. It is processed under a high voltage and consumes a lot of power in the process of use. Moreover, the prices of raw materials are also high. Because many reaction conditions need to be regulated and controlled, the degree of reaction is difficult to control precisely. Another

serious problem of MAO coating is the pores or cracks on the coating surface [218-219]. The pores and cracks are weak parts, especially the through-pores [220]. They provide tracks for corrosive solutions and cause penetration. To solve this problem and improve the protective effect of MAO coatings, researchers have recently combined the MAO method with other synthesis technologies and made some progress.

Table 2.3: Anti-corrosion properties of the MAO-coated Mg series materials, as reported in the literature.

Method	**Substrate**	**Coating**	**Corrosion behavior [Test conditions]**
MAO [76]	Pure Mg	MAO	Average corrosion rate was about 1.27 mg/cm^2·d [SBF (7 days)]
MAO [76]	Pure Mg	MAO HA	Average corrosion rate was about 0.87 mg/cm^2·d [SBF (7 days)]
MAO [221]	AZ31B Mg alloy	MgO $Mg_2B_2O_5$	Electrical impedance was 385.1 kΩ·cm^2 [0.01M NaOH solution]
MAO [222]	Mg-Ca alloy	MgO Mg_2SiO_4	H_2 evolution rate was about 0.007 mL/cm^2/day [Hank's solution]

MAO [223]	AZ31B Mg alloy	MgO Mg_2SiO_4	Electrical impedance was 41.6 $M\Omega \cdot cm^2$ [3.5% NaCl pH=6.7]
MAO [224]	AZ31B Mg alloy	Ca/P-HA	Corrosion current density was 1.33 $\mu A/cm^2$; Corrosion voltage was -1.328 V [Hank's solution (5 hours)]
MAO [225]	Mg-Zn-Ca alloy	$(Mg,Ca)_3(PO_4)_2$	Corrosion voltage was -1.64 V [300 mL SBF (10 minutes)]
MAO [225]	Mg-Zn-Ca alloy	$(Mg,Ca)_3(PO_4)_2$ HA	Corrosion voltage was -1.55 V [300 mL SBF (10 minutes)]
MAO [226]	AZ91 Mg alloy	MAO	MAO lowered the solution pH value [cell culture medium DMEM (2-7 days)]
MAO and EPD [226]	AZ91 Mg alloy	MAO $CaMgSi_2O_6$	Diopside coated samples the pH value was about 7.9-8.3 [cell culture medium DMEM]
MAO and CBD [227]	Pure Mg	Calcium phosphate	H_2 evolution rate was 1 mL/cm^2 [250 mL SBF (132 hours)]

MAO and PLA dipping [228]	AZ31 Mg alloy	PLA/MgO	Corrosion voltage was −1.50 ± 0.01 V; Corrosion current density was 1.83 ± 0.08 (μA/cm^2) Corrosion rate was 0.02 ± 0.01 (mg/cm$^{2\cdot}$day) [SBF]

2.2.3.2 Electrochemical Deposition (ED)

The electrochemical deposition (ED) method is a super easy and convenient coating technology with a long history [229-230]. Moreover, the working temperature is low. There are two common electrochemical deposition methods: one is the electrophoretic deposition (EPD) method [231-233], and another one is the plasma electrolytic oxidation (PEO) method [234-236]. Under the action of an electric field, the ions in the solution will be deposited on the surface of the matrix material through oxidation-reduction reactions. Generally, the experimental device is a 3-electrode system [237]. The substrate material is a working electrode, graphite/platinum is a counter electrode, and a reference electrode is applied for ED operation [238]. Besides, the coating material constitution is very versatile because the experimental parameters can control the components and properties of deposited coatings [239-241]. The applied potential, current, electrolyte solution composition, and deposition duration are variable in obtaining desired and expected coatings [242].

According to the review of previous developments in the electrochemical coating on Mg and Mg alloy samples, the ED process under the room temperature apparently improves the bio-degradation resistance compared with the high-temperature coating method [243]. Here are some

biomaterial examples from the research literature in the following **Table 2.4**. Different coatings are produced on the Mg-based substrates. And then, the corrosion behavior is also tested and discussed.

The electrochemical deposition method has similar shortcomings to MAO. Many parameters are adjustable during the deposition process. The current, voltage, solution concentration, and other factors work together to form the final coating. Moreover, Mg is very active, and the film is formed rapidly under the action of electrodes. Therefore, it is not easy to obtain uniform and even coating.

Table 2.4: Electrochemically deposited coatings on Mg alloys and corrosion test results, as reported in the literature.

Ref.	**Coating** **Substrate**	**Immersion test solution**	**Corrosion behavior**
[96]	HA AZ91D Mg alloy	SBF at 37 °C	E_{corr}: −1.36 V I_{corr}: 36.5 µA /cm^2
[104]	Ca-deficient HA Mg-Zn-Ca alloy	SBF at 37 °C	E_{corr}: -1414 mV I_{corr}: 25 µA/cm^2
[68]	Fluorine-doped HA Mg-Zn-Ca alloy	SBF at 37 °C	E_{corr}: −1.51 V I_{corr}: 2.51 µA/cm^2
[69]	Calcium phosphate	Hank's solution (10 days)	

	AZ31 Mg alloy		H_2 evolution rate: about 0.0011 mL/cm^2/day
[69]	Calcium phosphate Mg-1.0Ca alloy	Hank's solution (12 hours)	H_2 evolution volume: 0.6 mL
[81]	HA/Mg phosphate/Zn phosphate composite AZ31 Mg alloy	Hank's solution at 37 °C (21 days)	Corrosion rate: 1.04×10^{-8} mm/year Electrical impedance: 3247 kΩ·cm^2
[244]	DCPD Mg-1.0Ca alloy	Hank's solutions	E_{corr}: −1.46 V,
[245]	Calcium phosphate coatings Mg-Zn alloy	m-SBF (480 hours)	H_2 evolution: 0.5 mL/cm^2
[246]	DCPD Mg-Ca alloy	350 mL Kokubo solution at 37 °C pH=7.66	Electrical impedance: 4.61 kΩ·cm^2 Corrosion rate: 0.13 mm/year
[246]	Fluorine-doped HA Mg-Ca alloy	350 mL Kokubo solution at 37 °C pH=7.66	Electrical impedance: 3.31 kΩ·cm^2 Corrosion rate: 0.14 mm/year

[247]	Ca-deficient HA Mg-1Ca-3Zn alloy	350 mL Kokubo solution at 37 °C pH=7.66	Electrical impedance: 3.55 $k\Omega \cdot cm^2$
[247]	Fluorine doped HA Mg-1Ca-3Zn alloy	350 mL Kokubo solution at 37°C pH=7.66	Electrical impedance: 4.61 $k\Omega \cdot cm^2$
[248]	DCPD AZ31 Mg alloy	0.9% NaCl solution at 22 ± 2 °C	I_{corr}: 20.03 $\mu A/cm^2$

2.2.3.3 Physical Vapor Deposition (PVD)

Among the standard coating techniques, PVD is one of the most economical and environmentally friendly technologies for Mg alloy [249]. This technique uses physical processes to evaporate the target material into the vapor phase and then deposit the atoms or molecules on the sample to be a coating [250]. The process includes sputter deposition, pulsed-laser deposition, vacuum deposition, ion plating, and diffusion coatings [95]. It is a short-term and efficient coating method to obtain strong adhesion and uniform thin films on the substrates [251-252].

In the past few decades, the early research of PVD coating has shown a significant contribution to wear resistance and corrosion resistance in biomedical applications [253]. The PVD TiN coating was developed in the 1980s and was utilized for clinical arthroplasties during the 1990s [254-255]. After the early studies, the research topics of PVD coatings for biomedical metallic implants have significantly increased [253]. Due to its outstanding advantages, such as versatility, environmental friendliness, controllability, sustainability, and no-emission, PVD technology has

received increasing attention over recent years [251, 253, 256-258]. Moreover, PVD systems enable the deposition of an extensive type of materials such as metallic [259], ceramic [260], or hybrid coatings [261]. Some of these coatings show excellent corrosion behavior, high hardness, and good biocompatibility as well. Therefore, it has become a trend to use PVD to provide good protection for medical devices [250].

Nowadays, the function of this method in Mg-based material final surface is the production of wear-resistant and corrosion-resistant protection coatings [95]. However, there are still some challenges to be overcome in the process on Mg substrates. The first difficulty is the operating temperature. For most coating cases, the substrate temperature is about 400-550 ℃. Actually, the temperature of Mg alloy stability is about 180 ℃ [262]. A pulsed bias voltage is applied during deposition to reduce the deposition temperature significantly [262]. Also, the micropore is inevitable on the PVD coatings. It becomes the channel for the corrosive medium to contact the Mg-based substrate. And then, it forms a corrosive galvanic cell, which promotes corrosion. Another important issue is the processing variables. All parameters must be accurately regulated when a new experiment is being designed for the new desired coatings [263]. In a word, PVD is an up-and-coming method in coating technology. In the future, the influence of parameters in the PVD process needs more and further studies and research. Also, adding some new elements and new materials in the deposition would be a valuable improvement trending [250].

2.2.3.4 Chemical Bath Deposition (CBD)

Researchers have been using CBD technology since the 1960s [264]. It is a technology of depositing a film on top of basic material through a chemical reaction in an aqueous solution [265-

[269]. By this method, the deposition of different materials on different substrates or previously deposited layers is implemented. With the development of related science and technology, this thin film technique from aqueous solutions had much progress since the mid-1970s. In the 1990s, the CBD method at a low temperature was significantly accelerated reported in the literature [270-273]. The general deposition process involved three steps. The first step is to create the raw atomic or ionic species. Next, the species are transported through a medium. In the last step, the coating material is condensed and continue to grow on the substrate [264, 274]. The basic principle is the precipitation of the coating compound from a solution of its constituents on the substrate. In this way, the basic condition is that the ion concentration must be over the solubility product [264, 274].

In recent years, the CBD method has also been ubiquitous and successful in biomaterial implant coating on the Mg alloy substrate field. It has attracted great attention for a long time because of its low cost, low film-forming temperature, low material consumption, and final coating variety. Many materials can be deposited on the substrates by this method. Besides, it is suitable for preparing large-area films and makes it easy to realize continuous production [275-276]. The thin film coatings produced by the CBD method are uniform, high purity, high quality, and compact. Meanwhile, the formation of thin films is in control of changing the composition and concentration of the solution and the reaction temperature. In some cases, only CBD is not enough to make a perfect coating. The following post-treatment, which is very essential, can improve coating behavior effectively. To obtain more protective coatings, CBD is used to form the original coating.

Table 2.5: Compositions of CBD coatings on Mg and Mg alloys and corrosion test results, as reported in the literature.

Ref.	Substrate	Coating	Immersion test solution	Corrosion test result
[268]	AZ60 Mg alloy	HA	SBF	R_{HA}=38126 Ω·cm
[277]	HA/Mg composites	DCPD and HA	SBF	R_{DCPD}=2291 Ω·cm R_{HA}=4242 Ω·cm
[278]	Extruded Mg alloys	Zn-Ca phosphate	5% nitric acid alcohol solution	H_2 evolution rate was 0.014 mL/cm^2/h
[279]	AZ31 Mg alloy	Zn phosphate Zn-Ca phosphate	3.6 wt.% NaCl solution	Zn coating E_{corr}: −1.494 V I_{corr}: 41.8 μA/cm^2 Zn-Ca coating E_{corr}: −1.498 V I_{corr}: 11.5 μA/cm^2
[280]	Mg-Li-Ca alloy	Zn-Ca phosphate	Hank's solution	R=945 Ω·cm
[281]	AZ91D Mg alloy	DCPD	SBF	R_{DCPD}=4210 Ω·cm

[282]	AZ91 Mg alloy	$CaMgSi_2O_6$	SBF	R=5060.4Ω·cm
[283]	99.9% Mg	DCPD	SBF	Coated specimens had weight loss lower than that of the uncoated ones
[284]	AZ31 Mg alloy	$Mg_6Al_2(OH)_{16}CO_3{\cdot}4H_2O$	3.5% NaCl solution	R=1839 Ω·cm

2.3 Different Kinds of Coating Materials

In recent years, more and more different kinds of coatings have been gained on the Mg and Mg alloy substrates through different methods. To achieve application requirements, not only the dissolved speed should be slowed down, but also some bioactive abilities like bone attachment, biocompatibility, and nontoxicity must be considered. Nowadays, the most common coating classifications are ceramic coating, polymer coating, and composite coating. All the coatings have a protective effect to some extent. And researchers also tried to get the ideal producing conditions to enhance the properties of coatings.

2.3.1 Ceramic Coating

It is widely known that bioactive ceramics meet the criteria for ideal coatings used in Mg and Mg alloys bone-implant engineering [285]. Many very potential ceramic materials were formed and showed outstanding performance in the biomedical field. For example, MgO [221], $Na_2Ca_2Si_3O_9$ [286], Mg_2SiO_4 [287], $Mg_2B_2O_5$ [221], and n phosphate were obtained by different research groups [279].

Nowadays, the most regular ceramic coating material is calcium phosphate (Ca-P) coating. Over the last decade, Ca-P ceramics have attracted the great attention of many researchers for human health care purposes, including bone tissue engineering scaffolds [288], bone fillers [289-292], and bioactive coatings [289]. As biomaterials, Ca-P ceramics are reliable. They are also the main mineral substitutes in bone and tooth [293-296]. In the early 1980s, Brown and Chow first developed a self-setting Ca-P [297-300]. Since then, many Ca-P ceramics have been commonly utilized to repair human bone defects [301]. Ca-P ceramics have excellent biocompatibility, nontoxicity, bioactivity, and osteoconductivity [302-304]. They can delay the corrosion of the matrix in the human body [193, 305]; improve the biocompatibility of the implant [306-307]; promote the direct chemical bonding between the implant and natural bone tissue [308-310]; help the early stability of the implant [311-313]; shorten the healing period after operation [304, 314-315]. So, Ca-P coatings widely and frequently employed to manipulate the anti-corrosion behavior of an implant under the human ambient are considered [227, 316]. Up to now, Ca-P coatings have received significant interest from some scientists for being protective coatings on Mg alloys to delay the degradation processes [96, 317-318]. Besides, some researchers have found that Mg is good for Ca and P deposition [319]. Besides, the Ca-P can boost the direct attachment to the surrounding bone tissue bonding [10], and accelerate the growth of nature bones [320]. Therefore, the Ca/P-coated Mg-based biomaterial is very promising and desirable. However, the poor strength of Ca-P and poor cohesion between the substrate and coating greatly limit their clinical application [301]. Also, the biodegradation behavior of the Ca/P-coated Mg substrate needs further exploration [227]. There are many different types of calcium phosphate [114]. The common ones are hydroxyapatite (HA) [96, 281, 321], octa-calcium

phosphate (OCP) [322-323], tricalcium phosphate (TCP) [324-325], and dicalcium phosphate dihydrate (DCPD) [326-327].

2.3.1.1 HA ($Ca_{10}(PO_4)_6(OH)_2$)

Among these Ca-P materials, HA is most frequently used as a biomaterial [294-295, 328]. Because HA is a kind of weak alkaline calcium phosphate that is most stable and slightly soluble in the human body fluid [329-330]. With a 1.67 Ca/P ratio, it is also an essential inorganic component of vertebrate bone and teeth, accounting for 72% of human bone and 97% of dental bone [96, 321]. It can enhance bone healing due to its high chemical similarity and biocompatibility with natural bone [331-333]. Because of this, HA can chemically combine with natural bone [308-310]. And it does not have any toxic influence on the human body. In a word, HA is a kind of bio-ceramics material with high application value. From the perspective of development time, it is widely used in dental and artificial bones at the beginning [334-335]. Then, the application as a coating agent on biomedical implants shows a considerable process [336-337]. Nowadays, drugs and protein delivery are new and potential directions [338 339].

Three low-temperature methods of HA precipitation are chemical deposition [268], hydrothermal reaction method [340-342], and sol-gel method [343-345]. They have easy operation and reasonable practicability. Morphological characteristics of HA crystals obtained under different reaction conditions are also different. The familiar shapes of HA crystal are the rod [346-348], needle [349-350], fiber [351], whisker [352-353], nano-powder [306], acicular-like shape [306], and flower-like nanorods [354-355]. However, the low mechanical properties of conventional HA are presently limited the load-bearing implant applications [333, 356].

2.3.1.2 OCP ($Ca_8H_2(PO_4)_6{\cdot}5H_2O$)

Among different Ca-P ceramics, OCP is another the most widely applied in the coating of metallic bio-implants [357]. During the recent several years, the increasing attraction has been going to OCP, sometimes even superior to HA [358-359]. Different studies have shown that OCP is getting attractive because OCP displays relatively high biocompatible [358, 360-361], as well as osteoconductive characteristics [362-363]. Although HA is thermodynamically more stable [364-365], OCP is more soluble in the biological environment and readily hydrolyzes into HA within a solution environment [366]. Within 25 ℃ simulated body fluid, the solubility of OCP and HA are 0.0081 g/L and 0.0003 g/L, respectively [367]. Moreover, OCP coatings are easily absorbed by the human body during the healing of affected bone [366]. And it take part in the early stages of the tissue calcification process [297-300]. Thus, dissolved OCP can promote new and natural bone-tissue growth and regeneration by providing abundant beneficial elements such as Ca and P [364, 367-370] in living organisms [371]. Consequently, these merits make OCP emerge as an up-and-coming biomaterial alternative to HA [357, 369, 372]. Furthermore, some studies also demonstrated the potential of OCP as an implant coating [373]. In 2011, OCP was made to the coating top layer on Mg implants. As a result, both corrosion resistance and biocompatibility are promoted as expected [374]. In 2021, another group also made OCP coating on the MAO-coated Mg [366]. OCP coating had excellent corrosion protection and improved bone cell proliferation [366]. The OCP-coated Mg and Mg alloy were partly dissolved in the mice [375]. It suggested that OCP coating may also provide the sufficient potential to enhance new bone tissue ingrowth around the implant in vivo [376]. Only in the past few years, for the following reasons, several ways to make OCP coatings on metallic implants have drawn particular attention in biomedical applications [369, 372, 377-381]. First, OCP is rather hard to deposit stoichiometrically due to the relatively complex

formula of the OCP molecule [369]. Second, it is challenging to obtain OCP coating by direct physical methods thanks to its low thermal decomposition temperature. Third, it is well known that many OCP coatings have very low adhesion to the matrix [372, 378-379]. Also, the influence of OCP coating structure on corrosion resistance, bioactivity, and cytocompatibility needs systematic research [366]. Therefore, continuous study of obtaining OCP coating with the best-performing coating materials is significant [377, 382-383].

2.3.1.3 TCP ($Ca_3(PO_4)_2$)

TCP is another representative Ca-P biomaterial often applied in bone repair because of its outstanding biocompatibility [384], degradability [384], resorbability [385], and osteoconductivity [385]. In the degradation process, releasing Ca^{2+} and PO_4^{3-} and some other essential elements might have an important effect on improving bone repair efficiency [384, 386]. Here are three TCP polymorphs, β-TCP, α-, and α'-TCP [387]. α'-TCP only exists above 1430 °C and transforms to α-TCP in the cooling process [387]. Only α-TCP and β-TCP can be stabilized at room temperature and are suitable for practical applications [388]. β-TCP is the low-temperature form [389]. 1125 °C is the phase transiting temperature from β-TCP to α-TCP [390-391]. This process is also reversible [392-394]. α-TCP is a monoclinic crystal [387, 389], and its theoretical density is 2.866 g/cm^3 [388]. β-TCP crystallizes into the rhombohedral crystal system [387, 389]. Moreover, its theoretical density is denser than α-TCP, about 3.066 g/cm^3 [388]. These structural differences in physicochemical properties [389] are responsible for special and unique applications in practical [387-388]. Both α-TCP and β-TCP materials are used for medical purposes and could support bone cell growth and help bone healing [395]. In aqueous media, α-TCP has higher solubility [396] and reactivity [397]. So, it is widely used as the main powder material in various bone cement [398-402]. As for β-TCP, it is

already well used for bone regeneration in clinical [403-405]. Because it has relatively high mechanical strength. Also, the bone β-TCP shows a favorable bio-absorption rate [406-408]. And it could be absorbed in 12 months [409-411]. Although there has been much attention during the last few years, only a few works have been carried out to obtain TCP-coated implanting substrates. The reason is that the β-TCP dissolution is severe for bone tissue recovery [412]. Moreover, α-TCP is easily hydrolyzed with transformed [397]. Therefore, it is a more promising strategy to fabricate TCP into bio-ceramics and composites [413-416]. Several studies have mainly focused on Mg-based TCP composite and have achieved an optimum result in better anti-corrosion behavior and improving bone defect healing [5, 9, 98, 417].

2.3.1.4 DCPD ($CaHPO_4 \cdot 2H_2O$)

In the human body, DCPD primarily exists in callus, bone, and kidney stones [418]. It is used for tooth remineralization [419]. DCPD also shows good biocompatibility with different cell lines [304]. In 1989, Cogswell Laboratory produced DCPD coating on the prosthetic alloys and published their study results in 1990 [420]. In the following six years, this group continuously studied and got strongly adherent coatings [421]. The DCPD coating used as a protective coating on the Mg alloys started in around 2009 and is more and more attractive in the recent decade [422]. Here are some Mg-based materials with DCPD coating examples in the following **Table 2.6**.

Table 2.6: Calcium phosphate DCPD coated on Mg-based materials by different methods.

Method	Substrate material
ED [100]	AZ91D Mg alloy

ED [244]	Mg-1.0Ca alloy
ED [246]	Mg-Ca alloy
ED [248]	AZ31 Mg alloy
CBD [281]	AZ91D Mg alloy
CBD [283]	99.9% pure Mg
ED [423]	AZ91 Mg alloy
ED [424]	AZ91 Mg alloy
ED [425]	AZ91 Mg alloy
ED [426]	99.98% pure Mg

Although DCPD encounters a relatively high solubility [427], which is higher than other calcium phosphate compounds [246], it could be involved as an HA precursor phase [428-429]. Also, DCPD can be converted into HA in an alkaline environment, including body fluid [316, 430]. DCPD is discovered to convert into HA when soaked in SBF for about one week [314, 422, 431-441]. The normal pH value of body human body fluid is around 7.4 [442-443]. The ratio of calcium to phosphorus in DCPD is 1. In HA, the proportion is 1.667 [289, 296]. There are also calcium and phosphorus ions in the human body fluid, and they can be supplied in this transformation process. Therefore, it can supply raw materials for the growth of HA. Both DCPD and HA coatings can delay the start of Mg corrosion [193, 444], and improve osseointegration performance and corrosion resistance of Mg-based materials in vivo [445]. So, it would be better to apply a DCPD coating first to the Mg substrate rather than straight deposition of HA due to the existence of the conversion process [281].

Some researchers proved this conclusion [100, 281]. They found that DCPD immersed in SBF could be converted into HA to improve corrosion resistance. In 2012, a Chinese group found that DCPD could transform into HA after the SBF immersion test. In addition, they also found that dissolved DCPD could provide a good location for HA nucleation. With the increasing soaking time, more DCPD dissolved. It increased the supersaturation of the solution to HA. As a result, HA nucleated on the surface of the matrix and grew up at the same time [100]. As for DCPD-coated HA/Mg composite samples, DCPD coating was transferred into HA after the alkali post-treatment [277]. However, the Ca/P ratio for finished deposition is about 1.33, which is lower than the stoichiometric HA ratio (1.67). This result was in concordance with past studies in China and France [104, 446]. A new HA-mineralized layer was obtained on the DCPD film surface through one-week soaking in SBF. After soaking, the surface of the sample was denser, and there were no cracks. The ratio of Ca/P increased from 1.33 to about 1.57, closer to 1.67 [277]. Similar alkali treatments have been performed on DCPD coating AZ60 samples [268]. Before and after alkali treatment, the ratio of Ca/P changed from 0.845 to 1.667. The final ratio was consistent with the theoretical value of HA. However, some experiments show that the HA converted from DCPD in SBF cannot adhere to the substrate surface to produce a protective film. This process even accelerates DCPD film dissolution to fall off and makes the substrate be exposed directly to the corrosion environment. Yong Wang's group tested DCPD-coated Mg corrosion behavior in SBF and did not detect any HA on the sample surface from XRD. They explained Mg ions as the hindrance of HA deposition [283]. Some other groups also found the same conclusion that Mg would inhibit HA crystalline precipitation [447-450]. Another reason is the rapid dissolution of DCPD films. It mainly depends on the characteristics of DCPD. If the DCPD is neither dense nor thick, it will dissolve in a short time. Once DCPD dissolves, it cannot be converted into HA on

the matrix. After dissolution, ions enter the solution, and HA is formed and precipitated in the alkaline solution. So, HA could not be generated on the surface of the substrate [283]. In fact, the biomimetic HA formation is mainly decided by the matrix structure and composition [451-452]. Whether HA can be directly converted from DCPD in the SBF immersion process or not need further confirmation.

2.3.2 Polymer Coating and Composite Coating

The advanced application of polymer coatings on biomedical materials has been widely studied in the past decade. These studies and research have shown a great prospect in protecting Mg and Mg alloys with polymers. The protective function of biodegradable polymer coatings is different from inorganic coatings in many aspects. Degradable polymers have many good functional properties. They can increase the anti-corrosion behavior of substrates. Also, they show good biocompatibility, biodegradation, self-heal, and antibacterial property [453-456]. Therefore, degradable polymeric coatings exhibit a promising prospect. Some polymers are recognized as reliable coating materials. The most common materials are polylactic acid (PLA), poly-L-lactide (PLLA), poly (lactide-co-glycolic) acid (PLGA), and polycaprolactone (PCL) [457-459].

The first reliable material is hydrophobic PLA, owing to its good biodegradability and biocompatibility [453-456]. The constituent unit of PLA is lactic acid (LA). It is a chiral molecule with two enantiomers. They are L-lactide and D-lactide. The PLLA comes from L-lactide and can also offer a feasible coating. Despite these advantages, PLA is still insufficient in the application of degradable Mg alloy in biomedicine. The main disadvantage of this material as a protective barrier is that it is easy to hydrolyze in water [460]. As the degradation of Mg alloys, the

hydrogen released from the corrosion reaction will produce micro-pores and micro-cracks on the PLA coating. Ultimately, it will separate and peel off from the substrate [461]. Therefore, it is necessary to discuss the design of PLA film deposition. Like PLA, PLGA also shows excellent biocompatibility and is applied in the medical field [462-465]. It is a copolymer of two comonomers, lactic acid (LA) and glycolic acid (GA). Furthermore, PLGA properties can be designed by controlling the proportion of the LA and GA [460]. Different PLGA polymers with unique properties could be employed as protection on different Mg alloys. PCL is another commonly attractive coating material for bone replacement and implant engineering because of its excellent properties [466-468]. In addition, PCL is environment-friendly and beneficial for bone-implant contact. In this way, PCL is referred to as an outstanding coating to delay the biodegradation process [469-473].

Despite these positive polymers with their features, only a handful of study groups produced a single polymer layer on practical medical Mg-based devices. Typically, the corrosion resistance of a single polymer layer may not work as effectively as expected. Only a polymer coating cannot meet the actual and practical needs. Considering the complex application environment of Mg and its alloys as bone substitute implants, the combination of coating techniques to produce composite coating is promising. Recent publications demonstrate that the composition of ceramic and polymer coatings with excellent functionality is the most interesting problem. Although much progress has been made in ceramic-coated Mg substrates, many problems still need to be studied and solved as mentioned in **Section 2.3.1**. Most ceramic coatings have many pores and even cracks on the surface. They would become the pathways for the solution. And this would trigger the corrosion reactions [474]. Therefore, the best method of improving the protective effect

of ceramic coating is to fill in the pores and cracks on the surface with polymer materials to gain a compact coating. Both dipping and spinning are the most ordinary and straightforward methods to make polymer coatings. They are easy to operate and have good repeatability to control the coating thickness [475].

MAO is a widely applied technology for Mg substrate surface modification to delay the corrosion process [476]. In most cases, researchers combined the MAO or electrochemical deposition method and some other methods to make composite coatings. After a lot of studies and research, composite coatings with smooth and uniform surfaces were produced. Ping Shi et al. [228] gained the PLA/MAO composite coatings on AZ31 Mg alloy to enhance the anti-corrosion behavior. In this study, they first produced the MAO coating on the substrate by the traditional MAO process, and there were some pores and cracks on the coating surface. The average diameters of these pores were about 0.5 to 2 μm. Then they used the techniques of sol-gel and organic polymer composite to make the second PLA layer coating. The aim of adding this PLA layer on the top was to fill in the pores and cracks on the first MAO coating surface to seal it. Comparing the image of PLA-MAO-AZ31 and MAO-AZ31 surface morphology, it is clear that the PLA/MAO composite coating is relatively smoother and cleaner. The morphologies also proved that PLA could seal the pore effectively and had good coverage on the first MAO film. There were no cracks or even pores on the composite coating surface. It could show that the PLA coating can effectively fill the pores and cracks. The electrochemical impedance spectroscopy (EIS) data and soaking experimental behavior also provided evidence that the PLA coating had a protective effect. As shown in the following table, some progress and application examples have been gained in recent years. By methods mentioned before, microcracks and holes on the inner

layer are effectively sealed [477]. As a result, an anti-corrosion ceramic/polymer biomedical composition is produced. Generally, the protective ability of the inner coating on Mg alloys is improved obviously.

Although the composite coating is trendy, adhesion strength at interfaces requires great attention [478]. These interfaces include the face between the coating and the matrix and between different coatings. As increasing the interface layers, this drawback of the interfacial properties becomes more serious. Therefore, the adhesion test is necessary to evaluate the feasibility and stability of the composite coating. Furthermore, several challenges need to be solved. Most tests are only proceeded in vitro environments until now. As for the new generation of Mg implants, the following research should focus on composite coatings under in vivo conditions.

Table 2.7: Various synthesis methods of composite coatings on Mg-based materials.

Substrate	**Inner coating (Method)**	**Outer coating (Method)**	**Final coating material**
Mg-2Zn-3Ce Mg alloy	FHA (ED)	PCL (Dipping)	nFHA/PCL composite [99]
AZ31 Mg alloy	MAO coating (MAO)	PLA (Dipping)	PLA/MAO composite [228]
AZ91D Mg alloy	MAO coating (MAO)	Baking coating (B-coating)	MAOB [479]
WE43 Mg alloy	HA	PLLA (Dipping)	HA/PLLA [480]

	(CBD)		
AZ91D Mg alloy	$Zr(OH)_4$ gel (ED)	Ca-P coating (ED)	Ca-P/ZrO_2 [481]
AZ31 Mg alloy	Ca-P coating (ED)	PLGA (Spinning)	DCPD/PLGA [482]
Pure Mg	MAO coating (MAO)	PCL (Dipping)	MAO-PCL duplex [483]
AZ31 Mg alloy	PEO coating (PEO)	PLLA (Dipping)	PEO/PLLA composite [484]
AM50 Mg alloy	Ti-O coating (PVD)	PLA (Dipping)	Ti-O/PLA [485]

2.4 Immersion Test Solutions

As the most traditional method of corrosion experiment, the immersion test has considerable advantages in the accuracy of corrosion rate [71, 486-487]. Several types of simple solutions are used as simulated physiological solutions to determine the degradation rate of Mg in the soaking test. Different simulated solutions used result not only in different degradation rates of Mg but also different degradation products, suggesting different degradation pathways and degradation mechanisms. Therefore, choosing a suitable physiological solution for the evaluation of Mg degradation is of utmost importance. Compared with other solutions shown in **Table 2.8**, SBF has the closest composition to blood serum [488]. Since 1987, the application of SBF in bioactivity tests has increased explosively [489-490]. It is a solution that simulates the inorganic component and pH value of human body fluid [489, 491-492]. SBF is mainly composed of sodium

chloride, potassium chloride, potassium hydrogen phosphate, magnesium chloride, calcium chloride, Tris, sodium bicarbonate, etc. And the pH of SBF is 7.4 [283, 493-494].

After more than 20 years of research in this field, it has been concluded that the SBF is helpful in predicting the bone cell bioactivity of the implant in vivo [495-498]. Because of the existence of Ca and P as human fluids in SBF, the Ca-P deposition can be measured more accurately. The examination of Ca-P deposition on the material surface is not only instructive qualitatively but also quantitatively [499-500]. Until now, the view of most scientists in the biomaterial community has been that the immersion test of materials in SBF can be served to analyze their bioactivity and bone binding ability in vivo [495, 501-503]. Besides, the reliability of the experiment in SBF is high, and the repeatability of the experiment in vitro is good [489, 504-505]. Most studies of bone tissue implants use this buffer to illustrate their biological activity [3, 9, 282, 458, 494, 506-508]. Therefore, our research investigates the corrosion test in SBF to evaluate sample corrosion resistance.

Table 2.8: Comparison of the ion concentrations of human blood plasma and other synthetic physiological solutions.

Ion (mM)	**Na^+**	**K^+**	**Ca^{2+}**	**Mg^{2+}**	**Cl^-**	**HCO_3^-**	**HPO_4^{2-}**	**SO_4^{2-}**
Human blood plasma [509]	142.0	5.0	2.5	1.5	103.0	27.0	1.0	0.5
Simulated Body Fluid (SBF)	142.0	5.0	2.5	1.5	148.8	4.2	1.0	0.5

Simulated Blood Plasma (SBP) [510]	120.89	5.37	1.80	0.87	125.2	2.6	1.14	0.87
Earle's Balanced Salt Solution (EBSS) [511]	151	5.4	1.8	0.4	135	26.2	1	0.4
Hank's Balanced Salt Solution (HBSS) [512]	141.6	5.81	1.26	0.81	144.8	4.065	0.78	0.81
Kirkland's Biocorrosion Medium (KBM) [513]	120.3	5.0	2.5	0.5	102.5	26.2	0.9	0.5
Dulbecco's Modified Eagle Medium (DMEM) [514]	155.3	5.3	1.8	0.8	115.7	44.1	0.9	0.8
Minimum Essential Medium (MEM) [515]	144.4	5.3	1.8	0.8	126.2	26.2	1.0	0.4
E-MEM (Eagle's Minimal Essential Medium) [516]	151	5.4	1.8	0.8	125	26.2	0.9	0.8

REFERENCES

1. Kuwahara, H.; Al-Abdullat, Y.; Mazaki, N.; Tsutsumi, S.; Aizawa, T., Precipitation of magnesium apatite on pure magnesium surface during immersing in Hank's solution. Materials Transactions **2001,** 42 (7), 1317-1321.

2. Chen, J.; Chen, G.; Yan, H.; Su, B.; Gong, X.; Zhou, B., Correlation Between Microstructure and Corrosion Resistance of Magnesium Alloys Prepared by High Strain Rate Rolling. Journal of Materials Engineering and Performance **2017,** 26 (10), 4748-4759.

3. Ye, X.; Chen, M.; Yang, M.; Wei, J.; Liu, D., In vitro corrosion resistance and cytocompatibility of nano-hydroxyapatite reinforced Mg–Zn–Zr composites. Journal of Materials Science: Materials in Medicine **2010,** 21 (4), 1321-1328.

4. Roschger, P.; Gupta, H.; Berzlanovich, A.; Ittner, G.; Dempster, D.; Fratzl, P.; Cosman, F.; Parisien, M.; Lindsay, R.; Nieves, J., Constant mineralization density distribution in cancellous human bone. Bone **2003,** 32 (3), 316-323.

5. Feng, A.; Han, Y., The microstructure, mechanical and corrosion properties of calcium polyphosphate reinforced ZK60A magnesium alloy composites. Journal of Alloys and Compounds **2010,** 504 (2), 585-593.

6. Chen, B.; Yin, K.-Y.; Lu, T.-F.; Sun, B.-Y.; Dong, Q.; Zheng, J.-X.; Lu, C.; Li, Z.-C., AZ91 magnesium alloy/porous hydroxyapatite composite for potential application in bone repair. Journal of Materials Science & Technology **2016,** 32 (9), 858-864.

7. Yamashita, A.; Horita, Z.; Langdon, T. G., Improving the mechanical properties of magnesium and a magnesium alloy through severe plastic deformation. Materials Science and Engineering: A **2001,** 300 (1-2), 142-147.

8. Chang, T.-C.; Wang, J.-Y.; Chu, C.-L.; Lee, S., Mechanical properties and microstructures of various Mg–Li alloys. Materials Letters **2006,** 60 (27), 3272-3276.

9. Liu, D.-B.; Huang, Y.; Prangnell, P., Microstructure and performance of a biodegradable Mg–1Ca–2Zn–1TCP composite fabricated by combined solidification and deformation processing. Materials Letters **2012,** 82, 7-9.

10. Castellani, C.; Lindtner, R. A.; Hausbrandt, P.; Tschegg, E.; Stanzl-Tschegg, S. E.; Zanoni, G.; Beck, S.; Weinberg, A.-M., Bone–implant interface strength and osseointegration: Biodegradable magnesium alloy versus standard titanium control. Acta biomaterialia **2011,** 7 (1), 432-440.

11. Krause, A.; Von der Höh, N.; Bormann, D.; Krause, C.; Bach, F.-W.; Windhagen, H.; Meyer-Lindenberg, A., Degradation behaviour and mechanical properties of magnesium implants in rabbit tibiae. Journal of materials science **2010,** 45 (3), 624.

12. Lim, P.; Lam, R.; Zheng, Y.; Thian, E., Magnesium-calcium/hydroxyapatite (Mg-Ca/HA) composites with enhanced bone differentiation properties for orthopedic applications. Materials Letters **2016,** 172, 193-197.

13. Gröber, U.; Schmidt, J.; Kisters, K., Magnesium in prevention and therapy. Nutrients **2015,** 7 (9), 8199-8226.

14. Kannan, M. B.; Raman, R. S., In vitro degradation and mechanical integrity of calcium-containing magnesium alloys in modified-simulated body fluid. Biomaterials **2008,** 29 (15), 2306-2314.

15. Günther, T., Comment on the number of Mg 2+-activated enzymes. Magnesium research **2008,** 21 (3), 185-187.

16. Romani, A.; Scarpa, A., Regulation of cellular magnesium. Front Biosci **2000,** 5 (1), D720-D734.

17. Saris, N.-E. L.; Mervaala, E.; Karppanen, H.; Khawaja, J. A.; Lewenstam, A., Magnesium: an update on physiological, clinical and analytical aspects. Clinica chimica acta **2000,** 294 (1-2), 1-26.

18. Grubbs, R. D.; Maguire, M. E., Magnesium as a regulatory cation: criteria and evaluation. Magnesium **1987,** 6 (3), 113-127.

19. Bian, D.; Zhou, W.; Liu, Y.; Li, N.; Zheng, Y.; Sun, Z., Fatigue behaviors of HP-Mg, Mg–Ca and Mg–Zn–Ca biodegradable metals in air and simulated body fluid. Acta biomaterialia **2016,** 41, 351-360.

20. Barker, E. S.; Elkinton, J. R.; Clark, J. K., Studies of the renal excretion of magnesium in man. The Journal of clinical investigation **1959,** 38 (10), 1733-1745.

21. Li, Y.; Wen, C.; Mushahary, D.; Sravanthi, R.; Harishankar, N.; Pande, G.; Hodgson, P., Mg–Zr–Sr alloys as biodegradable implant materials. Acta biomaterialia **2012,** 8 (8), 3177-3188.

22. Kirkland, N. T.; Birbilis, N.; Staiger, M., Assessing the corrosion of biodegradable magnesium implants: a critical review of current methodologies and their limitations. Acta biomaterialia **2012,** 8 (3), 925-936.

23. Sanchez, A. H. M.; Luthringer, B. J.; Feyerabend, F.; Willumeit, R., Mg and Mg alloys: how comparable are in vitro and in vivo corrosion rates? A review. Acta biomaterialia **2015,** 13, 16-31.

24. Jafari, S.; Raman, R. S.; Davies, C. H., Corrosion fatigue of a magnesium alloy in modified simulated body fluid. Engineering Fracture Mechanics **2015,** 137, 2-11.

25. Li, N.; Zheng, Y., Novel magnesium alloys developed for biomedical application: a review. Journal of Materials Science & Technology **2013,** 29 (6), 489-502.

26. Witte, F.; Kaese, V.; Haferkamp, H.; Switzer, E.; Meyer-Lindenberg, A.; Wirth, C.; Windhagen, H., In vivo corrosion of four magnesium alloys and the associated bone response. Biomaterials **2005,** 26 (17), 3557-3563.

27. Huse, E., A new ligature. Chicago Med J Exam **1878,** 172 (2), 11.

28. Payr, E., Beitrage zur Technik der Blutgesfass und Nervennaht nebst Mittheilungen die Verwendung eines Resorbierharen Metalles in der Chirurgie. Arch. Klin. Chir. **1900,** 62, 67-71.

29. Payr, E., Blutgefäß-und Nervennaht (nebst Mittheilung über die Verwendung eines resorbirbaren Metalles in der Chirurgie)[Blood vessel and nerve suture (in addition to the use of a resorbable metal in surgery)]. Centralblatt Chir **1901,** 28, 31-37.

30. Payr, E., Zur Verwendung des Magnesiums für resorbirbare Darmknöpfe und andere chirurgisch-technische Zwecke. Centralblatt Chir **1901,** 28 (20), 513-515.

31. Payr, E.; Martina, A., Experimentelle und klinische Beiträge zur Lebernaht und leberresection (Magnesiumplattennaht)[Experimental and clinical contributions to the liver suture and liver resection (magnesium plate seam)]. Arch Klin Chir **1905,** 77, 962-998.

32. Payr, E., Ueber Verwendung von Magnesium zur Behandlung von Blutgefässerkrankungen. Deutsche Zeitschrift für Chirurgie **1902,** 63 (5), 503-511.

33. Payr, E., Zur Technik der Behandlung kavernöser Tumoren. Zentralbl Chir **1903,** 47, 233-237.

34. Payr, E., Weitere Erfahrungen über die Behandlung von Blutgefäßgeschwülsten mit Magnesiumpfeilen. Zentralbl Chir **1905,** 49, 1335-1340.

35. Höpfner, E., Ueber Gefässnaht, Gefässtransplantationen und Replantation von amputirten Extremitäten. 1903.

36. Chlumsky, V., Über die Wiederherstellung der Beweglichkeit des Gelenkes bei Ankylose. Zentralbl Chir **1900,** 37, 37.

37. Chlumský, V., Beiträge zur Darmknopffrage. Mitt Grenzgebieten Med Chir **1907,** 3, 416-451.

38. LAMBOTTE, A., Technique et indication des prothèses dans le traitement des fractures. Presse med **1909,** 17, 321.

39. Lambotte, A., L'utilisation du magnesium comme materiel perdu dans l'osteosynthèse. Bull Mem Soc Nat Chir **1932,** 28 (3), 1325-1334.

40. Lespinasse, V.; FISHER, G. C.; Eisenstaedt, J., A practical mechanical method of end-to-end anastomosis of blood-vessels: Using absorbable magnesium rings. Journal of the American Medical Association **1910,** 55 (21), 1785-1790.

41. Seelig, M., A study of magnesium wire as an absorbable suture and ligature material. Archives of surgery **1924,** 8 (2), 669-680.

42. Glass, E., Klinische und experimentelle Untersuchungen über die Payrsche Magnesiumpfeilbehandlung von Angiomen. Deutsche Zeitschrift für Chirurgie **1926,** 194 (5), 352-366.

43. Hoffheinz, S.; Dimitroff, N., Experimentelle Studie über die Resorption parenteral zugeführten metallischen Magnesiums. Deutsche Zeitschrift für Chirurgie **1928,** 208 (5), 346-353.

44. Verbrugge, J., La tolérance du tissu osseux vis-à-vis du magnésium métallique. Presse méd **1933,** 55, 1112-1114.

45. Verbrugge, J., Le Matériel métallique résorbable en chirurgie osseuse, par Jean Verbrugge. Masson: 1934.

46. Verbrugge, J., L'utilisation du magnésium dans le traitement chirurgical des fractures. Bull Mém Soc Nat Cir **1937,** 59 (59), 813-823.

47. McBride, E. D., Absorbable metal in bone surgery: a further report on the use of magnesium alloys. Journal of the American Medical Association **1938,** 111 (27), 2464-2467.

48. McBride, E., Magnesium screw and nail transfixion in fractures. Southern Medical Journal **1938,** 31 (5), 508-514.

49. Maier, O., Über die Verwendbarkeit von Leichtmetallen in der Chirurgie (metallisches Magnesium als Reizmittel zur Knochenneubildung). Deutsche Zeitschrift für Chirurgie **1940,** 253 (8), 552-556.

50. Stone, P.; Lord Jr, J., An experimental study of the thrombogenic properties of magnesium and magnesium-aluminum wire in the dog's aorta. Surgery **1951,** 30 (6), 987-993.

51. Wexler, B. C., Pathophysiologic responses of spontaneously hypertensive rats to arterial magnesium—aluminum wire implants. Atherosclerosis **1980,** 36 (4), 575-587.

52. Hussl, H.; Papp, C.; Höpfel-Kreiner, I.; Rumpl, E.; Wilflingseder, P., Resorption time and tissue reactions with magnesium rods in rats and rabbits. Chirurgia plastica **1981,** 6 (2), 117-126.

53. Wilflingseder, P.; Martin, R.; Papp, C., Magnesium seeds in the treatment of lymph-and haemangiomata. Chirurgia plastica **1981,** 6 (2), 105-116.

54. Song, G.; Atrens, A.; Stjohn, D.; Nairn, J.; Li, Y., The electrochemical corrosion of pure magnesium in 1 N NaCl. Corrosion Science **1997,** 39 (5), 855-875.

55. Song, G.; Atrens, A.; Wu, X.; Zhang, B., Corrosion behaviour of AZ21, AZ501 and AZ91 in sodium chloride. Corrosion science **1998,** 40 (10), 1769-1791.

56. Ambat, R.; Aung, N. N.; Zhou, W., Evaluation of microstructural effects on corrosion behaviour of AZ91D magnesium alloy. Corrosion science **2000,** 42 (8), 1433-1455.

57. Al-Abdullat, Y.; Tsutsumi, S.; Nakajima, N.; Ohta, M.; Kuwahara, H.; Ikeuchi, K., Surface modification of magnesium by NaHCO3 and corrosion behavior in Hank's solution for new biomaterial applications. Materials Transactions **2001,** 42 (8), 1777-1780.

58. Inoue, H.; Sugahara, K.; Yamamoto, A.; Tsubakino, H., Corrosion rate of magnesium and its alloys in buffered chloride solutions. Corrosion Science **2002,** 44 (3), 603-610.

59. Jiang, Y.; Guo, X.; Wei, Y.; Zhai, C.; Ding, W., Corrosion protection of polypyrrole electrodeposited on AZ91 magnesium alloys in alkaline solutions. Synthetic Metals **2003,** 139 (2), 335-339.

60. Zhang, E.; Xu, L.; Yang, K., Formation by ion plating of Ti-coating on pure Mg for biomedical applications. Scripta Materialia **2005,** 53 (5), 523-527.

61. Yfantis, C.; Yfantis, D.; Anastassopoulou, J.; Theophanides, T.; Staiger, M. In In vitro corrosion behavior of new magnesium alloys for bone regeneration, Proceedings of the 4th WSEAS International Conference on Environment, Ecosystems and Development, Venice, Italy, Citeseer: 2006; pp 20-22.

62. Liu, M.; Qiu, D.; Zhao, M.-C.; Song, G.; Atrens, A., The effect of crystallographic orientation on the active corrosion of pure magnesium. Scripta Materialia **2008,** 58 (5), 421-424.

63. Quach, N.; Uggowitzer, P.; Schmutz, P., Corrosion behaviour of an MgeYeRE alloy used in biomedical applications studied by electrochemical techniques, Compt. Rendus Chem **2008,** 11.

64. Zhang, S.; Zhang, X.; Zhao, C.; Li, J.; Song, Y.; Xie, C.; Tao, H.; Zhang, Y.; He, Y.; Jiang, Y., Research on an Mg–Zn alloy as a degradable biomaterial. Acta biomaterialia **2010,** 6 (2), 626-640.

65. op't Hoog, C.; Birbilis, N.; Estrin, Y., Corrosion of pure Mg as a function of grain size and processing route. Advanced Engineering Materials **2008,** 10 (6), 579-582.

66. Gu, X.; Zheng, W.; Cheng, Y.; Zheng, Y., A study on alkaline heat treated Mg–Ca alloy for the control of the biocorrosion rate. Acta Biomaterialia **2009,** 5 (7), 2790-2799.

67. Aung, N. N.; Zhou, W., Effect of grain size and twins on corrosion behaviour of AZ31B magnesium alloy. Corrosion Science **2010,** 52 (2), 589-594.

68. Meng, E.; Guan, S.; Wang, H.; Wang, L.; Zhu, S.; Hu, J.; Ren, C.; Gao, J.; Feng, Y., Effect of electrodeposition modes on surface characteristics and corrosion properties of fluorine-doped hydroxyapatite coatings on Mg–Zn–Ca alloy. Applied Surface Science **2011,** 257 (11), 4811-4816.

69. Chun-Yan, Z.; Rong-Chang, Z.; Cheng-Long, L.; Jia-Cheng, G., Comparison of calcium phosphate coatings on Mg–Al and Mg–Ca alloys and their corrosion behavior in Hank's solution. Surface and Coatings Technology **2010,** 204 (21-22), 3636-3640.

70. Xue, D.; Yun, Y.; Tan, Z.; Dong, Z.; Schulz, M. J., In vivo and in vitro degradation behavior of magnesium alloys as biomaterials. Journal of Materials Science & Technology **2012,** 28 (3), 261-267.

71. Walker, J.; Shadanbaz, S.; Kirkland, N. T.; Stace, E.; Woodfield, T.; Staiger, M. P.; Dias, G. J., Magnesium alloys: predicting in vivo corrosion with in vitro immersion testing. Journal of Biomedical Materials Research Part B: Applied Biomaterials **2012,** 100 (4), 1134-1141.

72. Argade, G.; Kandasamy, K.; Panigrahi, S.; Mishra, R., Corrosion behavior of a friction stir processed rare-earth added magnesium alloy. Corrosion Science **2012,** 58, 321-326.

73. Sunil, B. R.; Kumar, T. S.; Chakkingal, U.; Nandakumar, V.; Doble, M., Nano-hydroxyapatite reinforced AZ31 magnesium alloy by friction stir processing: a solid state processing for biodegradable metal matrix composites. Journal of Materials Science: Materials in Medicine **2014,** 25 (4), 975-988.

74. Hofstetter, J.; Martinelli, E.; Weinberg, A. M.; Becker, M.; Mingler, B.; Uggowitzer, P. J.; Löffler, J. F., Assessing the degradation performance of ultrahigh-purity magnesium in vitro and in vivo. Corrosion Science **2015,** 91, 29-36.

75. Salami, B.; Afshar, A.; Mazaheri, A., The effect of sodium silicate concentration on microstructure and corrosion properties of MAO-coated magnesium alloy AZ31 in simulated body fluid. Journal of Magnesium and Alloys **2014,** 2 (1), 72-77.

76. Zhao, L.; Cui, C.; Wang, X.; Liu, S.; Bu, S.; Wang, Q.; Qi, Y., Corrosion resistance and calcium–phosphorus precipitation of micro-arc oxidized magnesium for biomedical applications. Applied Surface Science **2015,** 330, 431-438.

77. Saha, P.; Roy, M.; Datta, M. K.; Lee, B.; Kumta, P. N., Effects of grain refinement on the biocorrosion and in vitro bioactivity of magnesium. Materials Science and Engineering: C **2015,** 57, 294-303.

78. Myrissa, A.; Agha, N. A.; Lu, Y.; Martinelli, E.; Eichler, J.; Szakacs, G.; Kleinhans, C.; Willumeit-Römer, R.; Schäfer, U.; Weinberg, A.-M., In vitro and in vivo comparison of binary Mg alloys and pure Mg. Materials Science and Engineering: C **2016,** 61, 865-874.

79. Sun, W.; Zhang, G.; Tan, L.; Yang, K.; Ai, H., The fluoride coated AZ31B magnesium alloy improves corrosion resistance and stimulates bone formation in rabbit model. Materials Science and Engineering: C **2016,** 63, 506-511.

80. Mukhametkaliyev, T.; Surmeneva, M.; Vladescu, A.; Cotrut, C. M.; Braic, M.; Dinu, M.; Vranceanu, M.; Pana, I.; Mueller, M.; Surmenev, R., A biodegradable AZ91 magnesium alloy coated with a thin nanostructured hydroxyapatite for improving the corrosion resistance. Materials Science and Engineering: C **2017,** 75, 95-103.

81. Huang, W.; Xu, B.; Yang, W.; Zhang, K.; Chen, Y.; Yin, X.; Liu, Y.; Ni, Z.; Pei, F., Corrosion behavior and biocompatibility of hydroxyapatite/magnesium phosphate/zinc phosphate composite coating deposited on AZ31 alloy. Surface and Coatings Technology **2017,** 326, 270-280.

82. Dehghanian, C.; Aboudzadeh, N.; Shokrgozar, M. A., Characterization of silicon-substituted nano hydroxyapatite coating on magnesium alloy for biomaterial application. Materials Chemistry and Physics **2018,** 203, 27-33.

83. Khalifeh, S.; Burleigh, T. D., Super-hydrophobic stearic acid layer formed on anodized high purified magnesium for improving corrosion resistance of bioabsorbable implants. Journal of Magnesium and Alloys **2018,** 6 (4), 327-336.

84. Cai, S.; Sun, J.; Liu, J.; Xu, G., Ultrasonic aqueous synthesis of corrosion resistant hydroxyapatite coating on magnesium alloys for the application of long-term implant. Ultrasonics sonochemistry **2019,** 58, 104677.

85. Rúa, J.; Zuleta, A.; Ramírez, J.; Fernández-Morales, P., Micro-arc oxidation coating on porous magnesium foam and its potential biomedical applications. Surface and Coatings Technology **2019,** 360, 213-221.

86. Li, L.-Y.; Cui, L.-Y.; Liu, B.; Zeng, R.-C.; Chen, X.-B.; Li, S.-Q.; Wang, Z.-L.; Han, E.-H., Corrosion resistance of glucose-induced hydrothermal calcium phosphate coating on pure magnesium. Applied Surface Science **2019,** 465, 1066-1077.

87. Yadav, V.; Sankar, M.; Pandey, L., Coating of bioactive glass on magnesium alloys to improve its degradation behavior: Interfacial aspects. Journal of Magnesium and Alloys **2020**.

88. Mehrjou, B.; Dehghan-Baniani, D.; Shi, M.; Shanaghi, A.; Wang, G.; Liu, L.; Qasim, A. M.; Chu, P. K., Nanopatterned silk-coated AZ31 magnesium alloy with enhanced antibacterial and corrosion properties. Materials Science and Engineering: C **2020,** 116, 111173.

89. Zhu, Y.; Zheng, L.; Liu, W.; Qin, L.; Ngai, T., Poly (l-lactic acid)(PLLA)/MgSO4· 7H2O Composite Coating on Magnesium Substrates for Corrosion Protection and Cytocompatibility Promotion. ACS Applied Bio Materials **2020,** 3 (3), 1364-1373.

90. Gonsalves, T. C.; Freitas, B. X. d.; Nunes, C. A.; Florenzano, F. H., Reduction of Magnesium Corrosion Rate by PMMA-co-PMAA Films. Materials Research **2021,** 24.

91. Genders, J. D.; Pletcher, D., Studies using microelectrodes of the Mg (II)/Mg couple in tetrahydrofuran and propylene carbonate. Journal of electroanalytical chemistry and interfacial electrochemistry **1986,** 199 (1), 93-100.

92. Baril, G.; Pebere, N., The corrosion of pure magnesium in aerated and deaerated sodium sulphate solutions. Corrosion Science **2001,** 43 (3), 471-484.

93. Zeng, R.-c.; Zhang, J.; Huang, W.-j.; Dietzel, W.; Kainer, K.; Blawert, C.; Wei, K., Review of studies on corrosion of magnesium alloys. Transactions of Nonferrous Metals Society of China **2006,** 16, s763-s771.

94. Zeng, R.; Dietzel, W.; Witte, F.; Hort, N.; Blawert, C., Progress and challenge for magnesium alloys as biomaterials. Advanced engineering materials **2008,** 10 (8), B3-B14.

95. Gray, J.; Luan, B., Protective coatings on magnesium and its alloys—a critical review. Journal of alloys and compounds **2002,** 336 (1-2), 88-113.

96. Song, Y.; Shan, D.; Han, E., Electrodeposition of hydroxyapatite coating on AZ91D magnesium alloy for biomaterial application. Materials letters **2008,** 62 (17-18), 3276-3279.

97. Zhao, M.-C.; Liu, M.; Song, G.-L.; Atrens, A., Influence of pH and chloride ion concentration on the corrosion of Mg alloy ZE41. Corrosion Science **2008,** 50 (11), 3168-3178.

98. He, S.-Y.; Yue, S.; Chen, M.-F.; Liu, D.-B.; Ye, X.-Y., Microstructure and properties of biodegradable β-TCP reinforced Mg-Zn-Zr composites. Transactions of Nonferrous Metals Society of China **2011,** 21 (4), 814-819.

99. Bakhsheshi-Rad, H.; Hamzah, E.; Kasiri-Asgarani, M.; Jabbarzare, S.; Iqbal, N.; Kadir, M. A., Deposition of nanostructured fluorine-doped hydroxyapatite–polycaprolactone duplex coating to enhance the mechanical properties and corrosion resistance of Mg alloy for biomedical applications. Materials Science and Engineering: C **2016,** 60, 526-537.

100. Liu, G.-y.; Tang, S.-w.; Chuan, W.; Jin, H.; Li, D.-c., Formation characteristic of Ca–P coatings on magnesium alloy surface. Transactions of Nonferrous Metals Society of China **2013,** 23 (8), 2294-2299.

101. Witte, F.; Hort, N.; Vogt, C.; Cohen, S.; Kainer, K. U.; Willumeit, R.; Feyerabend, F., Degradable biomaterials based on magnesium corrosion. Current opinion in solid state and materials science **2008,** 12 (5-6), 63-72.

102. Witte, F.; Fischer, J.; Nellesen, J.; Crostack, H.-A.; Kaese, V.; Pisch, A.; Beckmann, F.; Windhagen, H., In vitro and in vivo corrosion measurements of magnesium alloys. Biomaterials **2006,** 27 (7), 1013-1018.

103. Han, G.; Lee, J.-Y.; Kim, Y.-C.; Park, J. H.; Kim, D.-I.; Han, H.-S.; Yang, S.-J.; Seok, H.-K., Preferred crystallographic pitting corrosion of pure magnesium in Hanks' solution. Corrosion Science **2012,** 63, 316-322.

104. Wang, H.; Guan, S.; Wang, X.; Ren, C.; Wang, L., In vitro degradation and mechanical integrity of Mg–Zn–Ca alloy coated with Ca-deficient hydroxyapatite by the pulse electrodeposition process. Acta Biomaterialia **2010,** 6 (5), 1743-1748.

105. Kraus, T.; Fischerauer, S. F.; Hänzi, A. C.; Uggowitzer, P. J.; Löffler, J. F.; Weinberg, A. M., Magnesium alloys for temporary implants in osteosynthesis: in vivo studies of their degradation and interaction with bone. Acta biomaterialia **2012,** 8 (3), 1230-1238.

106. Ferrando, W., Review of corrosion and corrosion control of magnesium alloys and composites. Journal of Materials Engineering **1989,** 11 (4), 299-313.

107. Zhao, L.; Cui, C.; Wang, Q.; Bu, S., Growth characteristics and corrosion resistance of micro-arc oxidation coating on pure magnesium for biomedical applications. Corrosion Science **2010,** 52 (7), 2228-2234.

108. Xu, L.; Pan, F.; Yu, G.; Yang, L.; Zhang, E.; Yang, K., In vitro and in vivo evaluation of the surface bioactivity of a calcium phosphate coated magnesium alloy. Biomaterials **2009,** 30 (8), 1512-1523.

109. Gu, X.; Zheng, Y.; Cheng, Y.; Zhong, S.; Xi, T., In vitro corrosion and biocompatibility of binary magnesium alloys. Biomaterials **2009,** 30 (4), 484-498.

110. Gu, X.-N.; Zheng, Y.-F., A review on magnesium alloys as biodegradable materials. Frontiers of Materials Science in China **2010,** 4 (2), 111-115.

111. Jiang, B.; Xiang, Q.; Atrens, A.; Song, J.; Pan, F., Influence of crystallographic texture and grain size on the corrosion behaviour of as-extruded Mg alloy AZ31 sheets. Corrosion Science **2017,** 126, 374-380.

112. Anne, G.; Ramesh, M.; Nayaka, H. S.; Arya, S. B.; Sahu, S., Microstructure Evolution and Mechanical and Corrosion Behavior of Accumulative Roll Bonded Mg-2% Zn/Al-7075 Multilayered Composite. Journal of Materials Engineering and Performance **2017,** 26 (4), 1726-1734.

113. Feng, A.; Han, Y., Mechanical and in vitro degradation behavior of ultrafine calcium polyphosphate reinforced magnesium-alloy composites. Materials & Design **2011,** 32 (5), 2813-2820.

114. Yue, L.; Ma, J.; Zhang, J.; Zhao, J.; Dong, S.; Liu, Z.; Cui, G.; Chen, L., All solid-state polymer electrolytes for high-performance lithium ion batteries. Energy Storage Mater. **2016,** 5, 139-164.

115. Gusieva, K.; Davies, C.; Scully, J.; Birbilis, N., Corrosion of magnesium alloys: the role of alloying. International Materials Reviews **2015,** 60 (3), 169-194.

116. Ding, Y.; Wen, C.; Hodgson, P.; Li, Y., Effects of alloying elements on the corrosion behavior and biocompatibility of biodegradable magnesium alloys: a review. Journal of materials chemistry B **2014,** 2 (14), 1912-1933.

117. Hort, N.; Huang, Y.; Fechner, D.; Störmer, M.; Blawert, C.; Witte, F.; Vogt, C.; Drücker, H.; Willumeit, R.; Kainer, K., Magnesium alloys as implant materials–Principles of property design for Mg–RE alloys. Acta biomaterialia **2010,** 6 (5), 1714-1725.

118. Rana, R.; Purohit, R.; Das, S., Reviews on the influences of alloying elements on the microstructure and mechanical properties of aluminum alloys and aluminum alloy composites. International Journal of Scientific and Research Publications **2012,** 2 (6), 1-7.

119. Zhang, J.; Niu, X.; Qiu, X.; Liu, K.; Nan, C.; Tang, D.; Meng, J., Effect of yttrium-rich misch metal on the microstructures, mechanical properties and corrosion behavior of die cast AZ91 alloy. Journal of Alloys and Compounds **2009,** 471 (1-2), 322-330.

120. Song, G.; Atrens, A., Understanding magnesium corrosion—a framework for improved alloy performance. Advanced engineering materials **2003,** 5 (12), 837-858.

121. Feyerabend, F.; Fischer, J.; Holtz, J.; Witte, F.; Willumeit, R.; Drücker, H.; Vogt, C.; Hort, N., Evaluation of short-term effects of rare earth and other elements used in magnesium alloys on primary cells and cell lines. Acta biomaterialia **2010,** 6 (5), 1834-1842.

122. Yuen, C.; Ip, W., Theoretical risk assessment of magnesium alloys as degradable biomedical implants. Acta biomaterialia **2010,** 6 (5), 1808-1812.

123. Sigel, H., Metal Ions in Biological Systems: Volume 21: Applications of Magnetic Resonance to Paramagnetic Species. CRC Press: 1986; Vol. 21.

124. Seiler, H. G.; Sigel, H.; Sigel, A., Handbook on toxicity of inorganic compounds. **1988**.

125. Ilich, J. Z.; Kerstetter, J. E., Nutrition in bone health revisited: a story beyond calcium. Journal of the American college of nutrition **2000,** 19 (6), 715-737.

126. Nielsen, F. H., Importance of making dietary recommendations for elements designated as nutritionally beneficial, pharmacologically beneficial, or conditioinally essential. The Journal of Trace Elements in Experimental Medicine: The Official Publication of the International Society for Trace Element Research in Humans **2000,** 13 (1), 113-129.

127. Pichler, K.; Kraus, T.; Martinelli, E.; Sadoghi, P.; Musumeci, G.; Uggowitzer, P. J.; Weinberg, A. M., Cellular reactions to biodegradable magnesium alloys on human growth plate chondrocytes and osteoblasts. International orthopaedics **2014,** 38 (4), 881-889.

128. Hirano, S.; Suzuki, K. T., Exposure, metabolism, and toxicity of rare earths and related compounds. Environmental health perspectives **1996,** 104 (suppl 1), 85-95.

129. Luo, A. A., Recent magnesium alloy development for elevated temperature applications. International materials reviews **2004,** 49 (1), 13-30.

130. Staiger, M. P.; Pietak, A. M.; Huadmai, J.; Dias, G., Magnesium and its alloys as orthopedic biomaterials: a review. Biomaterials **2006,** 27 (9), 1728-1734.

131. Harris, I.; Varley, P., Factors influencing brittleness in aluminium-magnesium-silicon alloys. J. Inst. Metals **1954,** 82.

132. Chandrasekaran, M.; John, Y. M. S., Effect of materials and temperature on the forward extrusion of magnesium alloys. Materials Science and Engineering: A **2004,** 381 (1-2), 308-319.

133. Hassan, S.; Gupta, M., Development of high performance magnesium nano-composites using nano-Al2O3 as reinforcement. Materials Science and Engineering: A **2005,** 392 (1-2), 163-168.

134. Liao, J.; Hotta, M.; Motoda, S.-i.; Shinohara, T., Atmospheric corrosion of two field-exposed AZ31B magnesium alloys with different grain size. Corrosion Science **2013,** 71, 53-61.

135. Birbilis, N.; Ralston, K.; Virtanen, S.; Fraser, H.; Davies, C., Grain character influences on corrosion of ECAPed pure magnesium. Corrosion Engineering, Science and Technology **2010,** 45 (3), 224-230.

136. Ralston, K.; Williams, G.; Birbilis, N., Effect of pH on the grain size dependence of magnesium corrosion. Corrosion **2012,** 68 (6), 507-517.

137. Matsunoshita, H.; Edalati, K.; Furui, M.; Horita, Z., Ultrafine-grained magnesium–lithium alloy processed by high-pressure torsion: Low-temperature superplasticity and potential for hydroforming. Materials Science and Engineering: A **2015,** 640, 443-448.

138. Valiev, R. Z.; Islamgaliev, R. K.; Alexandrov, I. V., Bulk nanostructured materials from severe plastic deformation. Progress in materials science **2000,** 45 (2), 103-189.

139. Valiev, R. Z.; Estrin, Y.; Horita, Z.; Langdon, T. G.; Zechetbauer, M. J.; Zhu, Y. T., Producing bulk ultrafine-grained materials by severe plastic deformation. Jom **2006,** 58 (4), 33-39.

140. Huot, J.; Skryabina, N. Y.; Fruchart, D., Application of severe plastic deformation techniques to magnesium for enhanced hydrogen sorption properties. Metals **2012,** 2 (3), 329-343.

141. Kim, W.; Jeong, H.; Jeong, H., Achieving high strength and high ductility in magnesium alloys using severe plastic deformation combined with low-temperature aging. Scripta Materialia **2009,** 61 (11), 1040-1043.

142. Cao, F.; Shi, Z.; Song, G.-L.; Liu, M.; Dargusch, M. S.; Atrens, A., Influence of hot rolling on the corrosion behavior of several Mg–X alloys. Corrosion Science **2015,** 90, 176-191.

143. Nurislamova, G.; Sauvage, X.; Murashkin, M.; Islamgaliev, R.; Valiev, R., Nanostructure and related mechanical properties of an Al–Mg–Si alloy processed by severe plastic deformation. Philosophical Magazine Letters **2008,** 88 (6), 459-466.

144. Feng, A.; Ma, Z., Enhanced mechanical properties of Mg–Al–Zn cast alloy via friction stir processing. Scripta materialia **2007,** 56 (5), 397-400.

145. Kang, S.; Lee, Y.; Lee, J., Effect of grain refinement of magnesium alloy AZ31 by severe plastic deformation on material characteristics. Journal of Materials Processing Technology **2008,** 201 (1-3), 436-440.

146. Chen, Y.; Wang, Q.; Peng, J.; Zhai, C.; Ding, W., Effects of extrusion ratio on the microstructure and mechanical properties of AZ31 Mg alloy. Journal of materials processing technology **2007,** 182 (1-3), 281-285.

147. Kim, W.; Lee, J.; Kim, W.; Jeong, H.; Jeong, H., Microstructure and mechanical properties of Mg–Al–Zn alloy sheets severely deformed by asymmetrical rolling. Scripta Materialia **2007,** 56 (4), 309-312.

148. Xia, W.; Chen, Z.; Chen, D.; Zhu, S., Microstructure and mechanical properties of AZ31 magnesium alloy sheets produced by differential speed rolling. Journal of materials processing technology **2009,** 209 (1), 26-31.

149. Al-Samman, T.; Gottstein, G., Dynamic recrystallization during high temperature deformation of magnesium. Materials Science and Engineering: A **2008,** 490 (1-2), 411-420.

150. Cottam, R.; Robson, J.; Lorimer, G.; Davis, B., Dynamic recrystallization of Mg and Mg–Y alloys: Crystallographic texture development. Materials Science and Engineering: A **2008,** 485 (1-2), 375-382.

151. Sitdikov, O.; Kaibyshev, R., Dynamic recrystallization in pure magnesium. Materials Transactions **2001,** 42 (9), 1928-1937.

152. Muzyk, M.; Pakiela, Z.; Kurzydlowski, K., Generalized stacking fault energy in magnesium alloys: density functional theory calculations. Scripta Materialia **2012,** 66 (5), 219-222.

153. Sandlöbes, S.; Friák, M.; Zaefferer, S.; Dick, A.; Yi, S.; Letzig, D.; Pei, Z.; Zhu, L.-F.; Neugebauer, J.; Raabe, D., The relation between ductility and stacking fault energies in Mg and Mg–Y alloys. Acta Materialia **2012,** 60 (6-7), 3011-3021.

154. Shang, S.; Wang, W.; Zhou, B.; Wang, Y.; Darling, K.; Kecskes, L.; Mathaudhu, S.; Liu, Z., Generalized stacking fault energy, ideal strength and twinnability of dilute Mg-based alloys: a first-principles study of shear deformation. Acta Materialia **2014,** 67, 168-180.

155. Couret, A.; Caillard, D., An in situ study of prismatic glide in magnesium—II. Microscopic activation parameters. Acta Metallurgica **1985,** 33 (8), 1455-1462.

156. Chowdhury, A.; Mari, D.; Schaller, R., Thermal stress relaxation in magnesium matrix composites controlled by dislocation breakaway. Composites Science and Technology **2010,** 70 (1), 136-142.

157. McQueen, H.; Bourell, D., Thermomechanical processing of titanium, zirconium, magnesium, and zinc in the hcp structure. Journal of Materials Shaping Technology **1988,** 5 (3), 163-189.

158. Koike, J.; Kobayashi, T.; Mukai, T.; Watanabe, H.; Suzuki, M.; Maruyama, K.; Higashi, K., The activity of non-basal slip systems and dynamic recovery at room temperature in fine-grained AZ31B magnesium alloys. Acta materialia **2003,** 51 (7), 2055-2065.

159. Sandlöbes, S.; Zaefferer, S.; Schestakow, I.; Yi, S.; Gonzalez-Martinez, R., On the role of non-basal deformation mechanisms for the ductility of Mg and Mg–Y alloys. Acta Materialia **2011,** 59 (2), 429-439.

160. Myshlyaev, M.; McQueen, H.; Mwembela, A.; Konopleva, E., Twinning, dynamic recovery and recrystallization in hot worked Mg–Al–Zn alloy. Materials Science and Engineering: A **2002,** 337 (1-2), 121-133.

161. Del Valle, J.; Pérez-Prado, M. T.; Ruano, O. A., Texture evolution during large-strain hot rolling of the Mg AZ61 alloy. Materials Science and Engineering: A **2003,** 355 (1-2), 68-78.

162. Ion, S.; Humphreys, F.; White, S., Dynamic recrystallisation and the development of microstructure during the high temperature deformation of magnesium. Acta Metallurgica **1982,** 30 (10), 1909-1919.

163. Xiang, Q.; Jiang, B.; Zhang, Y.; Chen, X.; Song, J.; Xu, J.; Fang, L.; Pan, F., Effect of rolling-induced microstructure on corrosion behaviour of an as-extruded Mg-5Li-1Al alloy sheet. Corrosion Science **2017,** 119, 14-22.

164. Ma, Z., Friction stir processing technology: a review. Metallurgical and materials Transactions A **2008,** 39 (3), 642-658.

165. Besharati-Givi, M.-K.; Asadi, P., Advances in friction-stir welding and processing. Elsevier: 2014.

166. Chen, C.; Chen, J.; Yan, H.; Su, B.; Song, M.; Zhu, S., Dynamic precipitation, microstructure and mechanical properties of Mg-5Zn-1Mn alloy sheets prepared by high strain-rate rolling. Materials & Design **2016,** 100, 58-66.

167. Zhu, S.; Yan, H.; Chen, J.; Wu, Y.; Su, B.; Du, Y.; Liao, X., Feasibility of high strain-rate rolling of a magnesium alloy across a wide temperature range. Scripta Materialia **2012,** 67 (4), 404-407.

168. Iwahashi, Y.; Horita, Z.; Nemoto, M.; Wang, J.; Langdon, T. G., Principle of equal-channel angular pressing for the processing of ultra-fine grained materials. Scripta materialia **1996,** 35 (2).

169. Valiev, R. Z.; Langdon, T. G., Principles of equal-channel angular pressing as a processing tool for grain refinement. Progress in materials science **2006,** 51 (7), 881-981.

170. Saikrishna, N.; Reddy, G. P. K.; Munirathinam, B.; Sunil, B. R., Influence of bimodal grain size distribution on the corrosion behavior of friction stir processed biodegradable AZ31 magnesium alloy. Journal of magnesium and alloys **2016,** 4 (1), 68-76.

171. Nayak, S.; Bhushan, B.; Jayaganthan, R.; Gopinath, P.; Agarwal, R.; Lahiri, D., Strengthening of Mg based alloy through grain refinement for orthopaedic application. journal of the mechanical behavior of biomedical materials **2016,** 59, 57-70.

172. Tse, Y. Y.; Zhang, K.; Du, Y.; Maradze, D.; Liu, Y. In Effect of grain size, precipitation and texture on mechanical and corrosion properties of ECAPed AZ80, European Microscopy Congress 2016: Proceedings, Wiley Online Library: 2016; pp 902-903.

173. Alvarez-Lopez, M.; Pereda, M. D.; Del Valle, J.; Fernandez-Lorenzo, M.; Garcia-Alonso, M.; Ruano, O. A.; Escudero, M., Corrosion behaviour of AZ31 magnesium alloy with different grain sizes in simulated biological fluids. Acta Biomaterialia **2010,** 6 (5), 1763-1771.

174. Wang, H.; Estrin, Y.; Fu, H.; Song, G.; Zúberová, Z., The effect of pre-processing and grain structure on the bio-corrosion and fatigue resistance of magnesium alloy AZ31. Advanced Engineering Materials **2007,** 9 (11), 967-972.

175. Song, D.; Ma, A.; Jiang, J.; Lin, P.; Yang, D.; Fan, J., Corrosion behavior of equal-channel-angular-pressed pure magnesium in NaCl aqueous solution. Corrosion Science **2010,** 52 (2), 481-490.

176. Yu, Z.; Chen, J.; Yan, H.; Xia, W.; Su, B.; Gong, X.; Guo, H., Degradation, stress corrosion cracking behavior and cytocompatibility of high strain rate rolled Mg-Zn-Sr alloys. Materials Letters **2020,** 260, 126920.

177. Zou, Z.; Chen, J.; Yan, H.; Su, B.; Gong, X., Microstructure, Bio-corrosion Behavior, and Corrosion Residual Strength of High Strain Rate Rolled Mg-4Zn Alloy Sheet. Journal of Materials Engineering and Performance **2016,** 25 (5), 1974-1985.

178. Liu, Q.; Ma, Q.-x.; Chen, G.-q.; Cao, X.; Zhang, S.; Pan, J.-l.; Zhang, G.; Shi, Q.-y., Enhanced corrosion resistance of AZ91 magnesium alloy through refinement and homogenization of surface microstructure by friction stir processing. Corrosion science **2018,** 138, 284-296.

179. Seifiyan, H.; Sohi, M. H.; Ansari, M.; Ahmadkhaniha, D.; Saremi, M., Influence of friction stir processing conditions on corrosion behavior of AZ31B magnesium alloy. Journal of Magnesium and Alloys **2019,** 7 (4), 605-616.

180. Sidhu, H. S.; Singh, B.; Kumar, P., To study the corrosion behavior of friction stir processed magnesium alloy AZ91. Materials Today: Proceedings **2021,** 44, 4633-4639.

181. Eivani, A.; Mehdizade, M.; Chabok, S.; Zhou, J., Applying multi-pass friction stir processing to refine the microstructure and enhance the strength, ductility and corrosion resistance of WE43 magnesium alloy. Journal of Materials Research and Technology **2021,** 12, 1946-1957.

182. Patle, H.; Sunil, B.; Dumpala, R., Machining characteristics, wear and corrosion behavior of AZ91 magnesium alloy-fly ash composites produced by friction stir processing. Materialwissenschaft und Werkstofftechnik **2021,** 52 (1), 88-99.

183. Cao, G.; Zhang, D.; Zhang, W.; Zhang, W., In vitro corrosion study of friction stir processed WE43 magnesium alloy in a simulated body fluid. Materials **2016,** 9 (7), 542.

184. Zhang, X.; Yang, T.; Castagne, S.; Wang, J., Microstructure; bonding strength and thickness ratio of Al/Mg/Al alloy laminated composites prepared by hot rolling. Materials Science and Engineering: A **2011,** 528 (4-5), 1954-1960.

185. Koleini, S.; Idris, M. H.; Jafari, H., Influence of hot rolling parameters on microstructure and biodegradability of Mg–1Ca alloy in simulated body fluid. Materials & Design **2012,** 33, 20-25.

186. Wang, J.; Li, Q. In Grain Size and Mechanical Property of Magnesium Experienced Rolling and Post Heat Treatment, Thermomechanics & Infrared Imaging, Inverse Problem Methodologies and Mechanics of Additive & Advanced Manufactured Materials, Volume 7: Proceedings of the 2020 Annual Conference on Experimental and Applied Mechanics, Springer Nature: 2020; p 13.

187. Miao, Q.; Hu, L.; Wang, G.; Wang, E., Fabrication of excellent mechanical properties AZ31 magnesium alloy sheets by conventional rolling and subsequent annealing. Materials Science and Engineering: A **2011,** 528 (22-23), 6694-6701.

188. Zi, A.; Palkowski, H., Direct strip casting and hot rolling of an AZ31 magnesium alloy. Materials Science and Engineering: A **2010,** 528 (2), 559-565.

189. Chai, S.; Zhang, D.; Pan, F.; Dong, J.; Guo, F.; Dong, Y., Influence of post-weld hot rolling on the microstructure and mechanical properties of AZ31 magnesium alloy sheet. Materials Science and Engineering: A **2013,** 588, 208-213.

190. Zhu, S.; Yan, H.; Chen, J.; Wu, Y.; Liu, J.; Tian, J., Effect of twinning and dynamic recrystallization on the high strain rate rolling process. Scripta Materialia **2010,** 63 (10), 985-988.

191. Tewary, N.; Ghosh, S.; Bera, S.; Chakrabarti, D.; Chatterjee, S., Influence of cold rolling on microstructure, texture and mechanical properties of low carbon high Mn TWIP steel. Materials Science and Engineering: A **2014,** 615, 405-415.

192. Yahiro, A.; Masui, T.; Yoshida, T.; Doi, D., Development of nonferrous clad plate and sheet by warm rolling with different temperature of materials. ISIJ international **1991,** 31 (6), 647-654.

193. Hornberger, H.; Virtanen, S.; Boccaccini, A., Biomedical coatings on magnesium alloys–a review. Acta biomaterialia **2012,** 8 (7), 2442-2455.

194. Guo, H.; An, M., Growth of ceramic coatings on AZ91D magnesium alloys by micro-arc oxidation in aluminate–fluoride solutions and evaluation of corrosion resistance. Applied Surface Science **2005,** 246 (1-3), 229-238.

195. Tang, H.; Han, Y.; Wu, T.; Tao, W.; Jian, X.; Wu, Y.; Xu, F., Synthesis and properties of hydroxyapatite-containing coating on AZ31 magnesium alloy by micro-arc oxidation. Applied Surface Science **2017,** 400, 391-404.

196. Tekin, M.; Taslicay, C.; Muhaffel, F.; Cimenoglu, H. In Evaluation of Wear and Corrosion Resistances of Oxide Coatings Formed on Magnesium Alloys by Micro Arc Oxidation, Solid State Phenomena, Trans Tech Publ: 2017; pp 125-130.

197. Wang, Z.; Li, Q.; She, Z.; Chen, F.; Li, L., Low-cost and large-scale fabrication method for an environmentally-friendly superhydrophobic coating on magnesium alloy. Journal of Materials Chemistry **2012,** 22 (9), 4097-4105.

198. Bakin, B.; Delice, T. K.; Tiric, U.; Birlik, I.; Azem, F. A., Bioactivity and corrosion properties of magnesium-substituted CaP coatings produced via electrochemical deposition. Surface and Coatings Technology **2016,** 301, 29-35.

199. Kang, Z.; Li, W., Facile and fast fabrication of superhydrophobic surface on magnesium alloy by one-step electrodeposition method. Journal of industrial and engineering chemistry **2017,** 50, 50-56.

200. Liu, B.; Zhang, X.; Xiao, G.-y.; Lu, Y.-p., Phosphate chemical conversion coatings on metallic substrates for biomedical application: A review. Materials Science and Engineering: C **2015,** 47, 97-104.

201. Duan, G.; Yang, L.; Liao, S.; Zhang, C.; Lu, X.; Yang, Y.; Zhang, B.; Wei, Y.; Zhang, T.; Yu, B., Designing for the chemical conversion coating with high corrosion resistance and low electrical contact resistance on AZ91D magnesium alloy. Corrosion Science **2018,** 135, 197-206.

202. Lin, X.; Tan, L.; Zhang, Q.; Yang, K.; Hu, Z.; Qiu, J.; Cai, Y., The in vitro degradation process and biocompatibility of a ZK60 magnesium alloy with a forsterite-containing micro-arc oxidation coating. Acta biomaterialia **2013,** 9 (10), 8631-8642.

203. Zhang, X.; Zhao, Z.; Wu, F.; Wang, Y.; Wu, J., Corrosion and wear resistance of AZ91D magnesium alloy with and without microarc oxidation coating in Hank's solution. Journal of Materials Science **2007,** 42 (20), 8523-8528.

204. Zhang, R.; Zhang, S., Formation of micro-arc oxidation coatings on AZ91HP magnesium alloys. Corrosion Science **2009,** 51 (12), 2820-2825.

205. Krishna, L. R.; Sundararajan, G., Aqueous corrosion behavior of micro arc oxidation (MAO)-coated magnesium alloys: a critical review. Jom **2014,** 66 (6), 1045-1060.

206. Wu, G.; Ibrahim, J. M.; Chu, P. K., Surface design of biodegradable magnesium alloys—a review. Surface and Coatings Technology **2013,** 233, 2-12.

207. Nassif, N.; Ghayad, I., Corrosion protection and surface treatment of magnesium alloys used for orthopedic applications. Advances in Materials Science and Engineering **2013,** 2013.

208. Narayanan, T. S.; Park, I. S.; Lee, M. H., Strategies to improve the corrosion resistance of microarc oxidation (MAO) coated magnesium alloys for degradable implants: Prospects and challenges. Progress in Materials Science **2014,** 60, 1-71.

209. Butyagin, P.; Khokhryakov, Y. V.; Mamaev, A., Microplasma systems for creating coatings on aluminium alloys. Materials letters **2003,** 57 (11), 1748-1751.

210. Zhao, H.; Liu, Z.; Han, Z. In A comparison on ceramic coating formed on AM50 alloy by micro-arc oxidation in two electrolytes, Materials science forum, Trans Tech Publ: 2007; pp 575-578.

211. Chang, L.; Tian, L.; Liu, W.; Duan, X., Formation of dicalcium phosphate dihydrate on magnesium alloy by micro-arc oxidation coupled with hydrothermal treatment. Corrosion Science **2013,** 72, 118-124.

212. Malyshev, V.; Zorin, K., Features of microarc oxidation coatings formation technology in slurry electrolytes. Applied Surface Science **2007,** 254 (5), 1511-1516.

213. WEI, T.-b.; ZHANG, X.-j.; WANG, B.; TIAN, J.; YAN, F.-y., Effect of Current Density on Growth and Adhesion of Micro-Arc Oxidation Ceramic Coatings on Aluminum Alloy [J]. Materials Protection **2004,** 4.

214. Wang, Y.; Wang, F.; Xu, M.; Zhao, B.; Guo, L.; Ouyang, J., Microstructure and corrosion behavior of coated AZ91 alloy by microarc oxidation for biomedical application. Applied Surface Science **2009,** 255 (22), 9124-9131.

215. Seyfoori, A.; Mirdamadi, S.; Khavandi, A.; Raufi, Z. S., Biodegradation behavior of micro-arc oxidized AZ31 magnesium alloys formed in two different electrolytes. Applied Surface Science **2012,** 261, 92-100.

216. Liu, Y.-H.; Li, S., Current status and progress of study on micro-arc oxidation technology. MATERIALS PROTECTION-WUHAN- **2005,** 38 (6), 36.

217. Yong, X., RECENT DEVELOPMENT OF MICROARC OXIDATION TECHNOLOGY IN CHINA [J]. Corrosion & Protection **2003,** 4.

218. Duan, H.; Du, K.; Yan, C.; Wang, F., Electrochemical corrosion behavior of composite coatings of sealed MAO film on magnesium alloy AZ91D. Electrochimica Acta **2006,** 51 (14), 2898-2908.

219. Gao, J.; Guan, S.; Chen, J.; Wang, L.; Zhu, S.; Hu, J.; Ren, Z., Fabrication and characterization of rod-like nano-hydroxyapatite on MAO coating supported on Mg–Zn–Ca alloy. Applied Surface Science **2011,** 257 (6), 2231-2237.

220. Cui, L.-Y.; Zeng, R.-C.; Guan, S.-K.; Qi, W.-C.; Zhang, F.; Li, S.-Q.; Han, E.-H., Degradation mechanism of micro-arc oxidation coatings on biodegradable Mg-Ca alloys: The influence of porosity. Journal of Alloys and Compounds **2017,** 695, 2464-2476.

221. Fattah-Alhosseini, A.; Joni, M. S., Effect of KOH Concentration on the Microstructure and Electrochemical Properties of MAO-Coated Mg Alloy AZ31B. Journal of Materials Engineering and Performance **2015,** 24 (9), 3444-3452.

222. Gu, X.; Li, N.; Zhou, W.; Zheng, Y.; Zhao, X.; Cai, Q.; Ruan, L., Corrosion resistance and surface biocompatibility of a microarc oxidation coating on a Mg–Ca alloy. Acta Biomaterialia **2011,** 7 (4), 1880-1889.

223. Ezhilselvi, V.; Nithin, J.; Balaraju, J.; Subramanian, S., The influence of current density on the morphology and corrosion properties of MAO coatings on AZ31B magnesium alloy. Surface and Coatings Technology **2016,** 288, 221-229.

224. Chen, L. L.; Gu, Y. H.; Chen, F.; Yue, W.; Wang, H. D.; Zhang, L., Influence of HA in the electrolyte on the properties and corrosion behavior of MAO Ca/P coating. Materials and Corrosion **2016,** 67 (7), 702-709.

225. Ma, X.; Zhu, S.; Wang, L.; Ji, C.; Ren, C.; Guan, S., Synthesis and properties of a bio-composite coating formed on magnesium alloy by one-step method of micro-arc oxidation. Journal of Alloys and Compounds **2014,** 590, 247-253.

226. Razavi, M.; Fathi, M.; Savabi, O.; Razavi, S. M.; Heidari, F.; Manshaei, M.; Vashaee, D.; Tayebi, L., In vivo study of nanostructured diopside (CaMgSi2O6) coating on magnesium alloy as biodegradable orthopedic implants. Applied Surface Science **2014,** 313, 60-66.

227. Liu, G.; Hu, J.; Ding, Z.; Wang, C., Bioactive calcium phosphate coating formed on micro-arc oxidized magnesium by chemical deposition. Applied Surface Science **2011,** 257 (6), 2051-2057.

228. Shi, P.; Niu, B.; Shanshan, E.; Chen, Y.; Li, Q., Preparation and characterization of PLA coating and PLA/MAO composite coatings on AZ31 magnesium alloy for improvement of corrosion resistance. Surface and Coatings Technology **2015,** 262, 26-32.

229. Paunovic, M.; Schlesinger, M., Fundamentals of electrochemical deposition. john wiley & sons: 2006; Vol. 45.

230. Brenner, A., Electrodeposition of alloys: principles and practice. Elsevier: 2013.

231. Amiri, H.; Mohammadi, I.; Afshar, A., Electrophoretic deposition of nano-zirconia coating on AZ91D magnesium alloy for bio-corrosion control purposes. Surface and Coatings Technology **2017,** 311, 182-190.

232. Cordero-Arias, L.; Boccaccini, A. R.; Virtanen, S., Electrochemical behavior of nanostructured TiO2/alginate composite coating on magnesium alloy AZ91D via electrophoretic deposition. Surface and Coatings Technology **2015,** 265, 212-217.

233. Tian, Q.; Liu, H., Electrophoretic deposition and characterization of nanocomposites and nanoparticles on magnesium substrates. Nanotechnology **2015,** 26 (17), 175102.

234. Darband, G. B.; Aliofkhazraei, M.; Hamghalam, P.; Valizade, N., Plasma electrolytic oxidation of magnesium and its alloys: Mechanism, properties and applications. Journal of magnesium and alloys **2017,** 5 (1), 74-132.

235. Vatan, H. N.; Ebrahimi-Kahrizsangi, R.; Kasiri-Asgarani, M., Structural, tribological and electrochemical behavior of SiC nanocomposite oxide coatings fabricated by plasma electrolytic oxidation (PEO) on AZ31 magnesium alloy. Journal of Alloys and Compounds **2016,** 683, 241-255.

236. Yang, J.; Lu, X.; Blawert, C.; Di, S.; Zheludkevich, M. L., Microstructure and corrosion behavior of Ca/P coatings prepared on magnesium by plasma electrolytic oxidation. Surface and Coatings Technology **2017,** 319, 359-369.

237. Dharmadasa, I. M.; Madugu, M. L.; Olusola, O. I.; Echendu, O. K.; Fauzi, F.; Diso, D. G.; Weerasinghe, A. R.; Druffel, T.; Dharmadasa, R.; Lavery, B., Electroplating of CdTe thin films from cadmium sulphate precursor and comparison of layers grown by 3-electrode and 2-electrode systems. Coatings **2017,** 7 (2), 17.

238. Paunovic, M., Electrochemical deposition. Encyclopedia of Electrochemistry: Online **2007**.

239. Mohanty, U., Electrodeposition: a versatile and inexpensive tool for the synthesis of nanoparticles, nanorods, nanowires, and nanoclusters of metals. Journal of applied electrochemistry **2011,** 41 (3), 257-270.

240. Chen, H.; Wei, Z.; Zheng, X.; Yang, S., A scalable electrodeposition route to the low-cost, versatile and controllable fabrication of perovskite solar cells. Nano Energy **2015,** 15, 216-226.

241. Kim, P.; Epstein, A. K.; Khan, M.; Zarzar, L. D.; Lipomi, D. J.; Whitesides, G. M.; Aizenberg, J., Structural transformation by electrodeposition on patterned substrates (STEPS): a new versatile nanofabrication method. Nano letters **2011,** 12 (2), 527-533.

242. Prasannakumar, R.; Bhakyaraj, K.; Chukwuike, V.; Mohan, S.; Barik, R., An investigation of the effect of pulse electrochemical deposition parameters on morphology, hardness and corrosion behaviour in the marine atmosphere. Surface Engineering **2019,** 35 (12), 1021-1032.

243. Kannan, M. B., Electrochemical deposition of calcium phosphates on magnesium and its alloys for improved biodegradation performance: A review. Surface and Coatings Technology **2016,** 301, 36-41.

244. Zhang, C.-Y.; Zeng, R.-C.; Chen, R.-S.; Liu, C.-L.; Gao, J.-C., Preparation of calcium phosphate coatings on Mg-1.0 Ca alloy. Transactions of Nonferrous Metals Society of China **2010,** 20, s655-s659.

245. Song, Y.; Zhang, S.; Li, J.; Zhao, C.; Zhang, X., Electrodeposition of Ca–P coatings on biodegradable Mg alloy: in vitro biomineralization behavior. Acta Biomaterialia **2010,** 6 (5), 1736-1742.

246. Bakhsheshi-Rad, H.; Hamzah, E.; Daroonparvar, M.; Ebrahimi-Kahrizsangi, R.; Medraj, M., In-vitro corrosion inhibition mechanism of fluorine-doped hydroxyapatite and brushite coated Mg–Ca alloys for biomedical applications. Ceramics International **2014,** 40 (6), 7971-7982.

247. Bakhsheshi-Rad, H.; Hamzah, E.; Daroonparvar, M.; Yajid, M.; Kasiri-Asgarani, M.; Abdul-Kadir, M.; Medraj, M., In-vitro degradation behavior of Mg alloy coated by fluorine doped hydroxyapatite and calcium deficient hydroxyapatite. Transactions of Nonferrous Metals Society of China **2014,** 24 (8), 2516-2528.

248. Mhaede, M.; Pastorek, F.; Hadzima, B., Influence of shot peening on corrosion properties of biocompatible magnesium alloy AZ31 coated by dicalcium phosphate dihydrate (DCPD). Materials Science and Engineering: C **2014,** 39, 330-335.

249. Li, H.; Wang, Q.; Zhuang, M.; Wu, J., Characterization and residual stress analysis of TiN/TiCN films on AZ31 magnesium alloy by PVD. Vacuum **2015,** 112, 66-69.

250. Geyao, L.; Yang, D.; Wanglin, C.; Chengyong, W., Development and application of physical vapor deposited coatings for medical devices: A review. Procedia CIRP **2020,** 89, 250-262.

251. Sproul, W. D., Physical vapor deposition tool coatings. Surface and Coatings Technology **1996,** 81 (1), 1-7.

252. Habig, K. H., Chemical vapor deposition and physical vapor deposition coatings: properties, tribological behavior, and applications. Journal of Vacuum Science & Technology A: Vacuum, Surfaces, and Films **1986,** 4 (6), 2832-2843.

253. Qadir, M.; Li, Y.; Wen, C., Ion-substituted calcium phosphate coatings by physical vapor deposition magnetron sputtering for biomedical applications: A review. Acta biomaterialia **2019,** 89, 14-32.

254. Coll, B. F.; Jacquot, P., Surface modification of medical implants and surgical devices using TiN layers. Surface and coatings technology **1988,** 36 (3-4), 867-878.

255. Harman, M. K.; Banks, S. A.; Hodge, W. A., Wear analysis of a retrieved hip implant with titanium nitride coating. The Journal of arthroplasty **1997,** 12 (8), 938-945.

256. Mattox, D. M., Physical vapor deposition (PVD) processes. Metal Finishing **2002,** 100, 394-408.

257. Westwood, W., Physical vapor deposition. In Microelectronic Materials and Processes, Springer: 1989; pp 133-201.

258. Aliofkhazraei, M.; Ali, N., PVD Technology in fabrication of micro-and nanostructured coatings. **2014**.

259. Cicek, H.; Efeoglu, I.; Totik, Y.; Ezirmik, K. V.; Arslan, E., A low temperature in-situ crystalline TiNi shape memory thin film deposited by magnetron sputtering. Surface and Coatings Technology **2015,** 284, 90-93.

260. Kuo, C.; Soo, S.; Aspinwall, D.; Carr, C.; Bradley, S.; M'Saoubi, R.; Leahy, W., Development of single step drilling technology for multilayer metallic-composite stacks using uncoated and PVD coated carbide tools. Journal of Manufacturing Processes **2018,** 31, 286-300.

261. Öztürk, A.; Ezirmik, K.; Kazmanlı, K.; Ürgen, M.; Eryılmaz, O.; Erdemir, A., Comparative tribological behaviors of TiN, CrN and MoNCu nanocomposite coatings. Tribology International **2008,** 41 (1), 49-59.

262. Senf, J.; Berg, G.; Friedrich, C.; Broszeit, E.; Berger, C., Wear behaviour and wear protection of magnesium alloys using PVD coatings. **1998**.

263. Zipperian, D., Microstructural Analysis of Finished Surfaces. ASM Handbook, Surface Engg. ASM Int **1994,** 5, 139-143.

264. Ezekoye, B.; Offor, P.; Ezekoye, V.; Ezema, F., Chemical bath deposition technique of thin films: a review. International Journal of Scientific Research **2013,** 2 (8), 452-456.

265. Gonzalez-Nunez, M.; Nunez-Lopez, C.; Skeldon, P.; Thompson, G.; Karimzadeh, H.; Lyon, P.; Wilks, T., A non-chromate conversion coating for magnesium alloys and magnesium-based metal matrix composites. Corrosion Science **1995,** 37 (11), 1763-1772.

266. Chen, X.-B.; Birbilis, N.; Abbott, T., A simple route towards a hydroxyapatite–Mg (OH) 2 conversion coating for magnesium. Corrosion Science **2011,** 53 (6), 2263-2268.

267. Song, Y.; Shan, D.; Chen, R.; Zhang, F.; Han, E.-H., Formation mechanism of phosphate conversion film on Mg–8.8 Li alloy. Corrosion Science **2009,** 51 (1), 62-69.

268. Su, Y.; Li, G.; Lian, J., A chemical conversion hydroxyapatite coating on AZ60 magnesium alloy and its electrochemical corrosion behaviour. Int. J. Electrochem. Sci **2012,** 7 (11), 11497-11511.

269. Jung, H.-G.; Jeong, Y. S.; Park, J.-B.; Sun, Y.-K.; Scrosati, B.; Lee, Y. J., Ruthenium-based electrocatalysts supported on reduced graphene oxide for lithium-air batteries. ACS Nano **2013,** 7 (4), 3532-3539.

270. Nair, M.; Nair, P., Chemical bath deposition of CuxS thin films and their prospective large area applications. Semiconductor science and technology **1989,** 4 (3), 191.

271. Fatas, E.; Garcia, T.; Montemayor, C.; Medina, A.; Camarero, E. G.; Arjona, F., Formation of CuxS thin films through a chemical bath deposition process. Materials Chemistry and Physics **1985,** 12 (2), 121-128.

272. Pavaskar, N.; Menezes, C.; Sinha, A., Photoconductive CdS films by a chemical bath deposition process. Journal of the Electrochemical Society **1977,** 124 (5), 743.

273. Cheng, J.; Fan, D.; Wang, H.; Liu, B.; Zhang, Y.; Yan, H., Chemical bath deposition of crystalline ZnS thin films. Semiconductor science and technology **2003,** 18 (7), 676.

274. Chopra, K. L.; Das, S. R., Why thin film solar cells? In Thin film solar cells, Springer: 1983; pp 1-18.

275. Dubal, D.; Dhawale, D.; Salunkhe, R.; Jamdade, V.; Lokhande, C., Fabrication of copper oxide multilayer nanosheets for supercapacitor application. Journal of Alloys and Compounds **2010,** 492 (1-2), 26-30.

276. de Moure-Flores, F.; Nieto-Zepeda, K.; Guillén-Cervantes, A.; Gallardo, S.; Quiñones-Galván, J.; Hernández-Hernández, A.; Olvera, M. d. l. L.; Zapata-Torres, M.; Kundriavtsev, Y.; Meléndez-Lira, M., Effect of the immersion in CdCl2 and annealing on physical properties of CdS: F films grown by CBD. Journal of Physics and Chemistry of Solids **2013,** 74 (4), 611-615.

277. Su, Y.; Li, D.; Su, Y.; Lu, C.; Niu, L.; Lian, J.; Li, G., Improvement of the biodegradation property and biomineralization ability of magnesium–hydroxyapatite composites with dicalcium phosphate dihydrate and hydroxyapatite coatings. ACS Biomaterials Science & Engineering **2016,** 2 (5), 818-828.

278. Zeng, R.-C.; Zhang, F.; Lan, Z.-D.; Cui, H.-Z.; Han, E.-H., Corrosion resistance of calcium-modified zinc phosphate conversion coatings on magnesium–aluminium alloys. Corrosion Science **2014,** 88, 452-459.

279. Zeng, R.; Lan, Z.; Kong, L.; Huang, Y.; Cui, H., Characterization of calcium-modified zinc phosphate conversion coatings and their influences on corrosion resistance of AZ31 alloy. Surface and Coatings Technology **2011,** 205 (11), 3347-3355.

280. Zeng, R.-c.; Sun, X.-x.; Song, Y.-w.; Zhang, F.; Li, S.-q.; Cui, H.-z.; Han, E.-h., Influence of solution temperature on corrosion resistance of Zn-Ca phosphate conversion coating on biomedical Mg-Li-Ca alloys. Transactions of Nonferrous Metals Society of China **2013,** 23 (11), 3293-3299.

281. Hu, J.; Wang, C.; Ren, W.; Zhang, S.; Liu, F., Microstructure evolution and corrosion mechanism of dicalcium phosphate dihydrate coating on magnesium alloy in simulated body fluid. Materials Chemistry and Physics **2010,** 119 (1-2), 294-298.

282. Razavi, M.; Fathi, M.; Savabi, O.; Beni, B. H.; Razavi, S. M.; Vashaee, D.; Tayebi, L., Coating of biodegradable magnesium alloy bone implants using nanostructured diopside (CaMgSi2O6). Applied Surface Science **2014,** 288, 130-137.

283. Wang, Y.; Wei, M.; Gao, J., Improve corrosion resistance of magnesium in simulated body fluid by dicalcium phosphate dihydrate coating. Materials Science and Engineering: C **2009,** 29 (4), 1311-1316.

284. Zeng, R.-c.; Liu, Z.-g.; Zhang, F.; Li, S.-q.; He, Q.-k.; Cui, H.-z.; Han, E.-h., Corrosion resistance of in-situ Mg–Al hydrotalcite conversion film on AZ31 magnesium alloy by one-step formation. Transactions of Nonferrous Metals Society of China **2015,** 25 (6), 1917-1925.

285. Hench, L. L., Sol-gel materials for bioceramic applications. Current Opinion in Solid State and Materials Science **1997,** 2 (5), 604-610.

286. Chen, Q. Z.; Thompson, I. D.; Boccaccini, A. R., 45S5 Bioglass®-derived glass–ceramic scaffolds for bone tissue engineering. Biomaterials **2006,** 27 (11), 2414-2425.

287. Aktuğ, S. L.; Durdu, S.; Kutbay, I.; Usta, M., Effect of Na2SiO3· 5H2O concentration on microstructure and mechanical properties of plasma electrolytic oxide coatings on AZ31 Mg alloy produced by twin roll casting. Ceramics International **2016,** 42 (1), 1246-1253.

288. Dorozhkin, S. V., Nanodimensional and nanocrystalline apatites and other calcium orthophosphates in biomedical engineering, biology and medicine. Materials **2009,** 2 (4), 1975-2045.

289. Vallet-Regi, M.; González-Calbet, J. M., Calcium phosphates as substitution of bone tissues. Progress in solid state chemistry **2004,** 32 (1-2), 1-31.

290. Dorozhkin, S. V. In Calcium orthophosphate bioceramics, Journal of Biomimetics, Biomaterials and Tissue Engineering, Trans Tech Publ: 2010; pp 57-100.

291. Xia, L.; Lin, K.; Jiang, X.; Xu, Y.; Zhang, M.; Chang, J.; Zhang, Z., Enhanced osteogenesis through nano-structured surface design of macroporous hydroxyapatite bioceramic scaffolds via activation of ERK and p38 MAPK signaling pathways. Journal of Materials Chemistry B **2013,** 1 (40), 5403-5416.

292. Bohner, M.; Tadier, S.; van Garderen, N.; de Gasparo, A.; Döbelin, N.; Baroud, G., Synthesis of spherical calcium phosphate particles for dental and orthopedic applications. Biomatter **2013,** 3 (2), e25103.

293. Sato, K., Mechanism of hydroxyapatite mineralization in biological systems. Journal of the Ceramic Society of Japan **2007,** 115 (1338), 124-130.

294. Malmberg, P.; Nygren, H., Methods for the analysis of the composition of bone tissue, with a focus on imaging mass spectrometry (TOF-SIMS). Proteomics **2008,** 8 (18), 3755-3762.

295. Batchelar, D. L.; Davidson, M. T.; Dabrowski, W.; Cunningham, I. A., Bone-composition imaging using coherent-scatter computed tomography: Assessing bone health beyond bone mineral density. Medical physics **2006,** 33 (4), 904-915.

296. Märten, A.; Fratzl, P.; Paris, O.; Zaslansky, P., On the mineral in collagen of human crown dentine. Biomaterials **2010,** 31 (20), 5479-5490.

297. Brown, W.; Eidelman, N.; Tomazic, B., Octacalcium phosphate as a precursor in biomineral formation. Advances in dental research **1987,** 1 (2), 306-313.

298. Steuer, P.; Voegel, J.-C.; Cuisinier, F., First experimental evidence for human dentine crystal formation involving conversion of octacalcium phosphate to hydroxyapatite. Acta Crystallographica Section D: Biological Crystallography **1998,** 54 (6), 1377-1381.

299. Zapanta Le Geros, R., Variations in the crystalline components of human dental calculus: I. crystallographic and spectroscopic methods of analysis. Journal of dental research **1974,** 53 (1), 45-50.

300. Tung, M.; Brown, W., The role of octacalcium phosphate in subcutaneous heterotopic calcification. Calcified tissue international **1985,** 37 (3), 329-331.

301. Ren, W.; Song, W.; Yurgelevic, S.; Markel, D. C., Setting mechanism of a new injectable Dicalcium Phosphate Dihydrate (DCPD) forming cement. Journal of the mechanical behavior of biomedical materials **2018,** 79, 226-234.

302. Lin, K.; Wu, C.; Chang, J., Advances in synthesis of calcium phosphate crystals with controlled size and shape. Acta biomaterialia **2014,** 10 (10), 4071-4102.

303. LeGeros, R. Z., Properties of osteoconductive biomaterials: calcium phosphates. Clinical Orthopaedics and Related Research® **2002,** 395, 81-98.

304. Shadanbaz, S.; Dias, G. J., Calcium phosphate coatings on magnesium alloys for biomedical applications: a review. Acta biomaterialia **2012,** 8 (1), 20-30.

305. Wen, C.; Guan, S.; Peng, L.; Ren, C.; Wang, X.; Hu, Z., Characterization and degradation behavior of AZ31 alloy surface modified by bone-like hydroxyapatite for implant applications. Applied Surface Science **2009,** 255 (13-14), 6433-6438.

306. Wang, M.-C.; Chen, H.-T.; Shih, W.-J.; Chang, H.-F.; Hon, M.-H.; Hung, I.-M., Crystalline size, microstructure and biocompatibility of hydroxyapatite nanopowders by hydrolysis of calcium hydrogen phosphate dehydrate (DCPD). Ceramics International **2015,** 41 (2), 2999-3008.

307. Wang, J.; Tang, J.; Zhang, P.; Li, Y.; Wang, J.; Lai, Y.; Qin, L., Surface modification of magnesium alloys developed for bioabsorbable orthopedic implants: a general review. Journal of Biomedical Materials Research Part B: Applied Biomaterials **2012,** 100 (6), 1691-1701.

308. Barrère, F.; van Blitterswijk, C. A.; de Groot, K., Bone regeneration: molecular and cellular interactions with calcium phosphate ceramics. International journal of nanomedicine **2006,** 1 (3), 317.

309. Hench, L. L.; Paschall, H., Direct chemical bond of bioactive glass-ceramic materials to bone and muscle. Journal of biomedical materials research **1973,** 7 (3), 25-42.

310. Yan, W.-Q.; Nakamura, T.; Kawanabe, K.; Nishigochi, S.; Oka, M.; Kokubo, T., Apatite layer-coated titanium for use as bone bonding implants. Biomaterials **1997,** 18 (17), 1185-1190.

311. Duheyne, P.; Beight, J.; Cuckler, J.; Evans, B.; Radin, S., Effect of calcium phosphate coating characteristics on early post-operative bone tissue ingrowth. Biomaterials **1990,** 11 (8), 531-540.

312. Nguyen, H.; Deporter, D.; Pilliar, R.; Valiquette, N.; Yakubovich, R., The effect of sol–gel-formed calcium phosphate coatings on bone ingrowth and osteoconductivity of porous-surfaced Ti alloy implants. Biomaterials **2004,** 25 (5), 865-876.

313. Peter, B.; Gauthier, O.; Laïb, S.; Bujoli, B.; Guicheux, J.; Janvier, P.; van Lenthe, G. H.; Müller, R.; Zambelli, P. Y.; Bouler, J. M., Local delivery of bisphosphonate from coated orthopedic implants increases implants mechanical stability in osteoporotic rats. Journal of Biomedical Materials Research Part A: An Official Journal of The Society for Biomaterials, The Japanese Society for Biomaterials, and The Australian Society for Biomaterials and the Korean Society for Biomaterials **2006,** 76 (1), 133-143.

314. Yang, F.; Wolke, J.; Jansen, J., Biomimetic calcium phosphate coating on electrospun poly (ε-caprolactone) scaffolds for bone tissue engineering. Chemical Engineering Journal **2008,** 137 (1), 154-161.

315. Habibovic, P.; Barrere, F.; Van Blitterswijk, C. A.; de Groot, K.; Layrolle, P., Biomimetic hydroxyapatite coating on metal implants. Journal of the American Ceramic Society **2002,** 85 (3), 517-522.

316. Bajpai, I.; Kim, D. Y.; Kyong-Jin, J.; Song, I. H.; Kim, S., Response of human bone marrow-derived MSCs on triphasic Ca-P substrate with various HA/TCP ratio. Journal of Biomedical Materials Research Part B: Applied Biomaterials **2017,** 105 (1), 72-80.

317. Cui, F.-z.; Yang, J.-x.; Jiao, Y.-p.; Yin, Q.-s.; Zhang, Y.; Lee, I.-S., Calcium phosphate coating on magnesium alloy for modification of degradation behavior. Frontiers of Materials Science in China **2008,** 2 (2), 143-148.

318. Hiromoto, S.; Yamamoto, A., High corrosion resistance of magnesium coated with hydroxyapatite directly synthesized in an aqueous solution. Electrochimica Acta **2009,** 54 (27), 7085-7093.

319. Ascencio, M.; Pekguleryuz, M.; Omanovic, S., An investigation of the corrosion mechanisms of WE43 Mg alloy in a modified simulated body fluid solution: the influence of immersion time. Corrosion science **2014,** 87, 489-503.

320. Hench, L. L., Bioceramics: from concept to clinic. Journal of the american ceramic society **1991,** 74 (7), 1487-1510.

321. Tang, H.; Yu, D.; Luo, Y.; Wang, F., Preparation and characterization of HA microflowers coating on AZ31 magnesium alloy by micro-arc oxidation and a solution treatment. Applied Surface Science **2013,** 264, 816-822.

322. LeGeros, R. Z., Preparation of octacalcium phosphate (OCP): a direct fast method. Calcified tissue international **1985,** 37 (2), 194-197.

323. Kamakura, S.; Sasano, Y.; Homma, H.; Suzuki, O.; Kagayama, M.; Motegi, K., Implantation of octacalcium phosphate (OCP) in rat skull defects enhances bone repair. Journal of dental research **1999,** 78 (11), 1682-1687.

324. Mirtchi, A. A.; Lemaitre, J.; Terao, N., Calcium phosphate cements: study of the β-tricalcium phosphate—monocalcium phosphate system. Biomaterials **1989,** 10 (7), 475-480.

325. Urist, M. R.; Lietze, A.; Dawson, E., Beta-tricalcium phosphate delivery system for bone morphogenetic protein. Clinical orthopaedics and related research **1984,** (187), 277-280.

326. Oryan, A.; Alidadi, S., Application of Bioceramics in Orthope-dics and Bone Tissue Engineering. **2017**.

327. Hou, C.-h.; Chen, C.-w.; Hou, S.-m.; Li, Y.-t.; Lin, F.-h., The fabrication and characterization of dicalcium phosphate dihydrate-modified magnetic nanoparticles and their performance in hyperthermia processes in vitro. Biomaterials **2009,** 30 (27), 4700-4707.

328. Hassan, M. N.; Mahmoud, M. M.; Abd El-Fattah, A.; Kandil, S., Microwave-assisted preparation of Nano-hydroxyapatite for bone substitutes. Ceramics International **2016,** 42 (3), 3725-3744.

329. Fathi, M.; Hanifi, A.; Mortazavi, V., Preparation and bioactivity evaluation of bone-like hydroxyapatite nanopowder. Journal of materials processing technology **2008,** 202 (1-3), 536-542.

330. Ferraz, M.; Monteiro, F.; Manuel, C., Hydroxyapatite nanoparticles: a review of preparation methodologies. Journal of Applied Biomaterials and Biomechanics **2004,** 2 (2), 74-80.

331. Lafon, J.-P.; Champion, E.; Bernache-Assollant, D., Processing of AB-type carbonated hydroxyapatite Ca10− x (PO4) 6− x (CO3) x (OH) 2− x− 2y (CO3) y ceramics with controlled composition. Journal of the European Ceramic Society **2008,** 28 (1), 139-147.

332. Lombardi, M.; Palmero, P.; Haberko, K.; Pyda, W.; Montanaro, L., Processing of a natural hydroxyapatite powder: from powder optimization to porous bodies development. Journal of the European Ceramic Society **2011,** 31 (14), 2513-2518.

333. Zhou, H.; Lee, J., Nanoscale hydroxyapatite particles for bone tissue engineering. Acta biomaterialia **2011,** 7 (7), 2769-2781.

334. Jarcho, M., Calcium phosphate ceramics as hard tissue prosthetics. Clinical Orthopaedics and Related Research® **1981,** 157, 259-278.

335. Burg, K. J.; Porter, S.; Kellam, J. F., Biomaterial developments for bone tissue engineering. Biomaterials **2000,** 21 (23), 2347-2359.

336. Currey, J., Sacrificial bonds heal bone. Nature **2001,** 414 (6865), 699-699.

337. Lim, G.; Wang, J.; Ng, S.; Gan, L., Processing of fine hydroxyapatite powders via an inverse microemulsion route. Materials letters **1996,** 28 (4-6), 431-436.

338. Cheng, X.; Kuhn, L., Chemotherapy drug delivery from calcium phosphate nanoparticles. International journal of nanomedicine **2007,** 2 (4), 667.

339. Matsumoto, T.; Okazaki, M.; Inoue, M., SY amaguchi, T. Kusunose, T. Toyonaga, Y. Hamada, J. Takahashi. Biomaterials **2004,** 25, 3807-3812.

340. Hui, P.; Meena, S.; Singh, G.; Agarawal, R.; Prakash, S., Synthesis of hydroxyapatite bio-ceramic powder by hydrothermal method. Journal of Minerals and Materials Characterization and Engineering **2010,** 9 (08), 683.

341. Yoshimura, M.; Suda, H., Hydrothermal processing of hydroxyapatite: past, present, and future. Hydroxyapatite and Related Compounds. Boca Raton (EE. UU.): CRC Press Inc **1994**, 45-72.

342. Aminian, A.; Solati-Hashjin, M.; Samadikuchaksaraei, A.; Bakhshi, F.; Gorjipour, F.; Farzadi, A.; Moztarzadeh, F.; Schmücker, M., Synthesis of silicon-substituted hydroxyapatite by a hydrothermal method with two different phosphorous sources. Ceramics International **2011,** 37 (4), 1219-1229.

343. Kim, H.-W.; Kong, Y.-M.; Bae, C.-J.; Noh, Y.-J.; Kim, H.-E., Sol–gel derived fluor-hydroxyapatite biocoatings on zirconia substrate. Biomaterials **2004,** 25 (15), 2919-2926.

344. Liu, D.-M.; Troczynski, T.; Tseng, W. J., Water-based sol–gel synthesis of hydroxyapatite: process development. Biomaterials **2001,** 22 (13), 1721-1730.

345. Montenero, A.; Gnappi, G.; Ferrari, F.; Cesari, M.; Salvioli, E.; Mattogno, L.; Kaciulis, S.; Fini, M., Sol-gel derived hydroxyapatite coatings on titanium substrate. Journal of Materials science **2000,** 35 (11), 2791-2797.

346. Lin, K.; Chang, J.; Cheng, R.; Ruan, M., Hydrothermal microemulsion synthesis of stoichiometric single crystal hydroxyapatite nanorods with mono-dispersion and narrow-size distribution. Materials Letters **2007,** 61 (8-9), 1683-1687.

347. Sun, Y.; Yang, H.; Tao, D., Microemulsion process synthesis of lanthanide-doped hydroxyapatite nanoparticles under hydrothermal treatment. Ceramics International **2011,** 37 (7), 2917-2920.

348. García, C.; García, C.; Paucar, C., Controlling morphology of hydroxyapatite nanoparticles through hydrothermal microemulsion chemical synthesis. Inorganic Chemistry Communications **2012,** 20, 90-92.

349. Liang, T.; Qian, J.; Yuan, Y.; Liu, C., Synthesis of mesoporous hydroxyapatite nanoparticles using a template-free sonochemistry-assisted microwave method. Journal of Materials Science **2013,** 48 (15), 5334-5341.

350. Zou, Z.; Lin, K.; Chen, L.; Chang, J., Ultrafast synthesis and characterization of carbonated hydroxyapatite nanopowders via sonochemistry-assisted microwave process. Ultrasonics sonochemistry **2012,** 19 (6), 1174-1179.

351. Teshima, K.; Lee, S.; Sakurai, M.; Kameno, Y.; Yubuta, K.; Suzuki, T.; Shishido, T.; Endo, M.; Oishi, S., Well-formed one-dimensional hydroxyapatite crystals grown by an environmentally friendly flux method. Crystal Growth and Design **2009,** 9 (6), 2937-2940.

352. Taş, A. C., Molten salt synthesis of calcium hydroxyapatite whiskers. Journal of the American Ceramic Society **2001,** 84 (2), 295-300.

353. Ito, A.; Nakamura, S.; Aoki, H.; Akao, M.; Teraoka, K.; Tsutsumi, S.; Onuma, K.; Tateishi, T., Hydrothermal growth of carbonate-containing hydroxyapatite single crystals. Journal of crystal growth **1996,** 163 (3), 311-317.

354. Liu, J.; Li, K.; Wang, H.; Zhu, M.; Xu, H.; Yan, H., Self-assembly of hydroxyapatite nanostructures by microwave irradiation. Nanotechnology **2004,** 16 (1), 82.

355. Liu, J.; Li, K.; Wang, H.; Zhu, M.; Yan, H., Rapid formation of hydroxyapatite nanostructures by microwave irradiation. Chemical physics letters **2004,** 396 (4-6), 429-432.

356. Verma, D.; Katti, K.; Katti, D., Bioactivity in in situ hydroxyapatite–polycaprolactone composites. Journal of Biomedical Materials Research Part A: An Official Journal of The Society for Biomaterials, The Japanese Society for Biomaterials, and The Australian Society for Biomaterials and the Korean Society for Biomaterials **2006,** 78 (4), 772-780.

357. Mróz, W.; Bombalska, A.; Budner, B.; Burdyńska, S.; Jedyński, M.; Prokopiuk, A.; Menaszek, E.; Ścisłowska-Czarnecka, A.; Niedzielska, A.; Niedzielski, K., Comparative study of hydroxyapatite and octacalcium phosphate coatings deposited on metallic implants by PLD method. Applied Physics A **2010,** 101 (4), 713-716.

358. Suzuki, O., Octacalcium phosphate: osteoconductivity and crystal chemistry. Acta biomaterialia **2010,** 6 (9), 3379-3387.

359. Komlev, V. S.; Barinov, S. M.; Bozo, I. I.; Deev, R. V.; Eremin, I. I.; Fedotov, A. Y.; Gurin, A. N.; Khromova, N. V.; Kopnin, P. B.; Kuvshinova, E. A., Bioceramics composed of octacalcium phosphate demonstrate enhanced biological behavior. ACS applied materials & interfaces **2014,** 6 (19), 16610-16620.

360. Suzuki, O.; NAKAMURA, M.; MIYASAKA, Y.; KAGAYAMA, M.; SAKURAI, M., Bone formation on synthetic precursors of hydroxyapatite. The Tohoku journal of experimental medicine **1991,** 164 (1), 37-50.

361. Suzuki, O.; Nakamura, M.; Miyasaka, Y.; Kagayama, M.; Sakurai, M., Maclura pomifera agglutinin-binding glycoconjugates on converted apatite from synthetic octacalcium phosphate implanted into subperiosteal region of mouse calvaria. Bone and mineral **1993,** 20 (2), 151-166.

362. Suzuki, O.; Kamakura, S.; Katagiri, T.; Nakamura, M.; Zhao, B.; Honda, Y.; Kamijo, R., Bone formation enhanced by implanted octacalcium phosphate involving conversion into Ca-deficient hydroxyapatite. Biomaterials **2006,** 27 (13), 2671-2681.

363. Miyatake, N.; Kishimoto, K. N.; Anada, T.; Imaizumi, H.; Itoi, E.; Suzuki, O., Effect of partial hydrolysis of octacalcium phosphate on its osteoconductive characteristics. Biomaterials **2009,** 30 (6), 1005-1014.

364. Zhang, J.; Nancollas, G. H., Kinetics and mechanisms of octacalcium phosphate dissolution at 37. degree. C. The Journal of Physical Chemistry **1992,** 96 (13), 5478-5483.

365. Iijima, M.; Kamemizu, H.; Wakamatsu, N.; Goto, T.; Doi, Y.; Moriwaki, Y., Transition of octacalcium phosphate to hydroxyapatite in solution at pH 7.4 and 37 C. Journal of crystal growth **1997,** 181 (1-2), 70-78.

366. Li, C.; Yao, X.; Hang, R.; Zhang, X., Facile preparation of nanostructured octacalcium phosphate coatings on micro-arc oxidized magnesium with different functionalities for bone repair application. Colloids and Surfaces B: Biointerfaces **2021,** 197, 111426.

367. Bigi, A.; Boanini, E.; Cojazzi, G.; Falini, G.; Panzavolta, S., Morphological and structural investigation of octacalcium phosphate hydrolysis in the presence of polyacrylic acids: Effect of relative molecular weights. Crystal Growth & Design **2001,** 1 (3), 239-244.

368. Surmeneva, M. A.; Surmenev, R. A., Microstructure characterization and corrosion behaviour of a nano-hydroxyapatite coating deposited on AZ31 magnesium alloy using radio frequency magnetron sputtering. Vacuum **2015,** 117, 60-62.

369. Socol, G.; Torricelli, P.; Bracci, B.; Iliescu, M.; Miroiu, F.; Bigi, A.; Werckmann, J.; Mihailescu, I., Biocompatible nanocrystalline octacalcium phosphate thin films obtained by pulsed laser deposition. Biomaterials **2004,** 25 (13), 2539-2545.

370. Arellano-Jiménez, M.; García-García, R.; Reyes-Gasga, J., Synthesis and hydrolysis of octacalcium phosphate and its characterization by electron microscopy and X-ray diffraction. Journal of Physics and Chemistry of Solids **2009,** 70 (2), 390-395.

371. LeGeros, R. Z., Calcium phosphate-based osteoinductive materials. Chemical reviews **2008,** 108 (11), 4742-4753.

372. Stefanic, M.; Krnel, K.; Pribosic, I.; Kosmac, T., Rapid biomimetic deposition of octacalcium phosphate coatings on zirconia ceramics (Y-TZP) for dental implant applications. Applied surface science **2012,** 258 (10), 4649-4656.

373. Mihailescu, I.; Torricelli, P.; Bigi, A.; Mayer, I.; Iliescu, M.; Werckmann, J.; Socol, G., F. MIROIU, F. CUISINIER, R. ELKAIM, G. HILDEBRAND. Appl. Surf. Sci **2005,** 248, 344.

374. Tomozawa, M.; Hiromoto, S., Microstructure of hydroxyapatite-and octacalcium phosphate-coatings formed on magnesium by a hydrothermal treatment at various pH values. Acta Materialia **2011,** 59 (1), 355-363.

375. Hiromoto, S.; Inoue, M.; Taguchi, T.; Yamane, M.; Ohtsu, N., In vitro and in vivo biocompatibility and corrosion behaviour of a bioabsorbable magnesium alloy coated with octacalcium phosphate and hydroxyapatite. Acta biomaterialia **2015,** 11, 520-530.

376. Hiromoto, S., Self-healing property of hydroxyapatite and octacalcium phosphate coatings on pure magnesium and magnesium alloy. Corrosion Science **2015,** 100, 284-294.

377. Boanini, E.; Torricelli, P.; Fini, M.; Sima, F.; Serban, N.; Mihailescu, I. N.; Bigi, A., Magnesium and strontium doped octacalcium phosphate thin films by matrix assisted pulsed laser evaporation. Journal of inorganic biochemistry **2012,** 107 (1), 65-72.

378. Bao, L.; Liu, J.; Shi, F.; Jiang, Y.; Liu, G., Preparation and characterization of TiO2 and Si-doped octacalcium phosphate composite coatings on zirconia ceramics (Y-TZP) for dental implant applications. Applied surface science **2014,** 290, 48-52.

379. Ribeiro, A.; Balestra, R.; Rocha, M.; Peripolli, S.; Andrade, M.; Pereira, L.; Oliveira, M., Dense and porous titanium substrates with a biomimetic calcium phosphate coating. Applied surface science **2013,** 265, 250-256.

380. Bigi, A.; Bracci, B.; Cuisinier, F.; Elkaim, R.; Fini, M.; Mayer, I.; Mihailescu, I.; Socol, G.; Sturba, L.; Torricelli, P., Human osteoblast response to pulsed laser deposited calcium phosphate coatings. Biomaterials **2005,** 26 (15), 2381-2389.

381. Boanini, E.; Torricelli, P.; Forte, L.; Pagani, S.; Mihailescu, N.; Ristoscu, C.; Mihailescu, I. N.; Bigi, A., Antiresorption implant coatings based on calcium alendronate and octacalcium phosphate deposited by matrix assisted pulsed laser evaporation. Colloids and Surfaces B: Biointerfaces **2015,** 136, 449-456.

382. Smirnov, I.; Rau, J.; Fosca, M.; De Bonis, A.; Latini, A.; Teghil, R.; Kalita, V.; Fedotov, A. Y.; Gudkov, S.; Baranchikov, A., Structural modification of titanium surface by octacalcium phosphate via Pulsed Laser Deposition and chemical treatment. Bioactive materials **2017,** 2 (2), 101-107.

383. Birgani, Z. T.; Malhotra, A.; van Blitterswijk, C. A.; Habibovic, P., Human mesenchymal stromal cells response to biomimetic octacalcium phosphate containing strontium. Journal of Biomedical Materials Research Part A **2016,** 104 (8), 1946-1960.

384. Antoniac, I. V.; Filipescu, M.; Barbaro, K.; Bonciu, A.; Birjega, R.; Cotrut, C. M.; Galvano, E.; Fosca, M.; Fadeeva, I. V.; Vadalà, G., Iron Ion-Doped Tricalcium Phosphate Coatings Improve the Properties of Biodegradable Magnesium Alloys for Biomedical Implant Application. Advanced Materials Interfaces **2020,** 7 (16), 2000531.

385. Dorozhkin, S. V., Calcium orthophosphates. Journal of materials science **2007,** 42 (4), 1061-1095.

386. Chai, H.; Guo, L.; Wang, X.; Gao, X.; Liu, K.; Fu, Y.; Guan, J.; Tan, L.; Yang, K., In vitro and in vivo evaluations on osteogenesis and biodegradability of a β-tricalcium phosphate coated magnesium alloy. Journal of Biomedical Materials Research Part A **2012,** 100 (2), 293-304.

387. Sinusaite, L.; Renner, A. M.; Schuetz, M. B.; Antuzevics, A.; Rogulis, U.; Grigoraviciute-Puroniene, I.; Mathur, S.; Zarkov, A., Effect of Mn doping on the low-temperature synthesis of tricalcium phosphate (TCP) polymorphs. Journal of the European Ceramic Society **2019,** 39 (10), 3257-3263.

388. Sinusaite, L.; Grigoraviciute-Puroniene, I.; Popov, A.; Ishikawa, K.; Kareiva, A.; Zarkov, A., Controllable synthesis of tricalcium phosphate (TCP) polymorphs by wet precipitation: effect of washing procedure. Ceramics International **2019,** 45 (9), 12423-12428.

389. Carrodeguas, R. G.; De Aza, S., α-Tricalcium phosphate: Synthesis, properties and biomedical applications. Acta biomaterialia **2011,** 7 (10), 3536-3546.

390. Shi, H.; Zhang, W.; Liu, X.; Zeng, S.; Yu, T.; Zhou, C., Synergistic effects of citric acid-sodium alginate on physicochemical properties of α-tricalcium phosphate bone cement. Ceramics International **2019,** 45 (2), 2146-2152.

391. Siek, D.; Ślósarczyk, A.; Przekora, A.; Belcarz, A.; Zima, A.; Ginalska, G.; Czechowska, J., Evaluation of antibacterial activity and cytocompatibility of α-TCP based bone cements with silver-doped hydroxyapatite and CaCO3. Ceramics International **2017,** 43 (16), 13997-14007.

392. Duncan, J.; MacDonald, J. F.; Hanna, J. V.; Shirosaki, Y.; Hayakawa, S.; Osaka, A.; Skakle, J. M.; Gibson, I. R., The role of the chemical composition of monetite on the synthesis and properties of α-tricalcium phosphate. Materials Science and Engineering: C **2014,** 34, 123-129.

393. Cicek, G.; Aksoy, E. A.; Durucan, C.; Hasirci, N., Alpha-tricalcium phosphate (α-TCP): solid state synthesis from different calcium precursors and the hydraulic reactivity. Journal of Materials Science: Materials in Medicine **2011,** 22 (4), 809-817.

394. Brazete, D.; Abrantes, J.; Ferreira, J., Influence of the Ca/P ratio and cooling rate on the allotropic α↔ β-tricalcium phosphate phase transformations. Ceramics International **2018,** 44 (7), 8249-8256.

395. Thürmer, M. B.; Diehl, C. E.; dos Santos, L. A. L., Calcium phosphate cements based on alpha-tricalcium phosphate obtained by wet method: Synthesis and milling effects. Ceramics International **2016,** 42 (16), 18094-18099.

396. Dorozhkin, S. V.; Epple, M., Biological and medical significance of calcium phosphates. Angewandte Chemie International Edition **2002,** 41 (17), 3130-3146.

397. Boanini, E.; Gazzano, M.; Bigi, A., Ionic substitutions in calcium phosphates synthesized at low temperature. Acta biomaterialia **2010,** 6 (6), 1882-1894.

398. Yu, T.; Zeng, S.; Liu, X.; Shi, H.; Ye, J.; Zhou, C., Application of Sr-doped octacalcium phosphate as a novel Sr carrier in the α-tricalcium phosphate bone cement. Ceramics International **2017,** 43 (15), 12579-12587.

399. Shi, H.; Zeng, S.; Liu, X.; Yu, T.; Zhou, C., Effects of strontium doping on the degradation and Sr ion release behaviors of α-tricalcium phosphate bone cement. Journal of the American Ceramic Society **2018,** 101 (2), 502-508.

400. Zima, A.; Czechowska, J.; Siek, D.; Olkowski, R.; Noga, M.; Lewandowska-Szumieł, M.; Ślósarczyk, A., How calcite and modified hydroxyapatite influence physicochemical properties and cytocompatibility of alpha-TCP based bone cements. Journal of Materials Science: Materials in Medicine **2017,** 28 (8), 1-12.

401. Vásquez, A.; Domínguez, S.; Dos Santos, L. L., α-TCP cements prepared by syringe-foaming: Influence of Na2HPO4 and surfactant concentration. Materials Science and Engineering: C **2017,** 81, 148-155.

402. Roozbahani, M.; Alehosseini, M.; Kharaziha, M.; Emadi, R., Nano-calcium phosphate bone cement based on Si-stabilized α-tricalcium phosphate with improved mechanical properties. Materials Science and Engineering: C **2017,** 81, 532-541.

403. Chappard, D.; Guillaume, B.; Mallet, R.; Pascaretti-Grizon, F.; Basle, M. F.; Libouban, H., Sinus lift augmentation and β-TCP: A microCT and histologic analysis on human bone biopsies. Micron **2010,** 41 (4), 321-326.

404. Rokn, A.; Moslemi, N.; Eslami, B.; Abadi, H. K.; Paknejad, M., Histologic evaluation of bone healing following application of anorganic bovine bone and β-tricalcium phosphate in rabbit calvaria. Journal of Dentistry (Tehran, Iran) **2012,** 9 (1), 35.

405. Gaasbeek, R. D.; Toonen, H. G.; van Heerwaarden, R. J.; Buma, P., Mechanism of bone incorporation of β-TCP bone substitute in open wedge tibial osteotomy in patients. Biomaterials **2005,** 26 (33), 6713-6719.

406. Geng, F.; Tan, L.; Jin, X.; Yang, J.; Yang, K., The preparation, cytocompatibility, and in vitro biodegradation study of pure β-TCP on magnesium. Journal of Materials Science: Materials in Medicine **2009,** 20 (5), 1149-1157.

407. Luvizuto, E. R.; Tangl, S.; Zanoni, G.; Okamoto, T.; Sonoda, C. K.; Gruber, R.; Okamoto, R., The effect of BMP-2 on the osteoconductive properties of β-tricalcium phosphate in rat calvaria defects. Biomaterials **2011,** 32 (15), 3855-3861.

408. Famery, R.; Richard, N.; Boch, P., Preparation of α-and β-tricalcium phosphate ceramics, with and without magnesium addition. Ceramics International **1994,** 20 (5), 327-336.

409. Dong, J.; Uemura, T.; Shirasaki, Y.; Tateishi, T., Promotion of bone formation using highly pure porous β-TCP combined with bone marrow-derived osteoprogenitor cells. Biomaterials **2002,** 23 (23), 4493-4502.

410. Kondo, N.; Ogose, A.; Tokunaga, K.; Ito, T.; Arai, K.; Kudo, N.; Inoue, H.; Irie, H.; Endo, N., Bone formation and resorption of highly purified β-tricalcium phosphate in the rat femoral condyle. Biomaterials **2005,** 26 (28), 5600-5608.

411. Chazono, M.; Tanaka, T.; Komaki, H.; Fujii, K., Bone formation and bioresorption after implantation of injectable β-tricalcium phosphate granules–hyaluronate complex in rabbit bone defects. Journal of Biomedical Materials Research Part A: An Official Journal of The Society for Biomaterials, The Japanese Society for Biomaterials, and The Australian Society for Biomaterials and the Korean Society for Biomaterials **2004,** 70 (4), 542-549.

412. Kwon, S.-H.; Jun, Y.-K.; Hong, S.-H.; Kim, H.-E., Synthesis and dissolution behavior of β-TCP and HA/β-TCP composite powders. Journal of the European Ceramic Society **2003,** 23 (7), 1039-1045.

413. Ebrahimi, M.; Botelho, M. G.; Dorozhkin, S. V., Biphasic calcium phosphates bioceramics (HA/TCP): Concept, physicochemical properties and the impact of standardization of study protocols in biomaterials research. Materials Science and Engineering: C **2017,** 71, 1293-1312.

414. Zhang, H.; Li, X.; Wen, J.; Zhao, C., Preparation and characterisation of HA/TCP biphasic porous ceramic scaffolds with pore-oriented structure. Ceramics International **2017,** 43 (15), 11780-11785.

415. Taktak, R.; Elghazel, A.; Bouaziz, J.; Charfi, S.; Keskes, H., Tricalcium phosphate-Fluorapatite as bone tissue engineering: Evaluation of bioactivity and biocompatibility. Materials Science and Engineering: C **2018,** 86, 121-128.

416. Maji, K.; Dasgupta, S.; Pramanik, K.; Bissoyi, A., Preparation and characterization of gelatin-chitosan-nanoβ-TCP based scaffold for orthopaedic application. Materials Science and Engineering: C **2018,** 86, 83-94.

417. Narita, K.; Kobayashi, E.; Sato, T., Sintering behavior and mechanical properties of magnesium/β-tricalcium phosphate composites sintered by spark plasma sintering. Materials Transactions **2016,** 57 (9), 1620-1627.

418. Lee, D.; Kumta, P. N., Chemical synthesis and stabilization of magnesium substituted brushite. Materials Science and Engineering: C **2010,** 30 (7), 934-943.

419. Dorozhkin, S., Calcium orthophosphates in nature, biology and medicine. Materials 2: 399–498. 2009.

420. Redepenning, J.; McIsaac, J. P., Electrocrystallization of brushite coatings on prosthetic alloys. Chemistry of Materials **1990,** 2 (6), 625-627.

421. Redepenning, J. G., ELECTROCRYSTALLIZATION OF STRONGLY ADHERENT BRUSHITE COATINGS ON PROSTHETIC ALLOYS (continuation). **1995**.

422. Xu, L.; Zhang, E.; Yang, K., Phosphating treatment and corrosion properties of Mg–Mn–Zn alloy for biomedical application. Journal of Materials Science: Materials in Medicine **2009,** 20 (4), 859-867.

423. Kannan, M. B.; Wallipa, O., Potentiostatic pulse-deposition of calcium phosphate on magnesium alloy for temporary implant applications—An in vitro corrosion study. Materials Science and Engineering: C **2013,** 33 (2), 675-679.

424. Kannan, M. B., Improving the packing density of calcium phosphate coating on a magnesium alloy for enhanced degradation resistance. Journal of Biomedical Materials Research Part A **2013,** 101 (5), 1248-1254.

425. Kannan, M. B., Enhancing the performance of calcium phosphate coating on a magnesium alloy for bioimplant applications. Materials Letters **2012,** 76, 109-112.

426. Zhao, C.; Wu, H.; Hou, P.; Ni, J.; Han, P.; Zhang, X., Enhanced corrosion resistance and antibacterial property of Zn doped DCPD coating on biodegradable Mg. Materials Letters **2016,** 180, 42-46.

427. Driessens, F. C.; Verbeeck, R., Biominerals. CRC press: 1990.

428. Kibalczyc, W.; Zielenkiewicz, A., Calorimetric investigations of calcium phosphate precipitation. Journal of crystal growth **1987,** 82 (4), 733-736.

429. Bigi, A.; Gazzano, M.; Ripamonti, A.; Roveri, N., Effect of foreign ions on the conversion of brushite and octacalcium phosphate into hydroxyapatite. Journal of inorganic biochemistry **1988,** 32 (4), 251-257.

430. Pina, A. Sandra Cristina de. Universidade de Aveiro, 2009.

431. Kumar, M.; Dasarathy, H.; Riley, C., Electrodeposition of brushite coatings and their transformation to hydroxyapatite in aqueous solutions. Journal of Biomedical Materials Research: An Official Journal of The Society for Biomaterials, The Japanese Society for Biomaterials, and The Australian Society for Biomaterials **1999,** 45 (4), 302-310.

432. Walsh, D.; Tanaka, J., Preparation of a bone-like apatite foam cement. Journal of Materials Science: Materials in Medicine **2001,** 12 (4), 339-343.

433. Grøndahl, L.; Cardona, F.; Chiem, K.; Wentrup-Byrne, E.; Bostrom, T., Calcium phosphate nucleation on surface-modified PTFE membranes. Journal of Materials Science: Materials in Medicine **2003,** 14 (6), 503-510.

434. Lin, S.; LeGeros, R. Z.; LeGeros, J. P., Adherent octacalciumphosphate coating on titanium alloy using modulated electrochemical deposition method. Journal of Biomedical Materials Research Part A: An Official Journal of The Society for Biomaterials, The Japanese Society for Biomaterials, and The Australian Society for Biomaterials and the Korean Society for Biomaterials **2003,** 66 (4), 819-828.

435. Azevedo, H. S.; Leonor, I. B.; Alves, C. M.; Reis, R. L., Incorporation of proteins and enzymes at different stages of the preparation of calcium phosphate coatings on a degradable substrate by a biomimetic methodology. Materials Science and Engineering: C **2005,** 25 (2), 169-179.

436. Lu, X.; Leng, Y., Theoretical analysis of calcium phosphate precipitation in simulated body fluid. Biomaterials **2005,** 26 (10), 1097-1108.

437. Zainuddin, D., Hill, TV Chirila, AK Whittaker, and A. Kemp. Biomacromolecules **2006,** 7, 1758-65.

438. Zainuddin, ‡; Hill, D. J.; Chirila, T. V.; Whittaker, A. K.; Kemp, A., Experimental calcification of HEMA-based hydrogels in the presence of albumin and a comparison to the in vivo calcification. Biomacromolecules **2006,** 7 (6), 1758-1765.

439. Honda, Y.; Kamakura, S.; Sasaki, K.; Anada, T.; Masuda, T.; Suzuki, O. In DCPD/collagen scaffold and apatite formation in vitro, Key Engineering Materials, Trans Tech Publ: 2007; pp 479-482.

440. Juhasz, J. A.; Best, S. M.; Auffret, A. D.; Bonfield, W., Biological control of apatite growth in simulated body fluid and human blood serum. Journal of Materials Science: Materials in Medicine **2008,** 19 (4), 1823-1829.

441. Rakngarm, A.; Mutoh, Y., Electrochemical depositions of calcium phosphate film on commercial pure titanium and Ti–6Al–4V in two types of electrolyte at room temperature. Materials Science and Engineering: C **2009,** 29 (1), 275-283.

442. Tas, A. C.; Bhaduri, S. B., Rapid coating of Ti6Al4V at room temperature with a calcium phosphate solution similar to 10× simulated body fluid. Journal of materials research **2004,** 19 (9), 2742-2749.

443. Li, L.; Gao, J.; Wang, Y., Evaluation of cyto-toxicity and corrosion behavior of alkali-heat-treated magnesium in simulated body fluid. Surface and Coatings Technology **2004,** 185 (1), 92-98.

444. Dorozhkin, S. V., Calcium orthophosphate coatings on magnesium and its biodegradable alloys. Acta Biomaterialia **2014,** 10 (7), 2919-2934.

445. Zhang, J.; Dai, C.-S.; Wei, J.; Wen, Z.-H., Study on the bonding strength between calcium phosphate/chitosan composite coatings and a Mg alloy substrate. Applied surface science **2012,** 261, 276-286.

446. Dumelie, N.; Benhayoune, H.; Richard, D.; Laurent-Maquin, D.; Balossier, G., In vitro precipitation of electrodeposited calcium-deficient hydroxyapatite coatings on Ti6Al4V substrate. Materials Characterization **2008,** 59 (2), 129-133.

447. TenHuisen, K. S.; Brown, P. W., Effects of magnesium on the formation of calcium-deficient hydroxyapatite from CaHPO4· 2H2O and Ca4 (PO4) 2O. Journal of Biomedical Materials Research: An Official Journal of The Society for Biomaterials and The Japanese Society for Biomaterials **1997,** 36 (3), 306-314.

448. Bohner, M.; Theiss, F.; Apelt, D.; Hirsiger, W.; Houriet, R.; Rizzoli, G.; Gnos, E.; Frei, C.; Auer, J.; Von Rechenberg, B., Compositional changes of a dicalcium phosphate dihydrate cement after implantation in sheep. Biomaterials **2003,** 24 (20), 3463-3474.

449. Boskey, A.; Posner, A., Magnesium stabilization of amorphous calcium phosphate: a kinetic study. Materials Research Bulletin **1974,** 9 (7), 907-916.

450. Abbona, F.; Baronnet, A., A XRD and TEM study on the transformation of amorphous calcium phosphate in the presence of magnesium. Journal of Crystal Growth **1996,** 165 (1-2), 98-105.

451. Jonášová, L.; Müller, F. A.; Helebrant, A.; Strnad, J.; Greil, P., Biomimetic apatite formation on chemically treated titanium. Biomaterials **2004,** 25 (7-8), 1187-1194.

452. Kokubo, T., Formation of biologically active bone-like apatite on metals and polymers by a biomimetic process. Thermochimica Acta **1996,** 280, 479-490.

453. Li, X.; Chu, C.; Wei, Y.; Qi, C.; Bai, J.; Guo, C.; Xue, F.; Lin, P.; Chu, P. K., In vitro degradation kinetics of pure PLA and Mg/PLA composite: Effects of immersion temperature and compression stress. Acta biomaterialia **2017,** 48, 468-478.

454. Shi, Y.-j.; Pei, J.; Zhang, J.; Niu, J.-l.; Zhang, H.; Guo, S.-r.; Li, Z.-h.; Yuan, G.-y., Enhanced corrosion resistance and cytocompatibility of biodegradable Mg alloys by introduction of Mg (OH) 2 particles into poly (L-lactic acid) coating. Scientific reports **2017,** 7 (1), 1-11.

455. Butt, M. S.; Bai, J.; Wan, X.; Chu, C.; Xue, F.; Ding, H.; Zhou, G., Mg alloy rod reinforced biodegradable poly-lactic acid composite for load bearing bone replacement. Surface and Coatings Technology **2017,** 309, 471-479.

456. Zhao, C.; Wu, H.; Ni, J.; Zhang, S.; Zhang, X., Development of PLA/Mg composite for orthopedic implant: Tunable degradation and enhanced mineralization. Composites Science and Technology **2017,** 147, 8-15.

457. Rezwan, K.; Chen, Q.; Blaker, J. J.; Boccaccini, A. R., Biodegradable and bioactive porous polymer/inorganic composite scaffolds for bone tissue engineering. Biomaterials **2006,** 27 (18), 3413-3431.

458. Sun, J.; Zhu, Y.; Meng, L.; Chen, P.; Shi, T.; Liu, X.; Zheng, Y., Electrophoretic deposition of colloidal particles on Mg with cytocompatibility, antibacterial performance, and corrosion resistance. Acta biomaterialia **2016,** 45, 387-398.

459. Blacklock, J.; Sievers, T. K.; Handa, H.; You, Y.-Z.; Oupicky, D.; Mao, G.; Möhwald, H., Cross-linked bioreducible layer-by-layer films for increased cell adhesion and transgene expression. The Journal of Physical Chemistry B **2010,** 114 (16), 5283-5291.

460. Agarwal, S.; Curtin, J.; Duffy, B.; Jaiswal, S., Biodegradable magnesium alloys for orthopaedic applications: A review on corrosion, biocompatibility and surface modifications. Materials Science and Engineering: C **2016,** 68, 948-963.

461. Tomihata, K.; Suzuki, M.; Ikada, Y., The pH dependence of monofilament sutures on hydrolytic degradation. Journal of Biomedical Materials Research: An Official Journal of The Society for Biomaterials, The Japanese Society for Biomaterials, and The Australian Society for Biomaterials and the Korean Society for Biomaterials **2001,** 58 (5), 511-518.

462. Brown, A.; Zaky, S.; Ray Jr, H.; Sfeir, C., Porous magnesium/PLGA composite scaffolds for enhanced bone regeneration following tooth extraction. Acta biomaterialia **2015,** 11, 543-553.

463. Li, J.; Cao, P.; Zhang, X.; Zhang, S.; He, Y., In vitro degradation and cell attachment of a PLGA coated biodegradable Mg–6Zn based alloy. Journal of materials science **2010,** 45 (22), 6038-6045.

464. Danhier, F.; Ansorena, E.; Silva, J. M.; Coco, R.; Le Breton, A.; Préat, V., PLGA-based nanoparticles: an overview of biomedical applications. Journal of controlled release **2012,** 161 (2), 505-522.

465. Cifuentes, S. C.; Benavente, R.; Lieblich, M.; González-Carrasco, J. L., Biodegradable and bioabsorbable materials for osteosynthesis applications: state-of-the-art and future perspectives. Handbook of Composites from Renewable Materials, Biodegradable Materials **2017,** 5, 109-144.

466. Mamaghani, M. Y.; Pishvaei, M.; Kaffashi, B., Synthesis of latex based antibacterial acrylate polymer/nanosilver via in situ miniemulsion polymerization. Macromolecular Research **2011,** 19 (3), 243-249.

467. Wong, H. M.; Yeung, K. W.; Lam, K. O.; Tam, V.; Chu, P. K.; Luk, K. D.; Cheung, K. M., A biodegradable polymer-based coating to control the performance of magnesium alloy orthopaedic implants. Biomaterials **2010,** 31 (8), 2084-2096.

468. Yazdimamaghani, M.; Pourvala, T.; Motamedi, E.; Fathi, B.; Vashaee, D.; Tayebi, L., Synthesis and characterization of encapsulated nanosilica particles with an acrylic copolymer by in situ emulsion polymerization using thermoresponsive nonionic surfactant. Materials **2013,** 6 (9), 3727-3741.

469. Yazdimamaghani, M.; Razavi, M.; Vashaee, D.; Tayebi, L., Surface modification of biodegradable porous Mg bone scaffold using polycaprolactone/bioactive glass composite. Materials Science and Engineering: C **2015,** 49, 436-444.

470. Vandrovcova, M.; Douglas, T. E.; Mróz, W.; Musial, O.; Schaubroeck, D.; Budner, B.; Syroka, R.; Dubruel, P.; Bacakova, L., Pulsed laser deposition of magnesium-doped calcium phosphate coatings on porous polycaprolactone scaffolds produced by rapid prototyping. Materials Letters **2015,** 148, 178-183.

471. Wong, H. M.; Zhao, Y.; Leung, F. K.; Xi, T.; Zhang, Z.; Zheng, Y.; Wu, S.; Luk, K. D.; Cheung, K. M.; Chu, P. K., Functionalized polymeric membrane with enhanced mechanical and biological properties to control the degradation of magnesium alloy. Advanced healthcare materials **2017,** 6 (8), 1601269.

472. Domingos, M.; Intranuovo, F.; Gloria, A.; Gristina, R.; Ambrosio, L.; Bártolo, P.; Favia, P., Improved osteoblast cell affinity on plasma-modified 3-D extruded PCL scaffolds. Acta biomaterialia **2013,** 9 (4), 5997-6005.

473. Dash, T. K.; Konkimalla, V. B., Poly-ϵ-caprolactone based formulations for drug delivery and tissue engineering: A review. Journal of Controlled Release **2012,** 158 (1), 15-33.

474. Jiang, Y.; Wang, B.; Jia, Z.; Lu, X.; Fang, L.; Wang, K.; Ren, F., Polydopamine mediated assembly of hydroxyapatite nanoparticles and bone morphogenetic protein-2 on magnesium alloys for enhanced corrosion resistance and bone regeneration. Journal of Biomedical Materials Research Part A **2017,** 105 (10), 2750-2761.

475. Zhou, L.; Yuan, L.; Guan, Q.; Gu, A.; Liang, G., Building unique surface structure on aramid fibers through a green layer-by-layer self-assembly technique to develop new high performance fibers with greatly improved surface activity, thermal resistance, mechanical properties and UV resistance. Applied Surface Science **2017,** 411, 34-45.

476. Bakhsheshi-Rad, H.; Hamzah, E.; Ebrahimi-Kahrizsangi, R.; Daroonparvar, M.; Medraj, M., Fabrication and characterization of hydrophobic microarc oxidation/poly-lactic acid duplex coating on biodegradable Mg–Ca alloy for corrosion protection. Vacuum **2016,** 125, 185-188.

477. Li, X.; Shi, C.; Bai, J.; Guo, C.; Xue, F.; Lin, P.-H.; Chu, C.-L., Degradation behaviors of surface modified magnesium alloy wires in different simulated physiological environments. Frontiers of Materials Science **2014,** 8 (3), 281-294.

478. Tian, P.; Xu, D.; Liu, X., Mussel-inspired functionalization of PEO/PCL composite coating on a biodegradable AZ31 magnesium alloy. Colloids and Surfaces B: Biointerfaces **2016,** 141, 327-337.

479. Cui, X.-J.; Li, M.-T.; Yang, R.-S.; Yu, Z.-X., Structure and properties of a duplex coating combining micro-arc oxidation and baking layer on AZ91D Mg alloy. Applied Surface Science **2016,** 363, 91-100.

480. Diez, M.; Kang, M.-H.; Kim, S.-M.; Kim, H.-E.; Song, J., Hydroxyapatite (HA)/poly-L-lactic acid (PLLA) dual coating on magnesium alloy under deformation for biomedical applications. Journal of Materials Science: Materials in Medicine **2016,** 27 (2), 34.

481. Wang, M.-J.; Chao, S.-C.; Yen, S.-K., Electrolytic calcium phosphate/zirconia composite coating on AZ91D magnesium alloy for enhancing corrosion resistance and bioactivity. Corrosion Science **2016,** 104, 47-60.

482. Li, X.; Weng, Z.; Yuan, W.; Luo, X.; Wong, H. M.; Liu, X.; Wu, S.; Yeung, K.; Zheng, Y.; Chu, P. K., Corrosion resistance of dicalcium phosphate dihydrate/poly (lactic-co-glycolic acid) hybrid coating on AZ31 magnesium alloy. Corrosion Science **2016,** 102, 209-221.

483. Li, L.-H.; Narayanan, T. S.; Kim, Y. K.; Kong, Y.-M.; Park, I. S.; Bae, T. S.; Lee, M. H., Deposition of microarc oxidation–polycaprolactone duplex coating to improve the corrosion resistance of magnesium for biodegradable implants. Thin Solid Films **2014,** 562, 561-567.

484. Wei, Z.; Tian, P.; Liu, X.; Zhou, B., In vitro degradation, hemolysis, and cytocompatibility of PEO/PLLA composite coating on biodegradable AZ31 alloy. Journal of Biomedical Materials Research Part B: Applied Biomaterials **2015,** 103 (2), 342-354.

485. Abdal-hay, A.; Dewidar, M.; Lim, J.; Lim, J. K., Enhanced biocorrosion resistance of surface modified magnesium alloys using inorganic/organic composite layer for biomedical applications. Ceramics International **2014,** 40 (1), 2237-2247.

486. Johnston, S.; Shi, Z.; Atrens, A., The influence of pH on the corrosion rate of high-purity Mg, AZ91 and ZE41 in bicarbonate buffered Hanks' solution. Corrosion Science **2015,** 101, 182-192.

487. Jaiswal, S.; Kumar, R. M.; Gupta, P.; Kumaraswamy, M.; Roy, P.; Lahiri, D., Mechanical, corrosion and biocompatibility behaviour of Mg-3Zn-HA biodegradable composites for orthopaedic fixture accessories. Journal of the mechanical behavior of biomedical materials **2018,** 78, 442-454.

488. Bayrak, Ö.; Ghahramanzadeh Asl, H.; Ak, A., Comparison of SBF and DMEM in terms of electrochemical properties of common metallic biomaterials. Materials and Corrosion **2020,** 71 (2), 209-221.

489. Kokubo, T.; Takadama, H., How useful is SBF in predicting in vivo bone bioactivity? Biomaterials **2006,** 27 (15), 2907-2915.

490. Kokubo, T.; Ito, S.; Shigematsu, M.; Sanka, S.; Yamamuro, T., Fatigue and life-time of bioactive glass-ceramic AW containing apatite and wollastonite. Journal of Materials Science **1987,** 22 (11), 4067-4070.

491. Kokubo, T., Bioactive glass ceramics: properties and applications. Biomaterials **1991,** 12 (2), 155-163.

492. Kitsugi, T.; Yamamuro, T.; Nakamura, T.; Kokubo, T., The bonding of glass ceramics to bone. International orthopaedics **1989,** 13 (3), 199-206.

493. Mandel, S.; Tas, A. C., Brushite (CaHPO4· 2H2O) to octacalcium phosphate (Ca8 (HPO4) 2 (PO4) 4· 5H2O) transformation in DMEM solutions at 36.5 C. Materials Science and Engineering: C **2010,** 30 (2), 245-254.

494. Su, Y.; Guo, Y.; Huang, Z.; Zhang, Z.; Li, G.; Lian, J.; Ren, L., Preparation and corrosion behaviors of calcium phosphate conversion coating on magnesium alloy. Surface and Coatings Technology **2016,** 307, 99-108.

495. Bohner, M.; Lemaitre, J., Can bioactivity be tested in vitro with SBF solution? Biomaterials **2009,** 30 (12), 2175-2179.

496. Kim, H. M.; Miyaji, F.; Kokubo, T.; Nakamura, T., Preparation of bioactive Ti and its alloys via simple chemical surface treatment. Journal of Biomedical Materials Research: An

Official Journal of The Society for Biomaterials and The Japanese Society for Biomaterials **1996,** 32 (3), 409-417.

497. Miyazaki, T.; Kim, H. M.; Miyaji, F.; Kokubo, T.; Kato, H.; Nakamura, T., Bioactive tantalum metal prepared by NaOH treatment. Journal of Biomedical Materials Research: An Official Journal of The Society for Biomaterials and The Japanese Society for Biomaterials **2000,** 50 (1), 35-42.

498. Takadama, H.; Kim, H. M.; Kokubo, T.; Nakamura, T., TEM-EDX study of mechanism of bonelike apatite formation on bioactive titanium metal in simulated body fluid. Journal of Biomedical Materials Research: An Official Journal of The Society for Biomaterials, The Japanese Society for Biomaterials, and The Australian Society for Biomaterials and the Korean Society for Biomaterials **2001,** 57 (3), 441-448.

499. Nishiguchi, S.; Fujibayashi, S.; Kim, H. M.; Kokubo, T.; Nakamura, T., Biology of alkali-and heat-treated titanium implants. Journal of Biomedical Materials Research Part A: An Official Journal of The Society for Biomaterials, The Japanese Society for Biomaterials, and The Australian Society for Biomaterials and the Korean Society for Biomaterials **2003,** 67 (1), 26-35.

500. Kato, H.; Nakamura, T.; Nishiguchi, S.; Matsusue, Y.; Kobayashi, M.; Miyazaki, T.; Kim, H. M.; Kokubo, T., Bonding of alkali-and heat-treated tantalum implants to bone. Journal of Biomedical Materials Research: An Official Journal of The Society for Biomaterials, The Japanese Society for Biomaterials, and The Australian Society for Biomaterials and the Korean Society for Biomaterials **2000,** 53 (1), 28-35.

501. Zadpoor, A. A., Relationship between in vitro apatite-forming ability measured using simulated body fluid and in vivo bioactivity of biomaterials. Materials Science and Engineering: C **2014,** 35, 134-143.

502. Baino, F.; Yamaguchi, S., The Use of Simulated Body Fluid (SBF) for Assessing Materials Bioactivity in the Context of Tissue Engineering: Review and Challenges. Biomimetics **2020,** 5 (4), 57.

503. Bellucci, D.; Salvatori, R.; Anesi, A.; Chiarini, L.; Cannillo, V., SBF assays, direct and indirect cell culture tests to evaluate the biological performance of bioglasses and bioglass-based composites: Three paradigmatic cases. Materials Science and Engineering: C **2019,** 96, 757-764.

504. Kokubo, T.; Takadama, H., Simulated body fluid (SBF) as a standard tool to test the bioactivity of implants. Handbook of Biomineralization: Biological Aspects and Structure Formation **2007**, 97-109.

505. Kim, H.-M.; Himeno, T.; Kawashita, M.; Kokubo, T.; Nakamura, T., The mechanism of biomineralization of bone-like apatite on synthetic hydroxyapatite: an in vitro assessment. Journal of the Royal Society Interface **2004,** 1 (1), 17-22.

506. Khalajabadi, S. Z.; Kadir, M. R. A.; Izman, S.; Ebrahimi-Kahrizsangi, R., Fabrication, bio-corrosion behavior and mechanical properties of a Mg/HA/MgO nanocomposite for biomedical applications. Materials & Design **2015,** 88, 1223-1233.

507. Xin, Y.; Huo, K.; Hu, T.; Tang, G.; Chu, P. K., Corrosion products on biomedical magnesium alloy soaked in simulated body fluids. Journal of materials research **2009,** 24 (8), 2711-2719.

508. Kannan, M. B.; Koc, E.; Unal, M., Biodegradability of β-Mg17Al12 phase in simulated body fluid. Materials letters **2012,** 82, 54-56.

509. Marco, I.; Feyerabend, F.; Willumeit-Römer, R.; Biest, O. V. d. In Influence of testing environment on the degradation behavior of magnesium alloys for bioabsorbable implants, TMS 2015 144th Annual Meeting & Exhibition, Springer: 2015; pp 499-506.

510. Yang, L.; Zhang, E., Biocorrosion behavior of magnesium alloy in different simulated fluids for biomedical application. Materials science and engineering: C **2009,** 29 (5), 1691-1696.

511. Hänzi, A. C.; Gerber, I.; Schinhammer, M.; Löffler, J. F.; Uggowitzer, P. J., On the in vitro and in vivo degradation performance and biological response of new biodegradable Mg–Y–Zn alloys. Acta biomaterialia **2010,** 6 (5), 1824-1833.

512. Hanks, J. H.; Wallace, R. E., Relation of oxygen and temperature in the preservation of tissues by refrigeration. Proceedings of the Society for Experimental Biology and Medicine **1949,** 71 (2), 196-200.

513. Kirkland, N. T.; Waterman, J.; Birbilis, N.; Dias, G.; Woodfield, T. B.; Hartshorn, R. M.; Staiger, M. P., Buffer-regulated biocorrosion of pure magnesium. Journal of Materials Science: Materials in Medicine **2012,** 23 (2), 283-291.

514. Marco, I.; Myrissa, A.; Martinelli, E.; Feyerabend, F.; Willumeit-Römer, R.; Weinberg, A.; Van der Biest, O., In vivo and in vitro degradation comparison of pure Mg, Mg-10Gd and Mg-2Ag: a short term study. European cells & materials **2017,** 33, 90-104.

515. Kirkland, N.; Lespagnol, J.; Birbilis, N.; Staiger, M., A survey of bio-corrosion rates of magnesium alloys. Corrosion science **2010,** 52 (2), 287-291.

516. Yamamoto, A.; Hiromoto, S., Effect of inorganic salts, amino acids and proteins on the degradation of pure magnesium in vitro. Materials Science and Engineering: C **2009,** 29 (5), 1559-1568.

CHAPTER THREE: RESEARCH DESIGN AND METHODOLOGY

3.1 Experimental Section Overview

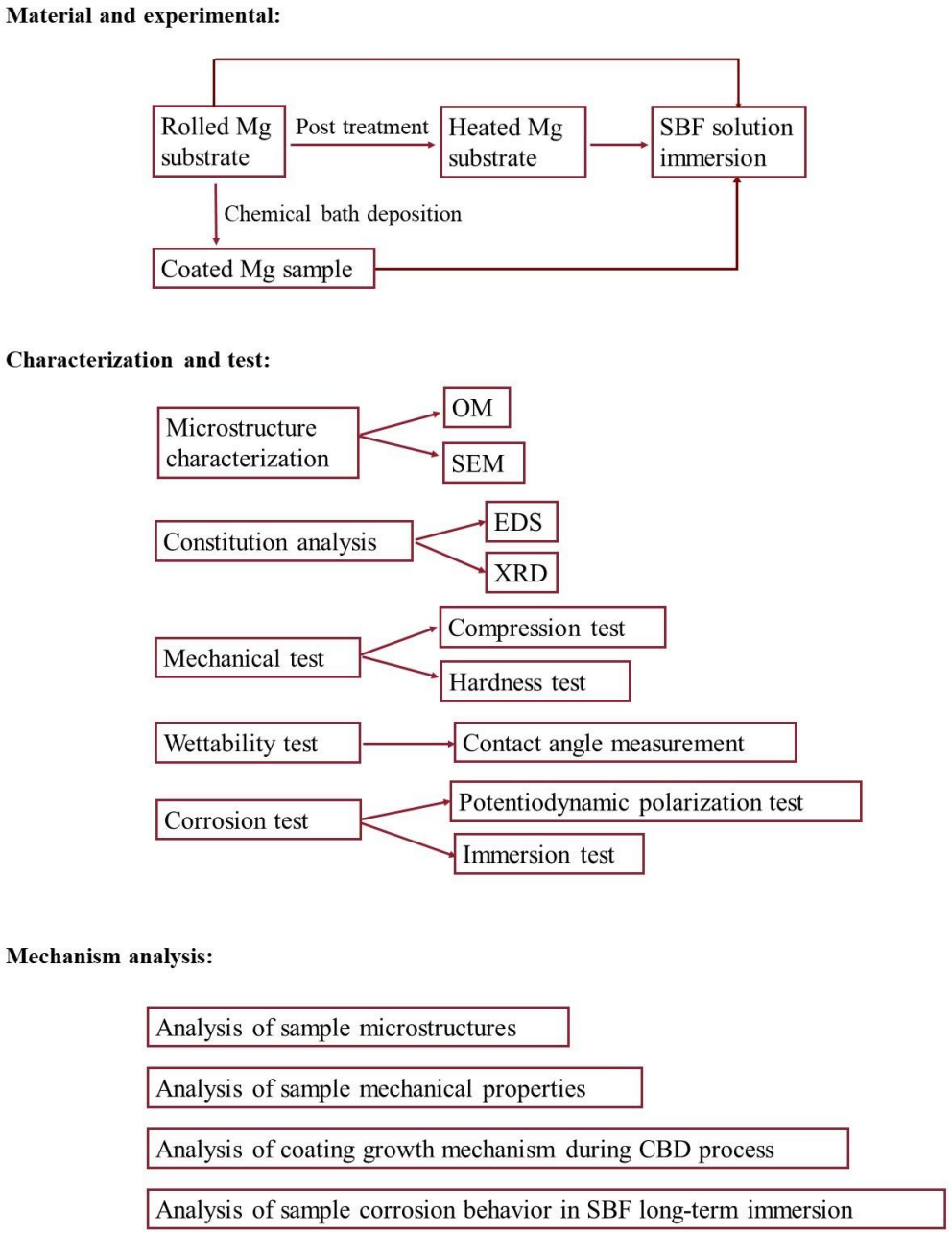

Figure 3.1: Schematic of the experimental process, characterizations, tests, and mechanism analysis.

Figure 3.1 describes the research design and methodology, characterizations, tests, and mechanism analysis. The sample preparation contained the rolling, post-treatment, and traditional chemical bath deposition processes. The microstructure and constitution of the sample were characterized. The mechanical properties and corrosion behavior tests in the SBF were carried out. The general information about experimental design and methodology in this dissertation is reported in this chapter. The details of the characterization and test results, result discussions, and mechanism analysis are given in the following chapters.

3.2 Materials

3.2.1 Preparation of Bare Mg Sample

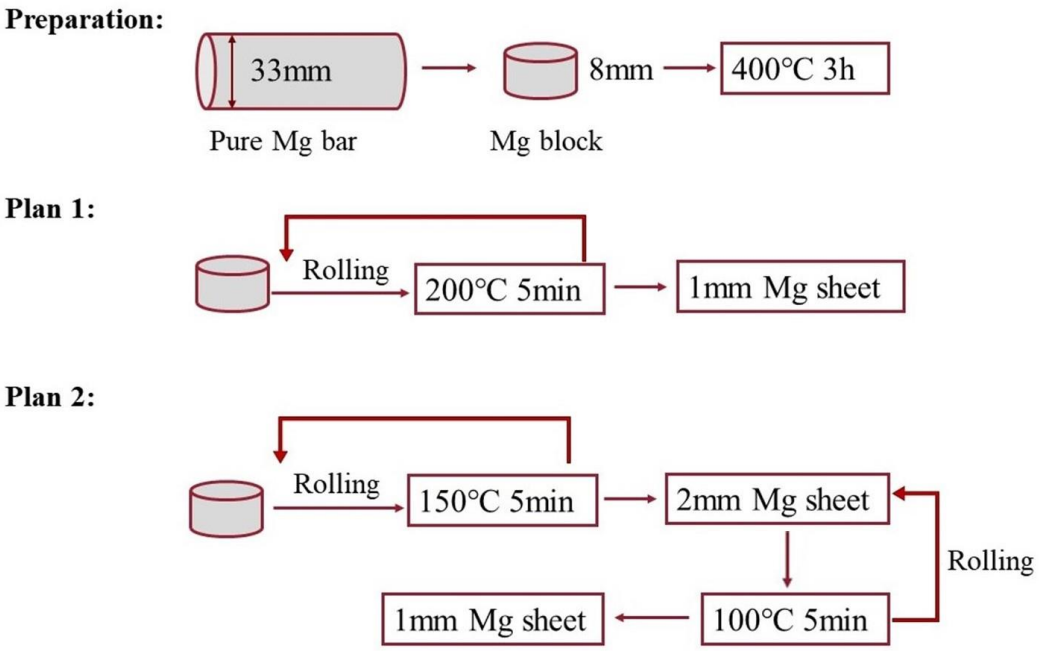

Figure 3.2: Schematic of the preparation and rolling process conditions of pure Mg substrate.

Figure 3.3: Mg block and Mg sheet before and after the rolling process.

In this study, the original material was a pure Mg casting bar with a diameter of 33 mm. The first step was the cutting of raw material. The pure Mg casting bar was cut into blocks with a thickness of 8 mm. Then, the casting block was placed in a 400 ℃ furnace for 3 hours as a pretreatment.

At the same time, two different employed process conditions in this study are given in detail in **Figure 3.2**. The furnace was set at different temperatures to provide different rolling conditions. After each rolling, the Mg substrate was placed in the furnace for 5 minutes. The reduced thickness of each roll was about 0.04 mm. The first rolling scheme was that the whole process was carried out at 200 °C. The second rolling scheme was non-isothermal. In this process, the initial temperature was 150 °C, and the final temperature was 100 °C. The Mg block was heated

to 150 °C and rolled from 8-mm height to 2-mm height. Then it was continuously rolled and finished to 1 mm at 100 °C. The resulting sheets rolled at the final rolling temperature of 100 °C, and 200 °C conditions were denoted as R100 and R200, respectively. Then, the 1 mm R200 Mg sheet was post-treated at 400 °C for 10 minutes, 30 minutes, 2 hours, 4 hours, 8 hours, and 24 hours to obtain different samples. After a period of post-treatment, the heated samples were named R200-H10min, R200-H30min, R200-H2hr, R200-H4hr, R200-H8hr, and R200-H24hr. The rolled Mg sheet was cut into 10 mm × 10 mm squares as the bare samples and the substrates of the coated ones.

3.2.2 Preparation of Coated Mg Sample

The coated Mg was obtained by the traditional chemical bath deposition method under different temperatures. The specific operation of the deposition is as follows. First, the prepared square matrix was polished, followed by the absolute ethanol wash and air drying. 40 mL of deionized water was placed in a beaker and heated to 37 °C, 55 °C, 70 °C, 85 °C, and 100 °C. Then, 0.8 g $CaCl_2$ and Mg matrix were added to the beaker sequentially. Next, 0.2687 g K_2HPO_4 was added and mixed well by a magnetic rotor. All the reagents mentioned above were analytic grades. Afterward, the solution was magnetic stirred and kept at the temperature for 2 hours for a sufficient reaction. After cooling and standing at room temperature for 24 hours, the sample was taken out of the beaker. Then, it was cleaned with absolute ethanol and dried with cold air. Finally, the coated Mg was obtained for the following characterizations and tests. The coated Mg samples with different substrates and coating temperatures were named R100-C37 and R200-C37, R100-C55 and R200-C55, R100-C70 and R200-C70, R100-C85 and R200-C85, and R100-C100 and R200-C100, respectively.

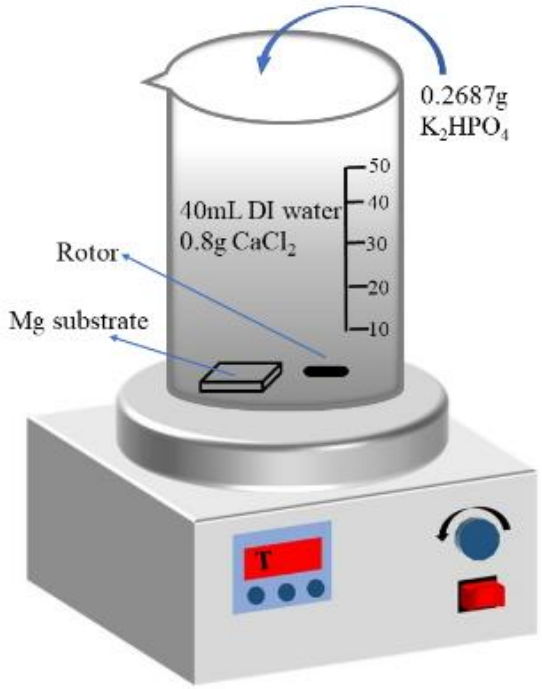

Figure 3.4: Schematic diagram of the coated Mg sample preparation.

3.2.3 Preparation of SBF Solution

This research tested the corrosion behavior in simulated body fluid (SBF) to evaluate sample corrosion resistance and analysis corrosion mechanisms. For making 1000 mL SBF, 700 mL of deionized water was put into a scratch-free beaker and covered with plastic wrap. It was stirred by a magneton and heated to 36.5 ± 0.5 ° C. Then, the reagents were dissolved orderly as listed in the following **Table 3.1** [1]. In the whole process, the solution was colorless and transparent. If any precipitation occurs during SBF configuration, the equipment must be cleaned again to restart preparation. The Tris and a small amount of HCl were used to adjust the pH value to reach 7.4 at 36.5 ± 0.5 °C [1]. It should be noticed that the reagents KCl, $K_2HPO_4{\cdot}3H_2O$, $MgCl_2{\cdot}6H_2O$, $CaCl_2$, and Na_2SO_4 are hygroscopic. For a more accurate measurement, the shorter the measurement time, the better. Additionally, the reagents must not be dissolved at the same

time. Only after the former reagent is entirely dissolved, the next one can be added to the container. The last step was to add more distilled water to the 1000-mL marked line to obtain the perfect SBF.

Table 3.1: Orders, amounts, weighing containers, purities, and formula weights of reagents for preparing 1000 mL of SBF [1].

Order	Reagent	Amount	Container	Purity	Formula weight
1	NaCl	8.035 g	Weighing paper	99.5%	58.4430
2	$NaHCO_3$	0.355 g	Weighing paper	99.5%	84.0068
3	KCl	0.225 g	Weighing bottle	99.5%	74.5515
4	$K_2HPO_4 \cdot 3H_2O$	0.231 g	Weighing bottle	99.0%	228.2220
5	$MgCl_2 \cdot 6H_2O$	0.311 g	Weighing bottle	98.0%	203.3034
6	1.0 M-HCl	39 mL	Graduated cylinder	--	--
7	$CaCl_2$	0.292 g	Weighing bottle	95.0%	110.9848
8	Na_2SO_4	0.072 g	Weighing bottle	99.0%	142.0428
9	Tris	6.118 g	Weighing paper	99.0%	121.1356
10	1.0 M-HCl	0-5 mL	Syringe	--	--

3.3 Characterization and Test

3.3.1 Microstructure Characterization

The microstructure of the sample was characterized by optical microscopy (OM) through metallographic preparation as shown in **Figure 3.5**. After the sample was mounted in epoxy, the

sample was first roughly and finely wet-grounded with SiC paper with different grit sizes (400, 600, 800, 1200, and 2500), then successively polished with polish cloth on a grinding machine and washed continuously with a small flow of alcohol. On the one hand, alcohol could reduce the temperature and prevent metal surface oxidation. On the other hand, alcohol could remove surface impurities and keep the sample surface clean. The fine-polished Mg surface was bright without scratches. Then the sample was rinsed with alcohol and dried with cold air for subsequent etching by a mixed solution. The etching solution was composed of 1 mL alcohol, 3 mL distilled water, 1 mL 1M acetic acid, and 1 mL 4.67 wt.% picric acid. The etching time was from 50 to 90 seconds. Next, the etched sample was washed with alcohol and dried with cold air. Then the metallography could be observed under an optical microscope. Photographs with different magnifications were taken for subsequent microstructural analysis. Then, the measurement of grain size was performed. For each kind of sample, over 1500 grains were measured the lengths of diameter.

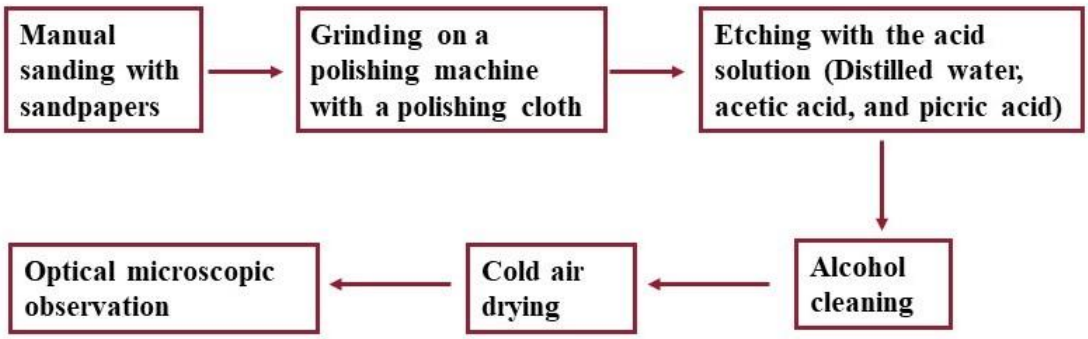

Figure 3.5: Schematic of the optical microscopic observation preparation process.

The morphologies of the coated samples obtained under different bath temperatures and the corroded samples after different immersion periods were also obtained by a scanning electron microscopy (FEI SEM Quanta 200F, Field Emission Instruments, USA).

3.3.2 Constitution Analysis

The X-ray diffraction (XRD) and the energy dispersive spectrometer (EDS) were used to examine and study the chemical composition of the deposited coating and corrosion product. The phase analysis by XRD test was performed with a Cu Kα radiation ($\lambda = 0.15406$ nm) in the 2θ range from 10° to 70°. The scanning rate was 4° per minute at 40 kV and 15 mA.

3.3.3 Mechanical Property Test

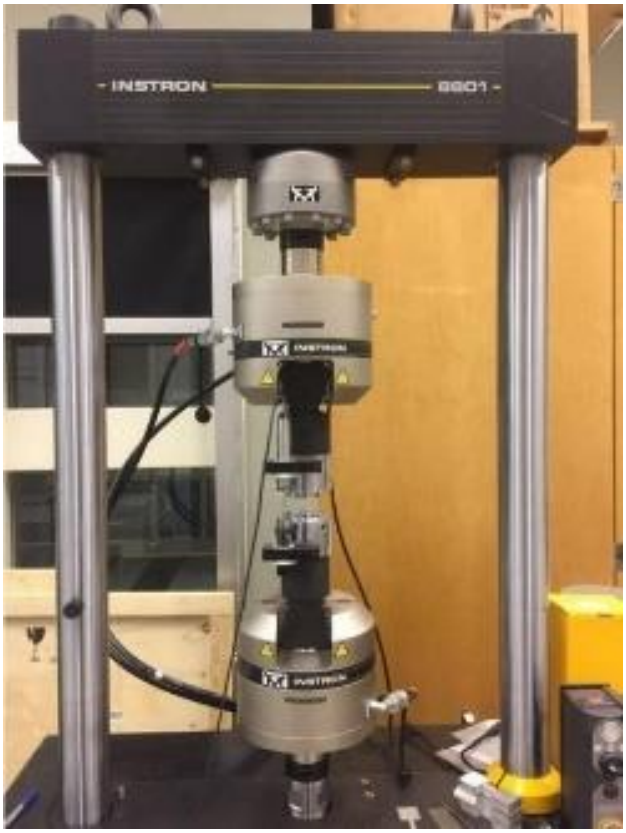

Figure 3.6: The apparatus for the mechanical test.

The test specimen was extracted from the core region of the rolled sheet to avoid the effect of edge cracks on the mechanical property analysis. The tensile sample was machined according to

the ASTM-E8-04 standard [2]. The tensile test was carried out using a universal testing machine at a displacement rate of ~10^{-3}/s at room temperature to obtain a tensile curve. Five parallel tests were done for each kind of sample. Yield strength, tensile strength, and strain at the fracture were obtained from the tensile stress-strain curve.

Also, the hardness was tested by a hardness of Vickers (HV) tester with an indenter load of 500 K duration for 10 seconds on the specimen. To ensure accuracy, at least 15 measurements were taken at room temperature at different positions of the sample. And the mean value was calculated from the measurements.

3.3.4 Wettability Test

The surface wettability was investigated by measuring the contact angle. In this study, distilled water was used as the solvent. The surface water contact angle was obtained and measured by a video optical contact angle analyzer with an introduction of 3 μL distilled water under ambient conditions. The contact angle from the shape of the drop had an accuracy of 0.1°. The average value of three different position measurements was calculated as the final static water contact angle to obtain reliable data. For the bare Mg sample, the surface was polished before the test to remove the oxide layer. Because all the bare samples were polished to the same level of roughness, the influence of the surface roughness on wettability was negligible.

3.3.5 Potentiodynamic Polarization Test

The potentiodynamic polarization was carried out in SBF at 37 ± 0.5 ℃ by a CHI660E electrochemical workstation. The experimental setup was composed of a traditional three-

electrode cell system [3]. Besides a saturated calomel electrode (SCE) and a platinum counter electrode, the tested sample was used as the working electrode [4]. Before the polarization test, the sample was stabilized in 30 mL SBF at the temperature of 37 ± 0.5 ℃ for 10 minutes. The open-circuit potential (OCP) was monitored for 400 seconds at first. Then, without any further delay, the polarization was started with a 0.01 V/s scanning rate. The polarization voltage range was ±0.25 V versus the OCP. The Tafel fit was employed and plotted by using CHI660E electrochemical analyzer software. To obtain the corrosion current densities and corresponding corrosion voltages from the polarization curves of the bare and coated Mg, the Tafel extrapolation was applied, as recommended by Kirkland et al. [5].

3.3.6 Immersion Test

The corrosion behavior of the bare and coated Mg was evaluated by not only the electrochemical test but also the immersion test in SBF.

In this research, a 30-day immersion was carried out in SBF as shown in **Figure 3.7** to evaluate sample corrosion resistance and analysis the mechanism. Before the soaking test, the bare Mg sample was gently polished to remove the oxide layer. The polished sample was cleaned with absolute ethanol and dried with cool air to get a clean and fresh surface. The sample with or without coating was individually submerged in 30 mL static and non-renewal SBF at human body temperature for different time durations to monitor the pH variation. The SBF was not stirred during the experiments, and the temperature was controlled with a water bath. The data from the pH-Meter was recorded at 2 hours intervals in the first 48 hours and then every 24 hours. The average of five repeated tests was used to plot the pH value curve. After the

immersion test, the sample was removed from the SBF and rinsed with deionized water for the following characterization.

Figure 3.7: The apparatus for the immersion test.

REFERENCES

1. Kokubo, T.; Takadama, H., How useful is SBF in predicting in vivo bone bioactivity? Biomaterials **2006,** 27 (15), 2907-2915.

2. Standard, A., E8-04,". Standard Test Methods for Tension Testing of Metallic Materials," Annual Book of ASTM Standards. **2004**.

3. Xin, Y.; Hu, T.; Chu, P. K., Degradation behaviour of pure magnesium in simulated body fluids with different concentrations of HCO3. Corrosion Science **2011,** 53 (4), 1522-1528.

4. Marco, I.; Van der Biest, O., Polarization measurements from a rotating disc electrode for characterization of magnesium corrosion. Corrosion Science **2016,** 102, 384-393.

5. Kirkland, N.; Birbilis, N.; Staiger, M., Assessing the corrosion of biodegradable magnesium implants: A critical review of current methodologies and their limitations. Acta biomaterialia **2012,** 8 (3), 925-936.

CHAPTER FOUR: GRAIN SIZE AND MECHANICAL PROPERTIES OF MAGNESIUM EXPERIENCED ROLLING AND POST-HEAT TREATMENT

Attribution

Written and submitted for publication in the Journal of Manufacturing and Materials Processing.

Author Contributions: Conceptualization and methodology, Jiaying Wang and Qizhen Li.; validation, Jiaying Wang.; formal analysis, Jiaying Wang.; writing—original draft preparation, Jiaying Wang.; writing—review and editing, Jiaying Wang and Qizhen Li.; supervision, Qizhen Li.; project administration, Qizhen Li.; funding acquisition, Qizhen Li.

4.1 Introduction

Mg and Mg-based materials have a big plus over most metallic and polymeric implants in bone healing and orthopedics due to the mechanical properties of the material themselves [1-3]. These properties make them ideal candidates as degradable implants for load-bearing applications [4-6]. In the following **Table 4.1**, a summary of the mechanical properties of various human-nature bones and pure Mg is given. These values of bone tissue are different in different parts or ages of people [5-9]. If the mechanical properties of materials can be controlled and adjusted, the probability of practical application of materials can be significantly improved.

Table 4.1: Mechanical properties of pure Mg and various human-nature bones.

Material/Tissue	**Density (g/cm^3)**	**Compressive yield strength (MPa)**	**Tensile strength (MPa)**	**Elastic moduli (GPa)**
Mg theory [10]	1.74	20-115	90-190	45
Mg sintered [11]	1.7385 ± 0.002	162 ± 5	195 ± 4	---
Cancellous bone [10]	1.0-1.4	1.5-9.3	1.5-38	0.01-1.57
Natural bone [12]	---	130-180	About 100	3-20
Cortical bone [13]	1.8-2.0	104.9-114.3	35-283	5-23
Compact bone Longitudinal [14]	---	205 ± 17.3	135 ± 15.6	---
Compact bone Transverse [14]	---	131±20.7	53 ± 10.7	---

Because the casting alloy has coarse grains with micropores, applying an appropriate method to refine the original grains is essential. Here are some standard processes that are employed in plastic machining. However, Mg and Mg alloys have limitations of machinability due to the hexagonal close-packed (HCP) type crystal structure [15-18]. Rolling, which produces refined grains, has been used by many researchers to obtain different shapes, like sheets, blocks, and rods. Also, the post-treatment after the rolling process is worth investigating because it also leads to the evolution of the microstructure. Furthermore, the degree of grain refinement is easily controlled and influenced by process conditions [19].

Some mechanical properties can be enhanced and achieved through the simple approach of the conventional rolling process introduced at different temperatures, followed by annealing [20-22]. The mechanical behavior can be regarded as the macro presentation of the microstructure characteristic. Some research has been conducted to find the influence of grain size in pure Mg and Mg alloys by changing the processing conditions [19, 23-24]. Past studies have found that both hardness and intensity primarily depend on the microstructure and the defects [23, 25-28]. Moreover, they are both reflexes of the capacity of the material against deformation and failure with the function of additional forces. From this, it is deduced that there should be a relative coherence between the hardness, intensity, and microstructure. Another common and widely accepted theory is the Hall-Petch relationship [29-31], which discusses the influence of average grain size on yield strength. The classical Hall-Petch relationship, shown as **Equation (4.1)**, has been well proved in many materials [31].

$$\sigma = \sigma_0 + k \times d^{-2} \quad \textbf{(4.1)}$$

For different materials and different preparation conditions, this formula is constantly adjusted to the **Equation (4.2)** after the tests and calculations [32].

$$\sigma = \sigma_0 + k \times d^{-n} \quad \textbf{(4.2)}$$

These equations show that the yield strength is improved with the decrease of the grain size. Moreover, the role of grain growth in hardness at ambient temperature is also revealed to fit into the Hall-Petch equation [31]. In recent years, some inverse Hall-Petch effects have also been found [30, 32-33]. This phenomenon occurs if the grain size is smaller than the critical value, usually the nanometer level [32, 34-35]. It is important to note that it appears in pure Mg when the grain sizes are within the range of a few micrometers, which is much coarser compared to that of face-centered cubic (FCC) and body-centered cubic (BCC) metals [30, 33, 35]. However, related research and detailed studies on the variation of the microstructural characterization and mechanical behavior of pure Mg after the hot-rolling and heat-treatment process are rarely conducted. Moreover, a more precise relationship between the strength, hardness, and grain size of the rolled Mg alloy sheets obtained from different initial temperatures needs to be further discussed comprehensively.

Generally, the macro property of rolled Mg is the microstructure reflection. So, the research on mechanical behaviors appears to be super essential. Therefore, in this study, a series of trials has been given to investigate the combined effect of rolling at different temperatures and following post-treatment on the microstructure and mechanical behavior of pure Mg.

4.2 Microstructure and mechanical properties of rolled Mg

The optical microstructure figures of original sample before rolling and the samples obtained by different rolling routines are exhibited in **Figure 4.1**. By measuring about 1500 grains, the grain size distribution of each sample is obtained. After further calculation, the grain average diameter of each sample is also obtained. The homogeneity of grain size can be reflected by the shape of distribution curve in **Figure 4.1 (b, d, f)**, the grain size variance is in **Table 4.2**. Also, the mechanical properties of the treated specimens were estimated by hardness, and tensile testing was carried out under ambient conditions. There were some cracks on the edges of rolled Mg sheet, as shown in **Figure 3.3**. The tensile specimens were entirely cut from the center part of the rolled sheets to eliminate the distortion of imperfect edges on the mechanical test result. Yield strength, tensile strength, and strain at fracture are obtained from the tensile stress-strain curves.

4.2.1 Microstructure Rolled Mg

The initial specimen grain is large and uneven, with a size of 104.19 ± 60.91 μm. Although Mg has a limitation in the number of active slip systems, in these rolled samples, the microstructures are obviously changed after the rolling treatment. The grain sizes of R200 and R100 are 15.62 ± 5.53 μm and 6.63 ± 2.69 μm, respectively. Their optical microstructures give clear evidence that under the condition of a slight reduction rolling process with a severe total deformation could obviously refine the grain size and strengthen the homogeneity.

At the very beginning of the rolling process, when the deformation is minimal, the grain size does not change because the amount of deformation is too small, resulting in insufficient storage energy to drive recrystallization. After the multiple rolling, the deformation is greater than the

critical deformation. The deformation degree is large, and the deformation structure is strongly broken and uniform. Grain refinement is mainly related to grain splitting thanks to the generation of recrystallization nuclei during rolling at high deformation. The more serious reduction, the smaller the grain. Because of the large deformation, high dislocation density is produced in the original large grains to refine them into small sizes. High-density dislocation has a significant effect on stored strain energy. It serves as a driving force for nucleation and growth, and the nucleation rate increases rapidly, so the original Mg grains are refined into uniform and fine equiaxed ones. The presence of dislocations in the seriously deformed grains also delays the appearance of grain coarsening. Therefore, the microstructure remains the refined size under ambient conditions.

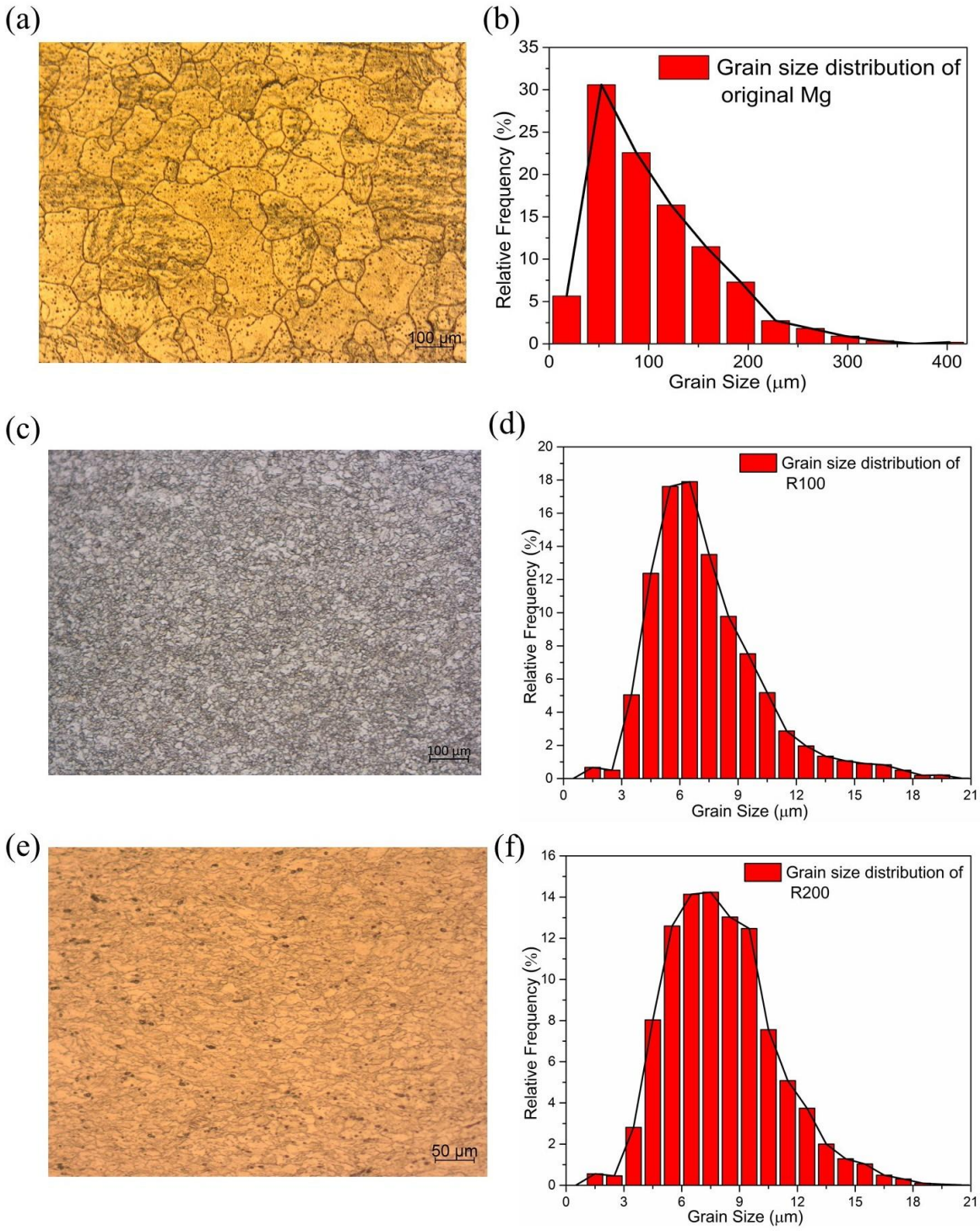

Figure 4.1: (a) Original Mg microstructure and (b) grain size distribution graph; (c) R100 Rolled Mg microstructure and (d) grain size distribution graph; (e) R200 Rolled Mg microstructure and (f) grain size distribution graph.

Also, in the present work, different initial and final rolling temperatures are set. The function of temperature on microstructure and mechanical performance is discussed in depth. The refined average grain size of R200 is around 9 μm larger than that of R100. Because during the rolling process, sharply increasing dislocations and the interaction among them, the residual stress is generated in the Mg. Besides, the severe lattice distortion and residual stress increase the free energy significantly in plastic deformation. So, the rolled Mg is unstable in thermodynamics and tends to return to a stable state. There is dynamic recovery due to the warm temperature simultaneously. With an improving rolling temperature, more energy is provided for the atom and grain boundary diffusion. The migration ability of the grain boundary is also enhanced. The migration ability of the grain boundary is also enhanced. The slip, climb, and cross slip of dislocation more easily occur, leading to faster grain recovery and growth rate of grain size. Therefore, R100 has the smallest and the most uniform grain in this study. It is concluded that the microstructure of the bare Mg sample is affected and controlled by the preparation temperature. The average grain size slightly goes up with the higher deformation temperature.

4.2.2 Mechanical Properties of Rolled Mg

The variation of the micro-hardness of the sample and the stress-strain results are shown in the **Table 4.2**. Significant differences in the mechanical property test are observed in the pure Mg subjected to rolling. Rolling is considered an easy method to improve metal hardness. R100 and R200 have the highest hardness values compared with other samples. In this study, R100 shows the highest hardness. As it is seen from the test data, with the rolling temperature raised to 200 ℃, the hardness decreases from 43.09 ± 2.51 HV to 37.99 ± 2.31 HV. In other words, the hardness has been enhanced due to the grain size cut down. In the hardness test, when the

external force acts on the surface of fine-grain material to form plastic deformation, the external force will be dispersed in the surrounding grains. The more refined the grain, the more grains around each grain that can disperse external forces. So, the greater the hardness of the material is. Hence, under the same deformation routine, the hardness reduces under a higher rolling temperature.

Like the hardness, the strain at the fracture is also affected by the grain size, which is due to the rolling temperature. In the more delicate grain structure, there are more grain boundaries, which could absorb more energy in the fracture process. At the same time, the finer the grain size, the larger the grain boundary area and the smaller the stress concentration is. So, the crack is hard to initiate in refined grain, and it is more unfavorable to crack propagation. Therefore, the strain at the fracture of R100, which shows better plasticity, is also higher than that of R200. The yield and tensile strength of R100 and R200 are respectively over 100 MPa and 180 MPa due to the fine grain strengthening and dislocation strengthening mechanisms. At the elevated temperature of 200 ℃, R200 shows an improvement in yield and tensile strength. In the rolling process, many dislocations are produced in the original large grains, and the grains are refined into small ones by dislocations. In the same volume of metal, the finer the grain is, the more the grain boundaries and the more obstacles. At the same time, a lot of distortion energy is accumulated within the metal due to the severe lattice distortion. For the rolled Mg, the work hardening phenomenon made the Mg in an unstable high-energy state. So, the rolled Mg samples have relatively high strength.

It is noticeable that the yield and tensile strengths of R200 are higher than those of R100, which means that inverse Hall-Petch effects have been found. The Hall-Petch relation is only applicable if the grain grows greater than a critical value. The grain size, which is less than the critical value, results in an inverse Hall-Petch phenomenon. In this study, the R100 grain size is the smallest, in the range of 3.94-9.32 μm. The reason for inverse Hall-Petch effects is not very clear. At present, the most widely accepted theory is that when the grain size is close to the size of structural defects, their contribution to strength will be greatly reduced. At the same time, when the grain is tiny, there is a losing dislocation stacking effect. Moreover, the small grain size is conducive to grain rotation and leads to reduce the yield strength.

Table 4.2: Grain sizes and mechanical test results of different rolled Mg samples.

	Grain size (μm)	**Hardness (HV)**	**Yield strength (MPa)**	**Tensile strength (MPa)**	**Strain at fracture (%)**
R100	6.63±2.69	43.09±2.51	109	182	11.42
R200	15.62±5.53	37.99±2.31	123	206	6

4.3 Microstructure and mechanical properties of post-treated Mg

4.3.1 Microstructure of Post-treated Mg

As mentioned before, the R200 rolled Mg is in a thermodynamically unstable state. Because the plastic deformation distorts microstructure and introduces dislocations, as well as some other defects, it results in more energy accumulation which is inclined to return to a steady status. At

room temperature, the accumulated energy is relatively low, the atomic activity is small. So, the recovery and the recrystallization process are extremely slow. Therefore, the following heat treatment is necessary to provide energy for the atomic activity to make the grain grow.

For all the rolled samples post-treated with different periods, the grain size and microstructure are changed in this process. The microstructures that remain equiaxed with different sizes are shown in the following figures and **Table 4.3**. In this study, the temperature of heat treatment is 400 ℃. The treatment period is 10 minutes, 30 minutes, 2 hours, 4 hours, 8 hours, and 24 hours. After different durations, the refined grains grow up, and their microstructures are different. The initial grain growth rate is fast up to the first 120 minutes, after which it slows down while prolonging heating time. The grain coarsening and abnormal growth are observed after 24 hours of treatment.

The annealing process brings three steps: recovery, recrystallization, and grain growth [7]. The recrystallization temperature of Mg is about 150 ℃ [36-40]. Therefore, when the Mg after rolling is treated at 400 ℃, the recovery and recrystallization process will be completed immediately. Therefore, this experimental result is obviously a growth process. Heating will provide energy to increase the diffusion ability of atoms. Thus, the equilibrium correlation between grain boundary migration and resistance is broken. Generally, the higher the energy in the grain boundary, the easier the migration of the grain boundary. The interface energy of the grain boundary is related to the orientation difference of adjacent grains. The interface energy of the small-angle grain boundary is low, so the driving force of interface movement is small, and the moving speed of the grain boundary is low. On the contrary, the large-angle grain boundary with high interface

energy has high mobility. This large-angle grain boundary movement will lead to swallowing other grains. As a result, grain growth in a short time is realized. As increasing the treating period, the grain grows gradually. Meanwhile, the total area of the grain boundary decreases, and the total interface energy decreases. So, the post-treated samples are in more stable states.

In this work, the grain grows up uniformly from 15.62 ± 5.53 μm to 23.16 ± 9.28 μm, 24.63 ± 9.70 μm, and 32.42 ± 11.20 μm after 10 minutes, 30 minutes, and 2 hours of heating, respectively. However, the grain size does not change significantly when the treatment time is extended to 8 hours. It is a common phenomenon. At a specific temperature, the grain size will have a limited value. In other words, when the grain grows to a limited size, the growth basically stops. The average grain size at this time is called the limit average grain size. It is because the driving force of regular grain growth is the release of total interfacial energy. In terms of the whole system, the process of grain growth is from energy instability to stability. When the system reaches a stable state, the grain boundary has no driving force to move. Therefore, the typical grain growth stops. The grain will continue to grow uniformly after increasing the temperature, or when the sufficient energy is accumulated after a long time period.

It is worth noting that further growth and grain coarsening growth are observed in R200-H24 after most of the grains grow to the limited average grain size. When the heating period is extended to 24 hours, the grain size increases significantly. Also, the grain size difference becomes extremely large. The main reason is the formation of surface thermal grooves, which have a binding force on the movement of grain boundaries. This phenomenon is common for rolled metal sheets [41-44]. Surface thermal grooves are formed at the intersection of the grain

boundary and surface, which tends to be thermodynamically stable, to reach the tension balance after long-time treatment. The thinner the metal sheet is, the greater the binding force of the surface thermal groove is. In this work, the sample height of this experiment was rolled from 8 mm to 1 mm. It can be seen from **Figure 3.3** that the deformation of the sample is significant. When the thin metal sheet is heated at 400 ℃ for a long time, like 24 hours, most of the grain boundaries of normal growing grains are pinned by the grooves, and only a few grains can grow preferentially. After a long period of energy accumulation, they can grow into very coarse grains. The final grain size becomes more and more uneven and highly heterogeneous.

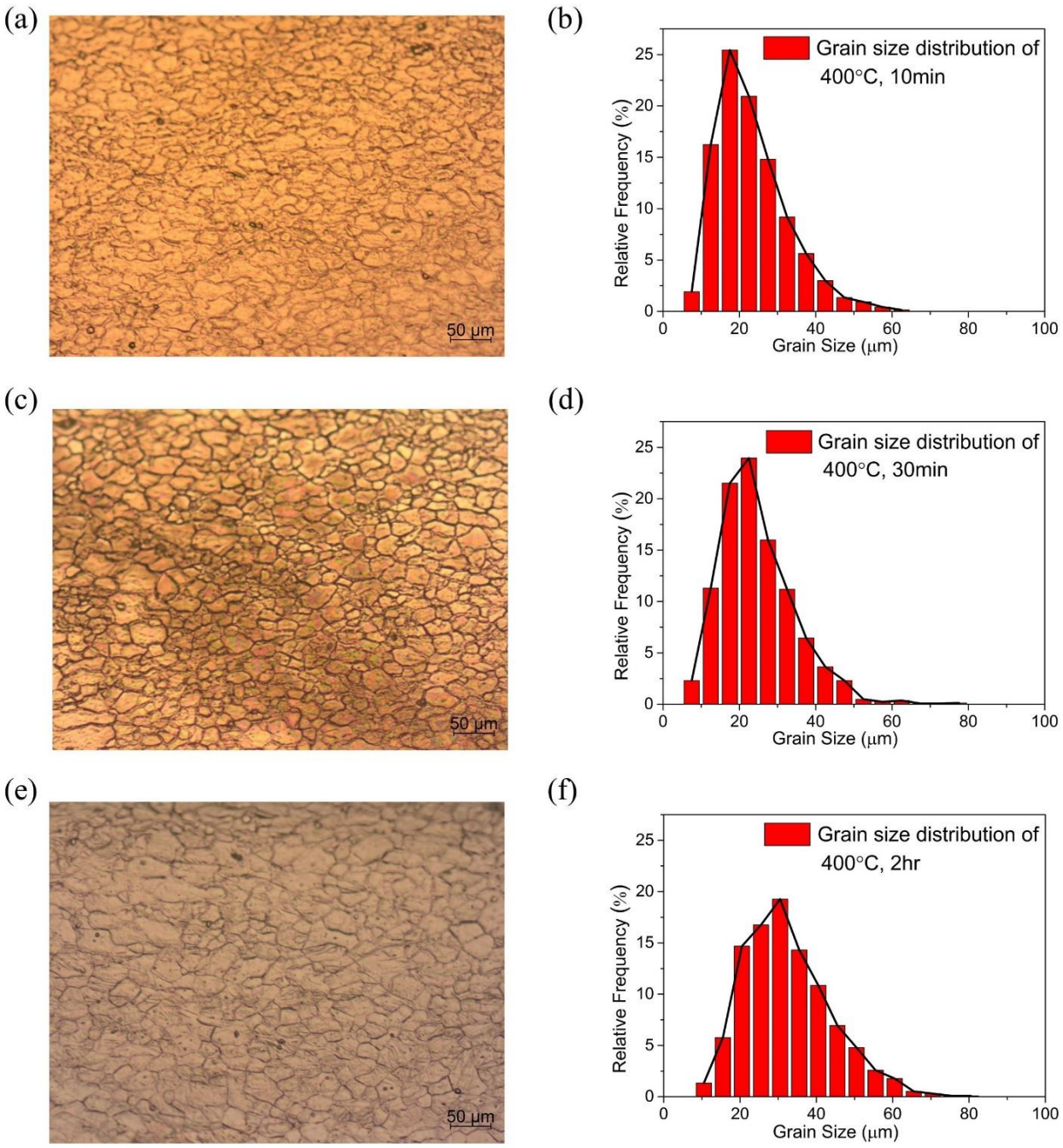

Figure 4.2: (a) Rolled Mg with 10min heat treatment microstructure and (b) grain size distribution graph; (c) Rolled Mg with 30min heat treatment microstructure and (d) grain size distribution graph; (e) Rolled Mg with 2hr heat treatment microstructure and (f) grain size distribution graph.

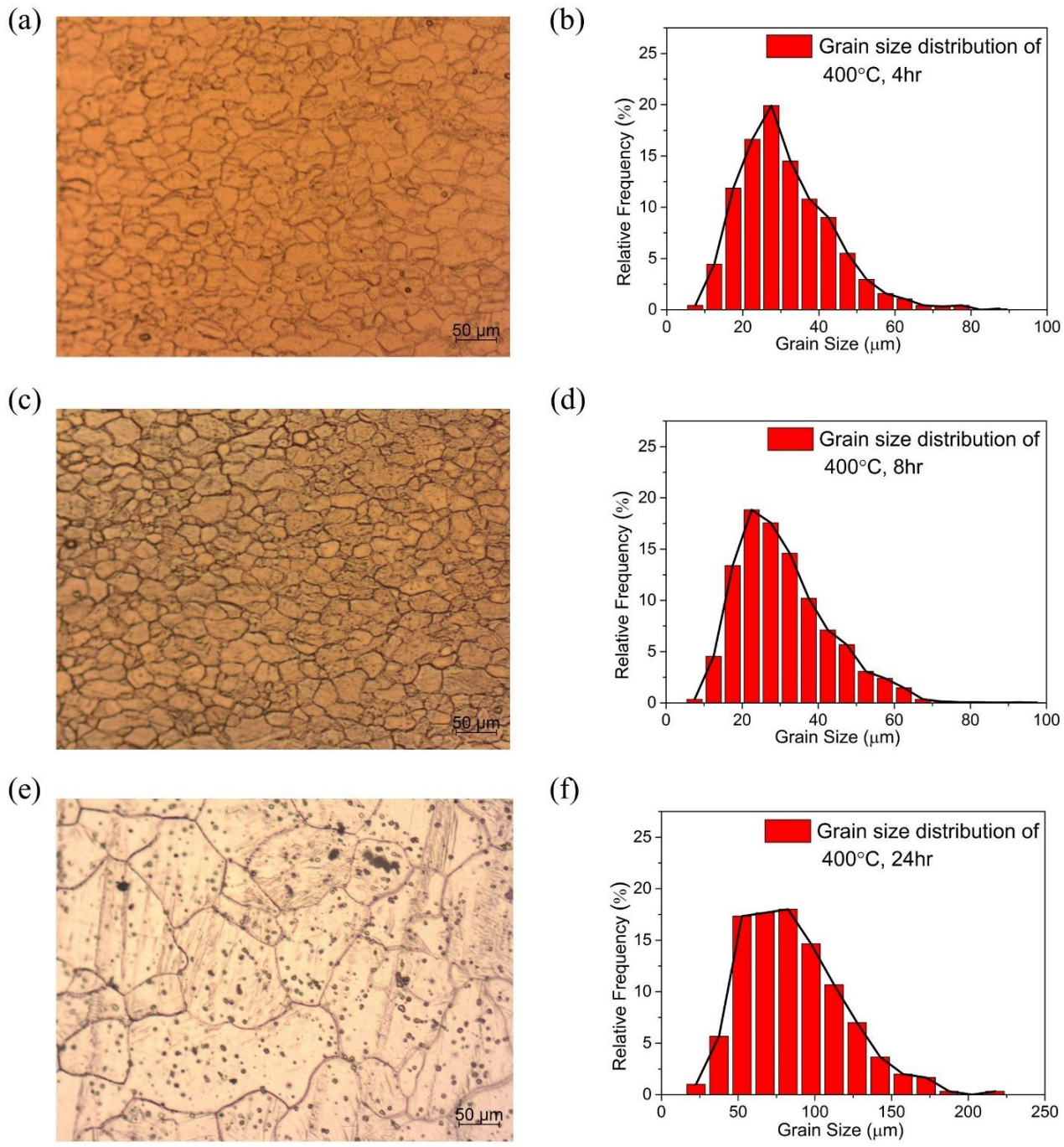

Figure 4.3: (a) Rolled Mg with 4hr heat treatment microstructure and (b) grain size distribution graph; (c) Rolled Mg with 8hr heat treatment microstructure and (d) grain size distribution graph; (e) Rolled Mg with 24hr heat treatment microstructure and (f) grain size distribution graph.

4.3.2 Mechanical Properties of Post-treated Mg

In this work, the hardness of various samples is also very close. It is easy to understand because the hardness of the metal is mainly decided by the strength of the metallic bond. So, the stronger the metal bond, the greater the hardness. Therefore, for pure metal, the variation range of metal hardness after machining is not wide. In general, after heating for 10 minutes to 8 hours, the hardness decreases slightly with the increase of heating time. In the heating process, as the grain grows, the grain boundaries and dislocations become less. Moreover, the work hardening in the rolling process and the residual stress after rolling are eliminated, so the metal is a little bit softened. After a long 24-hour treatment, the hardness rebounds but does not exceed that of the unheated sample. The inner reason is the microstructure in which the grain size is large with a very poor grain uniformity. It means that large grains and small grains exist at the same time. There are many small grains around large grains. These small grains play a great role in improving hardness. They locally increase the grain boundary and dislocation density which can disperse external forces. Therefore, R200-H24hr has a higher Vickers hardness value.

Figure 4.4 shows the stress-strain tensile curves of different samples, and the data are shown in **Table 4.3**. In the early stage of deformation, the stress-strain curves rose rapidly. With further tension, the stress-strain curves tended to be flat. Compared with post-treatment Mg, the rolled Mg R200 has the highest yield strength value and tensile strength value. Because the fine grain strengthening of metallic materials at room temperature has become a recognized fact, as mentioned before in **Section 4.2.2**. The rolled Mg R200 with heat treatment for 10 minutes, 30 minutes, 2 hours, 4 hours, and 8 hours had very similar results in the mechanical property test. The curve shapes of these samples are almost overlapped. It can be found by comparing with the

R200 that their yield and tensile strength decrease, and the strain at fracture increases after heating. The yield and tensile strength are generally combined with the Hall-Petch relation. The strength of pure Mg could be analyzed from the grain size view. So, in a word, the growth of Mg crystal leads to decreasing strength.

Table 4.3: Grain sizes and mechanical test results of different post-treated Mg samples.

Material	Grain size (μm)	Hardness (HV)	Yield strength (MPa)	Tensile strength (MPa)	Strain at fracture (%)
R200-H10min	23.16±9.28	35.03±3.44	83	177	10.3
R200-H30min	24.63±9.70	33.18±2.86	76	171	10
R200-H2hr	32.42±11.20	33.55±3.21	87	177	10.5
R200-H4hr	31.22±11.88	33.2±3.02	81	180	8.5
R200-H8hr	30.32±11.60	31.96±1.91	83	181	13
R200-H24hr	86.25±31.85	34.17±3.21	124	190	7

In the experimental testing, under the action of stress, dislocation must overcome the barriers of the grain boundary and the resistance of dislocation so that the deformation can be transferred to another grain. When the grain size increases, the number of grain boundaries and dislocations decreases. The transfer of dislocations becomes less. Moreover, internal stress concentration from the dislocation interaction and grain boundary blocking is weakened. In the process,

cracking is not easy to form. This is why after 8 hours heated, strain at the fracture of R200-H8hr is increased to a max value of 13%.

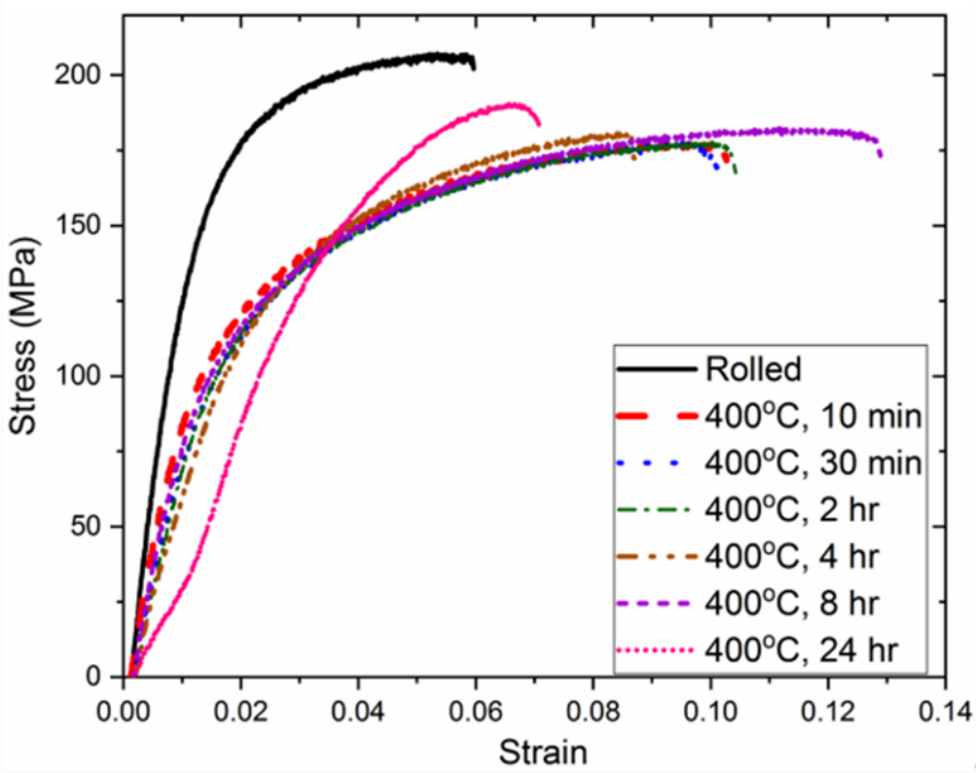

Figure 4.4: Tensile stress-strain curves of R200 series pure Mg samples.

In this study, it is worth noting that the strain-stress graphic of R200-H24hr shows the unique little bit S-shape because of the non-uniform microstructure. Even if rolled Mg grows up coarse markedly after 24 hours of heat treatment, its yield strength value and tensile strength value are outstanding and higher than those of other heat-treated samples. But its strain at the fracture drops to about 7%. At the beginning of the strain-stress curve, the dislocations move easily in the small grains. So, with the increase of strain, the stress increases slowly. Then, with the increase of strain deformation, the stress increases sharply because of the existence of coarse grains. Non-uniform grain size brings internal stresses and elastic stored energy within the Mg sheets in the test process. As a result, the resistance of tensile is as good as other post-treated Mg. The coarse

grains seem to determine the fracture result. Because the grain size distribution is very uneven, the place where the grain size of grain boundary density drops sharply is the place where the material is easily fractured and fails.

4.4 Conclusions

1. In this work, the pure Mg samples with different grain sizes are obtained by the same routine and at different temperatures. Compared to R200, R100 has the smaller and the most uniform grain with a size of 6.63 ± 2.69 μm.
2. The final grain size depends on the rolling temperatures. Because with an increase in rolling temperature, more energy is provided simultaneously for the atom and grain boundary diffusion to achieve dynamic recovery. Therefore, the sample rolled at lower temperature exhibits finer and equiaxed grains.
3. Under the same deformation routine, the Vickers hardness and strain at fracture decrease as the increasing deformation temperature. The smaller the grain size, the greater the number of grain boundaries, and the more grains around each grain are. So, more energy from the external force can be absorbed and dispersed in the fracture process. As a result, the crack is not easy to initiate in refined grain due to the lower stress concentration, and it is more unfavorable to crack propagation.
4. The rolled Mg samples R100 and R200 have relatively high strength due to the fine grain strengthening and dislocation strengthening mechanisms. Because the finer the grain is, the more the grain boundaries and the more obstacles are produced in the original large grains. In the present research, the yield and tensile strength of R200 are higher than those of R100. The inverse Hall-Petch phenomenon has been found at a decreased rolling

temperature of 100 ℃, which leads to the refined grain size within the scope of 3.94-9.32 μm. The reason for inverse Hall-Petch effects is that the small grain size is conducive to grain rotation and leads to reduce the yield strength. Moreover, when the grain size is close to the size of structural defects, structural defects and dislocation stacking effect contribution to strength will be significantly reduced.

5. R200 sample is heated under 400 ℃ for 10 minutes, 30 minutes, 2 hours, 4 hours, 8 hours, and 24 hours in the study. The crystalline growth is rapid initially, up to 120 minutes, after which it turns to slow down after a longer annealing period extended to 8 hours. Heating provides energy for normal grain growth at the beginning. When the system reaches a stable state with a limited average grain size, the grain size grows up slowly and even changes slightly. The grain coarsening and abnormal growth are observed after 24 hours of treatment due to the existence of surface thermal grooves which can pin most of the grain boundaries. After a long period of energy accumulation, several grains can grow preferentially into uneven and coarse grains.
6. The hardness of the pure metal is mainly related to the strength of the metallic bond. So, in this work, the hardness of Mg obtained under different conditions is very close. The work hardening in the rolling process and the residual stress are eliminated by heat treatment. Therefore, after 400 ℃ heating for 10 minutes to 8 hours, R200 is softened slightly with the increase in grain size. After a long 24-hour treatment, the hardness rebounds to a high Vicker hardness value because of the very poor grain size uniformity. The tiny grains that can disperse external forces play a significant role in improving hardness.
7. It can be found by comparing the rolled samples that the yield and tensile strength

decrease, and the strain at fracture increases after heating. It is generally consistent with the Hall-Petch relation, which is analyzed from the grain size point of view. Under the action of stress, the transfer of deformation becomes more challenging because the number of grain boundaries and dislocations decreases in the larger grains. So, the rolled Mg has the best resistance to strain. Moreover, strain at the fracture of R200-H8hr is improved to a max value of 13%. Because it is in a stable state after an 8-hour heating, internal stress concentration from the dislocation interaction and grain boundary blocking is weakened. In the process, cracking is not easy to form.

8. The strain-stress curve of R200-H24hr shows the unique little bit S-shape due to the non-uniform microstructure. At the beginning of increasing strain, the stress increases slowly because of the easy dislocation move in the small grains. Later, the existence of coarse grains leads to the stress sharply increment. The place where the grain size of grain boundary density drops sharply is the place where the material is easily fractured and fails. As a result, R200-H24hr has high yield strength, high tensile strength, and low strain at the fracture.

4.5 References

1. Mordike, B.; Ebert, T., Magnesium: Properties—applications—potential. Materials Science and Engineering: A **2001,** 302 (1), 37-45.

2. Lupescu, S.; Istrate, B.; Munteanu, C.; Minciuna, M. G.; Focsaneanu, S.; Earar, K., Characterization of some master Mg-X System (Ca, Mn, Zr, Y) alloys used in medical applications. Rev. Chim **2017,** 68 (6), 1408-1413.

3. Witte, F.; Kaese, V.; Haferkamp, H.; Switzer, E.; Meyer-Lindenberg, A.; Wirth, C.; Windhagen, H., In vivo corrosion of four magnesium alloys and the associated bone response. Biomaterials **2005,** 26 (17), 3557-3563.

4. Prakasam, M.; Locs, J.; Salma-Ancane, K.; Loca, D.; Largeteau, A.; Berzina-Cimdina, L., Biodegradable materials and metallic implants—a review. Journal of functional biomaterials **2017,** 8 (4), 44.

5. Shuai, C.; Li, S.; Peng, S.; Feng, P.; Lai, Y.; Gao, C., Biodegradable metallic bone implants. Materials Chemistry Frontiers **2019,** 3 (4), 544-562.

6. Chandra, G.; Pandey, A., Biodegradable bone implants in orthopedic applications: a review. Biocybernetics and Biomedical Engineering **2020,** 40 (2), 596-610.

7. Meyer Jr, R. A.; Desai, B. R.; Heiner, D. E.; Fiechtl, J.; Porter, S.; Meyer, M. H., Young, adult, and old rats have similar changes in mRNA expression of many skeletal genes after fracture despite delayed healing with age. Journal of orthopaedic research **2006,** 24 (10), 1933-1944.

8. Watson, N.; Haines, T.; Tran, P.; Keating, J. L., A comparison of the effect of one, three, or six weeks of immobilization on function and pain after open reduction and internal fixation of distal radial fractures in adults: a randomized controlled trial. JBJS **2018,** 100 (13), 1118-1125.

9. Makuch, A. M.; Skalski, K. R., Human cancellous bone mechanical properties and penetrator geometry in nanoindentation tests. Acta of Bioengineering and Biomechanics **2018,** 20 (3).

10. Yazdimamaghani, M.; Razavi, M.; Vashaee, D.; Tayebi, L., Surface modification of biodegradable porous Mg bone scaffold using polycaprolactone/bioactive glass composite. Materials Science and Engineering: C **2015,** 49, 436-444.

11. Rashad, M.; Pan, F.; Tang, A.; Asif, M.; Hussain, S.; Gou, J.; Mao, J., Improved strength and ductility of magnesium with addition of aluminum and graphene nanoplatelets (Al+ GNPs) using semi powder metallurgy method. Journal of Industrial and engineering chemistry **2015,** 23, 243-250.

12. Song, M.-S.; Zeng, R.-C.; Ding, Y.-F.; Li, R. W.; Easton, M.; Cole, I.; Birbilis, N.; Chen, X.-B., Recent advances in biodegradation controls over Mg alloys for bone fracture management: A review. Journal of materials science & technology **2019,** 35 (4), 535-544.

13. Bommala, V. K.; Krishna, M. G.; Rao, C. T., Magnesium matrix composites for biomedical applications: A review. Journal of Magnesium and Alloys **2019,** 7 (1), 72-79.

14. Qu, H.; Fu, H.; Han, Z.; Sun, Y., Biomaterials for bone tissue engineering scaffolds: A review. RSC advances **2019,** 9 (45), 26252-26262.

15. Koike, J.; Ohyama, R.; Kobayashi, T.; Suzuki, M.; Maruyama, K., Grain-boundary sliding in AZ31 magnesium alloys at room temperature to 523 K. Materials Transactions **2003,** 44 (4), 445-451.

16. Koike, J., Enhanced deformation mechanisms by anisotropic plasticity in polycrystalline Mg alloys at room temperature. Metallurgical and Materials Transactions A **2005,** 36 (7), 1689-1696.

17. Zhang, X.; Wang, H.; Scattergood, R.; Narayan, J.; Koch, C.; Sergueeva, A.; Mukherjee, A., Tensile elongation (110%) observed in ultrafine-grained Zn at room temperature. Applied physics letters **2002,** 81 (5), 823-825.

18. Matsunaga, T.; Kameyama, T.; Ueda, S.; Sato, E., Grain boundary sliding during ambient-temperature creep in hexagonal close-packed metals. Philosophical Magazine **2010,** 90 (30), 4041-4054.

19. Radha, R.; Sreekanth, D., Insight of magnesium alloys and composites for orthopedic implant applications–a review. Journal of magnesium and alloys **2017,** 5 (3), 286-312.

20. Ambat, R.; Aung, N. N.; Zhou, W., Evaluation of microstructural effects on corrosion behaviour of AZ91D magnesium alloy. Corrosion science **2000,** 42 (8), 1433-1455.

21. Birbilis, N.; Ralston, K.; Virtanen, S.; Fraser, H.; Davies, C., Grain character influences on corrosion of ECAPed pure magnesium. Corrosion Engineering, Science and Technology **2010,** 45 (3), 224-230.

22. Kubota, K.; Mabuchi, M.; Higashi, K., Review processing and mechanical properties of fine-grained magnesium alloys. Journal of Materials Science **1999,** 34 (10), 2255-2262.

23. Eivani, A.; Mehdizade, M.; Chabok, S.; Zhou, J., Applying multi-pass friction stir processing to refine the microstructure and enhance the strength, ductility and corrosion resistance of WE43 magnesium alloy. Journal of Materials Research and Technology **2021,** 12, 1946-1957.

24. Hosaka, T.; Yoshihara, S.; Amanina, I.; MacDonald, B. J., Influence of grain refinement and residual stress on corrosion behavior of AZ31 magnesium alloy processed by ECAP in RPMI-1640 medium. Procedia engineering **2017,** 184, 432-441.

25. Chang, T.-C.; Wang, J.-Y.; Chu, C.-L.; Lee, S., Mechanical properties and microstructures of various Mg–Li alloys. Materials Letters **2006,** 60 (27), 3272-3276.

26. Anne, G.; Ramesh, M.; Nayaka, H. S.; Arya, S. B.; Sahu, S., Microstructure Evolution and Mechanical and Corrosion Behavior of Accumulative Roll Bonded Mg-2% Zn/Al-7075 Multilayered Composite. Journal of Materials Engineering and Performance **2017,** 26 (4), 1726-1734.

27. Chai, S.; Zhang, D.; Pan, F.; Dong, J.; Guo, F.; Dong, Y., Influence of post-weld hot rolling on the microstructure and mechanical properties of AZ31 magnesium alloy sheet. Materials Science and Engineering: A **2013,** 588, 208-213.

28. Chen, Y.; Wang, Q.; Peng, J.; Zhai, C.; Ding, W., Effects of extrusion ratio on the microstructure and mechanical properties of AZ31 Mg alloy. Journal of materials processing technology **2007,** 182 (1-3), 281-285.

29. Armstrong, R. W.; Li, Q., Dislocation mechanics of high-rate deformations. Metallurgical and Materials Transactions A **2015,** 46 (10), 4438-4453.

30. Somekawa, H.; Mukai, T., Hall–Petch breakdown in fine-grained pure magnesium at low strain rates. Metallurgical and Materials Transactions A **2015,** 46 (2), 894-902.

31. Yu, H.; Xin, Y.; Wang, M.; Liu, Q., Hall-Petch relationship in Mg alloys: A review. Journal of Materials Science & Technology **2018,** 34 (2), 248-256.

32. Figueiredo, R. B.; Pereira, P. H. R.; Langdon, T. G., Effect of Numbers of Turns of High-Pressure Torsion on the Development of Exceptional Ductility in Pure Magnesium. Advanced Engineering Materials **2020,** 22 (1), 1900565.

33. Carvalho, A. P.; Figueiredo, R. B., The Effect of Ultragrain Refinement on the Strength and Strain Rate Sensitivity of a ZK60 Magnesium Alloy. Advanced Engineering Materials **2021**, 2100846.

34. Choi, H.; Kim, Y.; Shin, J.; Bae, D., Deformation behavior of magnesium in the grain size spectrum from nano-to micrometer. Materials Science and Engineering: A **2010,** 527 (6), 1565-1570.

35. Zheng, R.; Du, J.-P.; Gao, S.; Somekawa, H.; Ogata, S.; Tsuji, N., Transition of dominant deformation mode in bulk polycrystalline pure Mg by ultra-grain refinement down to sub-micrometer. Acta Materialia **2020,** 198, 35-46.

36. Li, Q.; Jiao, X., Recrystallization mechanism and activation energies of severely-deformed magnesium during annealing process. Materialia **2019,** 5, 100188.

37. Guo, L.; Fujita, F., Influence of rolling parameters on dynamically recrystallized microstructures in AZ31 magnesium alloy sheets. Journal of Magnesium and Alloys **2015,** 3 (2), 95-105.

38. Kaibyshev, R.; Sitdikov, O., Dynamic recrystallization of magnesium at ambient temperature. Zeitschrift fuer Metallkunde;(Germany). **1994,** 85 (10).

39. Lifei, W.; Yongqiao, L.; Hua, Z.; Zhengyong, Z.; Qingshan, Y.; Qiang, Z.; Hongxia, W.; Weili, C.; Shin, K. S.; Vedani, M., Achieving enhanced plasticity of magnesium alloys below recrystallization temperature through various texture control methods. **2020**.

40. Wang, L.; Li, Y.; Zhang, H.; Zhang, Z.; Yang, Q.; Zhang, Q.; Wang, H.; Cheng, W.; Shin, K. S.; Vedani, M., Achieving enhanced plasticity of magnesium alloys below recrystallization temperature through various texture control methods. Journal of Materials Research and Technology **2020,** 9 (6), 12604-12625.

41. Pei, R.; Korte-Kerzel, S.; Al-Samman, T., Normal and abnormal grain growth in magnesium: Experimental observations and simulations. Journal of Materials Science & Technology **2020,** 50, 257-270.

42. Abrivard, G.; Busso, E. P.; Forest, S.; Appolaire, B., Phase field modelling of grain boundary motion driven by curvature and stored energy gradients. Part I: theory and numerical implementation. Philosophical magazine **2012,** 92 (28-30), 3618-3642.

43. Abrivard, G.; Busso, E. P.; Forest, S.; Appolaire, B., Phase field modelling of grain boundary motion driven by curvature and stored energy gradients. Part II: application to recrystallisation. Philosophical magazine **2012,** 92 (28-30), 3643-3664.

44. Sunil, B. R.; Kumar, A. A.; Kumar, T. S.; Chakkingal, U., Role of biomineralization on the degradation of fine grained AZ31 magnesium alloy processed by groove pressing. Materials Science and Engineering: C **2013,** 33 (3), 1607-1615.

CHAPTER FIVE: CORROSION BEHAVIOR OF PURE MAGNESIUM WITH DIFFERENT GRAIN SIZES IN SIMULATED BODY FLUID

5.1 Introduction

Research about understanding the anti-corrosion of Mg is still a popular topic, with many articles published during the past several decades [1-2]. In the implant service, the serviceability of Mg-based dissoluble implants mainly depends on their dissolution behaviors in physiological environments. It is necessary to have some corrosion performance tests on materials. The effect of grain size on corrosion of Mg alloys became a field of intensive study and discussion because the contradictory conclusions are addressed in the recent studies [3-9]. Several research groups have concluded that changing the grain size by a reasonable mechanical deformation process is an alternative for better corrosion resistance performance of pure Mg and its alloy materials. They found smaller grain size was good for improving the corrosion resistance because of the grain boundary density increment. The average grain size of AZ31B Mg alloy increased from 60 to 250 μm by increasing the heat treatment temperature, which was performed for 3 hours. The corrosion rate in the 3.5% NaCl solution was found to be increased by 30% [9]. The typical function of crystalline size on the corrosion performance has also been investigated on as-rolled Mg alloy AZ31 sheets. The rolling process strongly introduced the grain boundaries and was attributed to the decrease in corrosion rate [7]. Some efforts have been put into pure Mg materials. Iranian scientists have reached some similar conclusions that the refined grains are probably the major cause explaining the higher polarization resistance of pure Mg wire obtained through the friction stir extrusion process [6]. In another paper, a conclusion was obtained according to the analysis of the electrochemical test results of pure Mg anode with different grain sizes. As the

extrusion temperature increases, the grain grew up also. At the same time, electrochemical activity increased, and resistance against charge transfer decreased [8]. All of the above findings are very much consonant with the higher resistance to an aggressive environment attributed to the grain refinement [5]. However, the opposite phenomenon was also observed in the very fine-grain pure Mg obtained by different processing histories. In some cases, increasing grain size can facilitate the anti-corrosion performance of Mg alloy. In 2009, a Chinese group discussed the dissolution behavior of pure ECAPed Mg through polarization and immersion tests. The influence of microstructure was also studied under optical and electron microscopy observation. They found that decreasing grain size weakens the ability of pure ECAPed Mg against NaCl aqueous medium corrosion [4]. Another research explored the electrochemical and immersion behavior of rolled Mg under different temperatures. Both the grain size and corrosion resistance improved with the increasing rolling temperature. In other words, the pure Mg sheet with the largest grain size showed the most excellent anti-corrosion properties [3]. Although it has been verified functionally in many references that the anti-corrosion property of Mg-based materials results in microstructural features [10-14], the grain size influence on corrosion rate and degree is not fully clear yet [15-17].

It is also worth noting that the corrosion resistance of biomaterials that need long-term service is a variable. Electrochemical tests are usually accomplished after the specimen is in the medium bath [10, 12, 18]. The test result mainly represents the thermodynamic stability and corrosive possibility of metal materials [18]. According to the application situation, the electrochemical test is not effective in providing information about long-term performance. It is more meaningful to study the actual corrosion rate and mechanism of Mg in practical work by immersion test.

In this chapter, both polarization technique and 30-day soaking experimental are conducted on pure Mg sheets with different rolling and post-treatment conditions. The relation between the grain size and degradation behavior will also be discussed, which is helpful for further clarifying the anti-corrosion behavior and mechanism of pure Mg. Furthermore, these results can also offer helpful comprehension of the models of suitable and favorable pure Mg sheets with a degradation rate. It has guiding significance for future application as a promising bioavailable material of bone substitute.

5.2 Electrochemical Corrosion Analysis of Bare Mg

The electrochemical technology of Tafel extrapolation is extensively applied to bring considerable information about the corrosion behavior of Mg. It is a quick, easy, and instantaneous technique that offers a potential calculation of the corrosion rate at a specific moment. All the electrochemical measurements were carried out in SBF at 37 °C in this work.

In the polarization curve, the cathodic branch of the curve represents the hydrogen generation on the electrode surface. And the anode branch of the curve mainly gives expression to the Mg corrosion. The corrosion potentials (E_{corr}) and corrosion current densities (i_{corr}) of bare Mg anodes can be calculated from the Tafel extrapolation technique. The voltage corresponding to the intersection of the two tangent lines of two half branches is the E_{corr}. For the calculation of i_{corr}, only the cathodic polarization branch is used. Because of the abnormal behavior during anodic dissolution, like the hydrogen evolution with the increase in the anodic polarization, the anodic branch was not considered. The obtained Tafel plots of the bare Mg samples in SBF and the electrochemical parameter calculated from the curves are shown in the following **Figure 5.1**

and **Table 5.1**. This information is especially helpful in comprehending the inner reason for the initial corrosion.

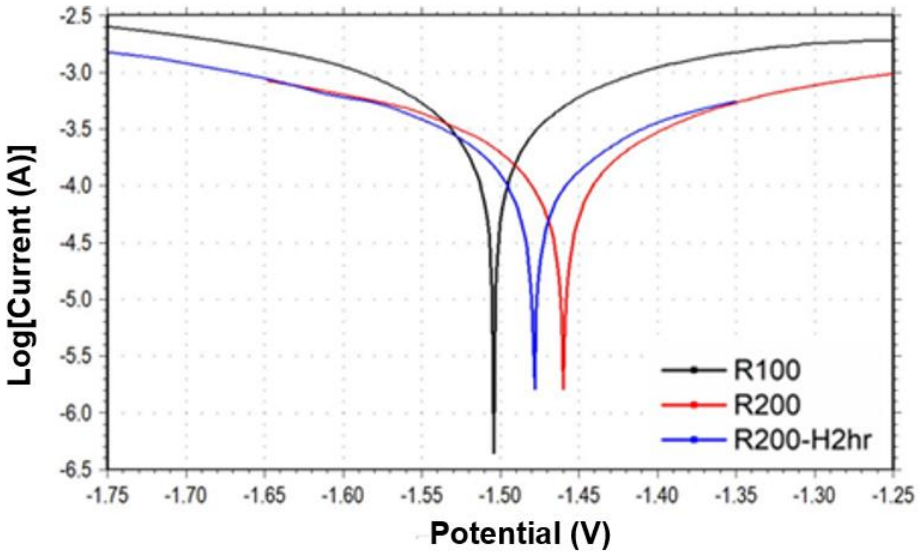

Figure 5.1: Polarization curves of the bare Mg samples in SBF solution at 37 °C.

The E_{corr} values of the bare Mg samples are all about -1.5 V in this work. The i_{corr} value could more precisely represent the reaction rate than that of E_{corr}. The corrosion potential (E_{corr}) is a thermodynamic data presenting the degradation trend [19]. The i_{corr} value significantly corresponds to the anodic corrosion kinetics. The lower value of i_{corr}, the lower the self-corrosion activation and tendency, and the better the anti-corrosion performance of the sample. Moreover, the i_{corr} derived from the polarization curves is the most important parameter to evaluate the corroded behavior. Because the i_{corr} (mA/cm^2) is quantitative correlated to the corresponding corrosion rate P_i (mm/year) according to the **Equation (5.1)** shown below [20]:

$$P_i = 22.85 \times i_{corr} \quad \textbf{(5.1)}$$

The greater the i_{corr} value, the faster the corresponding corrosion rate (P_i). Among these samples, R100 has the highest i_{corr} and poorest corrosion resistance R. The polarization resistance (R) of

pure Mg with various processing histories follows the sequence as R200 > R200-H2hr > R100. It is also the reverse order of the corresponding corrosion rate. Clearly, without other phases or purity, the intrinsic characteristic and detailed microstructure are the key roles in deciding the electrochemical performance of the pure Mg anode. Generally, the influence of rolling deformation and post-treatment on polarization resistance of Mg could be analyzed from three aspects: the grain size, the grain boundary and dislocation, and the induced residual stress.

Table 5.1: Electrochemical test results of various pure Mg series.

Material	**E_{corr} (V_{SCE})**	**i_{corr} (mA/cm^2)**	**R (Ω)**	**Maximum pH value**	**Immersion time to maximum (h)**
R100	-1.574±0.005	0.7818±0.0873	63±4	10.3	120
R200	-1.4685±0.010	0.2560±0.0227	181.5±10.5	10.567	40
R200-H2hr	-1.5.75±0.020	0.3414±0.0304	132±8	10.283	53

When the rolling temperature decreases from 200 °C to 100 °C, the corrosion resistance significantly drops from 181.5±10.5 Ω of R200 to 63±4 Ω of R100, with the average grain size refined from 15.62 ± 5.53 μm to 6.63 ± 2.69 μm. Besides, among these bare Mg samples, R100 has the highest i_{corr}. During the deformation processing, the improvement of temperature to 200 °C is significantly good for the anti-corrosion behavior of the pure Mg sheet. It is obtained from the polarization curve that the i_{corr} of R200 is about half of the i_{corr} of R100. The polarization resistance of R200 is about two times that of R100. Thereby, the electrochemical behavior of rolled Mg is strongly affected by the rolling temperature.

It is not hard to understand the reducing anti-corrosion performance of rolled pure Mg under lower temperatures. After the plastic machining of raw materials, the grain refinement produces a big grain boundary area and serious local lattice misorientation. The geometrically necessary dislocations are also formed in the deformed grains. It has been proved that these energetic grain boundaries and dislocations can act as crystallographic defects which are sensitive to aggressive environmental conditions [21]. The breakdown occurs primarily at these weak surface defects due to a large amount of stored energy and residual elastic stress. They can increase the chemical activity and make the metal easy to react with the surrounding medium [22]. Besides, these grain boundaries are weak and easy to be locally eroded. So, in the corrosive environment, it is more likely to trend to chemical dissolution. Decreasing the temperature offers more deformation and thus leads to more grain boundaries and dislocations, which restore more internal energy. Also, during the severe plastic deformation processing, there are more crystalline defects in the R100 pure Mg matrix. This is also supported by the high hardness value result obtained from the previous test. Meanwhile, high residual energy would diminish the corrosion resistance by crack generation. Thus, rolling at 100 °C is bad for the anodic dissolution of pure Mg in the electrochemical test. Meanwhile, these surface defects not only increase the reactivity of the surface but also provide more nucleation sites to rapidly form passive depositions. The Mg anode is soon covered by the discharge product, which is prone to slow down the anodic dissolution. This can explain why R100 has the lowest corrosion resistance, but it approaches the pH peak value using the longest time. And the reasonable high temperature leads to higher degradation resistance. Compared to the R100, the better resistance of R200 comes from the growth of grain size, a decrease in crystalline defects, and the release of residual stress. With the grain size growing up, the effect of grain boundary changes. The grain boundaries are physical obstacles

and effectively prevent the spread of pitting. It has been proposed that less energetic crystalline defects facilitate R200 surface stability and provide fewer nucleation sites to form a passive film. Meanwhile, R200 contains lower residual stress and can retard corrosion kinetics. Consequently, the dissolution rate of the rolled Mg and the formation of the initial protective film are slowed down. This also explains why R200 has the highest corrosion resistance and reaches the pH maximum value in the shortest period. In a word, when the crystalline size is super fine from the plastic deformation, as the crystalline size of R100, the adverse function of the grain boundary in anti-corrosion is obvious.

While in the case of R200 and R200-H2hr, post-heat does not appear to make an apparent function on their electrochemical corrosion. Because R200 and R200-H2hr specimens have close corrosion current densities values i_{corr} according to the Tafel extrapolation results. Due to the coarse-grained microstructure and less stored internal energy, which play the opposite roles, there is slightly weaker corrosion resistance in the R200-H2hr sample after heating compared to the R200 sample. In R200-H2hr coarse grains, the softening effect from the heating reduces the activation of the sample surface. The grain boundaries play a physical barrier role in resisting corrosion [12, 23]. But there are not plenty of grain boundaries to control the Mg plate dissolution. The negative effect of grain boundary reduction is greater. Therefore, heating for 2 hours slightly results in corrosion resistance reduction.

In summary, among these three kinds of pure Mg samples, R200 has the best anti-corrosion behavior in the electrochemical polarization test. And R100 is the poorest sample.

5.3 Immersion Test of Bare Mg

A continuing soak experiment is a more straightforward and explanatory way to perceive the dissolving process of these pure Mg species. The following immersion experiment is applied to the pure Mg samples to verify the long-term performance and estimate the corrosion mechanism. The soaking experiment, which can give reliable values in the late stage, is a helpful and common method. The post-degradation micrographs are obtained by SEM to understand more details about the degradation behavior of samples in SBF solution. Corroded sample surface wettability is also performed by the water contact angle. X-ray and EDS pattern of the corrosion products reveals their primary compositions. Based on the series of data and test results, the degradation mechanism is postulated as follows.

5.3.1 Macro-morphologies of Corroded Pure Mg Sheet

Before the soaking test, the as-polished Mg square sheet presented a silver metallic luster as shown in **Figure 5.6 (a)**. The morphologies of the bare Mg square sheet changed dramatically during the immersion test. After different immersion duration, to know the anti-corrosion performance, the samples were taken out from the solution, simply rinsed with distilled water, and cleaned with cold air. After suffering from 30-day soaking, R100, R200, and R200-H2hr samples can keep the basic shape, and the optical macro-morphologies of these bare pure Mg samples after immersion are generally the same. This process can also be reflected in **Figure 5.2** and **Figure 5.3**, represented by R100.

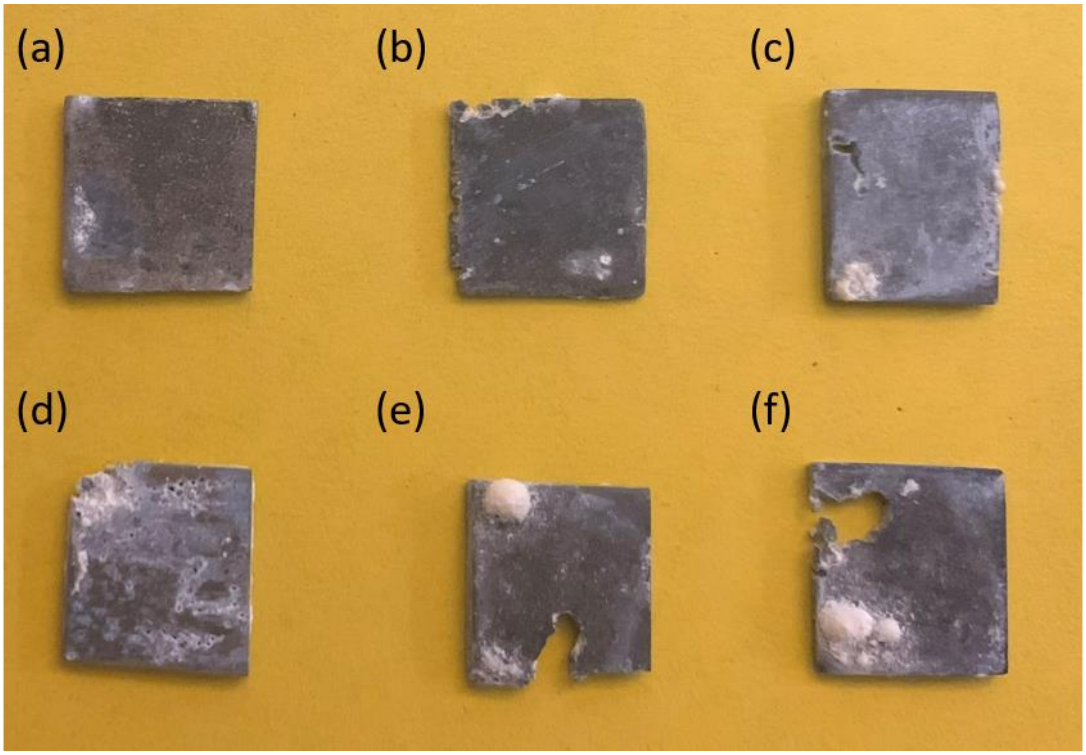

Figure 5.2: Macroscopic corrosion morphologies of R100 after (a) 2 days, (b) 4 days, (c) 7 days, (d) 14 days, (e) 21 days, and (f) 30 days immersion test.

In the beginning, the surface is not bright anymore, and there are some hydrogen bubbles visible to the naked eye. After two days, serious superficial uniform corrosion is found on the whole surface with some deposited areas in **Figure 5.2 (a)**. The scratches caused by the grinding process on the surface of the samples are still there in **Figure 5.3 (a)**. Because after rolling deformation, there will be some defects on the surface of the sample. The weaker the sites are, the greater the tendency to be corroded. Corrosion often starts in these positions. Next, many localized pitting holes appear on the sample surface. In the first 4-day immersion, the corrosion, which is not evenly distributed on the surface but first occurs locally, becomes more serious with several penetrating pits [24-26]. Due to the pitting corrosion being its most common corrosion type,

localized corrosion takes primary responsibility for the initial non-smooth macro-morphology [25-29]. Then, several localized and intense corrosion pits are seriously deep after a 7-day soak. Under the OM, the sample is also nearly fully covered by the compact corrosion product, and almost no fresh metallic areas are left on the surface in **Figure 5.3 (c)**.

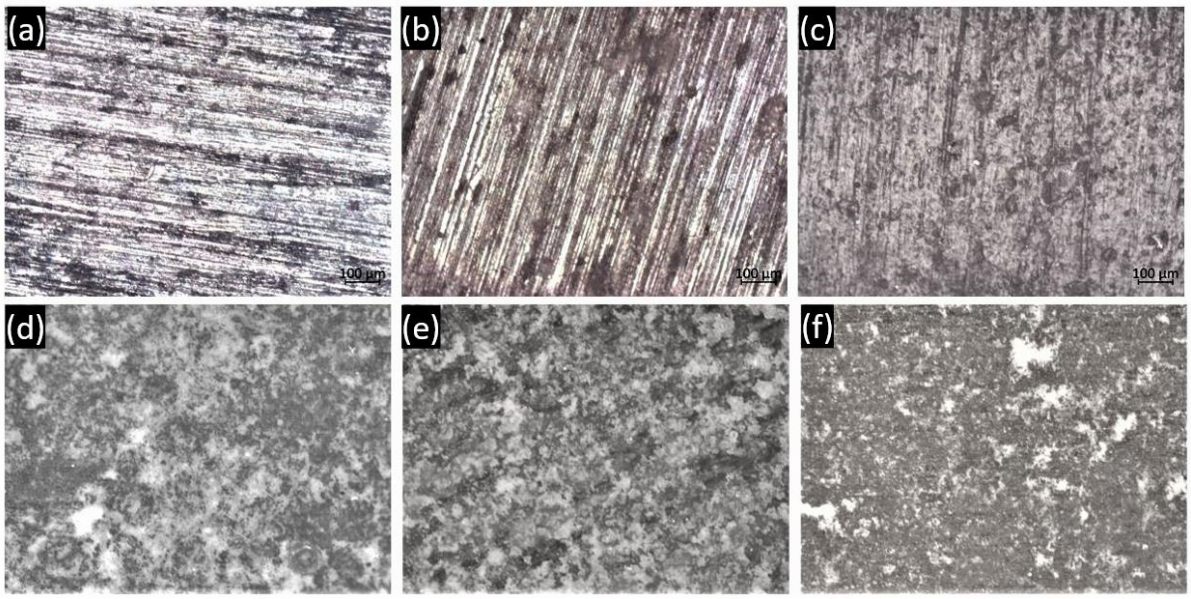

Figure 5.3: Optical micrographs of R100 after (a) 2 days, (b) 4 days, (c) 7 days, (d) 14 days, (e) 21 days, and (f) 30 days immersion test.

With the prolonged immersion period of 14, 21, and 30 days, Mg continues to be unevenly dissolved and pitted more and more seriously. In this way, these local pitting areas are getting larger and connected to each other. And then, the corrosion continues diffusing and spreading to the surroundings and leads to the bulk center part corrosion. While the Mg dissolution in SBF is carried out, white precipitate has been produced on the pure Mg surface. As the soaking bath period increases, more precipitate is left on the sample surface. As the macro figures show, the breakdown starts mainly from the sample edge and is more serious than the center part. And the

contact area between the edge of the sample and the corrosive environment is larger than that of the center surface, so the sample edge is easily eroded. Once the degradation starts, it will become a weak place, and the corrosion will continue to spread at this position. For the same reason, when sediments are deposited in several locations, these locations will become places where sediments continue to accumulate and grow up.

5.3.2 SBF Curves Analysis and Mechanism of Corrosion Process

SBF is a standard solution that contains the same inorganic salts composition and concentration as those of the human plasma [30]. It is essential to find out the corrosion mechanism of Mg to put forward appropriate methods to solve problems brought by rapid dissolution in the next step. In this study, after 30 days of immersion and pH monitoring record in static SBF at 37 °C, the pH value curve of bare Mg varies depending on the soaking period was obtained as shown in **Figure 5.4**.

The variations in pH during the corrosion test are applied to monitor the Mg dissolution rate for a period in vitro present and to assess the biocompatibility of potential biomaterials. Typically, Mg is very active and easy to dissolve [31]. Under corrosive aqueous conditions, the Mg electrochemical degradation reaction with water increases the pH value [27, 32]. The specific reaction equations are as follows [4, 31, 33-34]:

$$Mg = Mg^{2+} + 2e^{-} \text{ (anodic reaction)} \quad \textbf{(5.2)}$$

$$2H_2O + 2e^{-} = H_2\uparrow + 2OH^{-} \text{ (cathodic reaction)} \quad \textbf{(5.3)}$$

$$Mg^{2+} + 2OH^{-} = Mg(OH)_2 \quad \textbf{(5.4)}$$

$$Mg + 2H_2O = Mg(OH)_2 + H_2\uparrow \quad \textbf{(5.5)}$$

Above is the basic theory of pure Mg dissolution in the SBF. Because hydroxyl ion OH^- works as a significant part throughout the process, the solution pH value changes constantly. Therefore, the pH value is used to evaluate chemical stability. The change rate can also reflect the corrosion resistance and corrosion behavior. It should be noted that the actual degradation of bare Mg is very complex. It is closely associated with the corrosive medium, corrosion products, and the stability of corrosion medium and corrosion products [1, 35]. So, discussing the Mg corrosion mechanism and assessing its chemical stability and biocompatibility in long-term SBF immersion is essential.

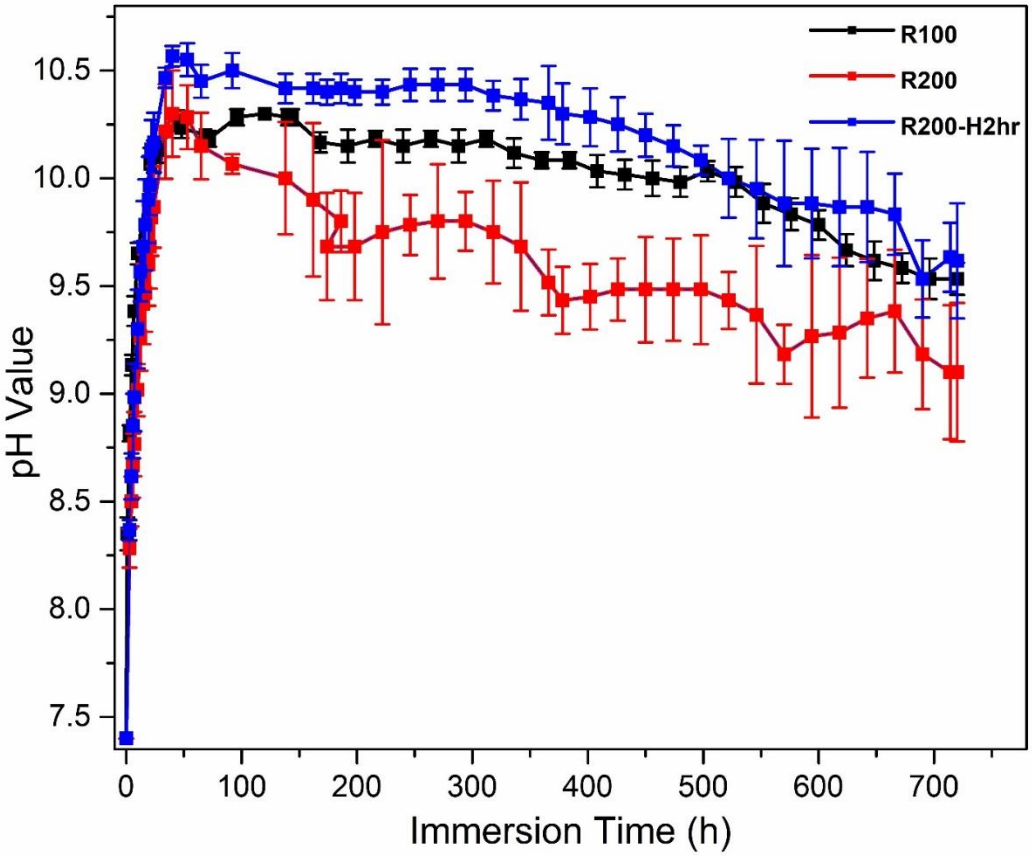

Figure 5.4: Immersion time-pH curves of the bare Mg samples in SBF solution at 37 °C.

On the time-pH value curves, these bare Mg samples obtained under different conditions exhibit a similar tendency and have approximately the same shape curves. It means that their anti-

corrosion behavior is almost the same in the static SBF immersion test. However, there are some differences in details. According to the pH-time curve trend, notably, the increase of pH value with the increasing immersion time is non-linear. The pH change in SBF is roughly analyzed in three stages. First, the pH value increases rapidly at the beginning. And then, the pH value continuously increases at a slow rate in the second stage. Finally, the pH value keeps fluctuating and even drops slightly.

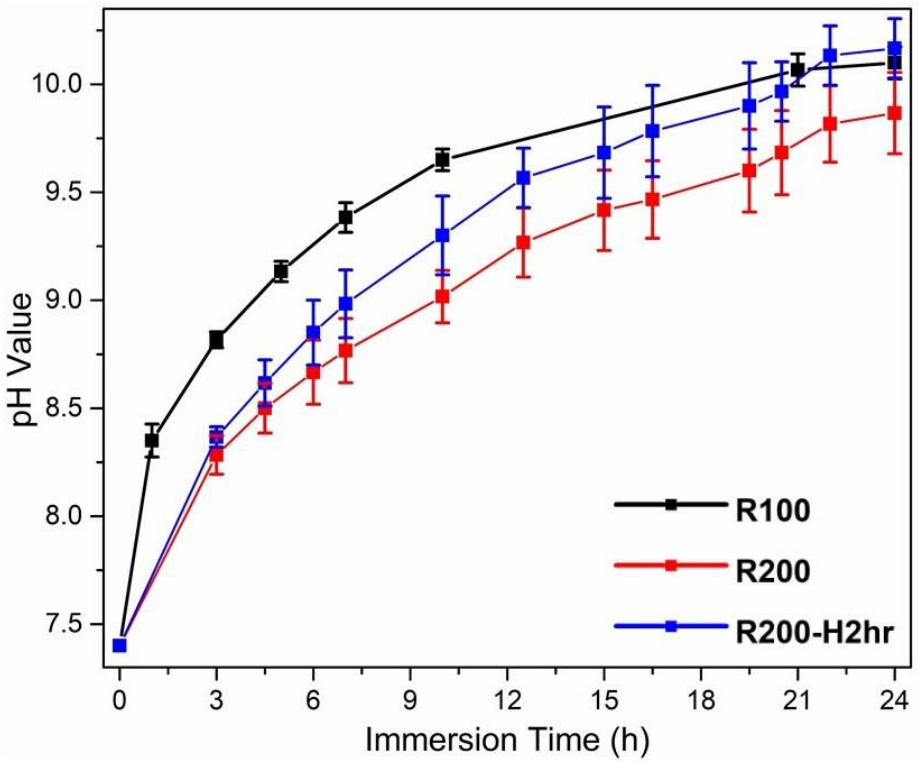

Figure 5.5: The first-24hr pH value of SBF solutions containing bare Mg samples.

In the first 24 hours, the pH value went up over 10, thanks to the rapid formation of lots of OH^- [36-37]. **Figure 5.5**, **Figure 5.6**, and **Table 5.2** show the changes in pH curve and R100 surface morphologies observed with SEM coupled with water contact angle in the first 24 hours of

immersion as the representative of bare Mg samples. It illustrates that the polished Mg sample suffered severe corrosion during the SBF incubation process at the preliminary stage.

Only 1 hour after the soaking, observed under the high magnification SEM, the pure Mg was heavily corroded. Owing to the strong alkalization near the Mg plate, the surrounding OH^- was connected to Mg^{2+}. So, some clusters of small and irregular $Mg(OH)_2$ were formed and deposited on the surface according to **Equation (5.4)**. In this process, Mg dissolution also generated H_2 gas, which is presented in **Equation (5.5)**. At the same time, pits and grooves were observed. They could also provide channels for H_2 gas release resulting in inner Mg exposure. It led to more and more severe corrosion. The water contact angle decreased from 87° to 69°. It means that decomposition reduced the surface smoothness of the sample, and the sample surface became uneven. With the continuous corrosion processed to 3 hours, the localized attack was more intense and inner than the 1-hour morphology. The irregular surface cracks with the wide degraded area and the cracked-earth appearance popped up in **Figure 5.6 (c)**. After 5 hours, the surface contact angle decreased slightly. The white $Mg(OH)_2$ resultant in flocculent morphology appeared. Moreover, it almost completely covered the substrate of bare Mg, as shown in **Figure 5.6 (d)**. This solid deposition can prevent the substrate from degradation [38-39]. From the perspective of thermodynamics, the stronger the alkalinity of the solution, the higher the stability of $Mg(OH)_2$, which served as a solid hinder on the surface of the specimen. However, these flocculent precipitates cannot form a stable, dense protective layer. Although the $Mg(OH)_2$ is protective and stable as the pH value is over 10 [31, 40], when the Cl^- concentration is over 30 mmol/L, chloride ions are still aggressive for the Mg [41]. In the SBF solution, Cl^- concentration is about 147.8 mmol/L [30]. The high concentration Cl^- with a small radius easily causes the solid

layer penetration. The transformation equation of the corrosion sediments undergoing breakdown in a chloride-containing solution is as follows [42-44].

$$Mg(OH)_2 + 2Cl^- = MgCl_2 + 2OH^- \quad \textbf{(5.6)}$$

When the immersion time to 9 hours, the sediments fell off, and there were still some cracks under them. It means that the corrosion of the inner pure Mg was furtherly severe. The corrosion products were dissolved at the same time. At this point, the contact angle on the sample surface decreased significantly to 46°. The angle degree of the sample was only about half of the initial value, indicating that the sample surface was becoming rougher and uneven. In **Figure 5.6 (f)** SEM morphology of the 24-hour immersed sample, a substrate with deep and wide mud cracks and an island-like structure appeared from almost the whole surface. In addition, the corrosion layer was non-uniform and thick but loose and blocky stacked. The destruction of the deposition layer was due to the Cl^- attack and H_2 release. The Mg further corrosion occurred in these exposure areas in the following stages.

Table 5.2: Water drop static contact angle test results of fresh R100 Mg sample and after different durations in first 24hr immersion.

Material	**R100 fresh Mg**	**After 1h**	**After 3h**	**After 5h**	**After 9h**	**After 24h**
Contact angle	87.3°	68.8°	64.5°	63.8°	46.4°	47.5°

According to these results, it can be concluded that bare Mg had severe and fast degradation in SBF solution at 37 ℃ in the first 24 hours. The degradation of pure Mg produced many hydroxyl ions, rapidly increasing pH value and a massive amount of corrosion products. These sediments

and cracks on the sample surface resulted in uneven morphologies and decreased water contact angles.

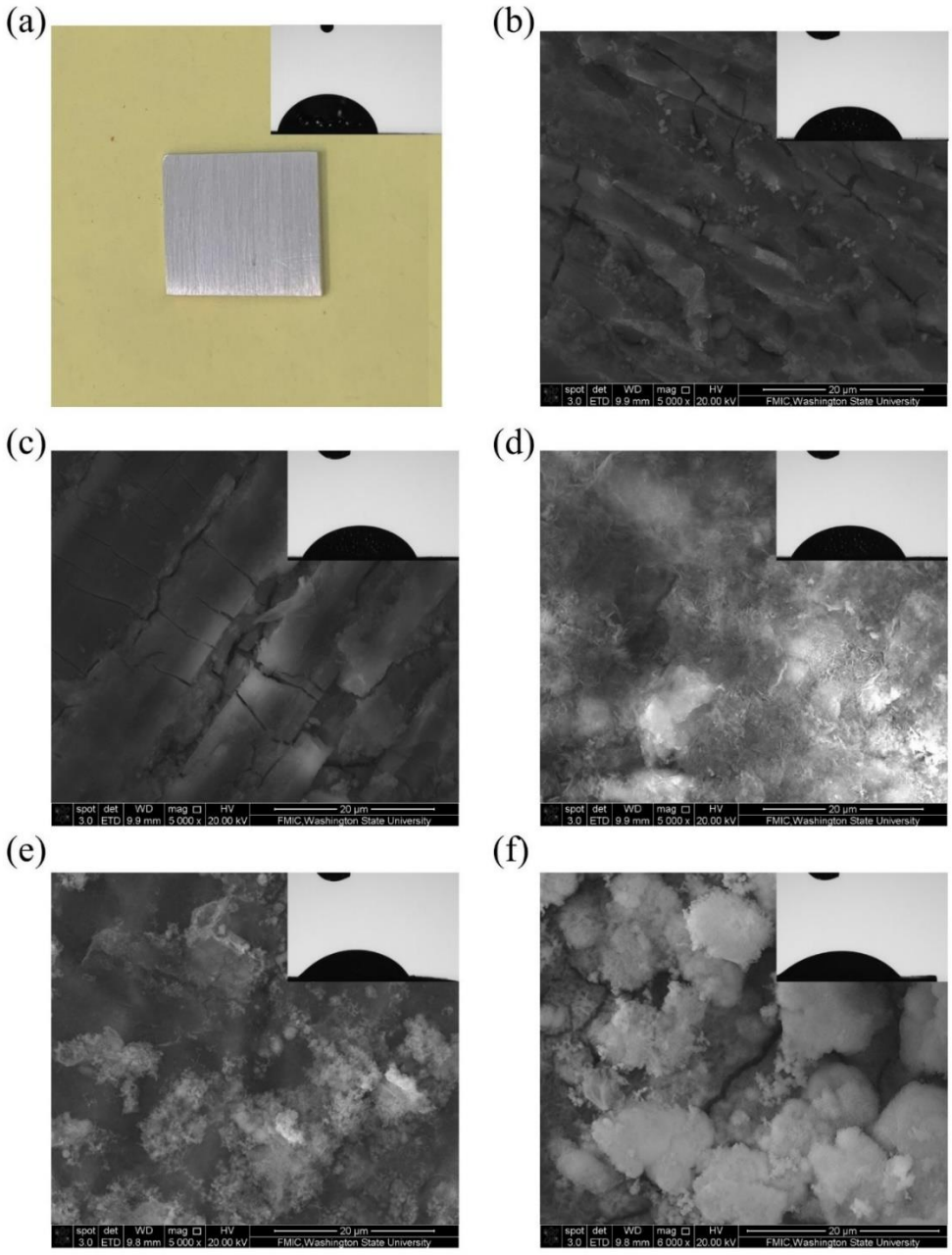

Figure 5.6: (a) R100 sample and its contact angle water drop; SEM image and contact angle water drop of R100 after (b) 1hr immersion, (c) 3hr immersion, (d) 5hr immersion, (e) 9hr immersion, and (f) 24hr immersion.

The second stage was from 24 hours to 140 hours. In this stage, the pH values of SBF containing different samples increased continuously. Then, the pH values reached the maximums one after another and stabilized near the peak values. R100 had the lowest polarization resistance in the electrochemical test, but it approached the pH peak value of 10.3 using the longest time, 120 hours. The reason is that grain boundaries and surface defects can increase the reactivity of the surface and provide more nucleation sites to form passive depositions. Consequently, R100 was fast eroded and covered by protective corrosion products, prone to slow down the long-time dissolution. It is worth noting that R200 had the best anti-corrosion resistance in the electrochemical test, but it was the first to reach the pH peak value. R200 pH value came up to about 10.283 after 40 hours. Subsequently, R200-H2hr arrived at the peak value, 10.567, after 53 hours. It is worth noting that R200 had the best anti-corrosion resistance in the electrochemical test, but it was the first to reach the pH peak value. R200 pH value came up to about 10.283 after 40 hours. Subsequently, R200-H2hr arrived at the peak value, 10.567, after 53 hours.

In this period, the rising speed of pH value slowed down due to the rapid generation of insoluble corrosion sediments on the Mg surface in the first stage. Because the deposition layer worked as an obstacle for Mg to be exposed to water and electrolytes, it slowed down the Mg substrate corrosion and the diffusion rate of OH^- from the sample to the medium. It finally reduced the pH increment of the surrounding environment. The deposited layer became thicker and thicker with the prolonged soaking time, and the surface without protection was less and less. Thus, the corrosion rate decreased after the initial rise in pH value, and then the pH curve tended to be flat. In the last stage of the 30-day immersion, the pH dropped in the form of fluctuation. After the long-term exposure, much attention should be paid to the deposition complexity due to many

other ions in SBF. The order of ions corrosivity for Mg soaked in SBF is Cl^-> SO_4^{2-}> HCO_3^-> $H_2PO_4^-$ [44]. Although SO_4^{2-} ions may convert $Mg(OH)_2$ into highly soluble $MgSO_4$, the corrosivity is limited since the concentration of SO_4^{2-} ion is low, about 0.5 mmol/L. Therefore, the pH value change is mainly due to the various reactions of the surface sediments, especially with the existence of HCO_3^- and HPO_4^{2-}. In the high pH value of the solution, first, the excess OH^- accelerates the destabilization of HCO_3^- and transformation into CO_3^{2-}. Besides negative ions, Ca^{2+} also has a great influence. Thus, $MgCO_3$ and $CaCO_3$ with low solubilities are formed. The relative reactions taking place are shown in the following **Equation (5.7)** and **Equation (5.8)**.

$$HCO_3^- + OH^- = CO_3^{2-} \quad \textbf{(5.7)}$$

$$Mg^{2+}\ (Ca^{2+}) + CO_3^{2-} = MgCO_3\ (CaCO_3) \quad \textbf{(5.8)}$$

Moreover, due to the relatively high local concentration of Mg^{2+} at the corrosion sites, these positive ions close to the sample surface linked to hydroxyl in SBF may be a barrier to calcium absorption. Thus, $MgCO_3$ is much easier to precipitate than $CaCO_3$.

Subsequently, owing to the Ca^{2+} and $H_2PO_4^-$, and the plenty of OH^- in the solution, different forms of ion clusters and some possible types of calcium phosphates would appear based on the following reactions[45 46-47]:

$$H_2PO_4^- + OH^- = HPO_4^{2-} + H_2O \quad \textbf{(5.9)}$$

$$HPO_4^{2-} + OH^- = PO_4^{3-} + H_2O \quad \textbf{(5.10)}$$

$$Ca^{2+} + HPO_4^{2-} + 2H_2O = CaHPO_4{\cdot}2H_2O\ (DCPD) \quad \textbf{(5.11)}$$

$$8Ca^{2+} + 2HPO_4^{2-} + 4PO_4^{3-} + 5H_2O = Ca_8(HPO_4)_2(PO_4)_4{\cdot}5H_2O\ (OCP) \quad \textbf{(5.12)}$$

$$3Ca^{2+} + 2PO_4^{3-} + 3H_2O = Ca_3(PO_4)_2 \cdot 3H_2O \text{ (ACP)} \quad \textbf{(5.13)}$$

$$3Ca^{2+} + 2PO_4^{3-} = Ca_3(PO_4)_2 \text{ (TCP)} \quad \textbf{(5.14)}$$

$$10Ca^{2+} + 6PO_4^{3-} + 2OH^- = Ca_{10}(PO_4)_6(OH)_2 \text{ (HA)} \quad \textbf{(5.15)}$$

Among these various phosphates, SBF cannot provide sufficient thermodynamic driving force for the $CaHPO_4 \cdot 2H_2O$ (DCPD) precipitation over the entire pH range [45]. Moreover, DCPD and $Ca_8(HPO_4)_2(PO_4)_4 \cdot 5H_2O$ (OCP) are not stable in alkaline conditions [48]. From the perspective of kinetics, it is conducive to the formation of amorphous calcium phosphate $Ca_3(PO_4)_2 \cdot 3H_2O$ (ACP) metastable phase and $Ca_{10}(PO_4)_6(OH)_2$ (HA) [49]. In addition, HA is the most thermodynamically stable material with a low solubility constant K_{sp} of 1.6×10^{-58} at pH 7.4, and the solubility decreases with the pH increase [50]. Furthermore, it is easy to nucleate and grow because of the supersaturation at alkaline pH conditions [51].

It should be noticed that Mg^{2+} can participate in and replace Ca^{2+} in the chemical reactions from **Equation (5.11)** to **Equation (5.15)**. Because the dissolution of the matrix brings a lot of Mg^{2+}, which has the same valence number of ions like Ca^{2+}, their electronegativity difference is just about 0.31 [52]. The solubility product constant K_{sp} for $Mg_3(PO_4)_2$ is only as low as 1.04×10^{-24} [44]. So, PO_4^{3-} can also bond with Mg^{2+} to form $Mg_3(PO_4)_2$ and the complicated compound solid solution of magnesium-substituted calcium phosphate $(Mg, Ca)_3(PO_4)_2$. The precipitation of complex Ca/Mg salts consumed lots of OH^-. It resulted in a decrease in pH value. Meanwhile, the dissolution of the inner Mg continued bringing more OH^-. Therefore, the curve had the fluctuating part because the reactions made the pH value increase and decrease coincided in this stage. The pH value did not change when there was a dynamic equilibrium between the

consumption and regrowth of OH^-. Consequently, after going up and reaching the peak value, the change of pH value presented a repeated fluctuation curve and decreased slowly within a small range.

The schematic illustration of these various corrosion products depositions by four steps is **Figure 5.9**. As previously stated, severe corrosion and intensive $Mg(OH)_2$ deposit start once the samples are soaked in SBF. $Mg(OH)_2$ precipitation on the surface forms the inner corrosion layer and offers many hydroxyl terminals. They are inducers and favorable sites for magnesium and calcium salts nucleation and deposition. These hydroxyl terminals can attract positively charged Ca^{2+}/Mg^{2+} in the SBF preferentially, followed by the negatively charged ions, mainly CO_3^{2-} and PO_4^{3-}. Finally, as the immersion time is prolonged, the insoluble sediments on the sample surface are two layers. The inner layer is mainly $Mg(OH)_2$. On the top of the $Mg(OH)_2$ layer, the outer layer is complex calcium/magnesium phosphates and calcium/magnesium carbonates because of the synergy of Ca^{2+}, Mg^{2+}, HCO_3^-, $H_2PO_4^-$, and OH^-. The inner layer is thick and massive. Meanwhile, the outer one is thin and stable.

In summary, at the final stage of the experiment, the decrease and stabilization of the pH value were mainly attributed to the production and the transformation of the massive amounts of $Mg(OH)_2$, MgO, and other Ca/Mg salts corrosion products. The compositions of these various corrosion depositions can be further analyzed according to the following analysis results of XRD and EDS.

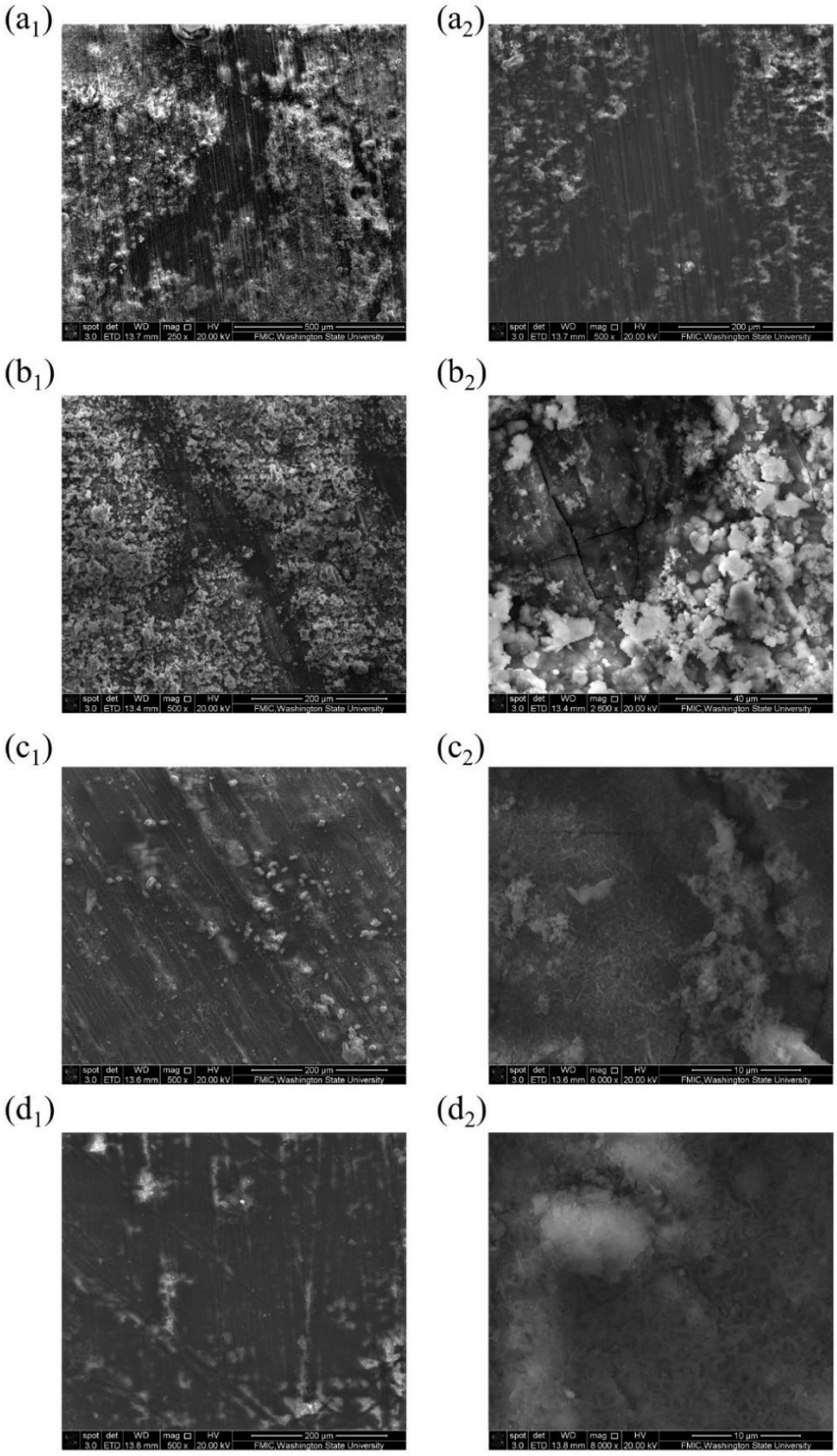

Figure 5.7: Surface morphology of R100 after different immersion time: (a_1 and a_2) 7 days; (b_1 and b_2) 14 days; (c_1 and c_2) 21 days; (d_1 and d_2) 30 days.

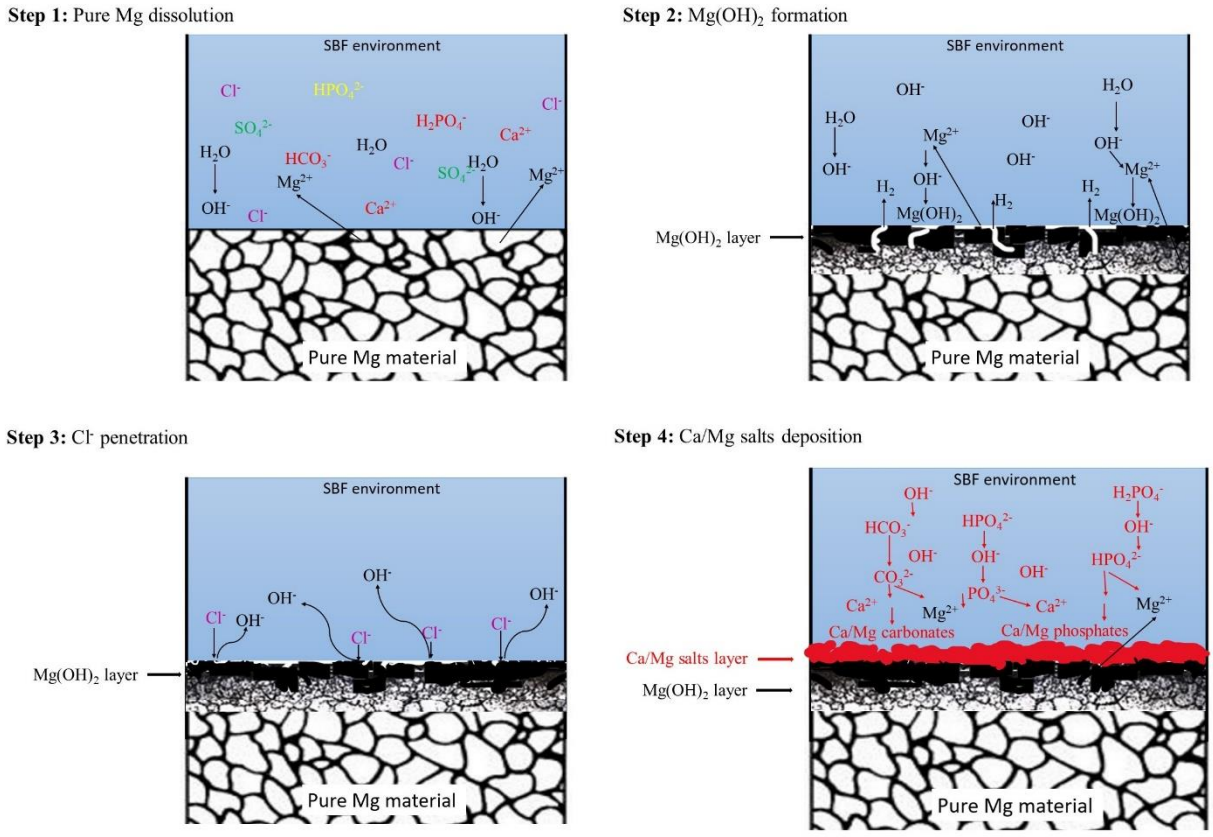

Figure 5.8: Schematic illustration of the formation of corrosion products on Mg.

5.3.3 Composition of Corrosion Products

The 30-day immersed samples were cleaned and dried before testing to analyze the corrosive products. Then, XRD and EDS techniques were used to probe the chemical compositions. In this X-ray pattern, the signal due to pure Mg has disappeared. It reveals that a large amount of Mg dissolves, and a lot of insoluble products also precipitate on the surface of the substrate after the long-term immersion. In addition, these precipitations almost completely cover the sample surface.

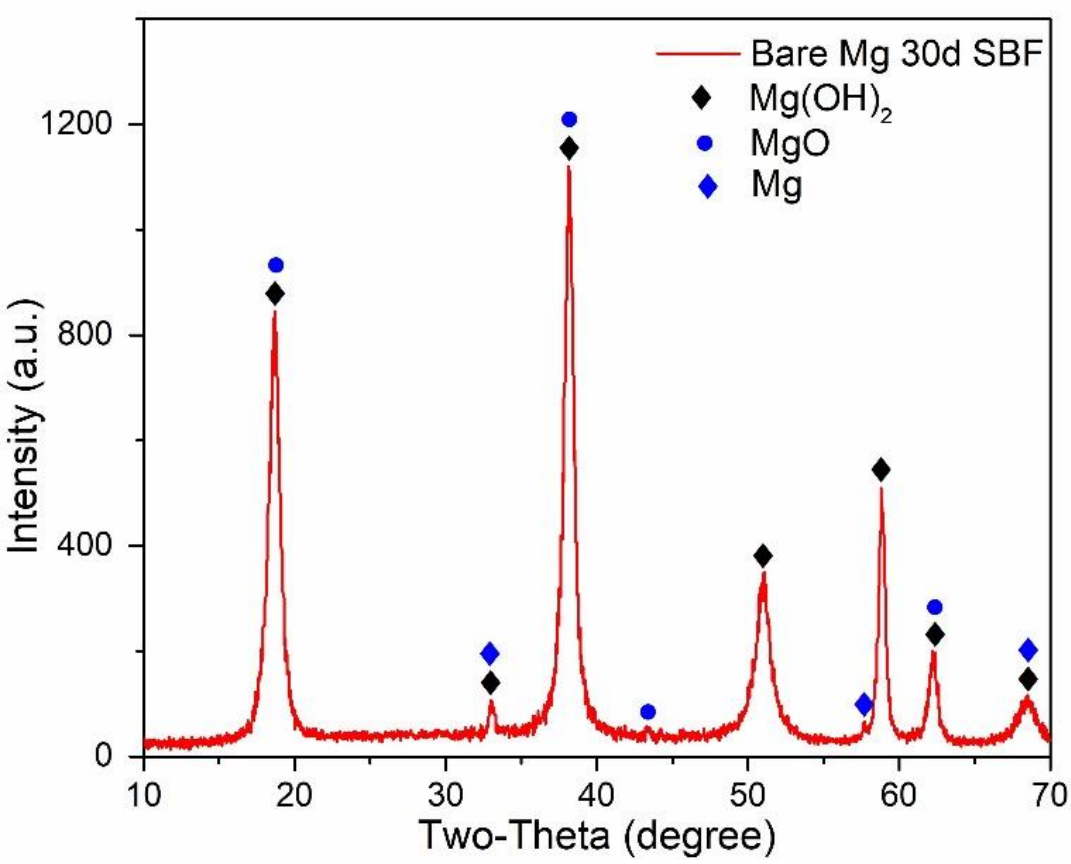

Figure 5.9: XRD pattern of corrosion product of pure Mg after immersion test for 30 days.

As previously stated, in case the samples are soaked in SBF, the intensive deposition of $Mg(OH)_2$ layers started. In the static soaking period, corrosion product film $Mg(OH)_2$ is obtained at the outer surface at first and protects the substrate to some extent. It is consistent with the result revealed from the XRD pattern that the corrosion sediments primarily consist of $Mg(OH)_2$. Because in this X-ray pattern, the characteristic peaks appear at 2θ=18.70°, 33.06°, 38.14°, 50.97°, 58.80°, 62.15°, and 68.52°, which correspond to the (001), (100), (101), (102), (110), (111) and (103) interplanar spacings of $Mg(OH)_2$ [4, 31, 33-34]. All characteristic Bragg peaks ascribed to $Mg(OH)_2$ are observed [4, 31, 33-34]. The narrow line widths and strong intensities of the diffraction peaks state that the crystallinity is relatively high. The corrosion precipitation reaction

is expressed as **Equation (5.16)**. So, it is concluded that the major degradation components of the pure Mg in the SBF solution primarily consist of $Mg(OH)_2$. Moreover, some authors point out that $Mg(OH)_2$ can spontaneously decompose into MgO and H_2O [31, 53-56]. Especially before the test, the sample is dried and dehydrated. So, there is MgO from the following hydrolysis reaction in **Equation (5.17)**. Moreover, the strong background and broad diffraction peaks can also be observed by XRD detection, which might correspond to the amorphous corrosion products and other complicated sediments.

$$Mg + 2H_2O = Mg(OH)_2 + H_2\uparrow \quad \textbf{(5.16)}$$

$$Mg(OH)_2 = MgO + H_2O \quad \textbf{(5.17)}$$

Then, the elemental constitution was determined by using SEM/EDS analysis. The precipitates have O, Ca, P, C, and Mg. The atomic contents of Ca (16.13%), P (11.04%), O (47.49%), and C (18.37%) are rich, and the atomic content of Mg (6.97%) is poor. Therefore, the nucleation and growth of carbonates and phosphates on the surface are well confirmed. However, there is no obvious peak corresponding to them in the XRD pattern. It indicates that the top corrosion products layer is super thin. The first reason is the limited amount of HCO_3^- and $H_2PO_4^-$ in SBF electrolytes. The second reason is that the locally high concentrations of Mg^{2+} and the hydrogen release can inhibit the nucleation of Ca/Mg carbonates and phosphates and impede their precipitation.

According to the combination with SEM/EDS and XRD results, it is inferred that the corrosion products of the composite surface are primarily $Mg(OH)_2$. The thin deposits at the top layer are carbonates and phosphates. Moreover, from the biocompatibility viewpoint, Ca/Mg-P salt compounds can further promote osteoinductivity [57].

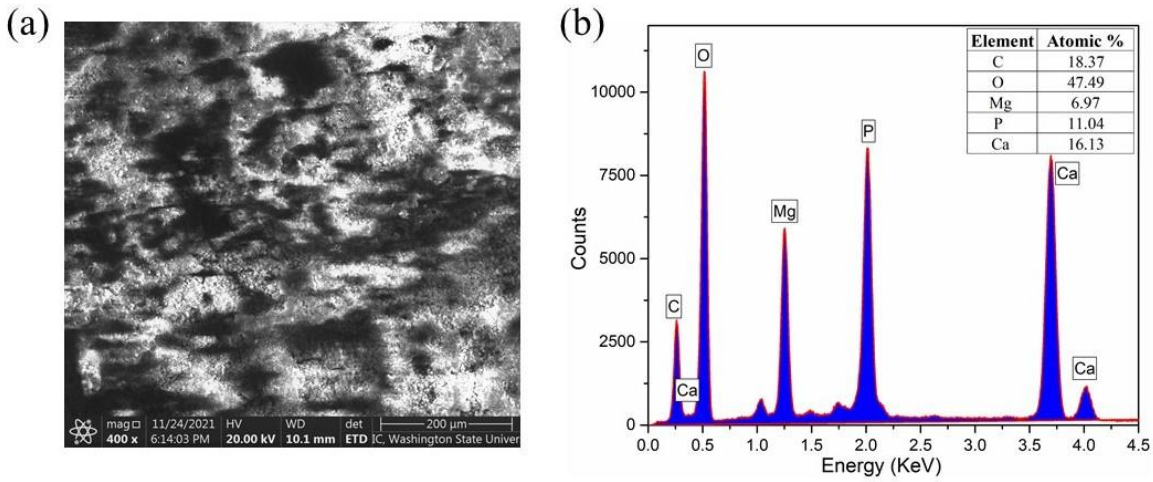

Figure 5.10: SEM figure (a) and corresponding EDS result (b) of R200 bare Mg sample after immersion for 30 days.

5.4 Conclusion

This chapter aims to discuss the influence of grain size on electrochemical results and the long-term degradation mechanism of pure Mg in SBF. Some statements are concluded according to a series of test results.

(1) The electrochemical corrosion behavior of the pure Mg sheets is affected by the processing route. The polarization resistance of R100 is the lowest. Those of R200 and R200-H2hr are close to each other.

(2) The 2-hour treatment conducted at 400 ℃ on R200 reduces the resistance modestly due to the fewer grain boundaries, which can be against the corrosion. But the finer grain with more grain boundaries from the lower rolling temperature significantly improves the pure Mg R100 sample corrosion activation. Because the grain size is very small, grain boundary and dislocation can be regarded as crystalline defects initiating the corrosion.

(3) The electrochemical test result is in very good agreement with the pH value curve obtained from long-period corrosion in static SBF. The corrosion process of R100 is the most rapid. R200 shows the best behavior with the slowest corrosion process and the lowest final pH value, which is close to 9.

(4) Macroscopically, the corrosion process begins at small-localized pits, gradually spreading in-depth and randomly on the surface. Subsequently, more and more white precipitates forms on the surface of the substrate. The corrosion products of the pure Mg were primarily $Mg(OH)_2$ film as the inner layer. Mg^{2+} and Ca^{2+} are attracted and linked to the hydroxyl-absorbed sites, which are negatively charged. The calcium/magnesium phosphates with carbonates grew preferentially and efficiently as the thin outer precipitates.

(5) In 30-day immersion, the corrosion of pure Mg is serious at the beginning, and the pH value increases rapidly. Then, the rising speed slows down to the peak value with the extension of soaking time thanks to the solid $Mg(OH)_2$ protective corrosion product. In the last stage, because of a series of reactions among Mg^{2+}, Ca^{2+}, Cl^-, SO_4^{2-}, HCO_3^-, and HPO_4^{2-}, after the pH value approaches stabilize, it keeps fluctuating and goes down to a certain range.

REFERENCES

1. Atrens, A.; Shi, Z.; Mehreen, S. U.; Johnston, S.; Song, G.-L.; Chen, X.; Pan, F., Review of Mg alloy corrosion rates. Journal of Magnesium and Alloys **2020,** 8 (4), 989-998.

2. Song, G., Recent progress in corrosion and protection of magnesium alloys. Advanced engineering materials **2005,** 7 (7), 563-586.

3. Etim, I.; Zhang, W.; Liu, T.; Zhao, H.; Tan, L.; Yang, K., The Role of Recrystallization and Local Misorientation on the Biodegradation Behavior of Mg. JOM **2021,** 73 (6), 1754-1764.

4. Song, D.; Ma, A.; Jiang, J.; Lin, P.; Yang, D.; Fan, J., Corrosion behavior of equal-channel-angular-pressed pure magnesium in NaCl aqueous solution. Corrosion Science **2010,** 52 (2), 481-490.

5. Silva, C. L.; Oliveira, A. C.; Costa, C. G.; Figueiredo, R. B.; de Fátima Leite, M.; Pereira, M. M.; Lins, V. F.; Langdon, T. G., Effect of severe plastic deformation on the biocompatibility and corrosion rate of pure magnesium. Journal of Materials Science **2017,** 52 (10), 5992-6003.

6. Sharifzadeh, M.; ali ANSARI, M.; Narvan, M.; Behnagh, R. A.; Araee, A.; Givi, M. K. B., Evaluation of wear and corrosion resistance of pure Mg wire produced by friction stir extrusion. Transactions of Nonferrous Metals Society of China **2015,** 25 (6), 1847-1855.

7. Jiang, B.; Xiang, Q.; Atrens, A.; Song, J.; Pan, F., Influence of crystallographic texture and grain size on the corrosion behaviour of as-extruded Mg alloy AZ31 sheets. Corrosion Science **2017,** 126, 374-380.

8. Zheng, T.; Hu, Y.; Yang, S., Effect of grain size on the electrochemical behavior of pure magnesium anode. Journal of magnesium and alloys **2017,** 5 (4), 404-411.

9. Aung, N. N.; Zhou, W., Effect of grain size and twins on corrosion behaviour of AZ31B magnesium alloy. Corrosion Science **2010,** 52 (2), 589-594.

10. Chen, J.; Chen, G.; Yan, H.; Su, B.; Gong, X.; Zhou, B., Correlation Between Microstructure and Corrosion Resistance of Magnesium Alloys Prepared by High Strain Rate Rolling. Journal of Materials Engineering and Performance **2017,** 26 (10), 4748-4759.

11. Eivani, A.; Mehdizade, M.; Chabok, S.; Zhou, J., Applying multi-pass friction stir processing to refine the microstructure and enhance the strength, ductility and corrosion resistance of WE43 magnesium alloy. Journal of Materials Research and Technology **2021,** 12, 1946-1957.

12. Argade, G.; Panigrahi, S.; Mishra, R., Effects of grain size on the corrosion resistance of wrought magnesium alloys containing neodymium. Corrosion Science **2012,** 58, 145-151.

13. Anne, G.; Ramesh, M.; Nayaka, H. S.; Arya, S. B.; Sahu, S., Microstructure Evolution and Mechanical and Corrosion Behavior of Accumulative Roll Bonded Mg-2% Zn/Al-7075 Multilayered Composite. Journal of Materials Engineering and Performance **2017,** 26 (4), 1726-1734.

14. Chai, S.; Zhang, D.; Pan, F.; Dong, J.; Guo, F.; Dong, Y., Influence of post-weld hot rolling on the microstructure and mechanical properties of AZ31 magnesium alloy sheet. Materials Science and Engineering: A **2013,** 588, 208-213.

15. Rad, H. R. B.; Idris, M. H.; Kadir, M. R. A.; Farahany, S., Microstructure analysis and corrosion behavior of biodegradable Mg–Ca implant alloys. Materials & Design **2012,** 33, 88-97.

16. Zhang, T.; Shao, Y.; Meng, G.; Cui, Z.; Wang, F., Corrosion of hot extrusion AZ91 magnesium alloy: I-relation between the microstructure and corrosion behavior. Corrosion Science **2011,** 53 (5), 1960-1968.

17. Hamu, G. B.; Eliezer, D.; Wagner, L., The relation between severe plastic deformation microstructure and corrosion behavior of AZ31 magnesium alloy. Journal of alloys and compounds **2009,** 468 (1-2), 222-229.

18. Curioni, M., The behaviour of magnesium during free corrosion and potentiodynamic polarization investigated by real-time hydrogen measurement and optical imaging. Electrochimica Acta **2014,** 120, 284-292.

19. Go, L. C.; Depan, D.; Holmes, W. E.; Gallo, A.; Knierim, K.; Bertrand, T.; Hernandez, R., Kinetic and thermodynamic analyses of the corrosion inhibition of synthetic extracellular polymeric substances. PeerJ Materials Science **2020,** 2, e4.

20. Jiang, Q.; Zhao, X.; Zhang, K.; Li, X.; Zhang, J.; Hou, B., Effect of the Precipitated Phases on Corrosion Behavior of Mg-Y-Nd Ternary Alloy. Int. J. Electrochem. Sci **2017,** 12, 10199-10210.

21. Gubicza, J.; Chinh, N. Q.; Krállics, G.; Schiller, I.; Ungár, T., Microstructure of ultrafine-grained fcc metals produced by severe plastic deformation. Current Applied Physics **2006,** 6 (2), 194-199.

22. Ahmadkhaniha, D.; Fedel, M.; Sohi, M. H.; Deflorian, F., Corrosion behavior of severely plastic deformed magnesium based alloys: A review. Surface Engineering and Applied Electrochemistry **2017,** 53 (5), 439-448.

23. Ralston, K.; Birbilis, N.; Davies, C., Revealing the relationship between grain size and corrosion rate of metals. Scripta Materialia **2010,** 63 (12), 1201-1204.

24. Kirkland, N.; Lespagnol, J.; Birbilis, N.; Staiger, M., A survey of bio-corrosion rates of magnesium alloys. Corrosion science **2010,** 52 (2), 287-291.

25. Song, G.; Atrens, A.; St John, D.; Wu, X.; Nairn, J., The anodic dissolution of magnesium in chloride and sulphate solutions. Corrosion Science **1997,** 39 (10-11), 1981-2004.

26. Song, G.; Atrens, A.; Stjohn, D.; Nairn, J.; Li, Y., The electrochemical corrosion of pure magnesium in 1 N NaCl. Corrosion Science **1997,** 39 (5), 855-875.

27. Witte, F.; Hort, N.; Vogt, C.; Cohen, S.; Kainer, K. U.; Willumeit, R.; Feyerabend, F., Degradable biomaterials based on magnesium corrosion. Current opinion in solid state and materials science **2008,** 12 (5-6), 63-72.

28. Witte, F.; Fischer, J.; Nellesen, J.; Crostack, H.-A.; Kaese, V.; Pisch, A.; Beckmann, F.; Windhagen, H., In vitro and in vivo corrosion measurements of magnesium alloys. Biomaterials **2006,** 27 (7), 1013-1018.

29. Han, G.; Lee, J.-Y.; Kim, Y.-C.; Park, J. H.; Kim, D.-I.; Han, H.-S.; Yang, S.-J.; Seok, H.-K., Preferred crystallographic pitting corrosion of pure magnesium in Hanks' solution. Corrosion Science **2012,** 63, 316-322.

30. Müller, L.; Müller, F. A., Preparation of SBF with different HCO3-content and its influence on the composition of biomimetic apatites. Acta biomaterialia **2006,** 2 (2), 181-189.

31. Song, G.; Atrens, A., Understanding magnesium corrosion—a framework for improved alloy performance. Advanced engineering materials **2003,** 5 (12), 837-858.

32. Virtanen, S., Biodegradable Mg and Mg alloys: Corrosion and biocompatibility. Materials Science and Engineering: B **2011,** 176 (20), 1600-1608.

33. Makar, G.; Kruger, J., Corrosion of magnesium. International materials reviews **1993,** 38 (3), 138-153.

34. Baril, G.; Pebere, N., The corrosion of pure magnesium in aerated and deaerated sodium sulphate solutions. Corrosion Science **2001,** 43 (3), 471-484.

35. Curioni, M.; Scenini, F.; Monetta, T.; Bellucci, F., Correlation between electrochemical impedance measurements and corrosion rate of magnesium investigated by real-time hydrogen measurement and optical imaging. Electrochimica Acta **2015,** 166, 372-384.

36. Kalb, H.; Rzany, A.; Hensel, B., Impact of microgalvanic corrosion on the degradation morphology of WE43 and pure magnesium under exposure to simulated body fluid. Corrosion Science **2012,** 57, 122-130.

37. Li, Z.; Song, G.-L.; Song, S., Effect of bicarbonate on biodegradation behaviour of pure magnesium in a simulated body fluid. Electrochimica Acta **2014,** 115, 56-65.

38. Braga, J. d. O.; de Carvalho, S. M.; Silva, L. M.; Soares, R. B.; Lins, V. F.; Mazzer, E. M.; Houmard, M.; Figueiredo, R. B.; Nunes, E. H., Fabrication and characterization of dicalcium phosphate coatings deposited on magnesium substrates by a chemical conversion route. Surface and Coatings Technology **2020,** 386, 125505.

39. Zeng, R.-C.; Li, X.-T.; Li, S.-Q.; Zhang, F.; Han, E.-H., In vitro degradation of pure Mg in response to glucose. Scientific reports **2015,** 5 (1), 1-14.

40. Phillips, V.; Kolbe, J.; Opperhauser, H., Effect of pH on the growth of Mg (OH) 2 crystals in an aqueous environment at 60 C. Journal of Crystal Growth **1977,** 41 (2), 228-234.

41. Oyane, A.; Kim, H. M.; Furuya, T.; Kokubo, T.; Miyazaki, T.; Nakamura, T., Preparation and assessment of revised simulated body fluids. Journal of Biomedical Materials Research Part A: An Official Journal of The Society for Biomaterials, The Japanese Society for Biomaterials, and The Australian Society for Biomaterials and the Korean Society for Biomaterials **2003,** 65 (2), 188-195.

42. Xin, Y.; Liu, C.; Zhang, X.; Tang, G.; Tian, X.; Chu, P. K., Corrosion behavior of biomedical AZ91 magnesium alloy in simulated body fluids. Journal of Materials Research **2007,** 22 (7), 2004-2011.

43. Zong, Y.; Yuan, G.; Zhang, X.; Mao, L.; Niu, J.; Ding, W., Comparison of biodegradable behaviors of AZ31 and Mg–Nd–Zn–Zr alloys in Hank's physiological solution. Materials Science and Engineering: B **2012,** 177 (5), 395-401.

44. Zhou, X.; Jiang, L.; Wu, P.; Sun, Y.; Yu, Y.; Wei, G.; Ge, H., Effect of aggressive ions on degradation of WE43 magnesium alloy in physiological environment. Int. J. Electrochem. Sci **2014,** 9, 304-314.

45. Lu, X.; Leng, Y., Theoretical analysis of calcium phosphate precipitation in simulated body fluid. Biomaterials **2005,** 26 (10), 1097-1108.

46. Mekmene, O.; Quillard, S.; Rouillon, T.; Bouler, J.-M.; Piot, M.; Gaucheron, F., Effects of pH and Ca/P molar ratio on the quantity and crystalline structure of calcium phosphates obtained from aqueous solutions. Dairy Science & Technology **2009,** 89 (3), 301-316.

47. Vidal, E.; Guillem-Marti, J.; Ginebra, M.-P.; Combes, C.; Rupérez, E.; Rodriguez, D., Multifunctional homogeneous calcium phosphate coatings: Toward antibacterial and cell adhesive titanium scaffolds. Surface and Coatings Technology **2021,** 405, 126557.

48. Gil, F.; Ginebra, M.; Driessens, F.; Planell, J.; Best, S., Calcium phosphate bone cements for clinical applications. Part II: precipitate formation during setting reactions. Journal of Materials Science: Materials in Medicine **1999,** 10 (3), 177-183.

49. Özcan, S. u. Preparation of Hydroxyapatite/Silk Protein Thin Film Implant Surfaces, Investigation of Their Microstructural Properties and Model Protein Interactions. Izmir Institute of Technology (Turkey), 2009.

50. Wang, Y.; Li, X.; Chen, M.; Zhao, Y.; You, C.; Li, Y.; Chen, G., In vitro and in vivo degradation behavior and biocompatibility evaluation of microarc oxidation-fluoridated hydroxyapatite-coated Mg–Zn–Zr–Sr alloy for bone application. ACS Biomaterials Science & Engineering **2019,** 5 (6), 2858-2876.

51. Lazić, S., Microcrystalline hydroxyapatite formation from alkaline solutions. Journal of crystal growth **1995,** 147 (1-2), 147-154.

52. Allred, A. L., Electronegativity values from thermochemical data. Journal of inorganic and nuclear chemistry **1961,** 17 (3-4), 215-221.

53. Song, G., Control of biodegradation of biocompatable magnesium alloys. Corrosion science **2007,** 49 (4), 1696-1701.

54. Song, G.-L.; Liu, M., The effect of surface pretreatment on the corrosion performance of electroless E-coating coated AZ31. Corrosion science **2012,** 62, 61-72.

55. Song, G.; Atrens, A.; Wu, X.; Zhang, B., Corrosion behaviour of AZ21, AZ501 and AZ91 in sodium chloride. Corrosion science **1998,** 40 (10), 1769-1791.

56. Baril, G.; Galicia, G.; Deslouis, C.; Pébère, N.; Tribollet, B.; Vivier, V., An impedance investigation of the mechanism of pure magnesium corrosion in sodium sulfate solutions. Journal of The Electrochemical Society **2006,** 154 (2), C108.

57. LeGeros, R. Z., Properties of osteoconductive biomaterials: calcium phosphates. Clinical Orthopaedics and Related Research® **2002,** 395, 81-98.

CHAPTER SIX: INFLUENCE OF THE SOLUTION TEMPERATURE ON CHEMICAL DEPOSITED MG AND CORROSION BEHAVIOR IN SIMULATED BODY FLUID

6.1 Introduction

From the viewpoint of hospitalization costs, traumas, inflammations, and patient suffering after the secondary operations, there is a huge demand for a rapid revolution of Mg implants [1-3]. In recent decades, special attention has been drawn to the strategies to overcome an initial loss of stability of the Mg alloy implants before the end of the healing process [4-5]. Although the optimization of the pure Mg microstructure is necessary, as discussed in the last chapter, the anti-corrosion resistance is just improved in a small range [6-12].

The protective coating is widely reckoned as an effective surface modification way to enhance the anti-corrosion ability of Mg-based materials [13-14]. A thin coating layer added to the Mg surface can be a barrier to separate the substrate from the corrosive environment [15-16]. Therefore, the substrate is protected [13-14]. After surface modification, there are usually few changes in bulk substrate mechanical and degradable properties, which is essential for the improvement of biomedical implants [1-2]. At present, there are some common surface treatments, like micro-arc oxidation [17-19], physical and chemical vapor deposition [20-24], and electro-plating deposition [25-27], which are considered available techniques for surface modification. Of these techniques employed to reduce the biodegradation rate, chemical bath deposition is regarded as one of the most suitable methods due to poor heat resistance and a low melting point of Mg [28-29]. Therefore, the application of the chemical deposited coating is the most direct and effective solution for

improving the anti-corrosion performance and potentially enhancing the bioactivity and osteointegration of Mg-based bio-implants. Also, compared with other methods, it is a simpler, more flexible, and more convenient way to form uniform and highly adhered coatings over the substrate surface [30-34]. Recently, research studies on fabricating coated Mg alloys as revolutionary implant materials through a simple chemical bath treatment have gained popularity from numerous investigators [35-38]. Besides the suitable surface treatment, anti-corrosion ability and biocompatibility should also be considered, which is also very important for biodegradable implant materials [39-40].

Calcium phosphate compounds have drawn extensive attention and are mostly used as potential materials as implant bio-friendly protection layers [41-45]. In the literature, natural human bone is composed of nanostructured inorganic apatite, organic Type I collagen fiber matrix, and water [44, 46]. The calcium phosphate salts are the most inorganic components of the bone tissue [46-49]. It is owing to the composition structural and chemical analogous to the bone that calcium phosphates are conducive to the direct connection to the surrounding hard tissue, accelerate bone concrescence, as well could slow down the dissolution [50-52]. Besides, there are different types of calcium phosphate salts [53-55]. They can be obtained and converted to each other through different reaction conditions and simple pH value changes [30-34]. In this way, it is valuable to find a good condition to obtain a uniform and even coating and discuss its formation mechanism [39-40]. Until now, the solution having calcium and phosphorus ingredients has been widely applied to easily obtain calcium phosphate depositions on Mg and its alloys through the traditional chemical conversion method over the years [50-52]. Some published articles conclude that the formation of calcium phosphate is a complicated process resulting in the mixture of many phases [53, 56-57]. So,

the quality and chemistry of the coatings are determined by the experimental parameters. Several key parameters making effects on the deposition of calcium phosphates are bath temperature [30-34], solution concentration [58-59], pH value [53-55], the existence of other ions, as well as bath duration [58-59]. Nevertheless, although some progress has been reported, research about the preparation of calcium phosphate film on Mg alloy is at the primary stage. Here are still open questions, and some works still need to be done. Unfortunately, there has been few reports or experimental data investigating and emphasizing the preparation conditions that can be found in the literature. Nowadays, there is a trend of current studies mainly focusing on the influences of preparation conditions.

Due to an imperative need for detailed research on the influence of the chemical bath pH in controlling the deposition of calcium phosphates, the objective of this chapter is of particular interest to systematically investigate the correlation among substrate preparation conditions, phosphating bath temperature, coating quality, and corrosion protection efficiency of calcium phosphate decompositions.

6.2 Electrochemical Corrosion Behavior

In this work, calcium phosphate layers from the different bath temperatures were prepared on two kinds of rolled pure Mg R100 and R200. To explore the effects of process temperature on the protective effect of coating, the electrochemical polarization examination test was carried out to evaluate the stability of coated Mg at first. Polarization is a powerful tool that can be used to analyze the corrosion of coated and bare Mg substrates. Tafel plots of the bare and chemical bath treated samples are shown in **Figure 6.1**. The rolled Mg R100 and R200 substrates are

references. In this study, all the electrochemical parameters of each kind representatives and the relative calculated data are summarized in **Table 6.1**.

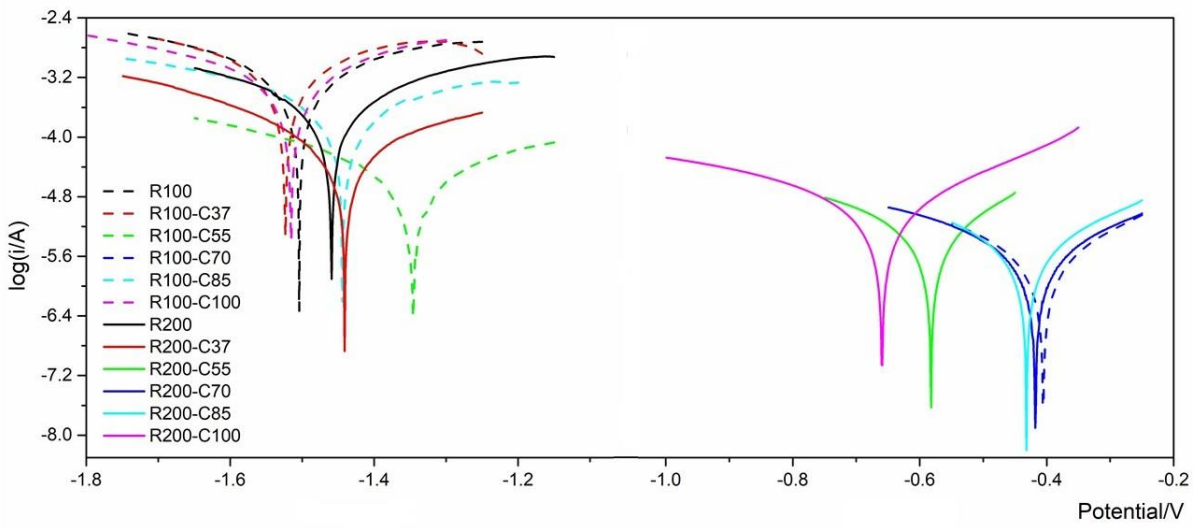

Figure 6.1: Polarization curves of the bare and coated Mg samples in SBF solution at 37 °C.

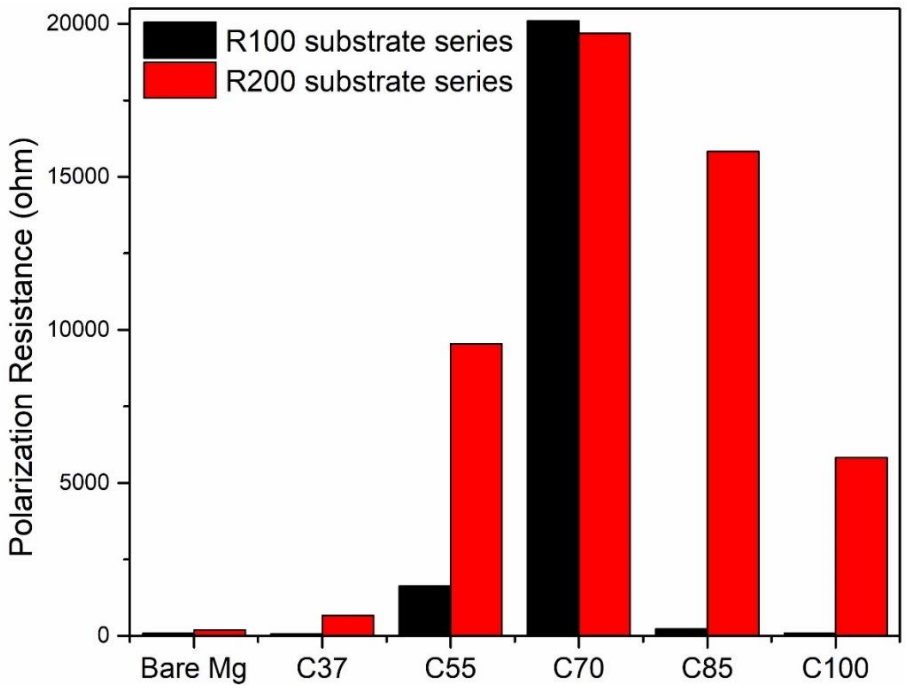

Figure 6.2: Polarization resistance bar chart of the bare and coated Mg samples in SBF solution at 37 °C.

According to the polarization curve, the corrosion potentials and current densities obtained for all the coated Mg specimens are found to be in the wide range, respectively, from -0.40 V to -1.53 V and from 7.166×10^{-4} A to 2.149×10^{-6} A. It is easy to conclude that chemical deposition in a Ca-P bath could enhance the electrochemical properties to different degrees due to different substrates and different bath temperatures.

Moreover, the extracted electrochemical parameters provide information about the quantitative evaluation and its corrosion properties. The corrosion potential (E_{corr}) is a thermodynamic data presenting the degradation trend [60]. After the coating process, the shift to the positive direction demonstrates the passivation occurrence. At the same time, the stability of the studied coatings is evaluated by corrosion current density (i_{corr}), which is a kinetic parameter obtained by plot extrapolation [60]. Also, the corrosion inhibition efficiency (n) of the coating can be calculated directly from the corrosion current density (i_{corr}) by the following equation [60]:

$$n = (i_{corr,bare} - i_{corr,coated})/ i_{corr,bare} \times 100\% \quad \textbf{(6.1)}$$

Where $i_{corr,bare}$ and $i_{corr,\ coated}$ are corrosion current density of bare Mg substrate and coated samples, respectively. Besides the corresponding corrosion potential (E_{corr}) and corrosion current density (i_{corr}), the value of polarization resistance (R) is also extracted from the Tafel plot. A well-known fact is that a good anti-corrosion performance is identified by high corrosion potential, weak corrosive current, and high polarization resistance. In general, the greater the polarization resistance, the better the corrosion resistance. Therefore, comparing the resistance value is convenient to estimate the anti-corrosion behavior of the sample at the initial corrosion stage. From the test results, on both kinds of substrate R100 and R200, with the increasing bath temperate from 37 °C to 100 °C, the R of coated Mg increased first and then went down. In

addition, the coating effects on different substrates were also very different at the same preparation temperature.

In addition, it is impossible to obtain a perfectly dense sample, because the pores on the sample surface are inevitable. The protection afforded by a coating is also proportional to the coating porosity because the aggressive ions would penetrate the substrate into the porosities. So, the porosity is an important and meaningful parameter that can reveal the enhancement of corrosion resistance caused by the coating. Coating porosity percentage P can be predicted and calculated by using the electrochemical parameters according to the following equation [61]:

$$P = (R_{bare} / R_{coated}) \times 10 \exp(-\Delta E_{corr}/ \beta_a) \times 100\% \quad \textbf{(6.2)}$$

In this equation, R_{bare} and R_{coated} are the corrosion resistance of the bare substrates and the coated samples, respectively. β_a represents the anode branch slop of the substrate, and ΔE_{corr} is the difference between the corrosion potential of the bare and the coated Mg.

Table 6.1: Polarization measurements and electrochemical parameters of coated Mg in SBF solution at 37 °C.

Sample	R (Ω)	E_{corr} (V)	i_{corr} (A)	β_a	n (%)	P (%)
R100-C100	91	-1.151	5.788×10^{-4}	4.69	-4.74	-152.6
R100-C37	72	-1.527	7.166×10^{-4}	4.34	-29.68	-119.25
R100-C85	225	-1.444	2.490×10^{-4}	3.23	54.94	36.195
R200-C37	667	-1.441	6.763×10^{-5}	4.10	71.01	28.495
R100-C55	1621	-1.346	3.054×10^{-5}	4.43	94.47	4.829

R200-C100	5828	-0.659	7.246×10^{-6}	5.59	96.89	2.348
R200-C55	9539	-0.582	4.400×10^{-6}	5.76	98.11	1.417
R200-C85	15831	-0.432	2.663×10^{-6}	5.32	98.86	0.777
R200-C70	19694	-0.418	2.221×10^{-6}	5.13	99.05	0.611
R100-C70	20093	-0.406	2.149×10^{-6}	5.33	99.61	0.263

After the 37 °C chemical bath treatment, R200-C37 had decreased i_{corr} and about 3.5 times the R of R200 because of these precipitates. Besides, the E_{corr} changed little, indicating that the R200-C37 sample with some depositions and exposed Mg still had a great corrosion trend, which should be attributed to the 28.495% high P. It means that there were Ca-P depositions on R200 at 37 °C but had a very limited protective effect. According to the electrochemical parameters and relative calculated results, R200-C37 had the worst coating effect among the coated R200 substrate series. The polarization curves of R100 and R100-C37 were very close and overlapped. The E_{corr} value of the R100-C37 was more negative, and its i_{corr} was higher. The resistance of R100-C37 was even lower than that of R100. From the viewpoint of electrochemistry, the protective film could not be formed on the R100 substrate by the 37 °C deposition process. This was also consistent with the negative corrosion inhibition efficiency.

When the coating temperature was 55 °C, the P values of the coatings on R100 and R200 were remarkably reduced to lower than 5%. Thanks to the deposition, their i_{corr} were decreased by one and two orders, respectively. It is easy to understand that the lower P resulted in a reduction in i_{corr}. It is because the electrochemically active region was lessened under the protection of the

corrosion layer. In addition, the E_{corr} and R of R100-C55 were not as significantly increased as R200-C55, which was due to the very active R100 substrate. It means the deposition layer with 4.829% P was not compact or protective enough for the R100 Mg, and the 55 ℃ operation condition had a better protective effect on the R200.

Continue improving the deposition temperature to 70 ℃, R100-C70 and R200-C70 showed the best and almost the same protective performance among all the coated Mg. Compared to the bare Mg, with the addition of the coating, the Tafel plots were shifted toward the E_{corr} more positive direction, corresponding to a low tendency toward corrosion in SBF. The i_{corr} of R100-C70 and R200-C70 samples remarkably decreased by two orders of magnitude to 2.15×10^{-6} A and 2.22×10^{-6} A, with the highest resistance values of 20093 Ω and 19694 Ω, respectively. Also, the n values of 70 ℃ coatings were both over 99%. In a word, after the proper 70 ℃ chemical bath deposit treatment, the obtained coating could inhibit the cathodic corrosion process effectively. Moreover, the influence of the substrate was very weak in this case. While the temperature rose further to 85 ℃ and 100 ℃, the higher temperature brought the reverse effect. For the R200 Mg substrate, this effect did not make a very big difference. The coated samples exhibited relatively good corrosion resistance with a slight decrement in R. It was different from the R200 that the high temperature had a serious negative effect on the R100 substrate. Also, the polarization performance of 85 ℃-coating and 100 ℃-coating turned downward sharply. And the higher the temperature, the greater the reverse effect. R100-C100 was even out of protection with the negative n and P values in **Table 6.1**.

In summary, according to the polarization curve, for the R100 Mg, only the coating obtained from the 70 °C bath possessed effective protection. For the R200 Mg, expecting R200-C37, other coated R200 had two orders decrease of i_{corr}. It demonstrates that pure Mg rolled under 200 °C was a suitable substrate, and 70 °C chemical bath temperature could generate the compact Ca-P coating with excellent performance.

6.3 The Influence of Temperature on Coating Formation

In this section, to reveal the coating formation mechanism under different temperatures, the detailed information was also further confirmed by using OM, SEM, EDS, and XRD characterization studies. Besides, the wettability of the coatings was evaluated using water contact angle measurements.

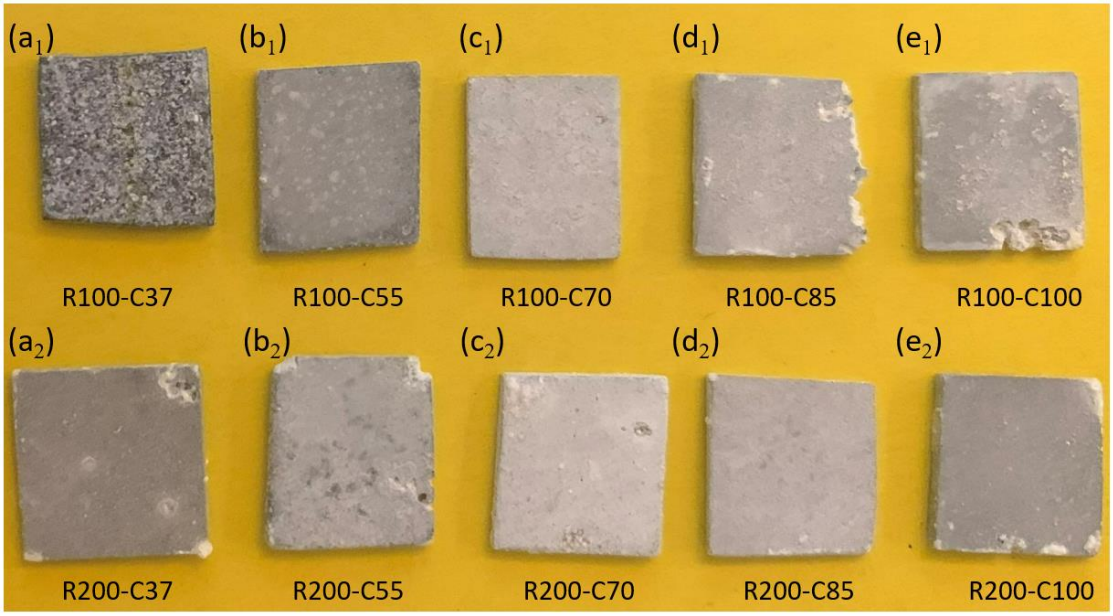

Figure 6.3: Macroscopic morphologies of coated Mg (a_1) R100-C37, (a_2) R200-C37, (b_1) R100-C55, (b_2) R200-C55, (c_1) R100-C70, (c_2) R200-C70, (d_1) R100-C85, (d_2) R200-C85, (e_1) R100-C100, and (e_2) R200-C100.

6.3.1 37 °C-coated Mg

R100-C37 and R200-C37 have the almost worst coating effect among the two different plastic deformed substrate series. According to their electrochemical parameters and relative calculated results, 37 °C chemical bath treatment has a very limited protective effect on the R200 substrate but has no effect on R100 one. Therefore, it can be inferred that completely different chemical reaction processes take place on the R100 and R200 Mg square sheets. This is also confirmed by the sample morphologies shown in **Figure 6.3**. In **Figure 6.3 (a_1)**, the R100-C37 sample was very uneven, with discontinuous white deposits on the surface. Under the SEM observation, the sample surface is very muddy because the products on the top appear to be stacked but not compact. Also, these sediments are not well-crystallized. At higher magnification, cracks can be seen under the sediments, and the inner fresh pure Mg is exposed from the cracks.

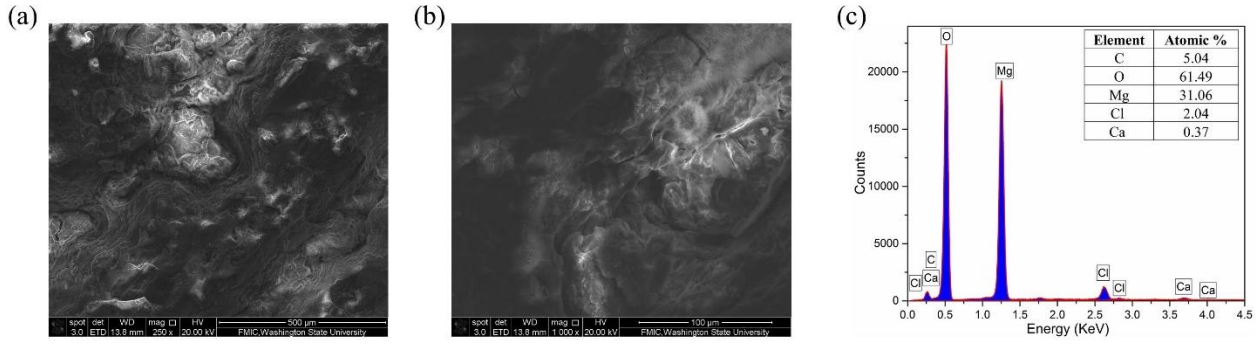

Figure 6.4: (a and b) SEM images and (c) corresponding EDS result of R100-C37.

To further understand the surface composition, EDS and XRD patterns of the R100-C37 are shown in **Figure 6.4 (c)** and **Figure 6.5**. From the EDS pattern, the elements of R100-C37 deposition are C, Mg, O, Cl, and Ca. The analytical results are also listed in the **Figure 6.4** (c) table. From EDS content, main elements O (61.49%) and Mg (31.06%) are distributed on the surface, and there is almost no trace of Ca and P. The atomic number ratio of Mg and O is also

almost close to 1:2, which suggests that the existence of $Mg(OH)_2$ accumulations. It is well consistent with the XRD spectra of conversion coating formed at 37 °C. There are 9 strong diffraction peaks observed in the R100-C37 XRD pattern. Compared with standard PDF data JCPDS card No. 35-0821 and JCPDS No.75-1527 [62-63], 4 peaks can be assigned as Mg peaks from the substate. And 5 peaks that can be assigned as $Mg(OH)_2$ peaks from the deposition process [62-63]. The strong Mg diffraction peak comes from the matrix material. These results confirm that the main crystalline corrosion product, which is not the full coverage on the sample surface, is $Mg(OH)_2$ instead of the Ca-P deposition. It is not difficult to estimate that it failed to form a suitable protective coating sample on R100 under the 37 °C condition.

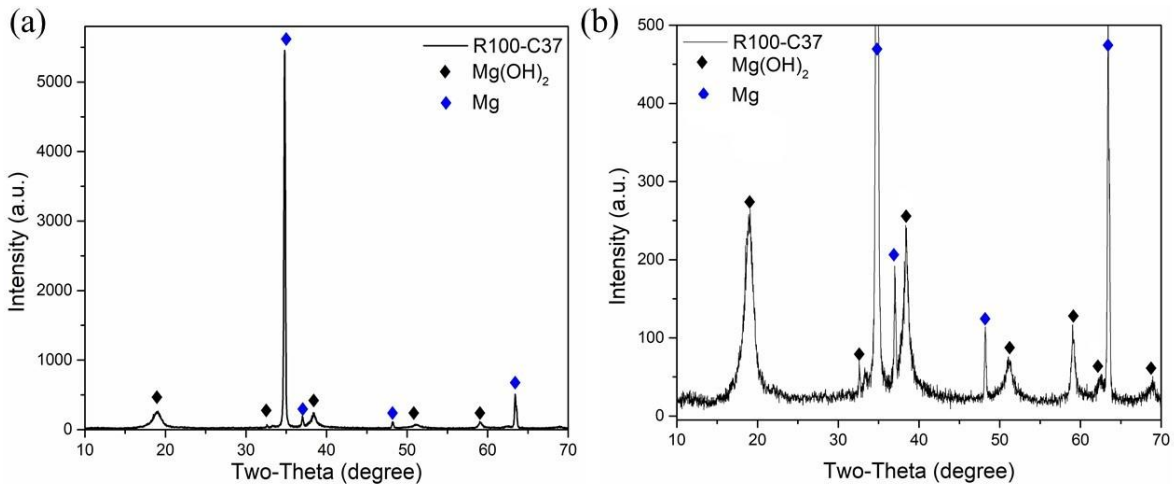

Figure 6.5: (a) Whole XRD pattern and (b) enlargement of the bottom peaks of R100-C37.

The main reason for this result is that the substrate dissolution is much greater than the Ca-P deposition. When the naked R100 Mg was immersed in the chemical coating solution, the serious pitting corrosion reactions occurred because of its chemical activity with H_2O and the serious aggression of Cl^-. The dissolution of Mg would easily occur and lead to massive Mg^{2+} ions surrounding the matrix surface. The appearance of gas in the precipitation period prevented

the coating deposition [64]. It has been pointed out that Mg ions are considered the strong inhibitors of the favored Ca-P nucleation, although there are sufficient Ca and P in the bath solution [64]. In addition, Mg ions are frequently reported to replace Ca ions in Ca-P compounds and could encourage the formation of amorphous and soluble Mg/Ca–P salts. Therefore, the appearance of Mg ions in the precipitation period causes poor crystallinity and prevention of coating growth [64].

Moreover, the low temperature did not provide sufficient Ca-P salt nucleation energy was responsible for the faint deposition reaction on the R100 surface. Combined with a series of the above test results of R100-C37, it can be deduced that only $Mg(OH)_2$ remained on the surface without calcium phosphate. Besides, the water contact angle of the uneven R100-C37 is about 60°, which is smaller than that of a smooth R100 bare Mg. So, the surface of the R100-C37 has stronger hydrophilicity. This angle is near to that of R100 after soaking in SBF for 4 days. It further confirms that the sample is more likely to be corroded after coating at 37 °C instead of to be coated. Combined with a series of above test results of R100-C37, it can be deduced that the low temperature and moderate deposition reaction on the Mg surface are responsible for the generation of $Mg(OH)_2$ with no Ca-P deposited on the R100 substrate.

When R200 is used as the base material, the result is much better and very different. Macroscopically, the coated R200-C37 presents a uniform and grey surface, and there is a little loss at the edge of the R200 substrate in **Figure 6.3 (a_2)**. Under the SEM observations in **Figure 6.6**, because the coating layer was discontinuous and thin, there were many long cracks on the Mg plate. By further magnification, the detailed structure in the loose layer is the flake-like,

plate-like, and dendritic shapes. The cracks and loose deposition layer might be responsible for the inner Mg continuously exposed to the solution, which would result in the following corrosion. The elements detected by EDS are O, Mg, P, Cl, and Ca, which are the elements of deposition coating mentioned in the above coating formation mechanism. And a small amount of K atoms come from the chemical bath solution. Because of these precipitates, R200-C37 has decreased i_{corr} and about 3.5 times the corrosion resistance of R200. Besides, the E_{corr} changes little, indicating that the R200-C37 sample with some depositions and exposed Mg still has a great corrosion trend, which should be attributed to the 28.495% high porosity. It indicates that Mg surface activation and Ca-P deposition do occur on the substrate, and the sediments remain on the surface. But these sediments did not form a complete and good coating.

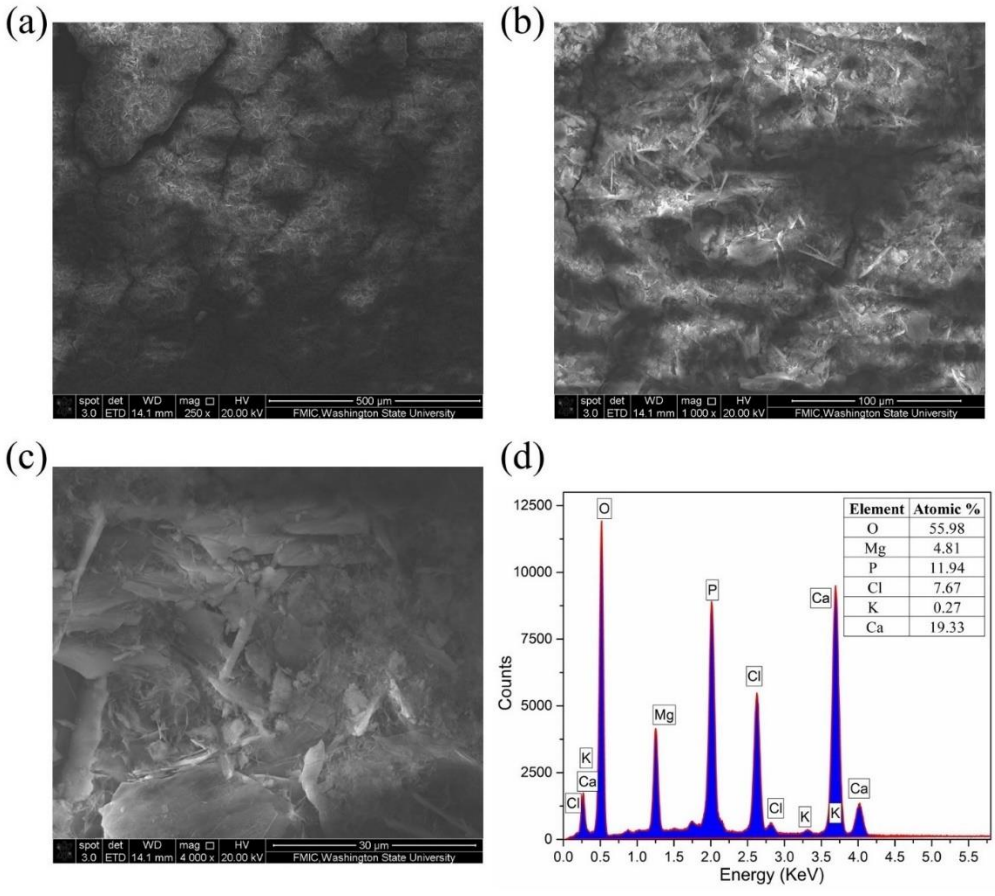

Figure 6.6: (a, b, and c) SEM images and (d) corresponding EDS result of R200-C37.

6.3.2 55 °C-coated Mg

According to the macro appearance in **Figure 6.3**, when the bath temperature is elevated from 37 °C to 55 °C, the Mg sheet maintains a complete shape, and there is a white and compact deposition layer on the surface. Great changes are shown under the SEM in **Figure 6.7**.

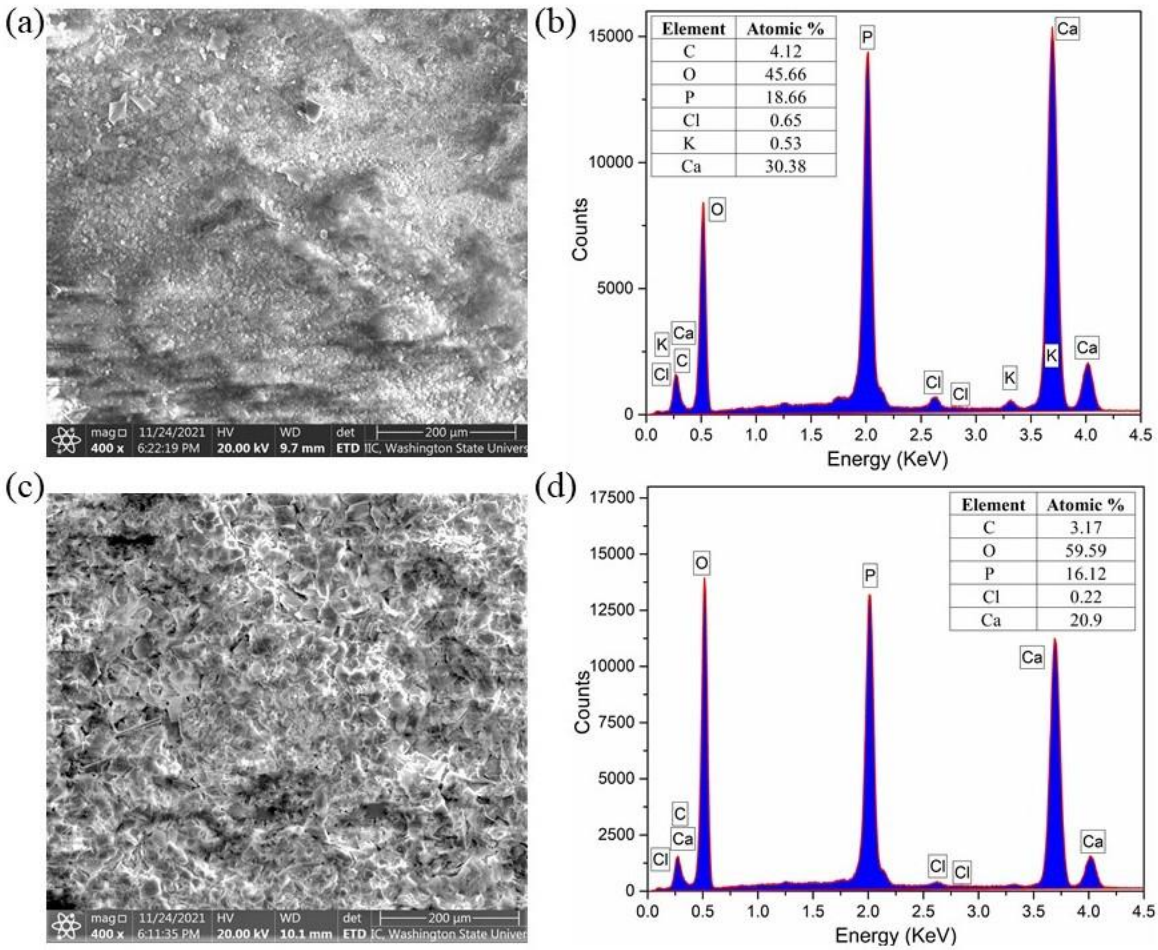

Figure 6.7: (a and c) SEM images and (b and d) corresponding EDS results of R100-C55 and R200-C55.

Both kinds of substrates were fully covered by flake-shaped depositions. The deposition layer was complete and flat, without any cracks. Moreover, the test results of EDS have also changed greatly. The elemental composition of the sample is no longer mainly Mg, O, and a small part of

impurities. Instead, it becomes the main components of Ca, P, and O. It means that the deposition reaction on the sample surface is greater than the corrosion reaction. A thin and defective Ca-P layer on the substrate is formed. The formation of the coating on R100 and R200 makes the porosity of the coating are remarkably reduced to 4.829% and 1.417%, respectively.

6.3.3 70 °C-coated Mg

Macroscopically, the 70 °C-coated samples with the best electrochemical behavior presented a uniform and grey surface. The coated sample presents a uniform and grey surface with no metallic luster in **Figure 6.3**. It means that the sample surface is covered by a layer of white material. No fresh substrate can be observed. Compared to the 55 °C-coated samples, the white material layer of 70 °C-coating was more compact and denser. R200-C70 and R100-C70 samples had the best, almost the same performance in a series of characterizations and tests. In other words, at 70 °C conditions, the substrate material did not mainly affect the coating results, and the temperature was a key factor in controlling the quality of the Ca-P coating. The reason was that the faster activation of the Mg surface under higher temperatures would cause an increase in locally OH^- concentration. In this case, there were more opportunities for coating crystals to initiate and nucleate on the dissolved Mg substrate. At the same time, the higher temperature also provided appropriate plenty of energy to promote the deposition growth rate. Therefore, the establishment of the coating dynamic balance was increased, and a denser and thicker Ca-P coating was formed. As a result, the coating products could completely cover the whole surface and effectively protect the substrate from further corroding. Obviously, in SEM micrographics, the phosphates layer was intact without any distinct pores or microcracks. The deposition particles well-crystallized precipitates are in inhomogeneous shapes. At higher

magnification, diverse morphologies of these precipitates with high crystallinity were visible on the 70 °C-coating surface. There are many flake shape sediments, and long needle particles are under these flake particles and in the gap between the flakes. The flake precipitation orientation is generally parallel to the matrix, and the needle-shaped with about 10 µm length points to the outside of the matrix. In addition, the well-oriented crystallite with high crystallinity is regarded as a significant character of bioactive coatings.

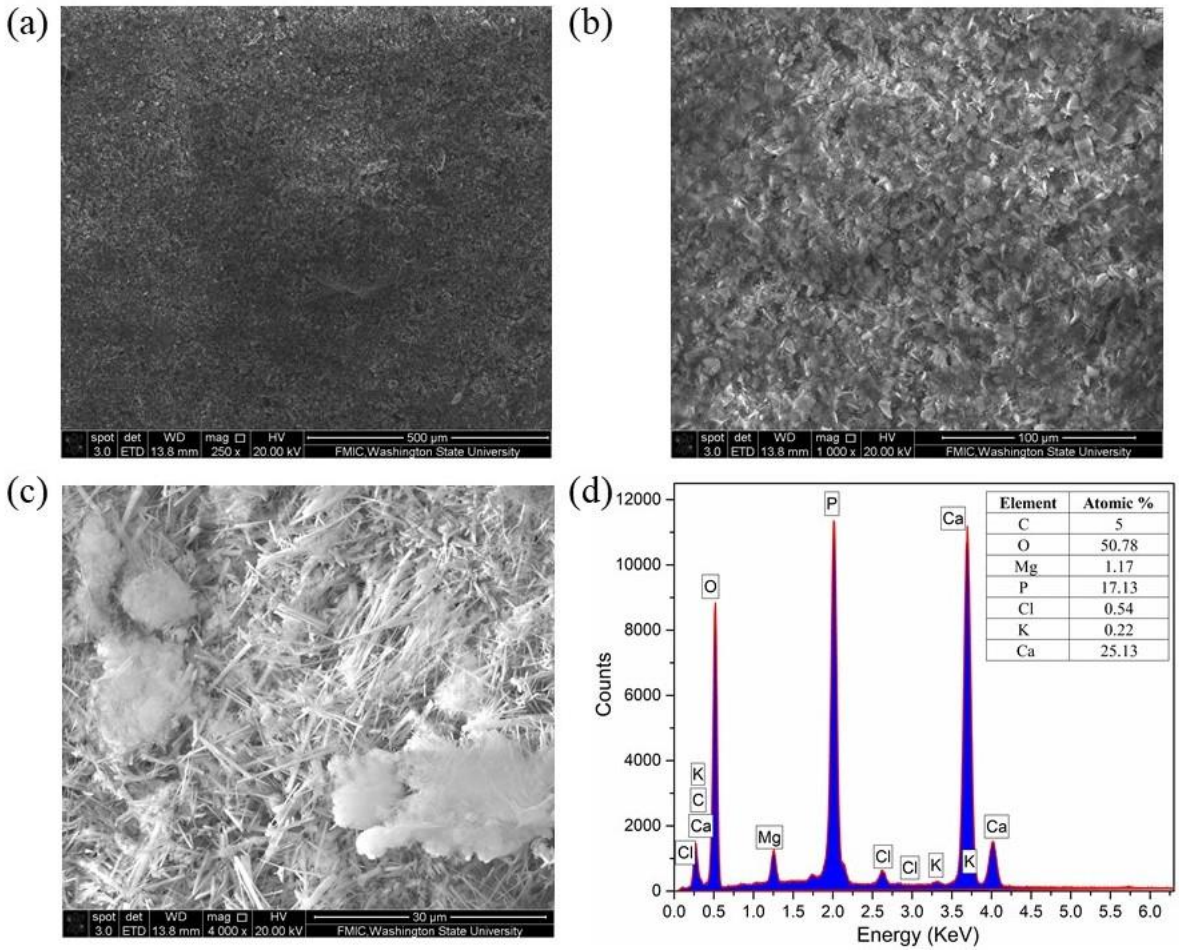

Figure 6.8: (a, b, and c) SEM images and corresponding EDS result (d) of R200-C70.

The attached energy dispersion and X-ray spectroscopy systems are used to acquire more detailed information about the chemical composition of the deposit. Except for small fractions of

minor impurity substances found by EDS analysis, the coating primarily contained O, Ca, and P, which are the main elements of the DCPD and HA. At the same time, small fractions of Mg and C with a few minor impurity substances are found by EDS analysis. It means a thick coating is produced successfully on the top, and the substrate is completely covered. Due to the existence of a protective deposition coating, the intensity of Mg peaks coming from the substrate is remarkably reduced.

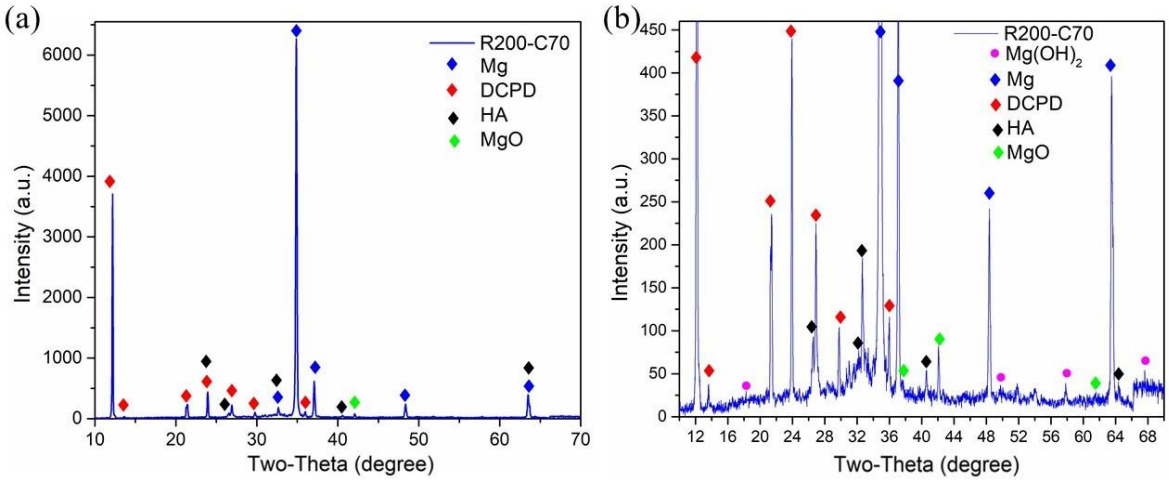

Figure 6.9: (a) Whole XRD pattern and (b) enlargement of the bottom peaks of R200-C70.

XRD analysis in **Figure 6.9** reveals the phase composition of the 70 °C chemical deposited samples. Besides the diffraction peaks originating from the Mg substrate, some new peaks from the chemical deposited coating are detected in the XRD patterns. There are four different components displayed. Not only the brushite DCPD is generated, but also the HA, $Mg(OH)_2$, and MgO with lower intensities displayed in the bottom-enlarged pattern. The strong peaks of DCPD could be seen in the range of 2θ=10–30°. The peaks appear at 12.18°, 26.88°, and 29.74° in the coated sample, which correspond to the (020), (002), and (141) interplanar spacings of brushite (DCPD, $CaHPO_4{\cdot}2H_2O$, JCPDS card No. 72-0713) [65]. DCPD displays a relatively high intensity

of the (020) diffraction peak, reflecting its preferential growth orientation of the monoclinic crystal phase. The characteristic peaks of HA at 2θ of 26.51° and 40.53° are detectable, according to the standard PDF data JCPDS card No. 74-566 [66]. But the intensities are lower compared with DCPD peaks. Also, by calculating the relative atomic percentage from EDS results, the ratio of Ca and P is about 1.47, which is between the theoretical ratio of DCPD and HA. It is concluded that the main components of the coating are DCPD and HA. The corrosion of matrix Mg was inevitable, which led to the existence of $Mg(OH)_2$. Because of its low XRD intensity, it indicated that the corrosion degree was not serious. Besides, some small Bragg reflections associated with MgO from the $Mg(OH)_2$ hydrolysis reaction as **Equation (5.17)** were observed at 2θ of 42.06° according to the standard PDF card No. 45-0946 [67].

Obviously, the temperature condition 70 °C plays a key role in controlling the corrosion initiation of the Mg substrate. The reason is that the faster activation of the Mg surface under higher temperatures would cause an increase in locally OH^- concentrate, while the solution temperature rises from 55 °C to 70 °C. In this case, coating crystals have more opportunities to nucleate on the dissolved Mg substrate easily. Also, the higher temperature also provides appropriate extra energy to promote the deposition growth rate. Therefore, the establishment of the dynamic coating balance is increased, and a denser and thicker Ca-P coating is formed. As a result, the coating products could completely cover the whole surface and protect the substrate from further corroding. From the above analysis of R100-C70 and R200-C70, it is difficult to distinguish which is better. For bio-plant materials, hydrophilicity is another very meaningful character. Although the influence of wettability on fibroblast cell adhesion is not very clear, it is considered that excess of both hydrophobic and hydrophilic surfaces are adverse to cell

attachment [68]. It is reported that the optimum water contact angle of the surface is in the range of 50° to 80° [69-70]. The DI water contact angle of R100-C70 is about 101°, which has good hydrophobicity and contributes to the good anti-corrosion at the beginning of corrosion. The DI water contact angle of R200-C70 is about 75°, which is better biofriendly. As for the more important long-term corrosion resistance, which of them can perform better, the following long-term experiments will answer in **Section 6.5**.

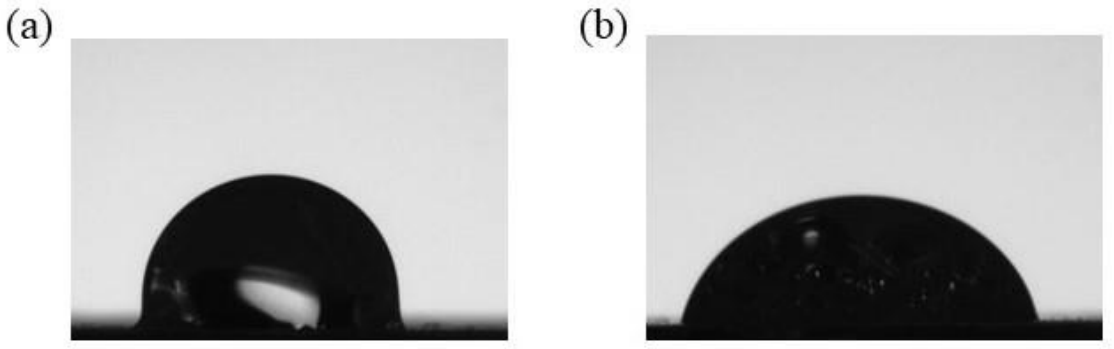

Figure 6.10: Images of water drop static contact angle test on 70 °C-coated Mg (a) R100-C70 and (b) R200-C70.

6.3.4 85 °C-coated and 100 °C-coated Mg

For the R200 Mg substrate, this effect does not make a big difference according to **Figure 6.3**. While the temperature rose further to 85 °C and 100 °C, compared to the R200-C70, the slight influence can also be seen from the macrography of the samples. By observing the appearance of the sample, compared to the coated R200 sample under 70 °C, fewer and fewer white deposits remain on the R200 surface of the substrate under the conditions of 85 °C and 100 °C. Under the SEM morphologies, the substrate surfaces were still completely covered by the deposition layer with more flake sediments and fewer high-crystalline ones in needle shape. The substrate surface

is still completely covered by the deposition layer, but it becomes thinner with the increase in temperature. It is consistent with the previous polarization test results. It was because the temperature rising could improve the activity of ions and provide more energy to accelerate the surface activation and the deposit reaction. Ca-P sediments were generated more rapidly, and deposition dynamic equilibrium was reached in a shorter time. So, it was hard for the coating sediments to deposit and grow to the thickness of R200-C70. At the same time, the EDS results of R200-C85 and R200-C100 in **Figure 6.11** are both O, Mg, P, Cl, K, and Ca. The contents of various elements are almost the same, but the microstructures of these two coated Mg are slightly different. With the increase in temperature, Ca-P sediments can form more rapidly and reach equilibrium in a shorter time. Therefore, under the SEM morphology, the needle-shaped sediments with high crystallinity in the deposition layer become less.

However, the essences of the effect of increasing temperature on R100 and R200 are different. Different from the R200, the temperature had a serious negative effect on the R100 substrate when it increased to 85 °C and 100 °C according to the characterization and test results. The polarization performance of R100 with 85 °C-coating and 100 °C-coating turns downward sharply. And the higher the temperature, the greater the reverse effect. The main reason for this phenomenon is that the matrix material R100 is seriously attacked by a high-temperature aqueous environment. Because too much hydrogen bubble is generated at the R100 surface at the beginning of the coating procedure, the rapid gas release hinders the nucleation and the growth of phosphate depositions to obtain a uniform coating layer. Even if the Ca-P layer can be formed due to the sufficient energy from the high temperature, the quick and increased hydrogen evolution and bubble bursting can probably destroy the calcification coating connection to the

substrate. The higher the reaction temperature, the faster the R100 dissolves, and the more obvious the barrier effect of rapid dissolution on the coating. This can also be seen intuitively that the edges of the coated R100 samples are corroded and consumed in **Figure 6.3**.

According to the electrochemical test result and 28.4% Ca and 17.53% P in EDS, it is inferred that the Ca-P coating was generated and played a certain degree of protective role in R100-C85. However, due to the serious corrosion of the substrate, there is no well-crystallized precipitation as shown in **Figure 6.12 (a)** SEM morphology.

The EDS test result of R100-C100 is totally different from that of R100-C85. Ca and P are hardly detected on the sample surface, but a large amount of Mg (27.76%) and O (66.46%) appear and the atomic content of Mg was also about half that of O, which was consistent with the corrosion product $Mg(OH)_2$ theoretical proportion. From the above discussion, it is inferred that the main component of the R100-C100 deposition is mainly the corrosion product $Mg(OH)_2$ without Ca-P salts. Because the rapid corrosion of the Mg substrate completely hindered the landing of Ca-P salts on the surface at 100 °C since Ca and P were hardly detected. R100 substrate is not under protection after the 100 °C chemical bath treatment. It should also be noticed that R100-C100 has similar low corrosion resistance and SEM morphology as the R100-C37.

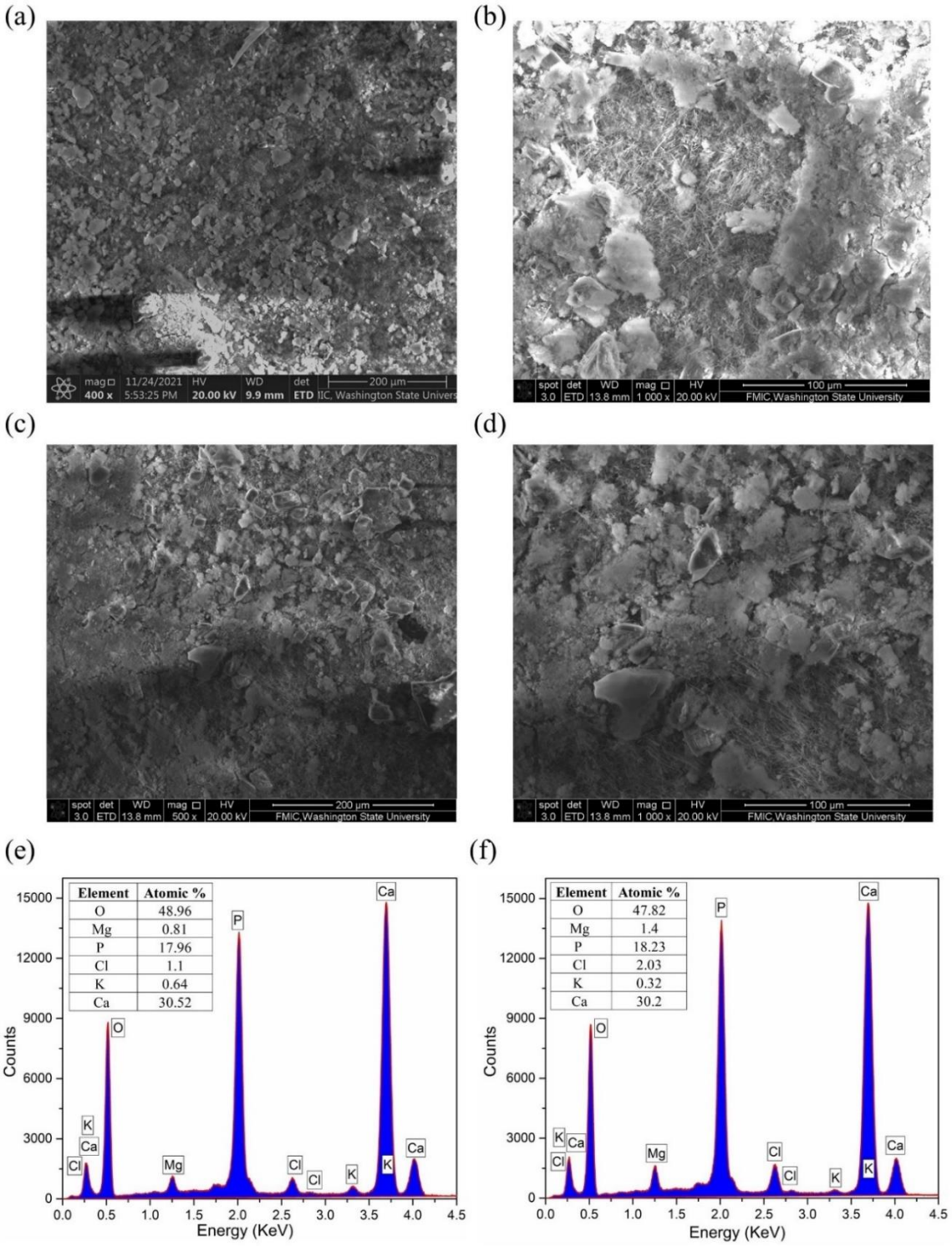

Figure 6.11: (a and b) SEM images and (e) corresponding EDS result of R200-C85; (c and d) SEM images and (f) corresponding EDS result of R200-C100.

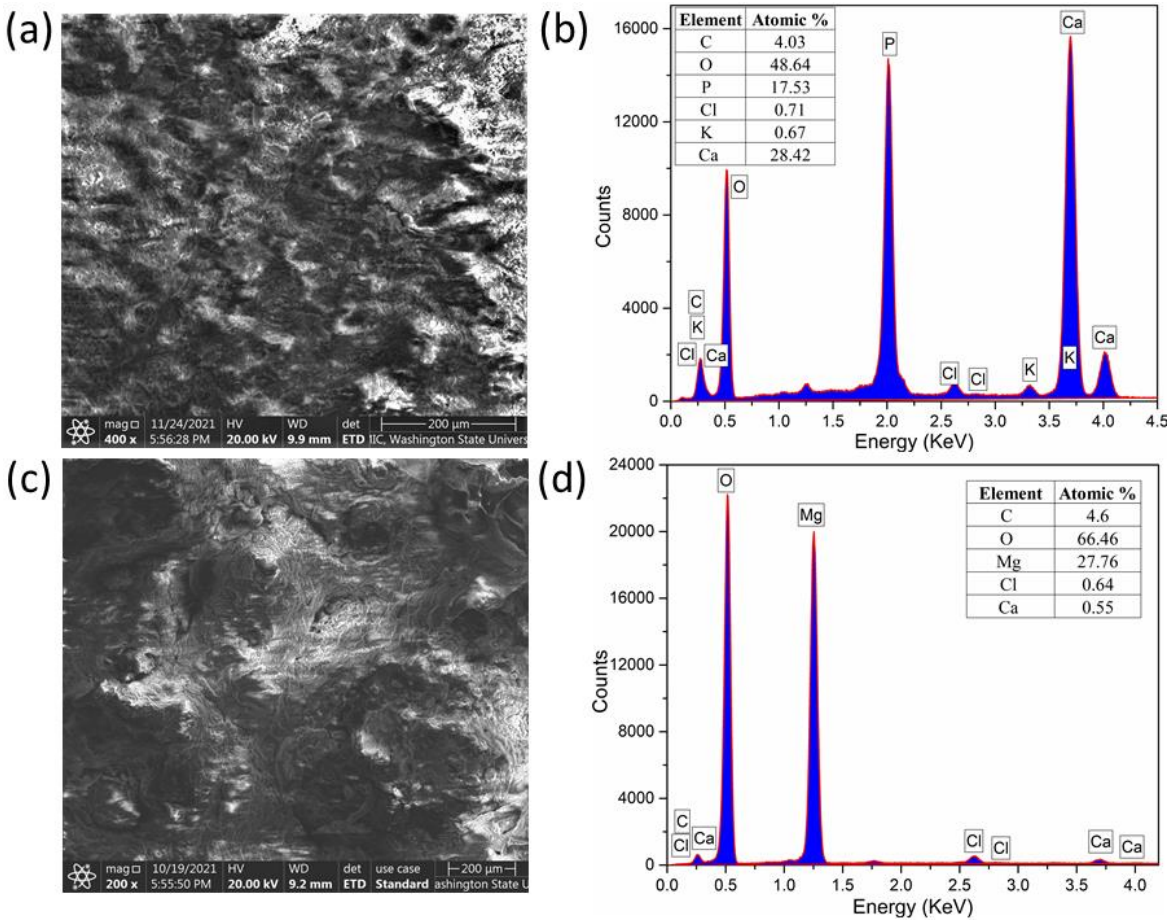

Figure 6.12: (a and c) SEM images and (b and d) corresponding EDS results of R100-C85 and R100-C100.

The polarization tests of the as-deposited samples show that chemical deposition in a Ca-P bath can enhance the electrochemical properties to different degrees due to different substrates and different bath temperatures. On both kinds of substrate R100 and R200, with the increasing bath temperate from 37 °C to 100 °C, the corrosion resistance of coated Mg rises first and then goes down. For the R100 Mg, only the coating obtained from the 70 °C bath possesses effective protection. For the R200 Mg, When the bath temperature is 37 °C, the polarization resistance of R200-C37 is the lowest among the coated R200. Expecting R200-C37, these coated R200 Mg

have two orders decrease of corrosion current density. It demonstrates that pure Mg rolled under 200 °C is a suitable substrate, and 70 °C bath temperature could generate the compact Ca-P coatings with effective protection.

6.4 Coating Formation Mechanism

According to the previous test result analysis, the coating formation processing can be explained by an association of several reactions. Here are four main steps, including acid-base activation, surface calcification, precipitate nucleation, and the growth of the depositions. The schematic diagrams of coated Mg sample formation and cross-sectional structure are shown in **Figure 6.13**.

The first step is surface activation which acts as the starting role in the formation of Ca-P coatings. Considering the active chemical properties of Mg, the acidic condition of the $CaCl_2$ solution could markedly enlarge the substrate surface activity. The stirring also exerts an important effect on the fast and uniform activation of the surface. In the bath solution, the substrate Mg was dissolved first and activated into Mg^{2+} [71-74]. Besides, the high concentration Cl^- with a small radius easily penetrated the barrier of solid $Mg(OH)_2$ on the sample surface [75-77]. The specific reaction equations are **Equation (5.5)** and **Equation (5.6)**. In this process, the $CaCl_2$ solution was stirred. So, the fast and uniform activation of Mg occurred under flowing conditions. At the same time, the calcification of the sample happened. Along with the Mg corrosion, there is a greatly promoted local alkalinity around the solution/sample interface. The hydroxyl groups are supposed to offer favorable linkage sites for coating nucleation because of the prominent alkalization nearby the surface. It has been pointed out that the negatively charged hydroxyl groups around its surface are conducive to the pre-calcification of the fresh Mg surface

in the bath with abundant ions of Ca^{2+}. It is shown that hydroxyl is a significant factor in the composition and structure of the Ca-P salts.

Next, after the K_2HPO_4 was added and mixed well by a magnetic rotor, according to the raw material added into the solution, a reaction took place between the surface absorbed Ca^{2+}, negative charged HPO_4^{2-}, and H_2O at first to form the deposition nuclei [78-79]. The specific reaction is **Equation (5.11)**.

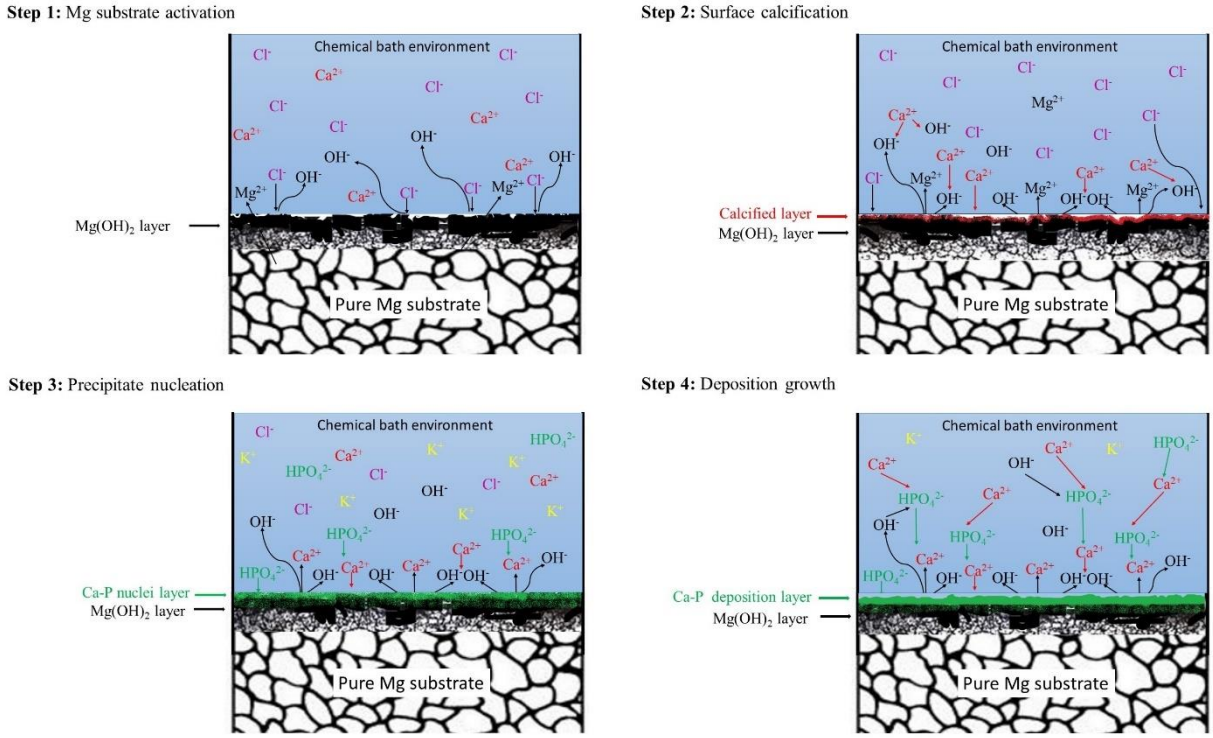

Figure 6.13: Schematic diagrams of coated Mg sample formation steps and corresponding cross-sectional structures.

In this way, the $CaHPO_4{\cdot}2H_2O$ (DCPD) film is induced directly on the substrate surface at the third step. It has been concluded from previous research that the bath solution pH value

influences the composition and structure of the coating [80]. In this study, the pH stability value of the mixture solution was about 4.5, which was lower than 5. Even if the ionization and hydration of HPO_4^{2-} were inevitable, the degrees were very small [81]. So, this acid environment was suitable for high-purity DCPD to deposit from the solution [82-83]. A small amount of HA was also detected in XRD. The possible reasons were as follows. The first reason was that the local pH value near the surface could rapidly increase due to a large amount of OH^- released at the early stage. HPO_4^{2-} in the solution near the surface was transformed into PO_4^{3-} and possibly resulted in HA generation with low solubility, as shown in the **Equation (5.10)** and **Equation (5.15)**.

The second reason was that DCPD was thought to be a precursor of HA [84-85]. Due to the exitance of OH^-, the precipitated DCPD phase could be converted to the stable HA phase on the substrate by the following **Equation (6.3)** [78, 86]. The formation of HA is a thermodynamically spontaneous reaction when pH>5.4 because the free energy change of HA precipitation driving force becomes negative. Also, the HA nucleation rate is seriously subject to the pH value. The more alkaline the solution, the more conducive to the nucleation of HA [87].

$$10CaHPO_4{\cdot}2H_2O + 12OH^- = Ca_{10}(PO_4)_6(OH)_2 + 4PO_4^{3-} + 30H_2O \quad \textbf{(6.3)}$$

This also showed that magnetic stirring was necessary and beneficial for the formation of single-component DCPD deposition with high purity. With the rapid nucleation of a large amount of Ca-P by consuming the surrounding Ca and P, the deposition layer was fabricated spontaneously. The following sufficient deposition period gave the Ca-P salts enough time to grow up into a smooth coating. As a result, the final coating on the bare Mg was double layered. The main component of the thin inner layer was $Mg(OH)_2$, which came from the sacrifice of the substrate. The outer layer was Ca-P coating which predominately consisted of DCPD with a small amount

of HA and MgO. As the substrate involves the formation of the coating, the interaction between the Mg substrate and treatment reagent takes place in situ. In this way, the coating layer adheres highly to the sample surface, which is effective in avoiding the potential possibility of coating delamination.

6.5 Immersion Test of Coated Mg in SBF

6.5.1 30-day Immersion Test Results of Coated Mg

Following the polarization, to further estimate and understand the long-term corrosion performance, the coated Mg samples were immersed in SBF for 30 days. After a long-term immersion test, the obvious macroscopical changes can be observed between **Figure 6.3** and **Figure 6.14**. Because the change of the pH value is a function of the soaking period, the pH value curves shown in **Figure 6.15** were used to analyze the dissolution behavior of these different coated samples.

R100-C37, R100-C85, and R100-C100 have the same trends as the bare Mg. Their pH curves had the same rapid rise trend in early immersion. Due to the poor coating effect, the substrate and coating were seriously corroded together after being immersed for 30 days, as shown in the macroscopic observation. For the rest of the samples, from the macro point of view, the Ca-P coating had a good protective effect. After a long-term immersion, they basically maintained their shape.

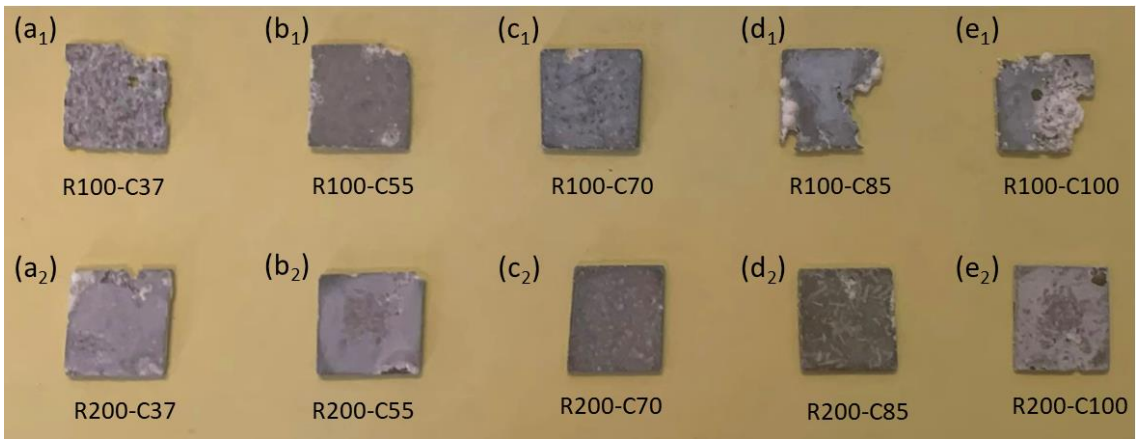

Figure 6.14: Macroscopic corrosion morphologies of coated Mg (a_1) R100-C37, (a_2) R200-C37, (b_1) R100-C55, (b_2) R200-C55, (c_1) R100-C70, (c_2) R200-C70, (d_1) R100-C85, (d_2) R200-C85, (e_1) R100-C100, and (e_2) R200-C100 after a 30-day immersion test.

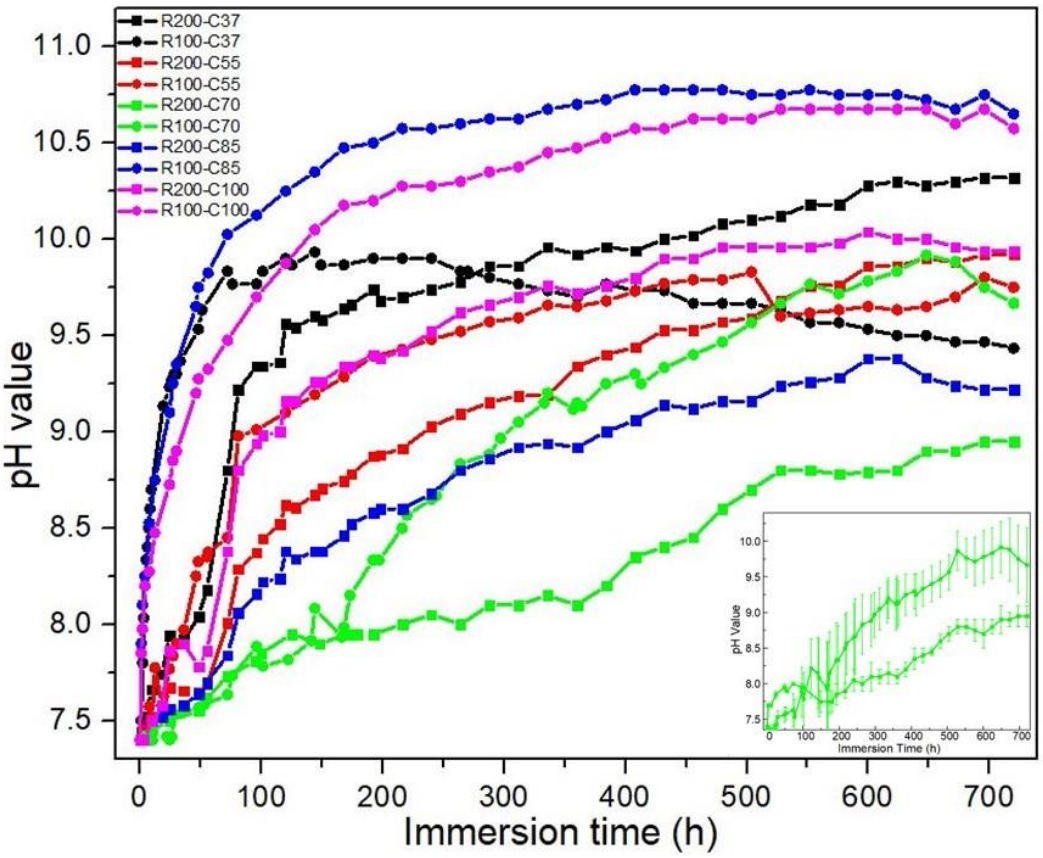

Figure 6.15: The pH value- immersion time curves of SBF solutions containing coated Mg.

The change in pH value could reflect the difference in their stability during soaking. R200-C37, R200-C55, R200-C100, and R100-C55 show slower pH value increasing rates at the early immersion stage, lower pH maximum values, and lower pH final values. The remaining three samples, R100-C70, R200-C70, and R200-C85, their Tafel curves overlap each other. It means that their degradation rate is significantly slowed down and has similar protective effects on the substrate at the initial stage of SBF immersion. Consistent with the previous electrochemical test results, the degradation rates of R100-C70 and R200-C70 significantly slowed down at the initial stage of SBF immersion because of their highest R values in comparison with the coated samples in the above electrochemical test. However, their long-term anti-corrosion behavior was not the same. In terms of pH value change, R200-C70 has the best long-term anti-corrosion behavior. After 30-day immersion, the final pH value of static SBF containing the R200-C70 was only increased by 1.6. During the soaking period, the pH value started to go up slowly from the beginning and with no rapid growth throughout the process. So, in this work, R200-C70 was the most corrosion-resistant and showed the best long-term stability.

6.5.2 Anti-corrosion Mechanism of Coated Mg in SBF

The immersion behavior of the coated samples is distinctly different from that of the bare Mg. The morphologies of R200-C70 before and after the soaking test are examined and recorded by an optical camera. After the 30-day immersion experiment, the sample can maintain the basic shape and only have slight defects and losses at the edges. Although the coating is consumed, a very thin and non-uniform corroded layer is clearly visible over the whole surface after the corrosion test. During the soaking test, the pH value increases slowly from 7.4 and finally reaches around 9.0 with no rapid growth. It means that the coating effectively protects the Mg

matrix. Although the Mg substrate is still corroded, the degradation degree is well-controlled during the whole process. To reveal its excellent anti-corrosion process and mechanism in SBF, the tested R200-C70 specimen is removed from the SBF bath, washed with distilled water, and air-cleaned after different periods of immersion. And then, it is observed and characterized by OM, SEM, XRD, and EDS for more detailed information about the complicated process in the SBF immersion experiment.

At the very beginning, the substrate Mg was well protected. The compact coating blocked the corrosive environment first and minimized the contact area between the Mg matrix and the corroding medium from surrounding solutions. Generally, DCPD coating is sensitive to the increase in pH value. Also, the higher solubility of DCPD can be triggered by the pH rise. It has been reported that DCPD is thermodynamically unstable and dissolves spontaneously in weakly alkaline SBF as the following transforming equation [88].

$$CaHPO_4{\cdot}2H_2O + OH^- = Ca^{2+} + PO_4^{3-} + 3H_2O \quad \textbf{(6.4)}$$

The dissolution of DCPD coating led to the free Ca^{2+} and PO_4^{3-} and, in turn, the re-precipitation of HA in SBF which was the same as the coating formation mechanism mentioned in **Section 6.4**. Because SBF is a supersaturated solution to HA. Especially, the extra Ca^{2+} and PO_4^{3-} could further accelerate the formation and growth of HA. So, the formation of HA is spontaneous. Because HA is the most stable Ca-P ceramic in alkaline conditions, HA in the coating will not undergo any dissolution or transformation reactions. However, HA has rarely been remained or detected on the sample surface in the present research [89]. Here are three main reasons for this result. Firstly, the DCPD coating obtained in the acid solution dissolves too rapidly after being soaked in SBF, resulting in HA difficult deposition. Secondly, once the inner substrate is

corroded, the released Mg^{2+} and hydrogen bubbles are a hindrance to the nucleation and adhesion of newly generated sediments on the specimens. Third, the HA nucleation is seriously subject to the pH value. During the immersion experiment, the solution is alkaline. This makes the re-precipitation of HA different from the formation of HA in the coating mechanism mentioned above. During the chemical treatment, the solution was acidic, and only the substrate surface was alkaline. So, HA could be deposited on the surface. However, during the immersion experiment, the overall solution here is alkaline. And the solubility of HA reduces as the pH goes up, which can result in the fall of some deposits from the substrate surface. HA formed in the supersaturated alkaline solution would fall off to the container bottom. Therefore, after DCPD is converted into HA, it would fall off and deposit at the bottom of the container.

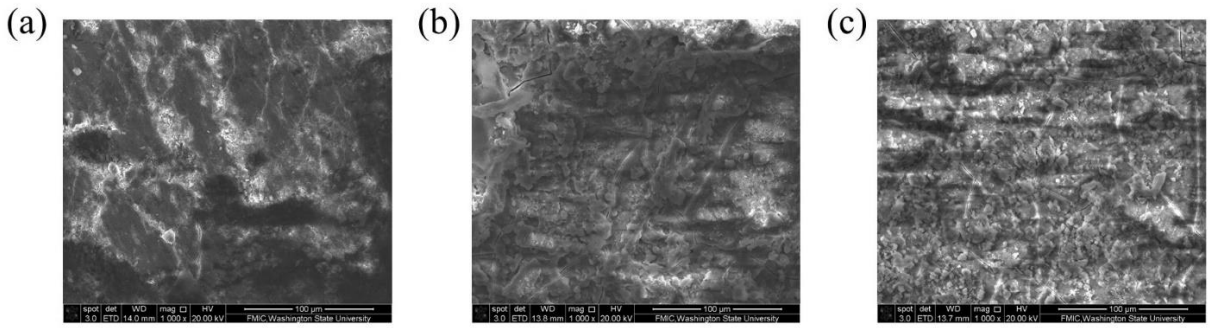

Figure 6.16: SEM images of R200-C70 after (a) 7 days, (b) 14 days, and (c) 21 days in SBF immersion tests.

The SEM/EDS results can demonstrate this process and mechanism. The SEM image of R200-C70 after 7-day soaking proved the dissolution of the coating. The original long-needle particles disappear, and the deposition layer is no longer intact or dense in the SEM figure of R200-C70 after a 7-day soaking. There was fewer stacked coating piece left on the top. And the coating still has good coverage with an uneven feature. It means that the coating dissolved but did not peel

off from the substrate. At the same time, in the pH-time curve the alkaline increase caused by Mg corrosion is not violent.

Once the coating was dissolved, the defects, cracks, and poor adhesion of the Ca-P coatings were inevitable, which allowed the easy penetration and attack of corrosive ions. In this way, the corrosion attack of the inner pure Mg matrix occurs at the coating structure defects in the corroding environment. So, in this period, the overall coating degradation and Mg local corrosion took place simultaneously. With the further increasing immersion time, accompanied by massive dissolution of coating, the substrate is still corroded in static SBF immersion with the new generated protective layer of corrosive products. This process is also reflected in the SEM figures. With the lapse of time, more and more network-like cracks on the micron scale are observed. It is the same as the bare Mg last degradation period. At the same time, some new flake-shape sediments are produced on the cracks. Further extension of immersion time to 30 days, the sample surface is almost fully covered by stacked sediments again under the SEM low magnitude in **Figure 6.17 (a)**. After the corrosion test, A very thin and non-uniform corroded layer was visible over the whole surface. In addition, compared to the EDS result before the soaking, the composition and the content of the element were almost unchanged. The amounts of Ca and P were slightly decreased, while the amount of Mg was hardly increased. It demonstrates that the coating can not only as a physical barrier to protect the substrate but also as a supplier to provide raw materials of Ca element and P element for the formation of new precipitates in the deposit reactions. After the part of the coating is sacrificed, the complicated corrosive products of the inner Mg substrate are formed and deposited on the surface. While the Ca element tends to be accompanied by the P element, preferably around the inner Mg, herein, the corrosion product

layers are mainly composed of O, P, and Ca elements. The newly constituted corrosion product layer, mainly composed of O, P, and Ca elements, could retard the further erosion of the inner Mg substrate. Due to this self-healing effect, the Mg substrate was protected from the beginning to the end instead of being rapidly corroded. As a result, the coated sample has better performance in this later stage, and the pH curve becomes slightly flatter. As a result, after a 30-day soaking in a static SBF solution, the surface mixture may have consisted of little residual DCPD and HA coating and many newly formed Ca-P corrosion products. They could continue to prevent the intrusion of the solution and provide a protective effect.

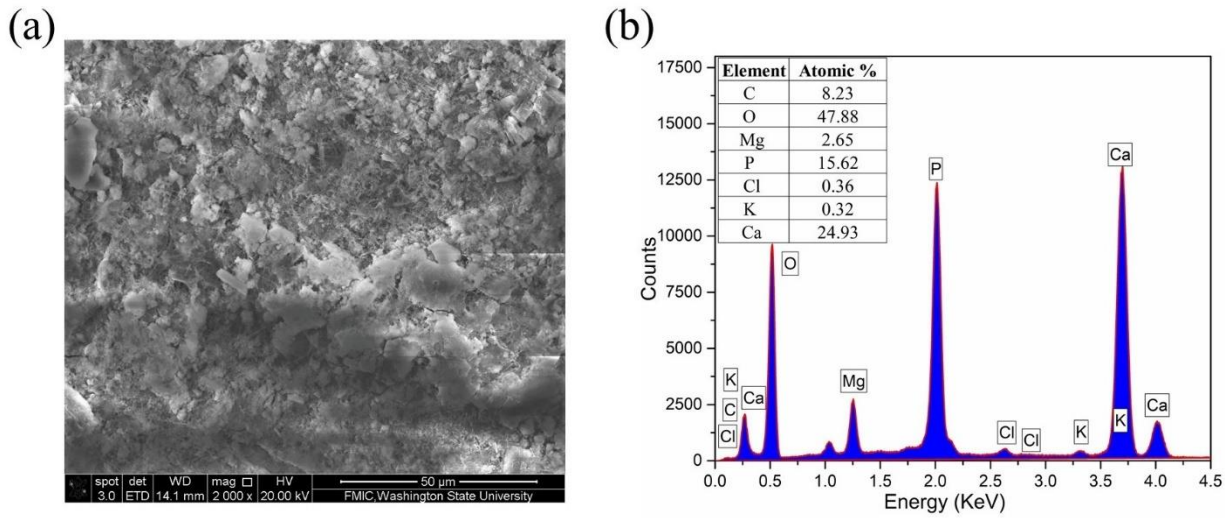

Figure 6.17: (a) SEM image of R200-C70 after 30 days in SBF immersion test and (b) corresponding EDS result.

Moreover, it is reposted that the physiological medium with a high pH value is not conducive to cell growth. So, the slow increment of pH value is bio-friendly and helpful in avoiding serious infections during the early postoperative period. For these good properties mentioned before,

chemical bath deposition of R200 Mg plate under 70 °C is an appropriate plan for the application of Ca-P coated Mg.

6.6 Conclusion

In this research, the calcium phosphate coating was obtained on the pure Mg sheet by dipping different rolled substrates into a mixed chemical solution containing Ca^{2+} and HPO_4^{2-} under different bath temperatures.

The electrochemical parameters and characterization results illustrated that R200 was a more suitable substrate, and the applied temperature played a dual role in the coating process. On the one hand, the higher temperature can offer more energy for the nucleation and growth of the precipitations. On the other hand, substrate dissolution is accelerated as well. As the temperature increased from 37 ℃ to 100 ℃, the polarization resistance of the coated Mg first increased and then decreased. It had the best effect at 70 ℃. The corrosion current density of 70 ℃-coated Mg was remarkably decreased by two orders of magnitude with an over 99% inhibition efficiency. After four steps, which were substrate activation, surface calcification, precipitate nucleation, and deposition growth, the protective layer was deposited in situ on the Mg substrate. The main components of the deposited coating were good-crystallized DCPD and a small amount of HA and MgO.

The corrosion mechanism of R200-C70 was also discussed by monitoring the SBF pH value and the change of sample morphology during a 30-day immersion test in this chapter. The substrate corrosion that should have been very serious has been under effective control. In the beginning,

the coating was sacrificed as a barrier in the SBF immersion test. As the Ca-P layer was gradually dissolved and penetrated, the coating and the exposed Mg substrate were corroded together. At the same time, the new protective deposits were constantly generated, and the substrate was covered again in the final. In addition, the new deposition layer, which can hinder the attack of the corrosive solution, is rich in Ca element and P element due to the Ca-P dissolution in SBF. Therefore, there was no steep pH value increase in SBF, and the Mg substrate was under long-term protection. In general, the coating obtained from the traditional chemical bath deposition at 70 °C can protect the pure Mg for a long period.

REFERENCES

1. Ferrando, W., Review of corrosion and corrosion control of magnesium alloys and composites. Journal of Materials Engineering **1989,** 11 (4), 299-313.

2. Zhao, L.; Cui, C.; Wang, Q.; Bu, S., Growth characteristics and corrosion resistance of micro-arc oxidation coating on pure magnesium for biomedical applications. Corrosion Science **2010,** 52 (7), 2228-2234.

3. Witte, F., The history of biodegradable magnesium implants: a review. Acta biomaterialia **2010,** 6 (5), 1680-1692.

4. Wang, H.; Guan, S.; Wang, X.; Ren, C.; Wang, L., In vitro degradation and mechanical integrity of Mg–Zn–Ca alloy coated with Ca-deficient hydroxyapatite by the pulse electrodeposition process. Acta Biomaterialia **2010,** 6 (5), 1743-1748.

5. Kraus, T.; Fischerauer, S. F.; Hänzi, A. C.; Uggowitzer, P. J.; Löffler, J. F.; Weinberg, A. M., Magnesium alloys for temporary implants in osteosynthesis: in vivo studies of their degradation and interaction with bone. Acta biomaterialia **2012,** 8 (3), 1230-1238.

6. Harris, I.; Varley, P., Factors influencing brittleness in aluminium-magnesium-silicon alloys. J. Inst. Metals **1954,** 82.

7. Chandrasekaran, M.; John, Y. M. S., Effect of materials and temperature on the forward extrusion of magnesium alloys. Materials Science and Engineering: A **2004,** 381 (1-2), 308-319.

8. Hassan, S.; Gupta, M., Development of high performance magnesium nano-composites using nano-Al2O3 as reinforcement. Materials Science and Engineering: A **2005,** 392 (1-2), 163-168.

9. Ambat, R.; Aung, N. N.; Zhou, W., Evaluation of microstructural effects on corrosion behaviour of AZ91D magnesium alloy. Corrosion science **2000,** 42 (8), 1433-1455.

10. Liao, J.; Hotta, M.; Motoda, S.-i.; Shinohara, T., Atmospheric corrosion of two field-exposed AZ31B magnesium alloys with different grain size. Corrosion Science **2013,** 71, 53-61.

11. Birbilis, N.; Ralston, K.; Virtanen, S.; Fraser, H.; Davies, C., Grain character influences on corrosion of ECAPed pure magnesium. Corrosion Engineering, Science and Technology **2010,** 45 (3), 224-230.

12. Ralston, K.; Williams, G.; Birbilis, N., Effect of pH on the grain size dependence of magnesium corrosion. Corrosion **2012,** 68 (6), 507-517.

13. Hornberger, H.; Virtanen, S.; Boccaccini, A., Biomedical coatings on magnesium alloys–a review. Acta biomaterialia **2012,** 8 (7), 2442-2455.

14. Gray, J.; Luan, B., Protective coatings on magnesium and its alloys—a critical review. Journal of alloys and compounds **2002,** 336 (1-2), 88-113.

15. Feng, A.; Han, Y., Mechanical and in vitro degradation behavior of ultrafine calcium polyphosphate reinforced magnesium-alloy composites. Materials & Design **2011,** 32 (5), 2813-2820.

16. Bakhsheshi-Rad, H.; Hamzah, E.; Kasiri-Asgarani, M.; Jabbarzare, S.; Iqbal, N.; Kadir, M. A., Deposition of nanostructured fluorine-doped hydroxyapatite–polycaprolactone duplex coating to enhance the mechanical properties and corrosion resistance of Mg alloy for biomedical applications. Materials Science and Engineering: C **2016,** 60, 526-537.

17. Guo, H.; An, M., Growth of ceramic coatings on AZ91D magnesium alloys by micro-arc oxidation in aluminate–fluoride solutions and evaluation of corrosion resistance. Applied Surface Science **2005,** 246 (1-3), 229-238.

18. Tang, H.; Han, Y.; Wu, T.; Tao, W.; Jian, X.; Wu, Y.; Xu, F., Synthesis and properties of hydroxyapatite-containing coating on AZ31 magnesium alloy by micro-arc oxidation. Applied Surface Science **2017,** 400, 391-404.

19. Tekin, M.; Taslicay, C.; Muhaffel, F.; Cimenoglu, H. In Evaluation of Wear and Corrosion Resistances of Oxide Coatings Formed on Magnesium Alloys by Micro Arc Oxidation, Solid State Phenomena, Trans Tech Publ: 2017; pp 125-130.

20. Mattox, D. M., Physical vapor deposition (PVD) processes. Metal Finishing **2002,** 100, 394-408.

21. Westwood, W., Physical vapor deposition. In Microelectronic Materials and Processes, Springer: 1989; pp 133-201.

22. Sproul, W. D., Physical vapor deposition tool coatings. Surface and Coatings Technology **1996,** 81 (1), 1-7.

23. Aliofkhazraei, M.; Ali, N., PVD Technology in fabrication of micro-and nanostructured coatings. **2014**.

24. Qadir, M.; Li, Y.; Wen, C., Ion-substituted calcium phosphate coatings by physical vapor deposition magnetron sputtering for biomedical applications: A review. Acta biomaterialia **2019,** 89, 14-32.

25. Wang, Z.; Li, Q.; She, Z.; Chen, F.; Li, L., Low-cost and large-scale fabrication method for an environmentally-friendly superhydrophobic coating on magnesium alloy. Journal of Materials Chemistry **2012,** 22 (9), 4097-4105.

26. Bakin, B.; Delice, T. K.; Tiric, U.; Birlik, I.; Azem, F. A., Bioactivity and corrosion properties of magnesium-substituted CaP coatings produced via electrochemical deposition. Surface and Coatings Technology **2016,** 301, 29-35.

27. Kang, Z.; Li, W., Facile and fast fabrication of superhydrophobic surface on magnesium alloy by one-step electrodeposition method. Journal of industrial and engineering chemistry **2017,** 50, 50-56.

28. Liu, B.; Zhang, X.; Xiao, G.-y.; Lu, Y.-p., Phosphate chemical conversion coatings on metallic substrates for biomedical application: A review. Materials Science and Engineering: C **2015,** 47, 97-104.

29. Duan, G.; Yang, L.; Liao, S.; Zhang, C.; Lu, X.; Yang, Y.; Zhang, B.; Wei, Y.; Zhang, T.; Yu, B., Designing for the chemical conversion coating with high corrosion resistance and low electrical contact resistance on AZ91D magnesium alloy. Corrosion Science **2018,** 135, 197-206.

30. Gonzalez-Nunez, M.; Nunez-Lopez, C.; Skeldon, P.; Thompson, G.; Karimzadeh, H.; Lyon, P.; Wilks, T., A non-chromate conversion coating for magnesium alloys and magnesium-based metal matrix composites. Corrosion Science **1995,** 37 (11), 1763-1772.

31. Chen, X.-B.; Birbilis, N.; Abbott, T., A simple route towards a hydroxyapatite–Mg (OH) 2 conversion coating for magnesium. Corrosion Science **2011,** 53 (6), 2263-2268.

32. Song, Y.; Shan, D.; Chen, R.; Zhang, F.; Han, E.-H., Formation mechanism of phosphate conversion film on Mg–8.8 Li alloy. Corrosion Science **2009,** 51 (1), 62-69.

33. Su, Y.; Li, G.; Lian, J., A chemical conversion hydroxyapatite coating on AZ60 magnesium alloy and its electrochemical corrosion behaviour. Int. J. Electrochem. Sci **2012,** 7 (11), 11497-11511.

34. Jung, H.-G.; Jeong, Y. S.; Park, J.-B.; Sun, Y.-K.; Scrosati, B.; Lee, Y. J., Ruthenium-based electrocatalysts supported on reduced graphene oxide for lithium-air batteries. ACS Nano **2013,** 7 (4), 3532-3539.

35. Nair, M.; Nair, P., Chemical bath deposition of CuxS thin films and their prospective large area applications. Semiconductor science and technology **1989,** 4 (3), 191.

36. Fatas, E.; Garcia, T.; Montemayor, C.; Medina, A.; Camarero, E. G.; Arjona, F., Formation of CuxS thin films through a chemical bath deposition process. Materials Chemistry and Physics **1985,** 12 (2), 121-128.

37. Pavaskar, N.; Menezes, C.; Sinha, A., Photoconductive CdS films by a chemical bath deposition process. Journal of the Electrochemical Society **1977,** 124 (5), 743.

38. Cheng, J.; Fan, D.; Wang, H.; Liu, B.; Zhang, Y.; Yan, H., Chemical bath deposition of crystalline ZnS thin films. Semiconductor science and technology **2003,** 18 (7), 676.

39. Wang, M.-C.; Chen, H.-T.; Shih, W.-J.; Chang, H.-F.; Hon, M.-H.; Hung, I.-M., Crystalline size, microstructure and biocompatibility of hydroxyapatite nanopowders by hydrolysis of calcium hydrogen phosphate dehydrate (DCPD). Ceramics International **2015,** 41 (2), 2999-3008.

40. Wang, J.; Tang, J.; Zhang, P.; Li, Y.; Wang, J.; Lai, Y.; Qin, L., Surface modification of magnesium alloys developed for bioabsorbable orthopedic implants: a general review. Journal of Biomedical Materials Research Part B: Applied Biomaterials **2012,** 100 (6), 1691-1701.

41. Bajpai, I.; Kim, D. Y.; Kyong-Jin, J.; Song, I. H.; Kim, S., Response of human bone marrow-derived MSCs on triphasic Ca-P substrate with various HA/TCP ratio. Journal of Biomedical Materials Research Part B: Applied Biomaterials **2017,** 105 (1), 72-80.

42. Paital, S. R.; Dahotre, N. B., Laser surface treatment for porous and textured Ca–P bio-ceramic coating on Ti–6Al–4V. Biomedical Materials **2007,** 2 (4), 274.

43. Cai, Y.; Tang, R., Calcium phosphate nanoparticles in biomineralization and biomaterials. Journal of Materials Chemistry **2008,** 18 (32), 3775-3787.

44. Vallet-Regi, M.; González-Calbet, J. M., Calcium phosphates as substitution of bone tissues. Progress in solid state chemistry **2004,** 32 (1-2), 1-31.

45. Biltz, R. M.; Pellegrino, E. D., The nature of bone carbonate. Clinical orthopaedics and related research **1977,** (129), 279-292.

46. Märten, A.; Fratzl, P.; Paris, O.; Zaslansky, P., On the mineral in collagen of human crown dentine. Biomaterials **2010,** 31 (20), 5479-5490.

47. Sato, K., Mechanism of hydroxyapatite mineralization in biological systems. Journal of the Ceramic Society of Japan **2007,** 115 (1338), 124-130.

48. Malmberg, P.; Nygren, H., Methods for the analysis of the composition of bone tissue, with a focus on imaging mass spectrometry (TOF-SIMS). Proteomics **2008,** 8 (18), 3755-3762.

49. Batchelar, D. L.; Davidson, M. T.; Dabrowski, W.; Cunningham, I. A., Bone-composition imaging using coherent-scatter computed tomography: Assessing bone health beyond bone mineral density. Medical physics **2006,** 33 (4), 904-915.

50. Song, Y.; Shan, D.; Han, E., Electrodeposition of hydroxyapatite coating on AZ91D magnesium alloy for biomaterial application. Materials letters **2008,** 62 (17-18), 3276-3279.

51. Cui, F.-z.; Yang, J.-x.; Jiao, Y.-p.; Yin, Q.-s.; Zhang, Y.; Lee, I.-S., Calcium phosphate coating on magnesium alloy for modification of degradation behavior. Frontiers of Materials Science in China **2008,** 2 (2), 143-148.

52. Hiromoto, S.; Yamamoto, A., High corrosion resistance of magnesium coated with hydroxyapatite directly synthesized in an aqueous solution. Electrochimica Acta **2009,** 54 (27), 7085-7093.

53. Yue, L.; Ma, J.; Zhang, J.; Zhao, J.; Dong, S.; Liu, Z.; Cui, G.; Chen, L., All solid-state polymer electrolytes for high-performance lithium ion batteries. Energy Storage Mater. **2016,** 5, 139-164.

54. Oryan, A.; Alidadi, S., Application of Bioceramics in Orthope-dics and Bone Tissue Engineering. **2017**.

55. Hou, C.-h.; Chen, C.-w.; Hou, S.-m.; Li, Y.-t.; Lin, F.-h., The fabrication and characterization of dicalcium phosphate dihydrate-modified magnetic nanoparticles and their performance in hyperthermia processes in vitro. Biomaterials **2009,** 30 (27), 4700-4707.

56. Zhang, J.; Nancollas, G. H., Kinetics and mechanisms of octacalcium phosphate dissolution at 37. degree. C. The Journal of Physical Chemistry **1992,** 96 (13), 5478-5483.

57. Zhang, C.-Y.; Zeng, R.-C.; Chen, R.-S.; Liu, C.-L.; Gao, J.-C., Preparation of calcium phosphate coatings on Mg-1.0 Ca alloy. Transactions of Nonferrous Metals Society of China **2010,** 20, s655-s659.

58. Chopra, K. L.; Das, S. R., Why thin film solar cells? In Thin film solar cells, Springer: 1983; pp 1-18.

59. Ezekoye, B.; Offor, P.; Ezekoye, V.; Ezema, F., Chemical bath deposition technique of thin films: a review. International Journal of Scientific Research **2013,** 2 (8), 452-456.

60. Go, L. C.; Depan, D.; Holmes, W. E.; Gallo, A.; Knierim, K.; Bertrand, T.; Hernandez, R., Kinetic and thermodynamic analyses of the corrosion inhibition of synthetic extracellular polymeric substances. PeerJ Materials Science **2020,** 2, e4.

61. Zaludin, M. A. F.; Jamal, Z. A. Z.; Derman, M. N.; Kasmuin, M. Z., Fabrication of calcium phosphate coating on pure magnesium substrate via simple chemical conversion coating:

surface properties and corrosion performance evaluations. Journal of Materials Research and Technology **2019,** 8 (1), 981-987.

62. Martin, J.; Nominé, A.; Stef, J.; Nominé, A.; Zou, J.; Henrion, G.; Grosdidier, T., The influence of metallurgical state of substrate on the efficiency of plasma electrolytic oxidation (PEO) process on magnesium alloy. Materials & Design **2019,** 178, 107859.

63. Zhu, Y.; Wu, G.; Zhang, Y.-H.; Zhao, Q., Growth and characterization of Mg (OH) 2 film on magnesium alloy AZ31. Applied Surface Science **2011,** 257 (14), 6129-6137.

64. Lee, D.; Kumta, P. N., Chemical synthesis and stabilization of magnesium substituted brushite. Materials Science and Engineering: C **2010,** 30 (7), 934-943.

65. Mekmene, O.; Quillard, S.; Rouillon, T.; Bouler, J.-M.; Piot, M.; Gaucheron, F., Effects of pH and Ca/P molar ratio on the quantity and crystalline structure of calcium phosphates obtained from aqueous solutions. Dairy Science & Technology **2009,** 89 (3), 301-316.

66. Ohtsu, N.; Hiromoto, S.; Yamane, M.; Satoh, K.; Tomozawa, M., Chemical and crystallographic characterizations of hydroxyapatite-and octacalcium phosphate-coatings on magnesium synthesized by chemical solution deposition using XPS and XRD. Surface and Coatings Technology **2013,** 218, 114-118.

67. Güney, H.; İskenderoğlu, D., Synthesis of MgO thin films grown by SILAR technique. Ceramics International **2018,** 44 (7), 7788-7793.

68. Ho, Y.-H.; Vora, H. D.; Dahotre, N. B., Laser surface modification of AZ31B Mg alloy for bio-wettability. Journal of biomaterials applications **2015,** 29 (7), 915-928.

69. Groth, T.; Altankov, G., Studies on cell-biomaterial interaction: role of tyrosine phosphorylation during fibroblast spreading on surfaces varying in wettability. Biomaterials **1996,** 17 (12), 1227-1234.

70. Wei, K.; Kim, B.-S.; Kim, I.-S., Fabrication and biocompatibility of electrospun silk biocomposites. Membranes **2011,** 1 (4), 275-298.

71. Song, G.; Atrens, A., Understanding magnesium corrosion—a framework for improved alloy performance. Advanced engineering materials **2003,** 5 (12), 837-858.

72. Makar, G.; Kruger, J., Corrosion of magnesium. International materials reviews **1993,** 38 (3), 138-153.

73. Baril, G.; Pebere, N., The corrosion of pure magnesium in aerated and deaerated sodium sulphate solutions. Corrosion Science **2001,** 43 (3), 471-484.

74. Song, D.; Ma, A.; Jiang, J.; Lin, P.; Yang, D.; Fan, J., Corrosion behavior of equal-channel-angular-pressed pure magnesium in NaCl aqueous solution. Corrosion Science **2010,** 52 (2), 481-490.

75. Xin, Y.; Liu, C.; Zhang, X.; Tang, G.; Tian, X.; Chu, P. K., Corrosion behavior of biomedical AZ91 magnesium alloy in simulated body fluids. Journal of Materials Research **2007,** 22 (7), 2004-2011.

76. Zong, Y.; Yuan, G.; Zhang, X.; Mao, L.; Niu, J.; Ding, W., Comparison of biodegradable behaviors of AZ31 and Mg–Nd–Zn–Zr alloys in Hank's physiological solution. Materials Science and Engineering: B **2012,** 177 (5), 395-401.

77. Zhou, X.; Jiang, L.; Wu, P.; Sun, Y.; Yu, Y.; Wei, G.; Ge, H., Effect of aggressive ions on degradation of WE43 magnesium alloy in physiological environment. Int. J. Electrochem. Sci **2014,** 9, 304-314.

78. Braga, J. d. O.; de Carvalho, S. M.; Silva, L. M.; Soares, R. B.; Lins, V. F.; Mazzer, E. M.; Houmard, M.; Figueiredo, R. B.; Nunes, E. H., Fabrication and characterization of dicalcium

phosphate coatings deposited on magnesium substrates by a chemical conversion route. Surface and Coatings Technology **2020,** 386, 125505.

79. Kuo, M.; Yen, S., The process of electrochemical deposited hydroxyapatite coatings on biomedical titanium at room temperature. Materials Science and Engineering: C **2002,** 20 (1-2), 153-160.

80. Chun-Yan, Z.; Rong-Chang, Z.; Cheng-Long, L.; Jia-Cheng, G., Comparison of calcium phosphate coatings on Mg–Al and Mg–Ca alloys and their corrosion behavior in Hank's solution. Surface and Coatings Technology **2010,** 204 (21-22), 3636-3640.

81. Zhao, C.; Wu, H.; Hou, P.; Ni, J.; Han, P.; Zhang, X., Enhanced corrosion resistance and antibacterial property of Zn doped DCPD coating on biodegradable Mg. Materials Letters **2016,** 180, 42-46.

82. Dorozhkin, S. V., Self-setting calcium orthophosphate formulations: cements, concretes, pastes and putties. International Journal of Materials and Chemistry **2011,** 1 (1), 1-48.

83. Ren, W.; Song, W.; Yurgelevic, S.; Markel, D. C., Setting mechanism of a new injectable Dicalcium Phosphate Dihydrate (DCPD) forming cement. Journal of the mechanical behavior of biomedical materials **2018,** 79, 226-234.

84. Kibalczyc, W.; Zielenkiewicz, A., Calorimetric investigations of calcium phosphate precipitation. Journal of crystal growth **1987,** 82 (4), 733-736.

85. Bigi, A.; Gazzano, M.; Ripamonti, A.; Roveri, N., Effect of foreign ions on the conversion of brushite and octacalcium phosphate into hydroxyapatite. Journal of inorganic biochemistry **1988,** 32 (4), 251-257.

86. Fulmer, M.; Brown, P., Hydrolysis of dicalcium phosphate dihydrate to hydroxyapatite. Journal of Materials Science: Materials in Medicine **1998,** 9 (4), 197-202.

87. Lu, X.; Leng, Y., Theoretical analysis of calcium phosphate precipitation in simulated body fluid. Biomaterials **2005,** 26 (10), 1097-1108.

88. Martin, R.; Brown, P., The effects of magnesium on hydroxyapatite formation in vitro from CaHPO4 and Ca4 (PO4) 2O at 37.4 C. Calcified tissue international **1997,** 60 (6), 538-546.

89. Wang, Y.; Wei, M.; Gao, J., Improve corrosion resistance of magnesium in simulated body fluid by dicalcium phosphate dihydrate coating. Materials Science and Engineering: C **2009,** 29 (4), 1311-1316.

CHAPTER SEVEN: CONCLUSIONS AND FUTURE RECOMMENDATIONS

7.1 Present Work Conclusions

In this work, many efforts were made to improve the mechanical and anti-corrosion properties of pure Mg. The microstructural refinement and grain growth were achieved by different rolling routes and post-treatments. The protective coating was directly produced on the Mg substrate by traditional chemical bath deposition under different temperatures.

The results of mechanical property tests and in vitro corrosion experiments indicate that post-treatment shows a dual effect. Generally, the finer the grain is, the more and longer the grain boundaries and the more obstacles are produced to enhance the mechanical properties and corrosion resistance. During the post-heating, the grain size goes up and the number of grain boundary decrease, and it causes a higher stress concentrate and a lower resistance of dissolution. It should be noticed that when the grain size of rolled Mg is close to a few micron meters, grain boundaries can be regarded as crystalline defects initiating failure and corrosion. Essentially, the length of the grain boundary plays a dual role.

In 30-day immersion, the corrosion of pure Mg begins from small-localized pits continuously spreading and expanding. At the same time, the pH value of SBF rises rapidly. Subsequently, more and more white precipitates are formed on the surface of the substrate. The corrosion products of the pure Mg are primarily $Mg(OH)_2$ film as the inner layer, which makes the rising speed of the pH value slow down to the peak value with the extension of soaking time. Due to the hydroxyl-absorbed passive sites on the $Mg(OH)_2$, calcium/magnesium phosphates with

calcium/magnesium carbonates grow preferentially and easily and form the outer non-uniform layer. After the pH value approaches stabilized, it keeps fluctuating and goes down to a specific range because of a series of reactions among Mg^{2+}, Ca^{2+}, Cl^{-}, SO_4^{2-}, OH^{-}, HCO_3^{-}, and HPO_4^{2-}. During the chemical bath deposition, the interaction between the Mg substrate and treatment reagent takes place in situ. Furthermore, the coating quality is influenced by the substrate and treatment temperature. As the bath temperate increases from 37 °C to 100 °C, the polarization resistance of coated Mg rises first and then goes down. Because the high temperature provides more energy for the precipitate deposition but accelerates the substrate dissolution at the same time. The immersion test result demonstrates that pure Mg rolled under 200 °C is a suitable substrate. Moreover, 70 °C bath temperature could generate a compact Ca-P coating with effective long-period protection. The deposited coating on the bare Mg is double layered. The main component of the thin inner layer is still $Mg(OH)_2$, which comes from the sacrifice of the substrate. The outer layer is a well-crystallized Ca-P coating, mainly composed of DCPD and a small amount of HA and MgO. During the immersion test in a static SBF solution, the deposition Ca-P layer can protect the substrate as a barrier and control the pH value rapid growth. After the part of the coating is sacrificed, the complicated corrosive products of the inner Mg substrate are constantly generated on the sample surface, and the substrate is covered again. In addition, the new deposition layer, which can hinder the attack of the corrosive solution, is also rich in Ca and P elements due to the dissolution of the original Ca-P coating. They could continue to prevent the intrusion of the solution and provide a protective effect. So, the Mg substrate is protected from the beginning to the end instead of rapidly corroding.

7.2 Recommendations for Future Work

The biodegradable Mg and its alloys are recognized as the most promising materials in clinical applications [1-2]. However, their severe corrosion behaviors are critical challenges [3-5]. Our study provides an excellent example of making a calcium phosphate bio-ceramics coating on an Mg substrate to overcome the fast dissolution in physiological conditions. Both the plastic deformation process and coating technology parameters in this work are helpful guidance for pure Mg and coated Mg as potential biomaterials. The present study is an initial step. The requirements of the ideal biomedical materials for bone implants are complicated. They should have not only excellent corrosion resistance but also good biodegradability and biocompatibility. So, the related experiments and tests should be conducted in future work.

The first is the service time of implant materials. In some cases, patients can return to typical study and work-life after 4-6 weeks [6-7]. Nevertheless, the natural bone healing periods of different parts or different ages of people have great differences [8-10]. There are lots of situations that require a long physical recovery time. For these cases, the length of the immersion tests may be not long enough to be compared with the bone tissue growth. Therefore, it is necessary and considerable to prolong the observation time in the coming research. And the anti-corrosion ability is still needed to be improved. Another primary concern with bio-implants is their mechanical stability. Because most bone implants are used under physiological loading conditions after surgical operations, the Mg biocorrosion would also reduce physical and mechanical properties and even the sudden failure of the implants before tissue healing. Some Mg particles would fall off from the implant along with the corrosion progression because of

stress corrosion cracking, as known as the chunk effect [3-4]. Therefore, the mechanical properties of the samples should be paid close attention to for a more extended immersion test.

The second direction that can be improved is that the experimental conditions should be as close as possible to the actual and different human environments. Though reasonable and accurate test conditions of the SBF solution, there are still many shortcomings in vitro experiments. Witte et al. have found that the Mg dissolution rate in vitro is faster than that in vivo [5, 11-12]. Furthermore, bioactivity like cell attachment, propagation, and tissue growth on the bone implants, is a very important requirement. It would be desirable if cell viability and cell morphology could be carried out to discern the biological performance. Therefore, it is worthwhile to further investigate the in vivo to get a more accurate degradation behavior. In next step, our group will focus on how to obtain a more sustainable coating for biomaterial application and control the in vivo degradation rate. The mechanism of pure Mg corrosion in vivo is much more complicated than that of in vitro because of the environmental conditions. Moreover, the exact prediction of the implant life is relatively difficult. The correlation between in vitro and in vivo results is still being investigated because the experimental results would deviate from the real application results. Thus, the in vitro and in vivo tests are not accurate enough to confirm diagnoses of the responses of Mg implants in living bodies. Besides, the reasonable different degradation performance must be taken into consideration when the Mg implants are applied to different body parts because of the big impact on surrounding environments. Otherwise, the dissolution behavior may be misestimated. At the same time, various mild foreign body reactions in the post-implantation and long-term service must be paid attention to. In this way, a series of animal

tests should be proceeded to estimate the physiological reactions of implants in the following work.

From the perspective of coating, the additional experiments should be considered to gain the coating with feasible and controllable degradation time for future applications. Besides deposited coatings, producing coated Mg by other methods is also very promising in biomaterial surface modification. In most cases, only one technology is insufficient to make a perfect coating. So, in the following research, coating method and material combinations can be studied to improve coating behavior effectively. In a word, these research ideas are worthy of further study to design and obtain more desirable protective coatings.

REFERENCES

1. Li, N.; Zheng, Y., Novel magnesium alloys developed for biomedical application: a review. Journal of Materials Science & Technology **2013,** 29 (6), 489-502.

2. Witte, F.; Kaese, V.; Haferkamp, H.; Switzer, E.; Meyer-Lindenberg, A.; Wirth, C.; Windhagen, H., In vivo corrosion of four magnesium alloys and the associated bone response. Biomaterials **2005,** 26 (17), 3557-3563.

3. Ferrando, W., Review of corrosion and corrosion control of magnesium alloys and composites. Journal of Materials Engineering **1989,** 11 (4), 299-313.

4. Zhao, L.; Cui, C.; Wang, Q.; Bu, S., Growth characteristics and corrosion resistance of micro-arc oxidation coating on pure magnesium for biomedical applications. Corrosion Science **2010,** 52 (7), 2228-2234.

5. Witte, F., The history of biodegradable magnesium implants: a review. Acta biomaterialia **2010,** 6 (5), 1680-1692.

6. Wang, H.; Guan, S.; Wang, X.; Ren, C.; Wang, L., In vitro degradation and mechanical integrity of Mg–Zn–Ca alloy coated with Ca-deficient hydroxyapatite by the pulse electrodeposition process. Acta Biomaterialia **2010,** 6 (5), 1743-1748.

7. Kraus, T.; Fischerauer, S. F.; Hänzi, A. C.; Uggowitzer, P. J.; Löffler, J. F.; Weinberg, A. M., Magnesium alloys for temporary implants in osteosynthesis: in vivo studies of their degradation and interaction with bone. Acta biomaterialia **2012,** 8 (3), 1230-1238.

8. Watson, N.; Haines, T.; Tran, P.; Keating, J. L., A comparison of the effect of one, three, or six weeks of immobilization on function and pain after open reduction and internal fixation of distal radial fractures in adults: a randomized controlled trial. JBJS **2018,** 100 (13), 1118-1125.

9. Shuai, C.; Li, S.; Peng, S.; Feng, P.; Lai, Y.; Gao, C., Biodegradable metallic bone implants. Materials Chemistry Frontiers **2019,** 3 (4), 544-562.

10. Meyer Jr, R. A.; Desai, B. R.; Heiner, D. E.; Fiechtl, J.; Porter, S.; Meyer, M. H., Young, adult, and old rats have similar changes in mRNA expression of many skeletal genes after fracture despite delayed healing with age. Journal of orthopaedic research **2006,** 24 (10), 1933-1944.

11. Willbold, E.; Gu, X.; Albert, D.; Kalla, K.; Bobe, K.; Brauneis, M.; Janning, C.; Nellesen, J.; Czayka, W.; Tillmann, W., Effect of the addition of low rare earth elements (lanthanum, neodymium, cerium) on the biodegradation and biocompatibility of magnesium. Acta biomaterialia **2015,** 11, 554-562.

12. Witte, F.; Fischer, J.; Nellesen, J.; Vogt, C.; Vogt, J.; Donath, T.; Beckmann, F., In vivo corrosion and corrosion protection of magnesium alloy LAE442. Acta biomaterialia **2010,** 6 (5), 1792-1799.